Technical Report Documentation Page

1. Report No. MN/RC 2019-XX	2.	3. Recipients Accession No.	
4. Title and Subtitle Performance Benefits of Fiber-reinforced Thin Concrete Pavement and Overlays		5. Report Date [June 2021]	
		6.	
7. Author(s) Manik Barman, Souvik Roy, Amarjeet Tiwari, Tom Burnham		8. Performing Organization Report No. University of Minnesota Duluth	
9. Performing Organization Name and Address Department of Civil Engineering University of Minnesota Duluth 1049 University Dr, Duluth, MN 55812		10. Project/Task/Work Unit No.	
		11. Contract (C) or Grant (G) No. 1003325	
12. Sponsoring Organization Name and Address Minnesota Department of Transportation Office of Research & Innovation 395 John Ireland Boulevard, MS 330 St. Paul, Minnesota 55155-1899		13. Type of Report and Period Covered Final Report	
		14. Sponsoring Agency Code National Road Research Alliance	
15. Supplementary Notes http://mndot.gov/research/reports/2019/2019XX.pdf			

16. Abstract (Limit: 250 words)

This study investigates the performance benefits of synthetic structural fibers in mitigating distresses in thin concrete pavements and overlays. In this study, two ultra-thin (3 and 4 inches thick) and four thin (5 and 6 inches thick) concrete pavements placed on a gravel base, along with two thin unbonded concrete overlay cells (5 inches thick) placed on an existing concrete pavement were constructed at the Minnesota Road Research (MnROAD) facility in 2017. This report discusses the objectives and methodology of the research, including the construction of the test cells, instrumentation, traffic load application, and data collection and analysis procedures. The structural responses and distresses observed over three years, such as fatigue cracking and faulting, as well as the joint performance measured in each cell, were discussed and compared.

| 17. Document Analysis/Descriptors

Concrete Pavement, Overlays, Synthetic fibers, crack, faulting,

joint performance, | | 18. Availability Statement

No restrictions. Document available from:

National Technical Information Services,

Alexandria, Virginia 22312 | |
| 19. Security Class (this report)

Unclassified | 20. Security Class (this page)

Unclassified | 21. No. of Pages | 22. Price |

Performance Benefits of Fiber-reinforced Thin Concrete Pavement and Overlays

FINAL REPORT

Prepared by:

Manik Barman, Souvik Roy, Amarjeet Tiwari
Department of Civil Engineering
University of Minnesota Duluth

Tom Burnham
Minnesota Department of Transportation

June 2021

ACKNOWLEDGMENTS

TABLE OF CONTENTS

LIST OF FIGURES

LIST OF TABLES

EXECUTIVE SUMMARY

Ultra-thin and thin concrete overlays and pavements for low-volume roads can economize pavement structures by saving taxpayers' dollars in materials costs. In the last few decades, transportation agencies constructed thin concrete overlays with observable benefits. The concrete overlays are constructed either on moderately distressed existing asphalt or concrete pavement surface. These concrete overlays are typically 3 to 6 inches thick and constructed with small-size panels like 6 ft x 6 ft. Because of the inadequate cover thickness, joint load transfer devices like standard dowel bars are often not used; instead, some transportation agencies use synthetic structural fiber-reinforced concrete (FRC). The success of the application of structural fibers in the overlays has also invoked interest to construct ultra-thin and thin FRC concrete pavements on a new or existing gravel base.

Previous laboratory and field performance studies have demonstrated that synthetic structural fibers can improve the performance of concrete by holding cracks tight, increasing the load transfer between slabs, and arresting slab migration. While it is evident that synthetic structural fibers can improve the performance of concrete overlays or pavements, limited research was conducted to understand the performance benefit of FRC and to quantify the influence of the structural fibers in mitigating the distresses in them. This lack of knowledge gap is probably the reason that the current concrete pavement and overlay design procedures do not accurately account for the benefits of the inclusion of structural fibers.

This study, funded by the National Road Research Alliance (NRRA), is designed to understand and quantify the influence of synthetic structural fibers in mitigating common distresses like panel fatigue cracking and transverse joint faulting in thin concrete overlays and thin concrete pavements on a gravel base. In addition, this study explored whether the construction of 3 and 4 inches thick ultra-thin FRC pavements is feasible for low-volume roads and city streets. The study also looked at whether the use of FRC can allow for large panel sizes in thin concrete overlays to decrease the cost of saw-cuts.

Under the scope of this study, the Minnesota Department of Transportation (MnDOT) constructed eight test cells at MnROAD in 2017. Seven cells were constructed with FRC, and one control cell was constructed with plain concrete (Cell 506). Cells 139 (3 inches thick) and 239 (4 inches thick) were constructed as ultra-thin FRC pavements (8 lbs./cy synthetic structural fiber dosage) on an un-stabilized marginal (6 inches thick) gravel base. Cells 506, 606, 706, and 806 were constructed as thin concrete pavements (5 to 6 inches thick) on a relatively stiff (11 inches thick) un-stabilized gravel base with

varying fiber dosages (0%, 5, 8, and 11.7 lbs./cy fiber dosages, respectively). Cells 705 and 805 (5 inches thick) were constructed as thin unbonded concrete overlays on an existing concrete pavement, with varying panel widths (~6ft vs ~12 ft); these two cells contained a 5 lbs./cy fiber dosage. Cell 139 and 239 were constructed on the low volume test track, and the other cells were constructed on the interstate traffic-loaded portion of MnROAD. Exposing several test sections to live interstate traffic allowed for accelerated development of distresses. All eight cells were equipped with different types of sensors for measuring responses such as (i) dynamic strain due to wheel loads, (ii) strain induced by the environmental forces, (iii) pavement temperature and gradient, and (iv) transverse joint movement. Periodical surveys of cracks, spalling, and faulting were conducted to keep track of the distresses. Falling weight deflectometer (FWD) tests were periodically conducted to determine joint performance in different seasons.

The entire research work was divided into different tasks. The very first task dealt with a literature search on the application of FRC in concrete overlays and pavements. Task 2A, B, and C dealt with the analysis of the pavement distresses and structural responses on a yearly basis throughout the duration of the project (summer 2017 through spring 2020). Tasks 3, 4, and 5 dealt with investigating the effect of synthetic structural fibers on the panel fatigue cracking, joint faulting, and panel size, respectively. Some key findings from all the above-mentioned tasks are listed below:

1) Between the two ultra-thin cells constructed in this study, it was found that the 4-inch thick Cell 239 provided significantly better performance compared to the 3-inch thick Cell 139. The construction of a 3-inch thick pavement on a marginal base layer may not be a good design, irrespective of the inclusion of the structural fibers. Many panels under Cell 139 were shattered (but remain intact), with the pavement surface depressed along the wheel path. The performance of Cell 239 indicated that longitudinal fatigue cracking would be the most critical distress by far.

2) The distresses observed in thin pavement Cells 506-806 indicated that 5 to 6 inches thick concrete pavements placed on a stiff gravel base layer are not prone to fatigue cracks for the typical low volume road design life (2 million ESALs). The contribution of the fibers was evident in mitigating transverse joint faulting, with faulting magnitudes decreasing with an increase in fiber dosage. Compared to Cell 806, which incorporated a much higher dosage rate than typically specified by most road agencies (11.7 lbs./cy fiber dosage), Cell 506 (no fiber) experienced more than twice the amount of faulting at two million ESALs. The IRI results also

clearly showed the contribution of fibers in improving the riding quality of the thin concrete pavements.

3) Regarding the unbonded concrete overlays placed on a fabric interlayer (Cells 705 and 805), it was seen that Cell 805 with narrow panels resulted in less percentage of cracked slabs (35%) than the wide panels in Cell 705 (50% cracked) after three years of traffic and climate (~ 3 million ESALs). Cell 705 experienced more longitudinal cracks compared to Cell 805, which experienced more transverse cracks. The transverse and corner cracks of Cell 805 and 705 were comparable. It seems the higher slab curvature for thin overlays can create more longitudinal cracks. Faulting and IRI values were also more prominent for Cell 705.

4) This study determined the magnitudes of many important structural responses that would be typical for thin concrete overlays and pavements, like typical temperate gradients, environmental strains, dynamic strains, crack with openings, and slab curvatures, etc.

5) This study has provided quantifiable evidence that structural fibers can positively influence joint performance, transverse joint faulting, IRI, etc. Therefore, it will be prudent to take the initiative to incorporate the performance benefits of the structural fibers into the mechanistic-empirical design procedure, which currently just artificially enhances the material flexural strength to account for the fibers' inclusion.

Lastly, it should be cautioned that the results from this experiment represent the behavior of three dosages of one synthetic fiber. It should not be construed that the results represent the behavior of other types and dosages of synthetic fibers or concrete mixtures, for that matter.

1 INTRODUCTION

1.1 GENERAL

Ultra-thin and thin concrete overlays and pavements for low-volume roads can economize pavement structures by saving taxpayers' dollars in materials costs. In the last few decades, transportation agencies constructed thin concrete overlays with observable benefits. The concrete overlays are constructed either on moderately distressed existing asphalt or concrete pavement surface. These concrete overlays are typically 3 to 6 inches thick and constructed with small-sized panels like 6 ft x 6 ft. Because of inadequate cover thickness, joint load transfer devices like standard dowel bars are often not used; instead, some transportation agencies use synthetic structural fiber-reinforced concrete (FRC). The success of the application of structural fibers in the overlays has also invoked interest to construct FRC ultra-thin and thin concrete pavements on a new or existing gravel base.

Structural fibers are presently available in different material compositions (steel and synthetic), stiffnesses, shapes, lengths, and aspect ratios (ratio of length to effective diameter). The typical length of structural fibers used in concrete pavements is 1.5 inches or greater. Synthetic structural fibers are more predominantly used in pavements than steel fibers due to their ease of handling, better dispersion characteristics, and corrosion resistance. The most popular synthetic fiber material is polypropylene. They can be of straight, crimped, twisted, or embossed geometry along the length.

Previous laboratory and field performance studies have demonstrated that synthetic structural fibers have improved the performance of concrete pavement and overlays by holding cracks tight, transferring the wheel load between adjacent slabs, and arresting slab migration. While the benefit of the synthetic structural fiber-reinforced concrete is evident, research need arises in quantifying the contribution of structural fibers in mitigating panel fatigue cracking and transverse joint faulting in thin concrete overlays and pavement on grade. There is interest in understanding the effects of fiber-reinforced concrete on panel size, especially for thinner slabs (like 5 inches thick), and exploring if the concrete slab thickness can be decreased as low as 3 inches for the low-volume roads.

To this end, the Minnesota Department of Transportation (MnDOT) constructed eight pavement test cells at the Minnesota Road Research (MnROAD) facility in the summer and fall of 2017. MnROAD is a pavement test facility owned and operated by MnDOT and located on westbound I-94, northwest of the

Twin Cities metropolitan area. These test cells included two ultra-thin (3 to 4 inches thick) and four thin (5 to 6 inches thick) FRC pavements on a granular base layer and two thin unbonded concrete (5 inches thick) overlays on existing concrete pavement. This research project was funded by the National Road Research Alliance (NRRA). All eight cells were equipped with different types of sensors for measuring responses such as (i) dynamic strain due to wheel load, (ii) strain induced by the environmental forces, (iii) pavement temperature and gradient, and (iv) transverse joint movement. Periodical surveys of cracks, spalling, and faulting were conducted to keep track of the distresses. Falling weight deflectometer (FWD) tests were periodically conducted to determine joint performance in different seasons. This report provides comprehensive detail of the distresses observed in all the test cells. It analyzes and discusses the responses measured by different sensors throughout the study period (Summer 2017 to spring 2020) and finally provides the conclusions and recommendations on the influence of the synthetic structural fibers on fatigue cracking, transverse joint faulting, and structural responses.

1.2   GOAL AND OBJECTIVES

The goal of this study is to identify and quantify the contribution of synthetic structural fibers in mitigating different distresses that typically occur in thin concrete pavements and overlays. The following are the list of the objectives:

- Determining the contribution of fibers in reducing panel fatigue cracking
- Determining the influence of fibers in joint faulting and joint performance
- Determining whether wide-paneled thin concrete overlays can be constructed using synthetic structural fibers
- Determining whether the construction of 3 and 4 inches thick ultra-thin FRC pavements is feasible for low-volume roads and city streets

-

2   RESEARCH METHODOLOGY

The research started with the construction of the test cells at MnROAD in the summer and fall of 2017. The detailed construction report can be found at MnDOT (2018). All the cells were instrumented with various sensors. MnDOT has collected sensor, distress, and performance data throughout the duration of the study (2017 summer to Spring 2020) and provided them to the research team. The entire research work was divided into different tasks. The very first task dealt with a literature search on the application of FRC in concrete overlays and pavements. Task 2A, B, and C dealt with the analysis of the pavement distresses and structural responses on a yearly basis throughout the duration of the project. Tasks 3, 4, and 5 dealt with investigating the effect of synthetic structural fibers on the panel fatigue cracking, joint faulting, and panel size, respectively.

This chapter briefly discusses the critical information of the test cells, including pavement design variables, traffic loadings, sensor layout, and data collection and analysis procedures.

2.1   MNROAD FRC TEST CELL DESIGN

The schematic plan of the research cells at the MnROAD test facility is shown in Figure 2-1; these cells are referred to as '2017 FRC test cells' in this report.

Table 2-1 presents a summary of the designs and materials used in these test cells. A total of eight cells were constructed, among which seven cells were constructed with FRC and one control cell with plain concrete (Cell 506). Cells 139 and 239, constructed on the low volume road (LVR) test track, were ultra-thin (3-inch) and thin (4-inch) concrete pavements on a 6-inch thick un-stabilized gravel base. These two cells were constructed to

3

investigate whether synthetic structural fibers could be helpful toward constructing 3 to 4 inches thick pavements on low-volume roads and city streets. A fiber dosage of 8 lbs./cy (see

Table 2-1 for the dosage information) was used in these two cells. This "enhanced" dosage (30% RSR [residual strength ratio] from ASTM 1609 test) was chosen over a more typical dosage (20% RSR from ASTM 1609) to aid in the expected high levels of strain that might be experienced by such thin concrete panels. Cells 506, 606, 706, and 806 were constructed as thin concrete pavement with 5 and 6 inches thick slabs on an 11 inches thick un-stabilized gravel base. These four cells were constructed with various fiber dosages (0, 5, 8, and 11.7 lbs./cy) to investigate the influence of synthetic structural fibers on joint performance, faulting, and fatigue cracks. Cells 705 and 805 were constructed as thin unbonded concrete overlays (5-inch) on an existing deteriorated concrete pavement. The objective for the construction of these two cells was to investigate whether wider slabs (~12 ft) could be constructed using synthetic structural fibers. A fiber dosage of 5 lbs./cy (corresponding to 20%RSR) was used in these two cells. As shown in Figure 2-1, Cells 705, 805, and 506 - 806 were constructed on the I-94 interstate traffic mainline portion of MnROAD.

Table 2-2 presents the paving dates of different cells. Figure 2-2 shows a photograph of the fiber used in all the seven FRC cells. Table 2-3 presents the concrete mixture-related information.

2017 FRC test cells on LVR test track
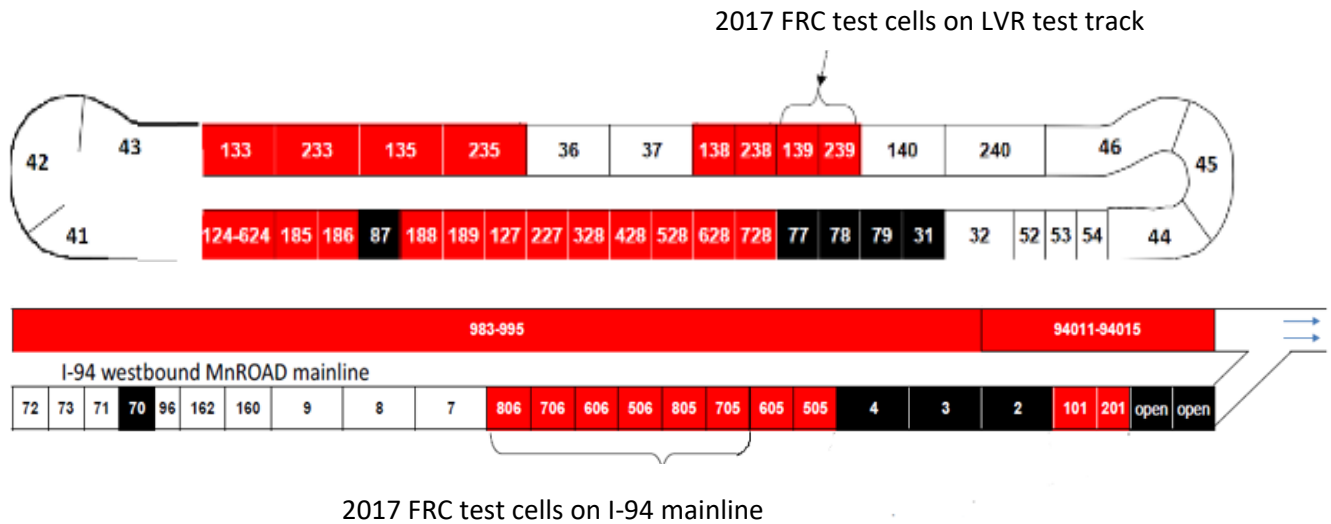
Figure 2-1: Location of the 2017 FRC test cells at the MnROAD test facility (MnDOT, 2018).

Table 2-1: Pavement design summary of the 2017 FRC test cells.

Cell number	Length (ft)	Pavement/ overlay Type	Underlying layer (constr. year)	Type of concrete/ fiber dosage*	Panel size W ft x L ft	Panel thickness (inch)	Number of panels
139	270	Ultra-thin Pavement on gravel base	6 in. class 5 aggregate base (2017)	FRC/ enhanced	6 x 6	3	180

5

Cell number	Length (ft)	Pavement/ overlay Type	Underlying layer (constr. year)	Type of concrete/ fiber dosage*	Panel size W ft x L ft	Panel thickness (inch)	Number of panels
239	273	Thin Pavement on gravel base	6 in. class 5 aggregate base (2017)	FRC/ enhanced	6 x 6	4	176
506	144	Thin pavement on gravel base	11 in. Class 5Q aggregate base (2017)	*Plain concrete*	6 x 6	5	96
606**				*FRC/ standard*			92
706	138			*FRC/ enhanced*			76
806				*FRC/ high*			88
705	144	Thin unbonded overlay on concrete pavement (w/fabric interlayer)	Concrete (1993)	FRC/ standard	*Driving: 14 x 12 Passing: 12 x 12*	5	22
805	124				*Driving: 6 x 12 and 8 x 12 Passing: 6 x 12 and 6 x 12*	5	40

* Fiber dosages: standard (5 lbs./cy) - corresponding to 20% residual strength ratio (ASTM C1609); enhanced (8 lbs./cy)- corresponding to 30% residual strength ratio (ASTM C1609); high (11.7 lbs./cy) – corresponding to 0.75 fibers volume fraction.

** Even though the design thickness was 5 inches, the actual measured thickness was found to be 6 inches.

Table 2-2. Paving dates and times 2017 FRC test cells.

CELL	Date	Approximate Time
139	7/17/2017	9:15:00 AM
239	7/17/2017	9:15:00 AM

CELL	Date	Approximate Time
506	6/26/2017	9:20:00 AM
606	6/27/2017	9:15:00 AM
706	6/29/2017	8:45:00 AM
806	6/30/2017	8:00:00 AM
705	9/5/2017	2:00:00 PM
805	9/5/2017	3:00:00 PM

Figure 2-2: Photograph of the fibers used in MnROAD 2017 FRC test cells.

Table 2-3. Mix designs for 2017 FRC test cells (includes control mix with no fibers) (MnDOT, 2018).

Mix/Cell	Water (lbs.)	Cement (lbs.)	Fly ash (lbs.)	Fly ash %)	FA #1 (lbs.)	CA #1 (lbs.)	Fibers (lbs./cy)	Fibers (% of conc. vol.)	W/C Ratio	Target RSR (%)	Slump range (in.)	Air (%)

MR-3A21FC/ 506	239	400	170		1222	1798	0	0		0		
MR-3A21F1/ 705,805,606	248	413	177	30	1204	1773	5	0.33	0.42	20	0.5-3	7.0
MR-3A21F2/ 139,239,706	252	420	180		1196	1761	8	0.52		30		
MR-3A21F3/ 806	258	430	185		1184	1743	11.66	0.75		NA		

Table 2-4 presents the results from test beams prepared at the project site for the ASTM C 1609 test. The average 28-day residual strength for the concrete used in Cells 606, 706, and 806 were 124, 156, and 254 psi, respectively. The average 28-day residual strength for Cells 139 and 239 was 185 psi, and 116.53 psi for Cells 705 and 805. The 28-day modulus of rupture (MOR) values for Cell 506, 606, 706, and 806 were 650, 635, 675, and 680 psi, respectively. The MOR for Cells 139 and 239 was 610 psi, and 542 psi for Cells 705 and 805. The other relevant fresh and hard concrete test results, including the ASTM C-1609 test results for all of the cells, can be found in the Appendix.

Table 2-4: Measured properties of concretes used in the FRC test cells.

Cell number	Hardened concrete properties		
	28-day MOR (psi)	28-day residual strength (psi)	28-day RSR (%)
139	610	185	30.4
239			
705	542	116	21.5
805			
506	650	No applicable (NA)	NA
606	640	124	19.4
706	680	156	23.0
806	680	254	37.4

2.2   TRAFFIC LOAD

The low volume road portion of the MnROAD facility, where Cells 139 and 239 were constructed, has two lanes, referred to as the inside and outside lanes. The inside lane is exposed to traffic load, and the outside lane is reserved for studying the influence of the environmental loads alone on the pavement. The traffic loads on the low volume road is provided by a 356-kN, 5-axle, tractor/trailer combination, which averages approximately 70 laps per day, equivalent to 30,000 to 40,000 ESALs per year. Thin pavement Cells 506 to 806 and the two overlay cells (Cells 705 and 805) were constructed on the high volume interstate traffic "mainline" segment of MnROAD, which consists of two lanes running parallel to the original westbound interstate highway I-94. These two lanes receive live traffic diverted off westbound I-94 approximately 75 percent of the time. Approximately one million ESALs are applied yearly on the high volume segment of MnROAD. It shall be mentioned that when collecting data from dynamic (traffic) response sensors, the MnROAD LVR truck is used in all test cells (mainline and LVR) to apply known loadings.

2.3   SENSOR PLAN

MnROAD 2017 FRC test cells were instrumented with four types of sensors: joint opening, dynamic strain gauge, vibrating wire strain gauge, and temperature sensors (thermocouples). Figure 2-3 and Figure 2-4 show the sensor plans for Cell 139 and 506, respectively. Both the plans are for the inner lane /driving lane, which was exposed to traffic and environmental loads. The sensor plans for all other cells are provided in APPENDIX. Table 2-5 presents the statistics of different sensors for each of the eight cells.
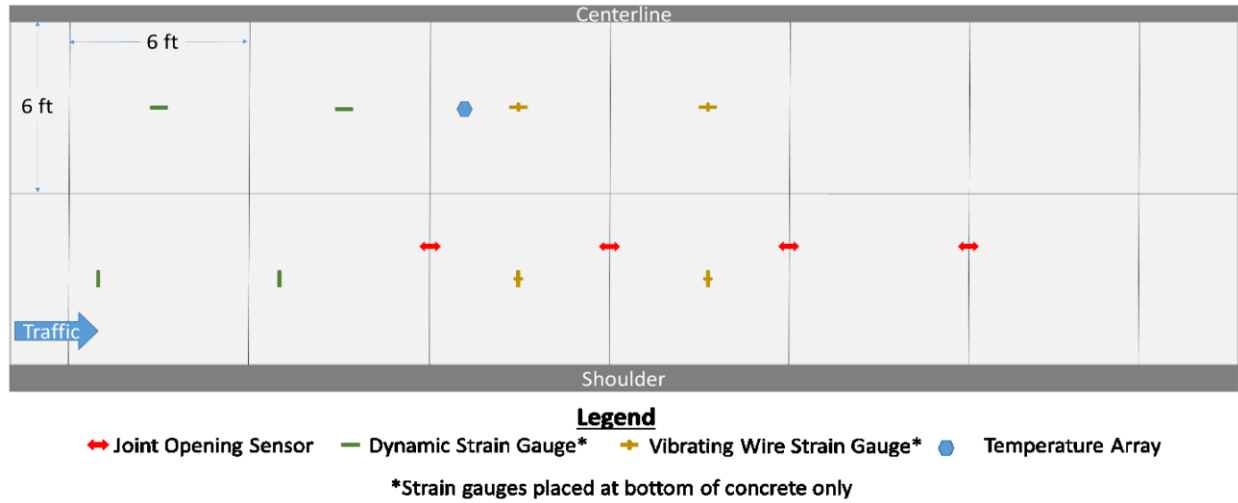
Figure 2-3: Sensor plan for Cell 139 inner lane.
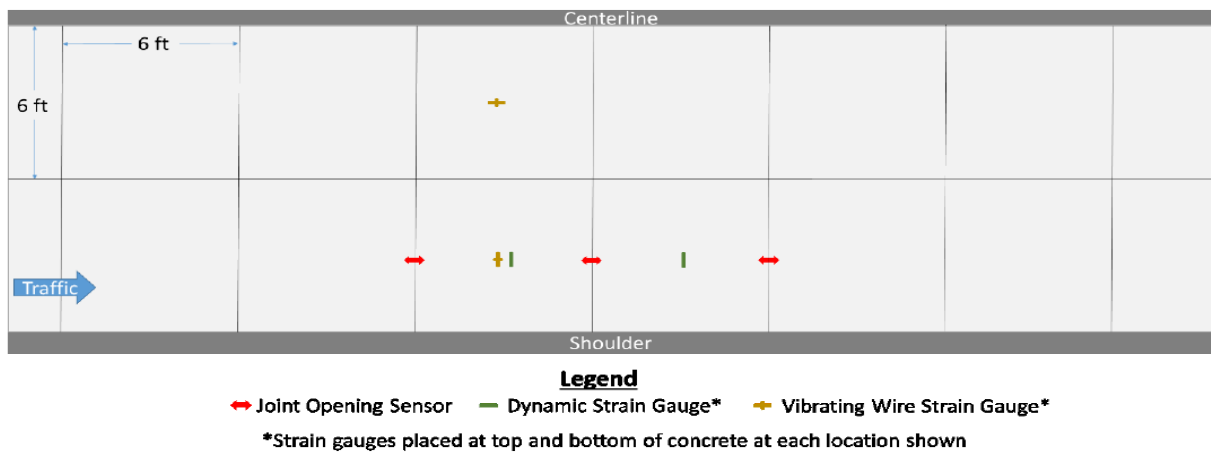
Figure 2-4: Sensor plan for Cell 506, driving lane.

10

Table 2-5: Sensor statistics for the FRC test Cells.

Cell number/lane(s) where sensors installed	Trans. joint opening	Dynamic strain gauge/ direction (long or trans.)	Vibrating wire strain gauge direction (long or trans.)	Thermocouple
139/inner lane	4	2/long.; 2/trans.	2/long.; 2/trans.	16
239/both lanes	8	2/long.; 2/trans.	2/long.; 2/trans.	16
705/driving lane	4	4/long.; 4/trans.	4/long.; 4/trans.	8
805/driving lane	4	4/long.; 4/trans.	4/long.; 4/trans.	12
506/driving lane	3	4/trans.	2/long.; 2/trans.	None
606/driving lane	3	4/trans.	2/long.; 2/trans.	8
706/driving lane	3	4/trans.	2/long.; 2/trans.	None
806/driving lane	3	4/trans..	2/long.; 2/trans.	None

2.3.1   Temperature Sensors

Thermocouple sensors were installed to capture the variations of temperature and temperature-gradient in the concrete slab. Thermocouples were installed at different depths within and beneath the concrete slabs. Figure 2-5 shows an example of a thermocouple sensor tree before it was installed. One sensor tree was installed in each of the Cells 139, 705, and 805; two trees were installed in Cells 239 and 606, located at two different offsets from the centerline. To distinguish between the two sensor trees in Cells 239 and 606, the farthest sensor tree from the centerline was designated as the outer sensor, and the sensor tree closer to the centerline as the inner sensor. Temperature data was collected from all of the thermocouple sensors ta every 15 minutes. In addition to collecting pavement temperature data, ambient temperature data were also collected at MnROAD using an external weather station, which can collect other ambient parameters like precipitation, relative humidity, wind speed, wind direction, etc.
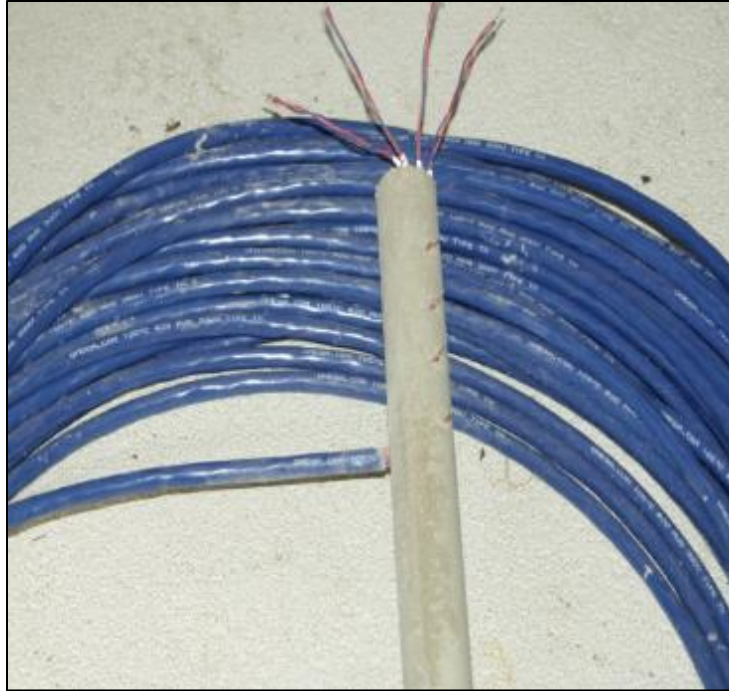
Figure 2-5. Example of a thermocouple sensor tree.

2.3.2 Vibrating Wire Sensor (Environmental strain)

Vibrating wire (VW) sensors were installed in all the cells to measure the strains caused by responses to environmental-based changes within the slabs. A photograph of a vibrating sensor is shown in Figure 2-6. The raw data from this type of sensor is converted to estimate the environmental strain exerted on the concrete due to the change in the moisture state, temperature and temperature gradient, freezing of underlying layers, and joint locking. Data was collected from VW sensors every 15 minutes.

Figure 2-6. Photograph of a vibrating wire sensor.

2.3.3   Dynamic Strain Sensor

A photograph of the dynamic sensor is provided in Figure 2-7. This type of sensor records the dynamic strain in the slab when a vehicle (in this case, MnDOT's five-axle truck) passes over them. As the tire offset (distance of the wheel from the sensor in the transverse direction) affects the readings, MnDOT's truck was run multiple times for each data collection date. The raw data collected from the sensors were processed, and peaks, valleys, and baseline (Figure 2-8) were determined using the MnDOT's Peak-Pick Program (Burnham and Tewfik, 2007) for each run. Figure 2-8 is an example of the plot generated for each run with the peaks and valleys noted. As the truck has five axles, each sensor documents five peaks and five valleys for each run. These plots were used to determine the strain experienced by each sensor under each of the five axle loads. The difference between the peaks and baseline is considered as the measured strain. The maximum of five strain values from all the runs on the measurement date are compared with each other, and the largest value of them is reported as the dynamic strain for the sensor in question.

Figure 2-7. Photograph of a dynamic strain sensor.
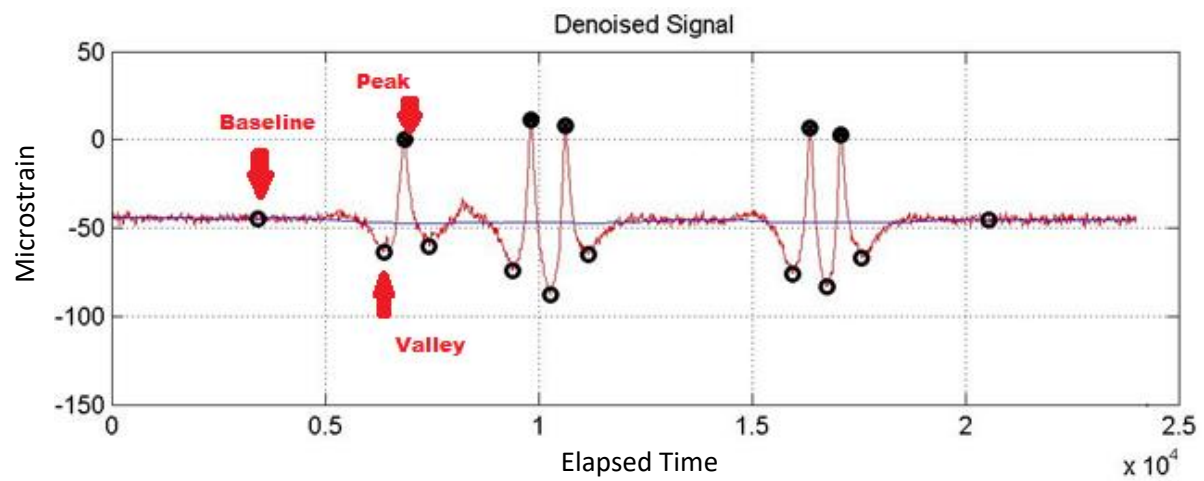
Figure 2-8. An example of a plot of strain due to the dynamic load exerted by the MnDOT truck.

2.3.4 Joint Opening Sensor

A new type of joint opening sensor (spring-loaded potentiometer) was installed in MnROAD 2017 FRC test cells. A sketch and two photographs of this type of joint opening sensors are provided in Figure 2-9. This sensor was used installed in selected transverse joints to track joint movement throughout the year.
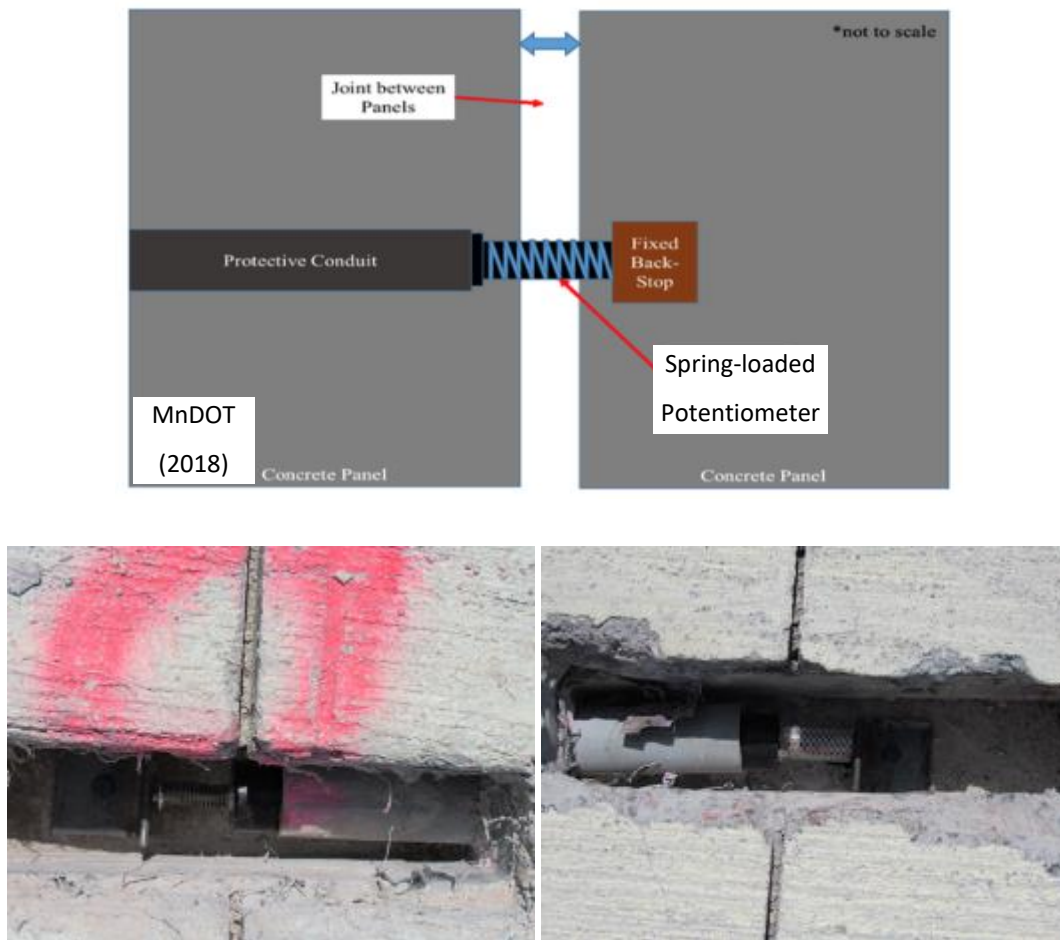
Figure 2-9. Sketch and photographs of joint opening sensors before installation of protective covering.

2.4 DISTRESS AND PERFORMANCE SURVEYS

2.4.1 Cracks and Spalling

The LTPP (FHWA, 2015) style cracking surveys were periodically conducted by MnDOT, with results recorded manually on MnROAD pavement distress survey sheets, which were then used to generate consolidated color-coded distress maps. A panel or slab is considered to be cracked when it is divided into three or fewer pieces. The cracks must be at least 2-feet long. Joint spalling can occur along both transverse and longitudinal joints.

2.4.2 Joint Performance

Transverse joint performance was evaluated by conducting Falling Weight Deflectometer (FWD) tests across select joints. FWD data was used to determine the load transfer efficiency (LTE), differential displacement, and loaded-side displacement. The LTE is the ratio of the deflections at the unloaded side to the loaded side and is expressed as a percentage. The differential displacement is the absolute difference between the loaded-side deflection and unloaded-side deflection. Further, FWD deflection data was used to investigate the presence of voids underneath the slabs.

2.4.3 Transverse Joint Faulting

Transverse joint faulting is defined as the difference in elevations between two adjacent concrete pavement slabs. Repeated heavy axle loads crossing transverse joints create the potential for joint faulting. Excessive edge and corner deflections that cause erosion and pumping of fines from beneath a loaded leave slab result in faulting. The progression rate of faulting depends on the combination of poor load transfer, heavy axle loads, free moisture beneath the pavement, and erosion and pumping of the supporting layers (Khazanovich et al., 2004). Eroded fines may get deposited under the approach slab, which normally raises the approach slab over the leave slab, known as positive faulting. The negative faulting, which is uncommon, occurs when the leave slabs raise over the approach slabs.

For the current study, joint faulting was measured at ten randomly selected transverse joints in each cell, with four readings along each joint. The MnROAD (Georgia DOT style, Stone, 1991) fault-meter was used for faulting measurements. It should be noted that the surface texture depth for concrete pavements is usually around 0.04 inch or 1 mm on average; therefore, any readings below 1 mm may

not indicate any notable faulting. Faulting for each cell is the average of all the faulting readings (total 40) taken in a cell. In addition to comparing the faulting values between the cells, this study also proposed a parameter called "Faulting Index" to compare the faulting behavior between the cells and to compare the faulting trend with the International Roughness Index (IRI).

2.4.4   Pavement Condition Surveys

Pavement Roughness was evaluated using International Roughness Index (IRI). The IRI is equal to the total vertical movement of a standard vehicle accumulated over a unit length of the road. The IRI is typically reported in units of inches/mile (or mm/km in SI unit), i.e., vertical inches of movement per mile traveled (Janisch, 2015). Janisch, in his study, developed a relationship between IRI and Ride Quality Index (RQI), which MnDOT uses to rate the riding quality of the pavement (Table 2-6). It has a range of 0.0 to 5.0, with 0.0 being very poor ride quality and 5.0 being very good. The following equation was proposed by Janisch (2015) to convert RQI into IRI for concrete pavements.

$$RQI = 6.634 - (0.353) * (\sqrt{IRI}) \tag{1}$$

The above equation was used to compute the corresponding IRI value from the RQI to determine the IRI values for different pavement riding ratings, as presented in Table 2-6.

Table 2-6: RQI and IRI rating scale

Verbal Rating	RQI	IRI (in./mile)
Very good	4.1 - 5.0	20 - 55
Good	3.1 - 4.0	56 - 105
Fair	2.1 - 3.0	106 - 172
Poor	1.1 - 2.0	173 - 255
Very Poor	0.0 – 1.0	256 - 353

3 INFLUENCE OF FIBERS ON FATIGUE CRACKING AND SLAB WIDTH

One of the objectives of this study was to investigate the effect of synthetic structural fibers on mitigating and/or slowing the rate of deterioration of fatigue cracking. The other objective was to study whether these fibers can permit designers to use wider slabs. This chapter presents a comprehensive analysis of the fatigue cracking data. The effort was given to understand the nature of fatigue cracks that occur in the ultrathin and thin pavements. Fatigue crack data were compared between the cells to understand the influence of the fibers on the fatigue cracks and slab size. Prediction equations were developed for fatigue crack based on the field data. Finite element analysis was performed to understand the influence of the fibers on the fatigue life of the pavement.

3.1   FATIGUE CRACKING DATA

FHWA Long Term Pavement Performance (LTPP) style cracking surveys were periodically conducted by MnDOT, with results recorded manually on MnROAD color-coded distress maps. Table 3-1 shows the different dates of the surveys, including the approximate ESALs accumulated by the date of each survey. The following section elaborates on the distresses observed in each cell.

Table 3-1. List of distress survey dates and accumulated ESALs.

Cell	Construction Dates in 2017	2018 Distress Survey Dates/ ESALs	2019 Distress Survey Dates / ESALs	2020 Distress Survey Dates /ESALs
139	Jul 17	May 1/ 49K	Mar 18/ 82K; Dec 4/ 114K	Mar 24/ 195K
239	Jul 17	May 1/ 38K	Mar 18/ 62K; Dec 4/ 122K	Mar 24/ 146K
705	Sep 5	Mar 13/ 750K Apr 25/ 825K	Mar 18/ 1,800K; Oct 23/ 2,400K	Mar 5/2700K
805	Sep 5	Mar 13/ 750K; Apr 25/ 825K	Mar 18/ 1,800K; Oct 23/ 2,400K	Mar 5/2700K
506	Jun 26	Mar 14/ 750K	Mar 19/ 1,800K; Oct 25/ 2,400K	Mar 5/2700K
606	Jun 27	Mar 14/ 750K	Mar 19/ 1,800K; Oct 25/ 2,400K	Mar 5/2700K
706	Jun 29	Mar 14/ 750K	Mar 19/ 1,800K; Oct 25/ 2,400K	Mar 5/2700K
806	Jun 30	Mar 14/ 750K	Mar 19/ 1,800K; Oct 25/ 2,400K	Mar 5/2700K

3.1.1 Cells 139 and 239

Cell 139 was inadvertently exposed to early loads from construction trucks that were using the crossover segment to access other cells under construction, resulting in many early-age cracks. Placement of shoulder materials with heavy equipment may have also caused some of these early cracks to form. Figure 3-1 shows a picture of a couple of such early-age cracks in this cell. These cracks continued to develop and propagated with age and MnROAD truck loadings, which eventually led to the shattering of many slabs by the end of the summer of 2018, as shown in Figure 3-2. Besides that, there was a considerable amount of depression along the outer wheel path at some locations; this distress looked like rutting that occurs in asphalt pavements. Because of this cell's significantly different distress pattern compared to other cells (slab shattering vs fatigue cracking), Cell 139's crack data was not included in studying fibers' influence on the development of fatigue cracks. The distress survey sheet for this Cell is provided in the Appendix.
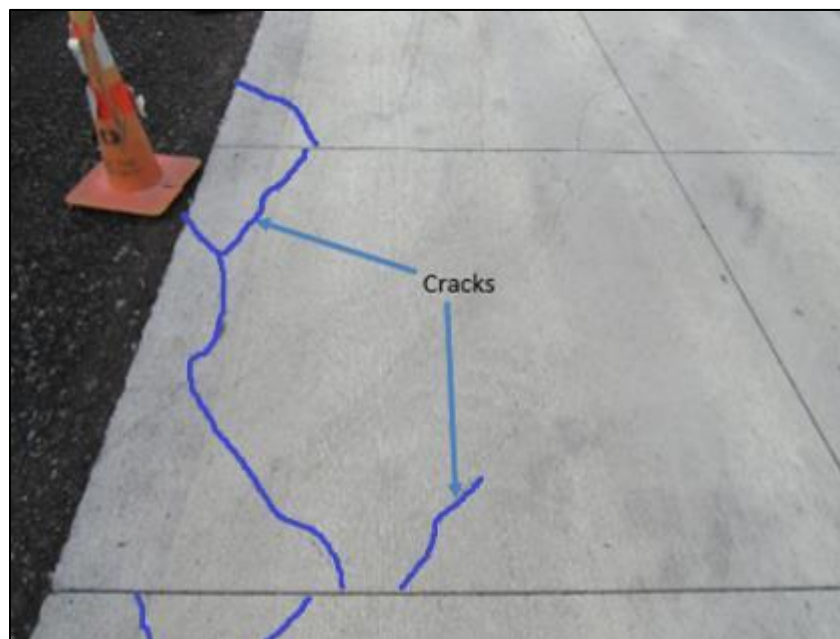
Figure 3-1. Cell 139 after exposure to construction trucks.

Figure 3-2: Shattered slabs and depression along the wheel path in Cell 139 after MnROAD truck loadings.

Due to the occurrence of the high severity distresses (slab shattering and depression along the wheel path), 14 of the 44 slabs in the inside lane of Cell 139 were replaced on September 27, 2018. The replacement slabs were 4-inch thick, with eight of them containing fiber reinforced concrete and the other six with plain concrete. The fibers used in the replacement slabs were different and laterally stiffer than those used in 2017, as shown in Figure 3-3. The dosage of the fiber was 5.5 lbs./cy, which corresponds to a 30% residual strength ratio. The replacement slabs have performed well, with only one crack noticed in the spring 2020 distress survey.
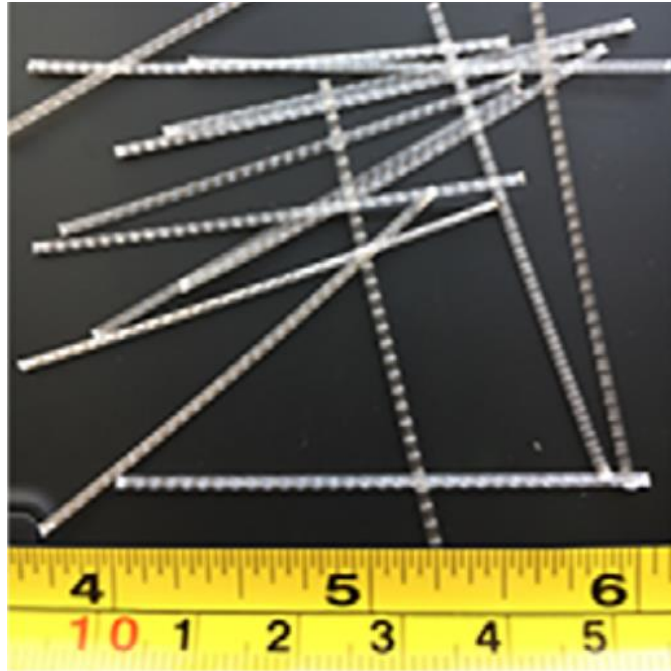
(a)

Figure 3-3. Photograph of fibers used in the replacement slabs of Cell 139.

On the other hand, unrepaired (original) slabs continued to develop distress with traffic load and age, with primary longitudinal and secondary transverse and diagonal cracks. Based on the December 2019 distress survey data, it was found that as much as 75% of the slabs had cracked in Cell 139 after 114,000 ESALs were applied to them. Figure 3-4 shows four photographs of Cell 139 taken in October 2019. The unrepaired slabs eventually failed and became undrivable in the middle of the third year of service (2020).

Figure 3-4. A few photographs of Cell 139 during October 2019.

While the slab thickness (only 3-inch thick) and early-age loading were probably the main reasons for the initiation of the distresses of Cell 139, the relatively weak base layer and some drainage issues were believed to have aggravated the distress of this cell.

Cell 239 also experienced longitudinal and corner cracks, as shown in Figure 3-5 and Figure 3-6, respectively. Figure 3-7 shows the consolidated distress map indicating the cracks measured at different seasons and years. Some of the corner cracks along the shoulder were thought to be caused by the placement of the shouldering material. This cell performed significantly better than Cell 139 throughout the three years of observation. Based on the distress survey data until March 2020, 35 panels have cracked in this cell, with 27 in the inside lane. A total of 20% of slabs had cracked after 145,000 ESALs in this cell compared to more than 75% cracked slabs in Cell 139 with a similar traffic load.
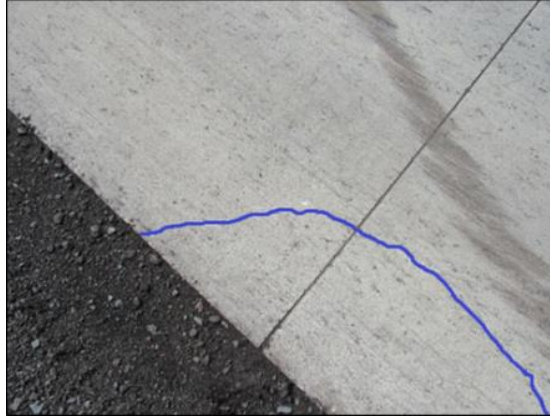
Figure 3-5. Corner cracks in Cell 239 (2018).

Figure 3-6. Longitudinal cracks in Cell 239 (April 2019)
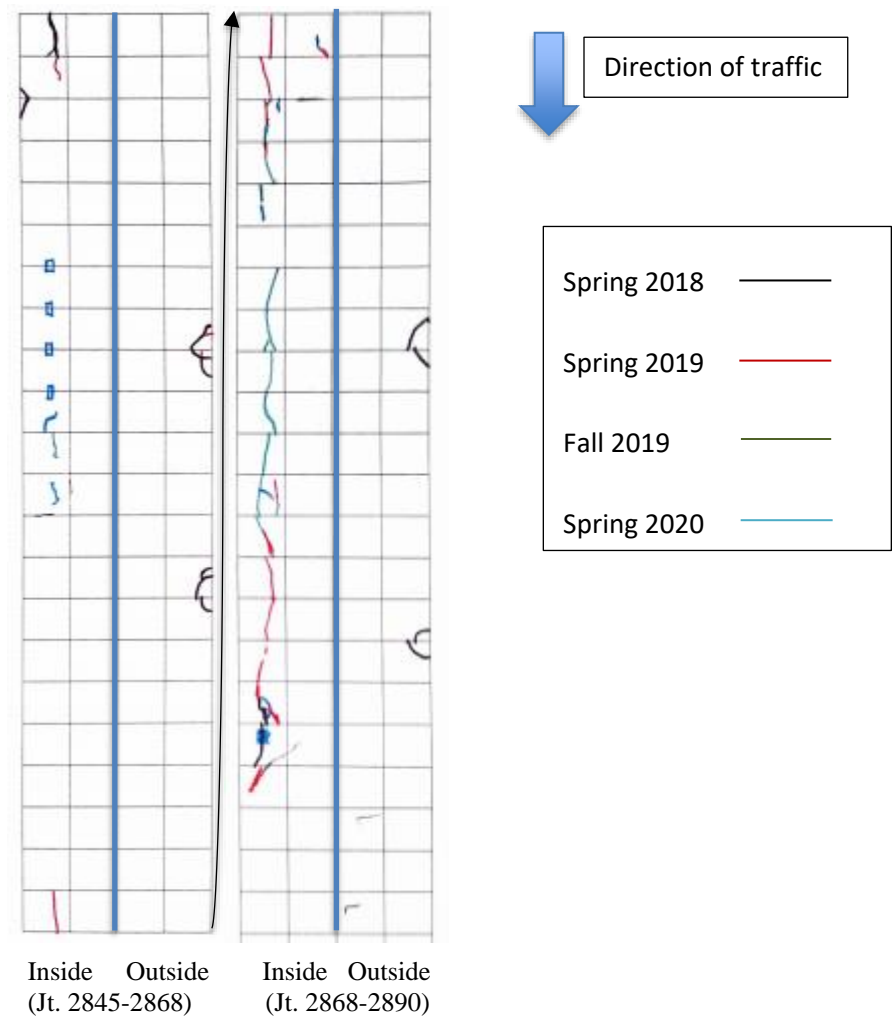
Figure 3-7: Color-coded distress map for Cell 239 (MnROAD truck load was applied to the inside lane).

3.1.2 Cells 506 through 806

Cell 506, control cell, which is a concrete pavement on a gravel base, constructed without any fibers, experienced one transverse crack and spalling on 15 transverse joints before April 2018. The October 2019 distress survey reveals that Cell 506 experienced one diagonal crack and two more transverse cracks in addition to the cracks observed in 2018. Figure 3-8 and Figure 3-9 show photographs of the transverse crack and joint spalling documented in April 2018. Figure 3-10 shows the photograph of the cracks in 2019. All three cracks developed in three adjacent slabs, with their condition severely

deteriorating to the point they had to be replaced in the summer of 2020. Figure 3-11 shows a photograph of distressed slabs of Cell 506 before they were replaced in June 2020.

Regarding the spalling in Cell 506, upon looking closer at multiple spalling locations, it was found that joint gaps were filled with hardened saw-cut residue; it is assumed that concrete residues were not cleaned out of the joints after sawing. There was a clear correlation between the spalling and the presence of the residue. It was up to ¼" deep and completely spanned the saw cut. Thus, when the joints closed in the summer, the spalls formed in these locations. Figure 3-12 shows two photographs of hardened saw-cut residue found at the spalled joints of Cell 506. No visible saw-cut residue was noticed in the joints of other cells.

Figure 3-8. Transverse crack in Cell 506 (control, non-FRC) observed in the year 2018.

Figure 3-9. Spalling in Cell 506 (control, non-FRC) observed in the year 2018.

Figure 3-10. Photographs of transverse and diagonal cracks in Cell 506 (October 2019)

Figure 3-11. Cell 506 before replacement on June 2020
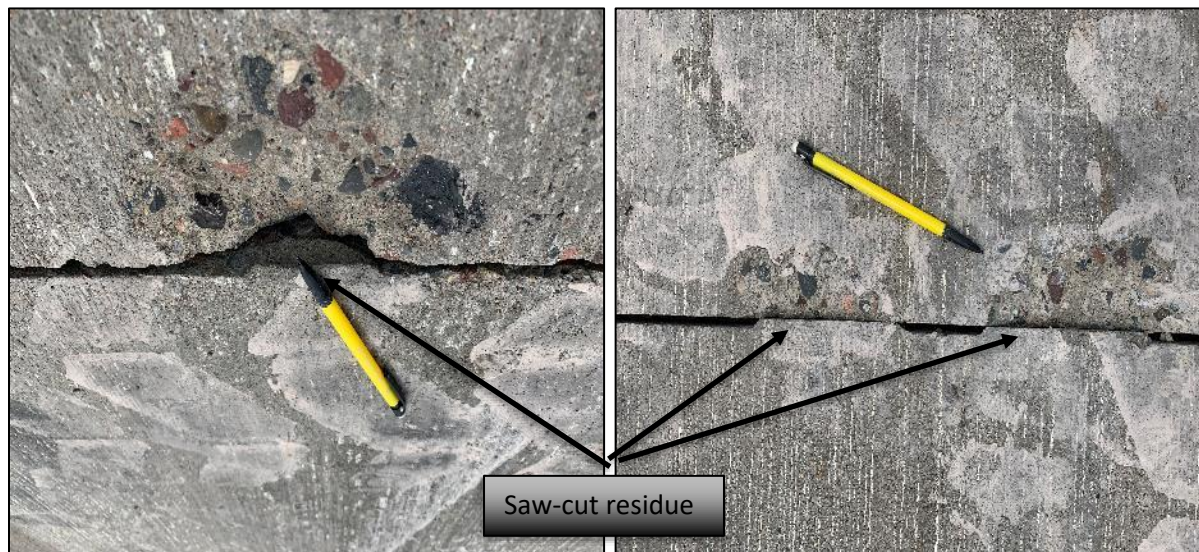
Saw-cut residue

Figure 3-12. Hardened saw-cut residue found at the spalled joints of Cell 506.

Cell 606, which was constructed with 5 lbs. /cy (20% residual strength) of synthetic structural fibers, experienced one corner crack prior to April 2018. This corner crack was the only crack observed during the 2019 distress survey as well. Figure 3-13 shows photographs of the crack in April 2018 and October 2019. It can be seen that the severity of this crack did not change much as compared to what has happened for the cracks in Cell 506 (Figure 3-8 vs. Figure 3-10). As this crack is located in the last panel next to a cell transition joint, it can be assumed that this crack is not a typical fatigue-related crack; it occurred because of a construction issue. The distress survey conducted in March 2020 found one joint with spalling and two additional low severity corner cracks. Figure 3-14 shows the color-coded distress map for Cells 506 and 606, where the locations of the crack in Cell 506 can be seen.

(a)   (b)
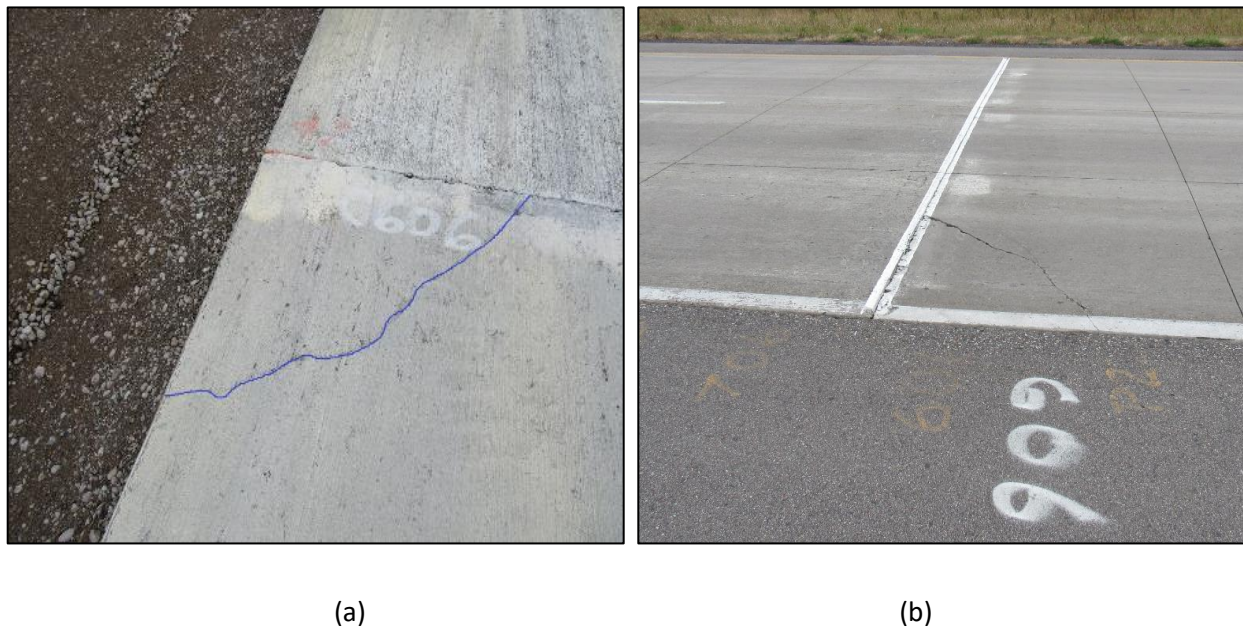
Figure 3-13. Corner crack (construction issue) in the last panel of Cell 606 observed (a) in the year 2018 and (b) 2019.
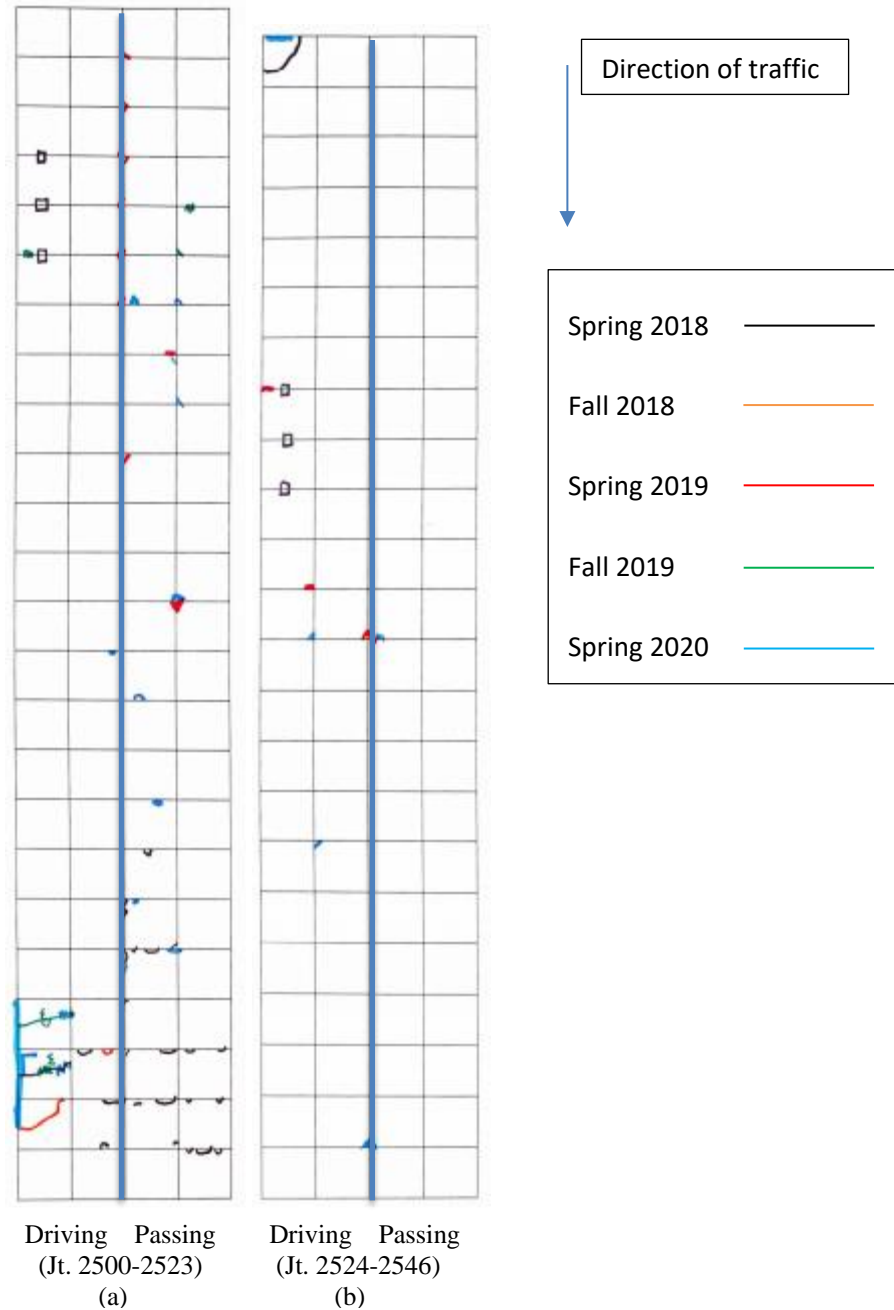
Figure 3-14: Distress Maps (a) Cell 506 (b) Cell 606.

Cells 706 and **806**, which were constructed with fiber dosages of 8 and 11.7 lbs./cy, respectively, did not experience any cracks or spalling before October 2019 except for a couple of narrow cracks in Cell 806 originating at the location of a joint opening sensor (Figure 3-15). The March 2020 distress survey did not report any additional cracks for these two cells.

Figure 3-15. Narrow cracks in Cell 806, originated at the location of the joint opening sensor

A summary of the fatigue cracks documented in Cells 239 and 506 through 806 until March 2020 is provided in Figure 3-16. This figure does not include the unique distresses that developed in Cell 139. A close looking of Figure 3-7, Figure 3-14, and Figure 3-16 confirm that 4-inch thick Cell 239 (with 8 lbs./cy fibers) has more visible cracks than 5-inch thick 506 and 6-inch thick 606 (with 5 lbs./cy fibers), despite significantly fewer traffic loadings in the low volume test track.

The comparison of the fatigue-related cracks or distresses between Cells 139 and 239 indicates the primary distresses for the ultrathin pavements would be the longitudinal cracks along the wheel path, and the 3-inch-thick pavement would likely experience a significant amount of depression and slab shattering along the wheel path as well. However, the fatigue crack pattern of such ultrathin pavements should be reconfirmed by constructing similar pavements on a thicker, more stable base layer before making a generalized conclusion.

The fatigue crack data of the thin pavement Cells 506-806 confirms that fatigue cracks may not be the dominant distresses for such pavement designs, especially when slabs are constructed on thicker and more stable bases.
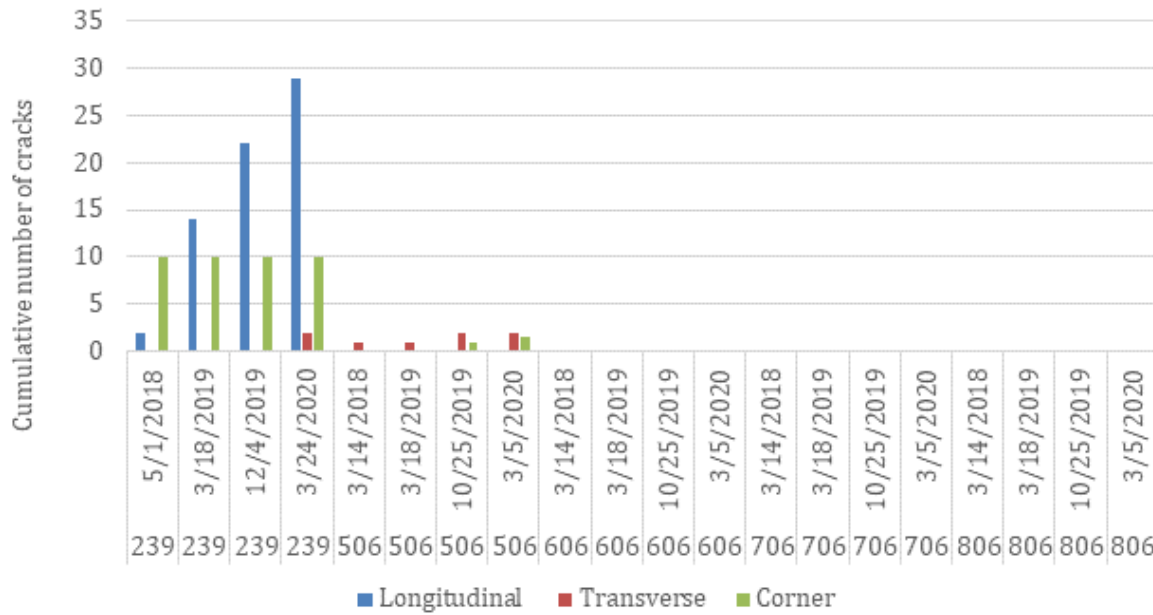
Figure 3-16: Summary of fatigue cracks of cells on gravel base until March 2020 (Cell 139 not shown).

3.1.3 Cells 705 and 805

Cell 705 was constructed as a 5-inch thick unbonded concrete overlay placed over a nonwoven geotextile fabric secured to an existing 7.5-inch-thick concrete pavement constructed in 1993. Cell 705 was constructed with large slabs, 12 ft Wide (W) x 12 ft Long (L) (passing lane), and 14 ft W x12 ft L (driving lane). Figure 3-17 to Figure 3-21 show different types of fatigue cracks recorded in the distress surveys conducted at various times from 2018 through 2020.

Figure 3-17. Longitudinal crack in Cell 705 (2018).

Figure 3-18. Transverse crack in Cell 705 (2018).
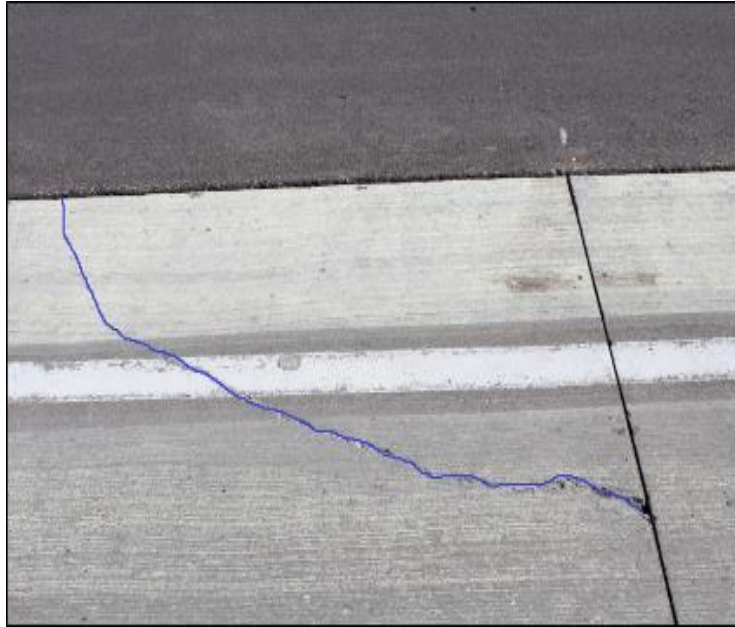
Figure 3-19. Corner crack in Cell 705 (2018).
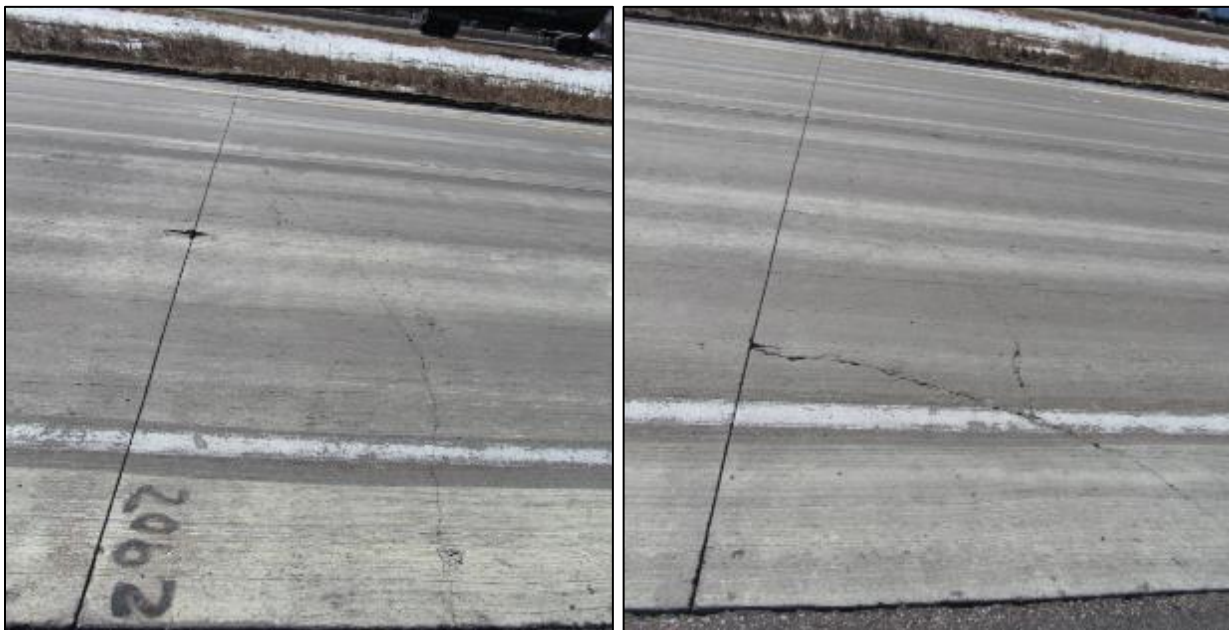
Figure 3-20. Photographs of transverse and corner cracks in Cell 705 as observed during April 2019.

Figure 3-21. Photograph of Cell 705 before replacement on September 2020.

Cell 805, which was also constructed as a 5-inch thick unbonded concrete overlay, has narrower slabs compared to Cell 705, as shown in

Table 2-1. This cell also experienced longitudinal cracks, transverse cracks, and corner cracks. Figure 3-22 to Figure 3-26 show different types of cracks observed in the distress surveys conducted at various times.

Color-coded distress maps for Cell 705 and 805 are provided in Figure 3-27, where the locations of the cracks in the cell can be seen. Figure 3-28 presents the cumulative numbers of cracks on different dates for the two cells. Based on the distress survey data available until March 2020, 11 out of 22 panels were

cracked in Cell 705, of which eight were in the driving lane; a total of 50% slabs had cracked after 2.7 million ESALs. For Cell 805, 14 out of 40 slab panels have cracked, of which 13 were in the driving lane; 65% of the slabs in the driving lane and 35% of total slab panels cracked (15% less than Cell 705) after 2.7 million ESALs. Cell 705 experienced more longitudinal cracks than transverse and corner cracks. The reason for the larger number of longitudinal cracks in this cell may be due to the higher amount of curvature of thin wider slabs. Cell 805 experienced longitudinal, transverse, and corner cracks in comparable quantities. Like Cell 705, the concrete overlay in the driving lane of this cell was eventually taken out of service during the third year of service, after approximately 3 million ESALs.

Figure 3-22. Longitudinal crack in Cell 805 (2018)

Figure 3-23. Transverse crack in Cell 805 (2018)
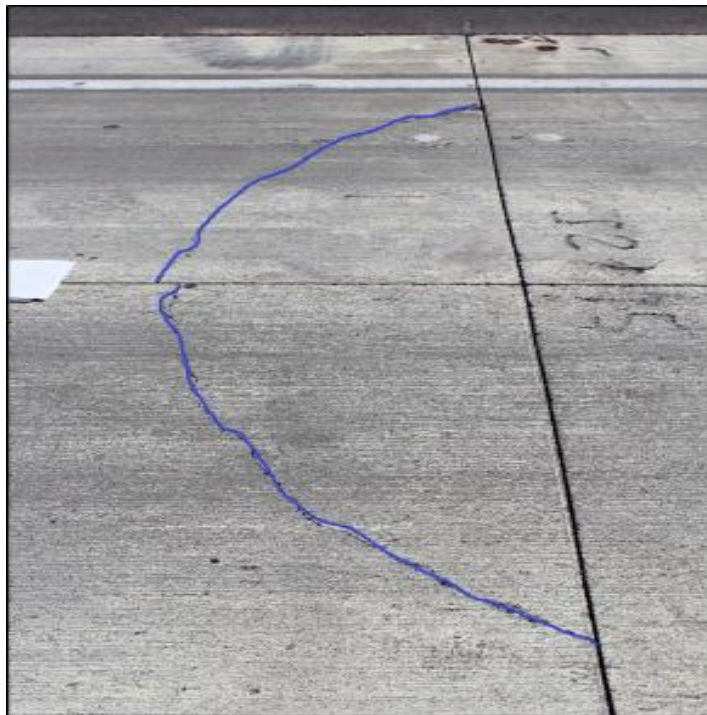
Figure 3-24. Corner crack in Cell 805 (2018)

Figure 3-25. Photographs of observed cracks in Cell 805 during April 2019.

Figure 3-26. Photograph of Cell 805 before removal on September 2020.

Direction of traffic

Spring 2018 ——————
Fall 2018 ——————
Spring 2019 ——————
Fall 2019 ——————
Spring 2020 ——————

Driving   Passing   Driving   Passing
(Jt. 2900-2909)   (Jt. 2910-2918)
(a)   (b)
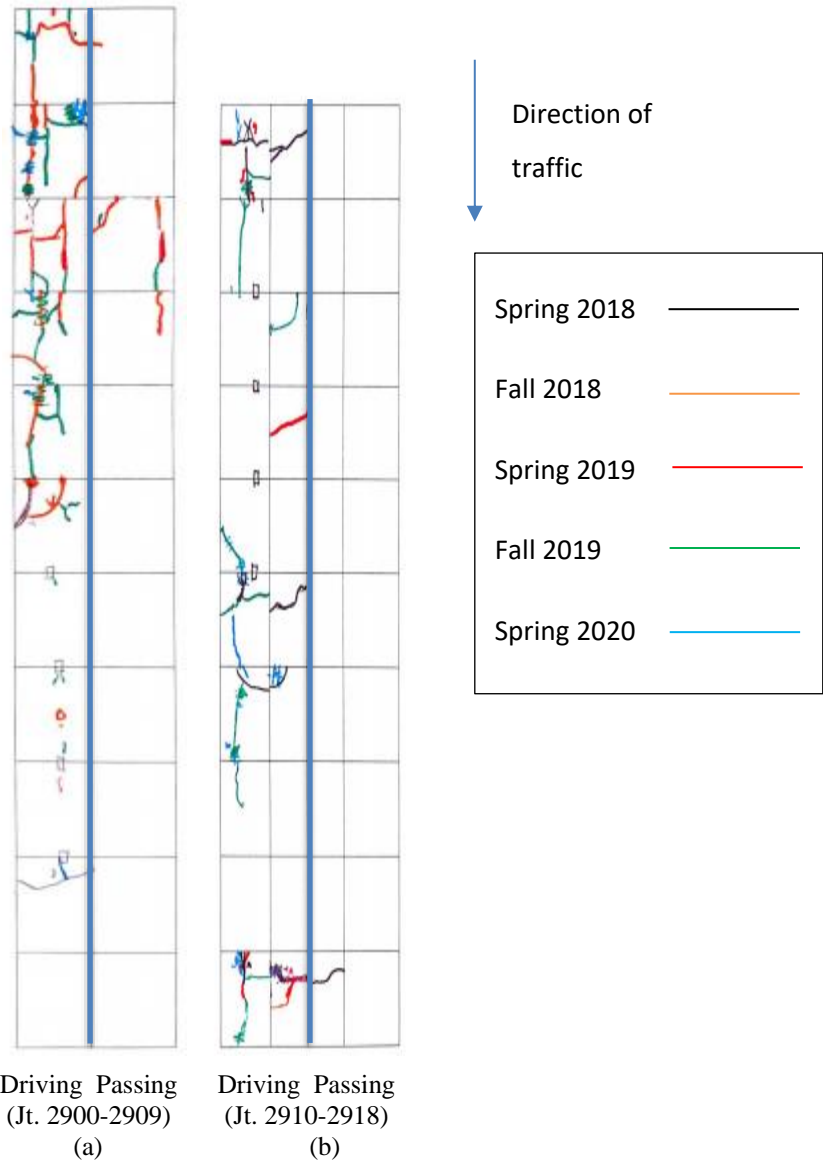
Figure 3-27: Distress Survey Maps (a) Cell 705 (b) Cell 805.
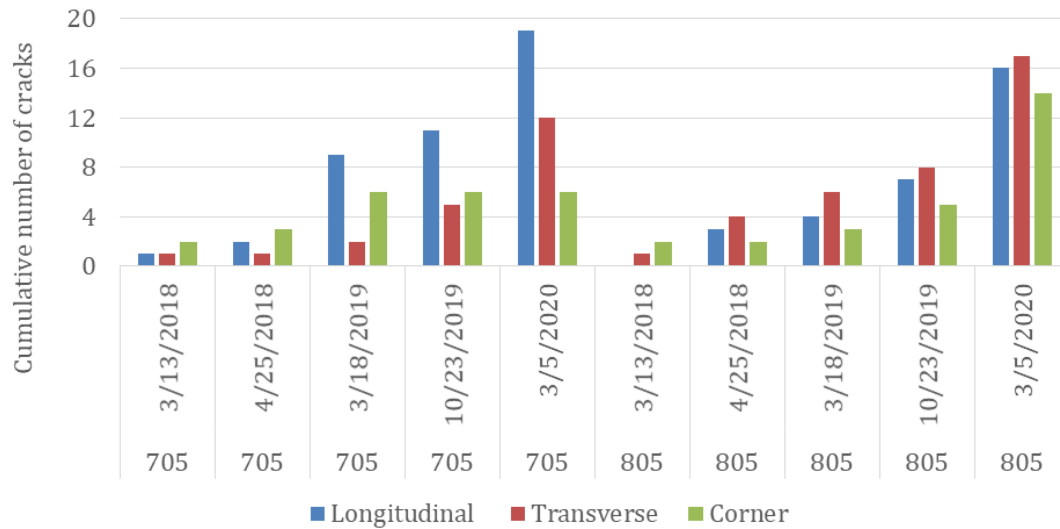
Figure 3-28. Cumulative number of various cracks in Cell 705 and 805.

3.2 FATIGUE CRACK PROGRESSION WITH AGE AND TRAFFIC

Figure 3-29 shows the percentage of cracked slabs with respect to age (months) and ESAL for both lanes (combined) of Cells 239 and 506 through 806. Compared to the thin cells (on 11 inches thick unstabilized base), the ultrathin Cell 239 (4 inches panel on 6 inches thick unstabilized base) resulted in significantly higher cracks. Approximately 20% of the slabs of Cell 239 had cracked by 150,000 ESALs; neither of the thin fiber-reinforced cells experienced that many cracked slabs even after 2.8 million ESALs. Figure 3-30 shows the percentage of cracked slabs only on the driving lanes. As much as 30% of the slabs in the driving lanes cracked after 2.8 million ESALs. It may be noted that the reason for the increased amount of fatigue cracks in Cell 239 compared to Cells 506 through 806 is the less structure in Cell 239; thicknesses of both surface and base layers are lower for Cell 239.
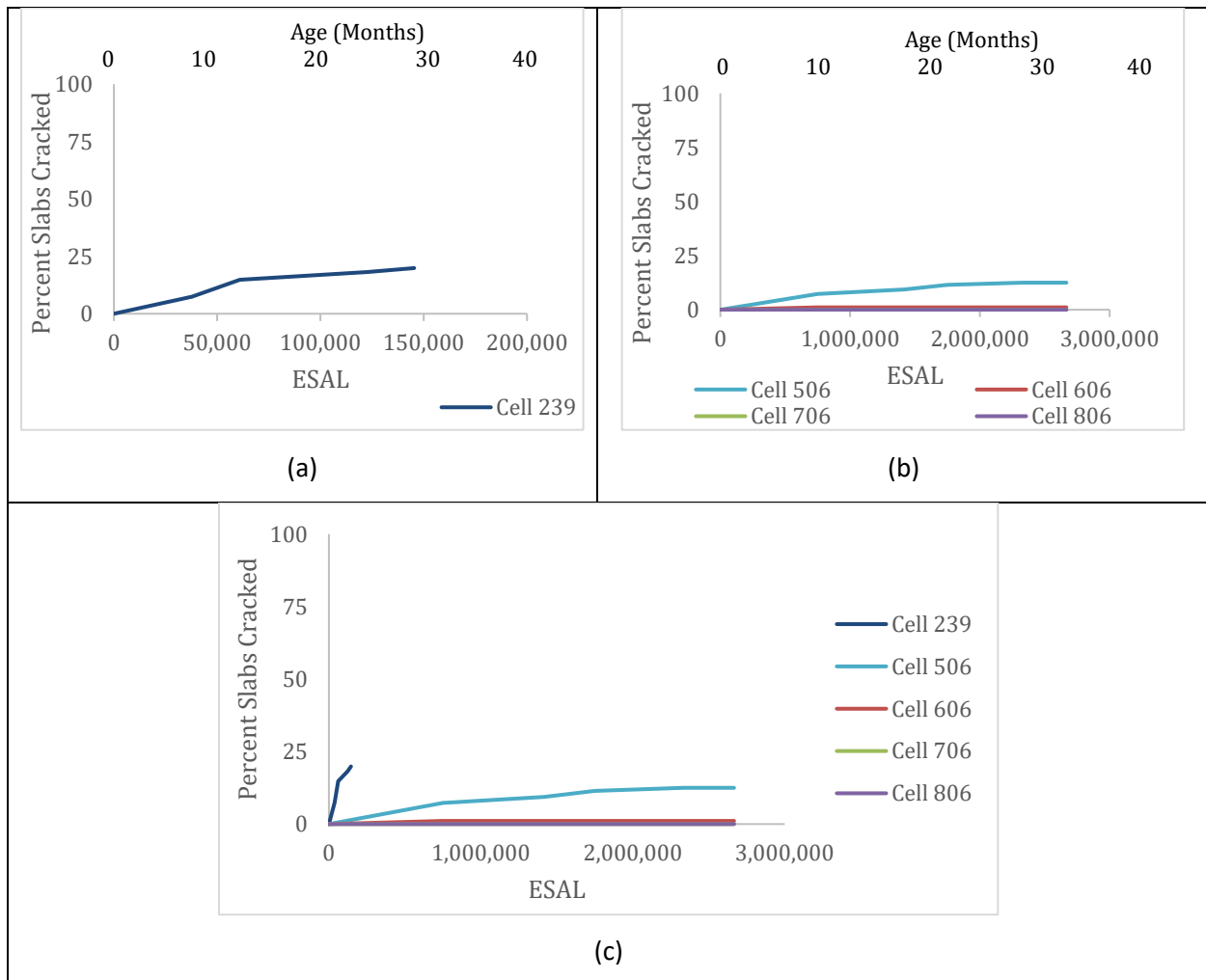
Figure 3-29: Percentage Crack vs. ESAL for both lanes (a) 239 (b) 506,606,706, and 806 (c) 239, 506, 606, 706, and 806.
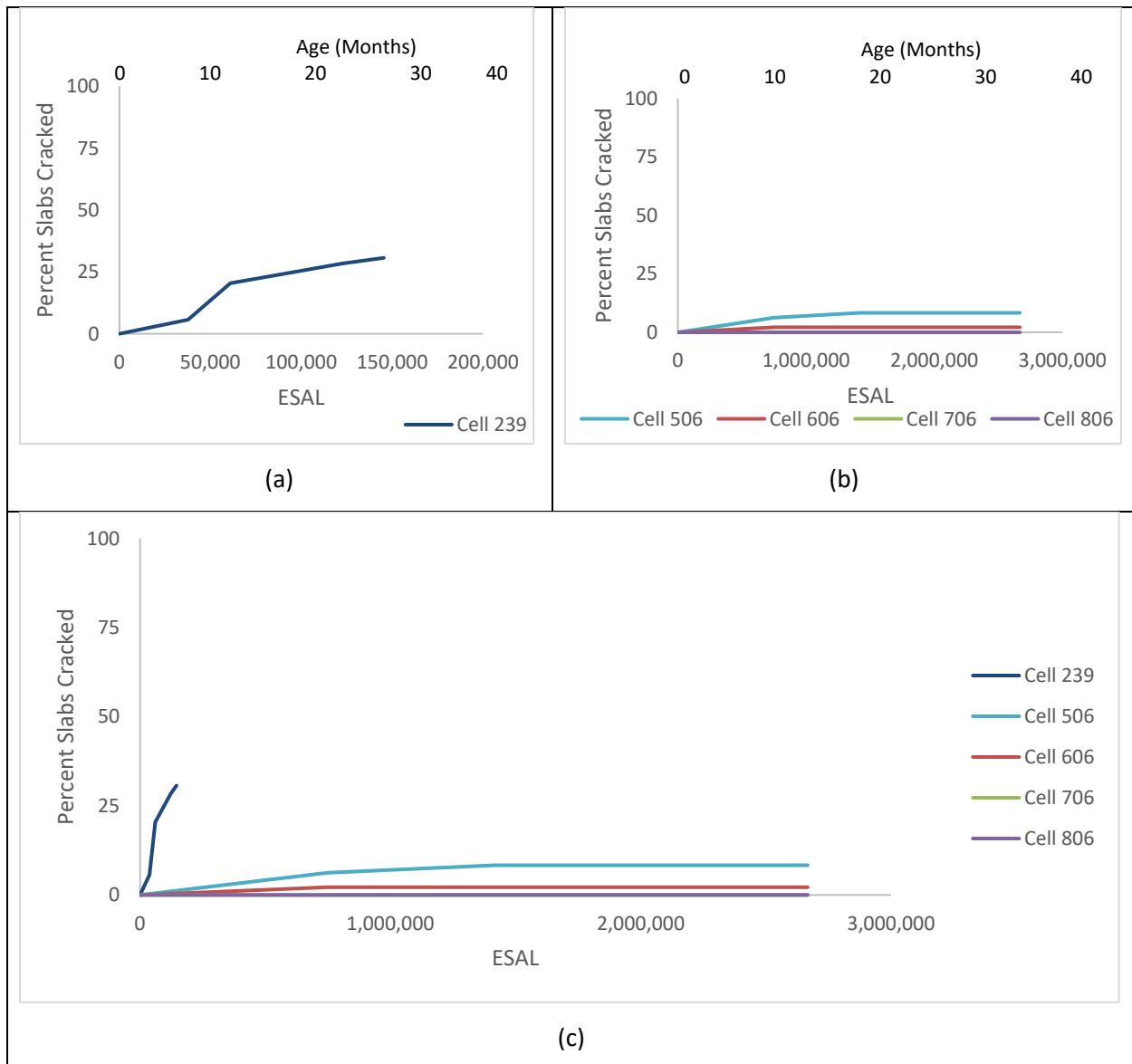
Figure 3-30: Percentage Crack vs. ESAL for the driving lane only (a) 239 (b) 506,606,706, and 806 (c) 239, 506, 606, 706, and 806.

While the number of cracks and the percentage of cracked slabs are good indicators to picture the overall cracking scenario, they do not distinguish between the small, medium, or long cracks. Therefore, documenting the crack length may be a better approach (than percent cracked slabs) to quantify the crack progression and understand the rate of deterioration of the cracks. The crack length vs ESAL relationship can trace the crack propagation history. Figure 3-31 and Figure 3-32 compare the crack

length between the cells for both lanes and the driving lane (only), respectively. The total crack length for ultrathin Cell 239 was 184 feet compared to 44 feet for Cell 506 after three years of service. Only around 150,000 ESALs were enough to create a total of 184 feet in Cell 239, while the same level of ESALs only created around 10 feet cracks in the thin cells (only in Cell 506, which did not have any fiber).
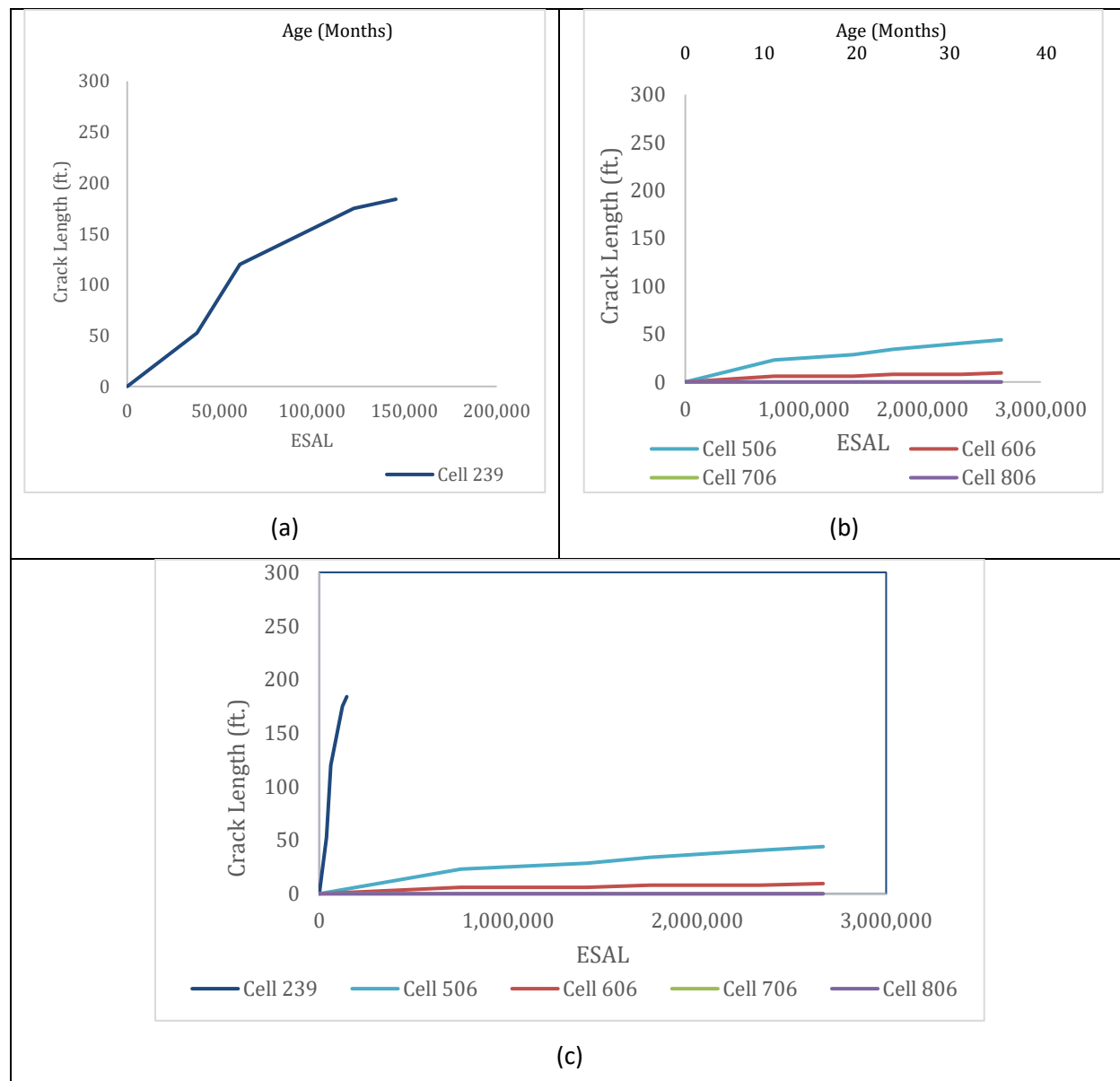
Figure 3-31: Crack Length vs. ESAL for both lanes (a) 239 (b) 506,606,706, and 806 (c) 239, 506, 606, 706, and 806
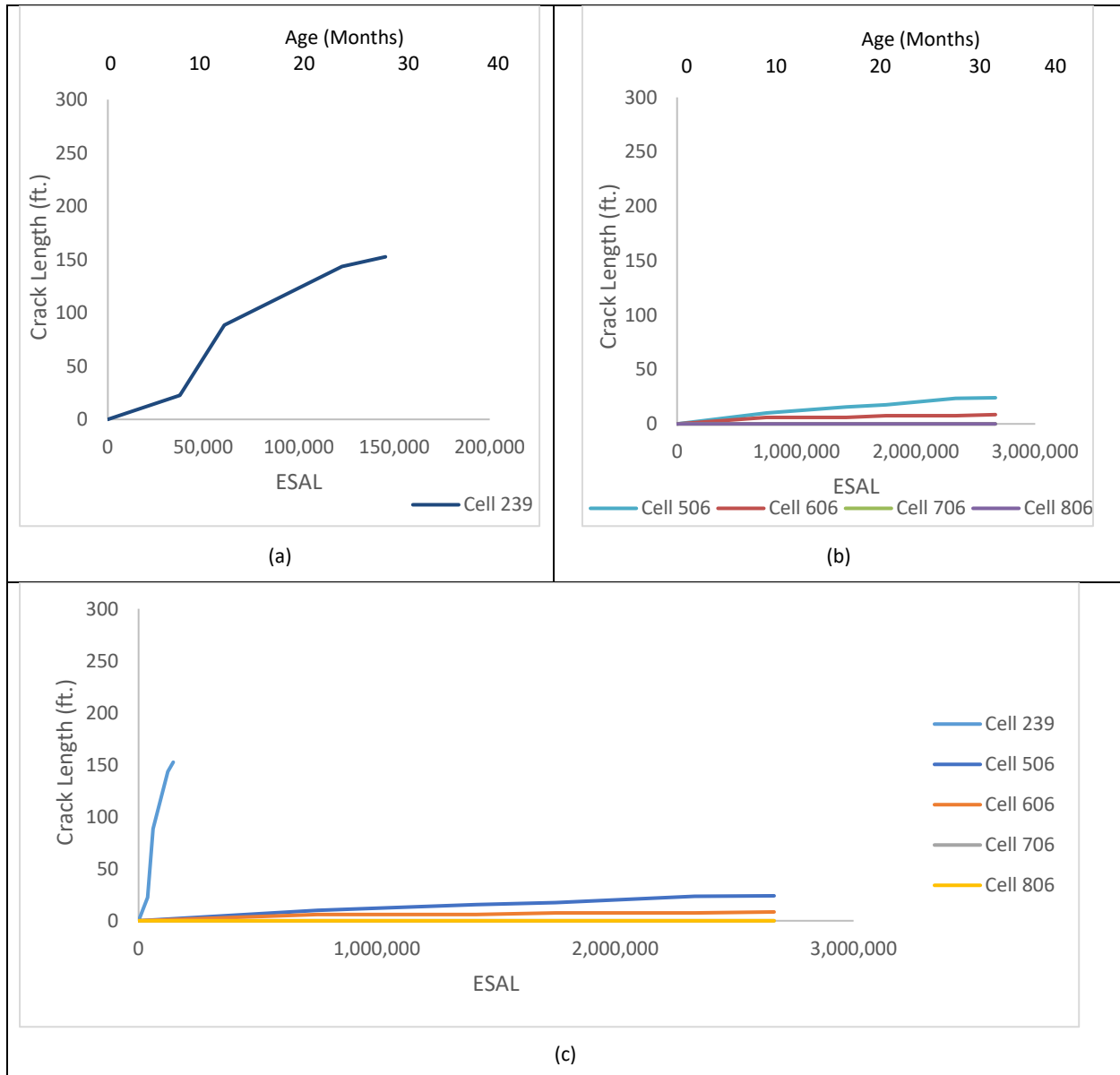
Figure 3-32: Crack Length vs. ESAL for driving lanes (a) 239 (b) 506,606,706, and 806 (c) 239, 506, 606, 706, and 806.

However, as the number of slabs and total pavement surface of the cells are different, a factor termed as the 'crack index' has been introduced in this study to include the pavement surface area in the comparison. The crack index (unit = 1/ft) is the ratio of the crack length in ft and the total area of the cell in ft^2. Figure 3-33 and Figure 3-34 compare the crack index between the cells. Based on the crack index, Cell 239 had experienced almost twice the cracks (per unit area) than Cell 506.
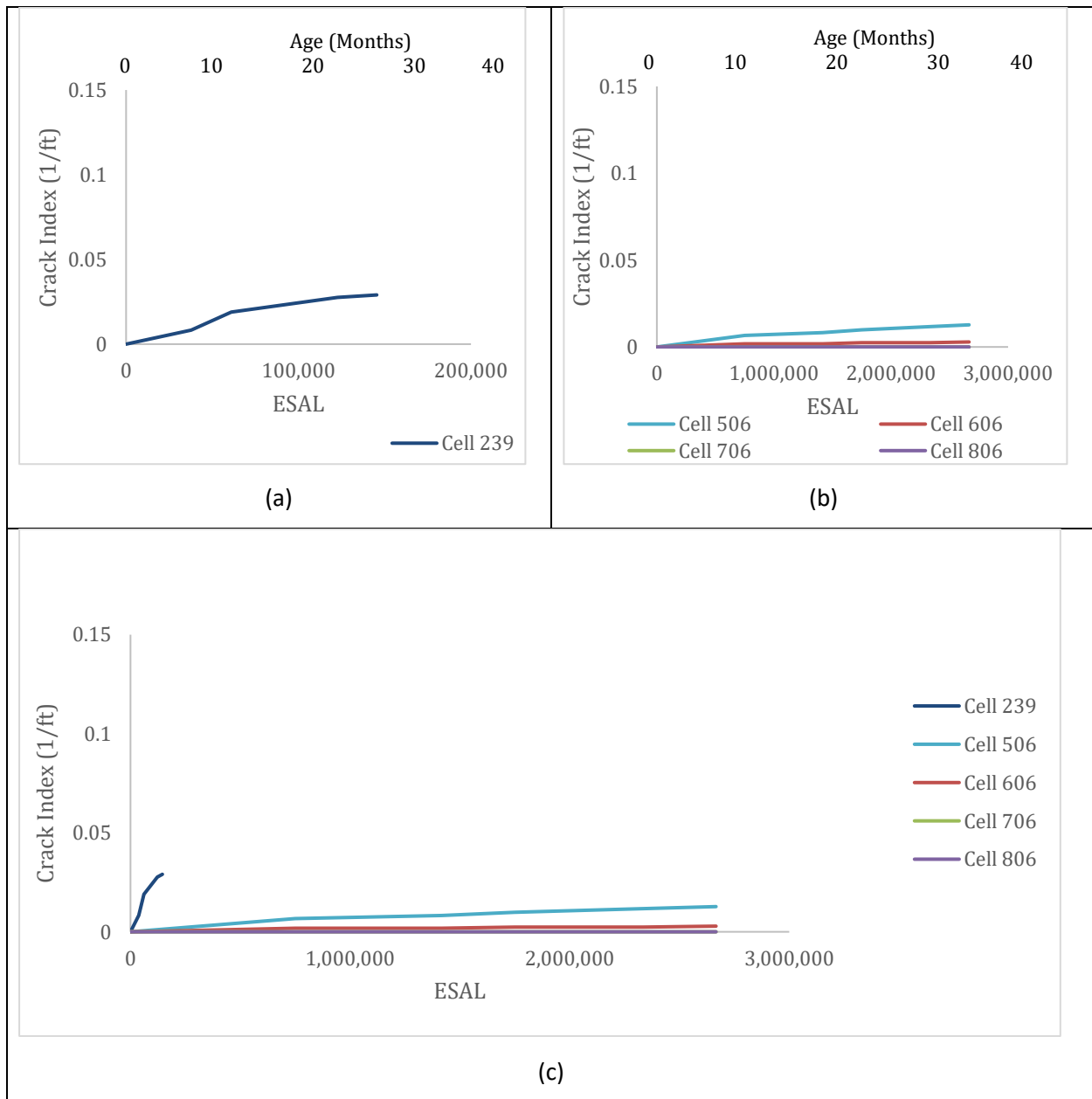
Figure 3-33: Crack Index vs. ESAL for both lanes (a) 239 (b) 506,606,706, and 806 (c) 239, 506, 606, 706, and 806.
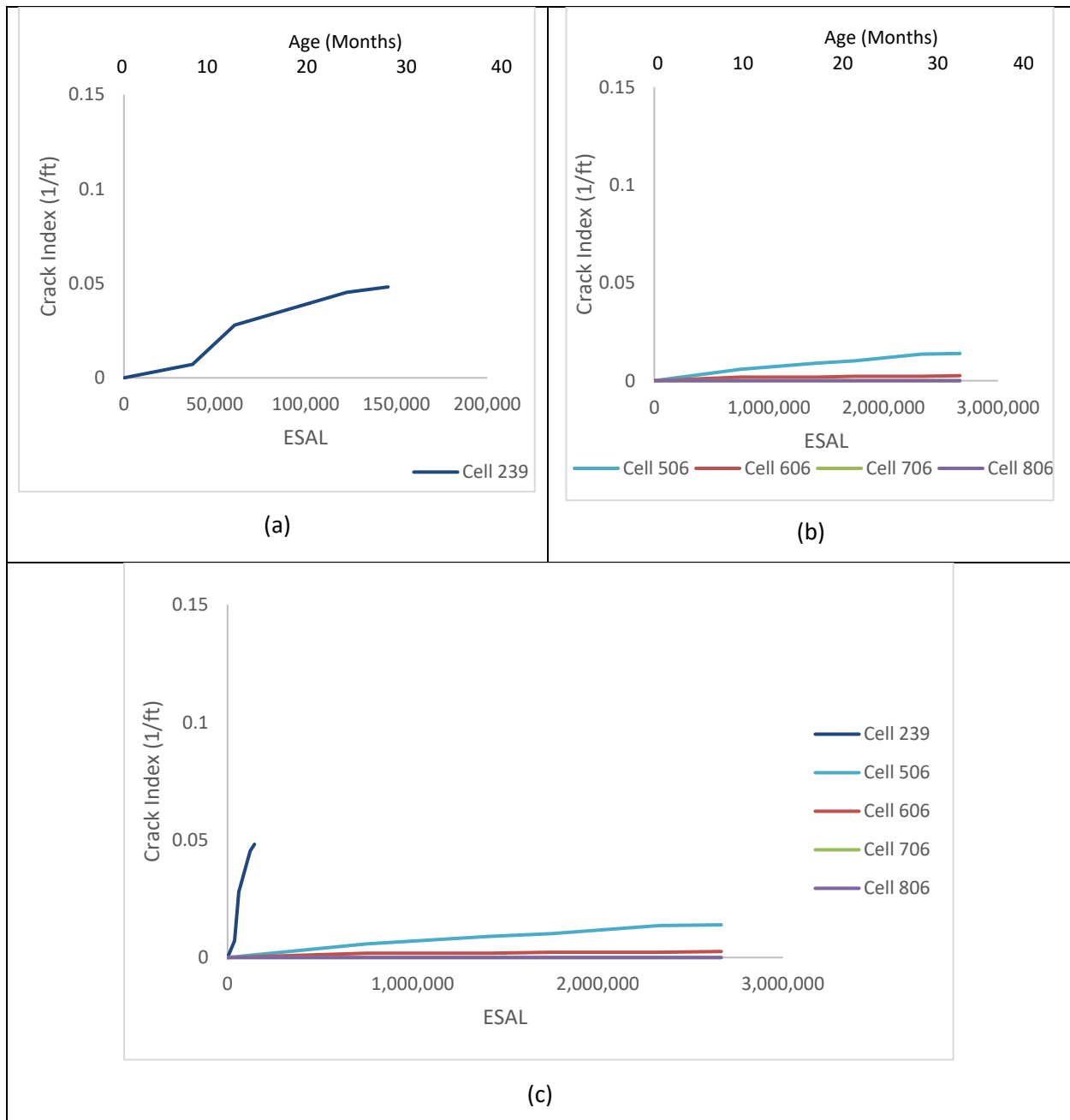
Figure 3-34. Crack Index vs. ESAL for driving lanes (a) 239 (b) 506,606,706, and 806 (c) 239, 506, 606, 706, and 806.

Regarding the concrete overlays (Cells 705 and 805), as mentioned in Section 3.1.3, it was seen that Cell 805 with smaller slabs resulted in less percentage of cracked slabs (35%) than Cell 705 (50%) after three years of traffic and climate. Figure 3-35 through Figure 3-37 compare fatigue crack parameters between Cells 705 and 805. When the comparison was made with respect to the crack length, it was found that

the total length of the cracks (both lanes) in Cell 705 was 30% more than Cell 805 after 2.7 million ESALs, as shown in Figure 3-35. However, when the comparison was made with respect to crack index, the difference between the two cells has minimized; the driving lanes of both the cells experienced almost the same crack index, which indicates the crack length on the unit pavement area is similar for both the cells. The above finding suggests that construction of wider panels with synthetic fibers (at least for the dosages and type used in Cells 705 and 805) may not be a better design than using narrower panels in terms of performance.

The preference for the construction of narrower panels vs wider panels shall not, however, be decided only on the total number of cracks or crack index. Other factors like the rate of crack progression and ease of repair of the cracked slabs shall also be considered. Based on Figure 3-35 and Figure 3-36, it appears that smaller panels (Cell 805) develop cracking at a slower pace, which may be an advantage to delay the repair work. But whether it is easy to repair a higher number of narrower panels than a smaller number of wider panels is a different question and shall be considered while making the decision for slab size. The faulting and riding quality of these two cells described in the following chapters will provide more insights into the performance comparison.
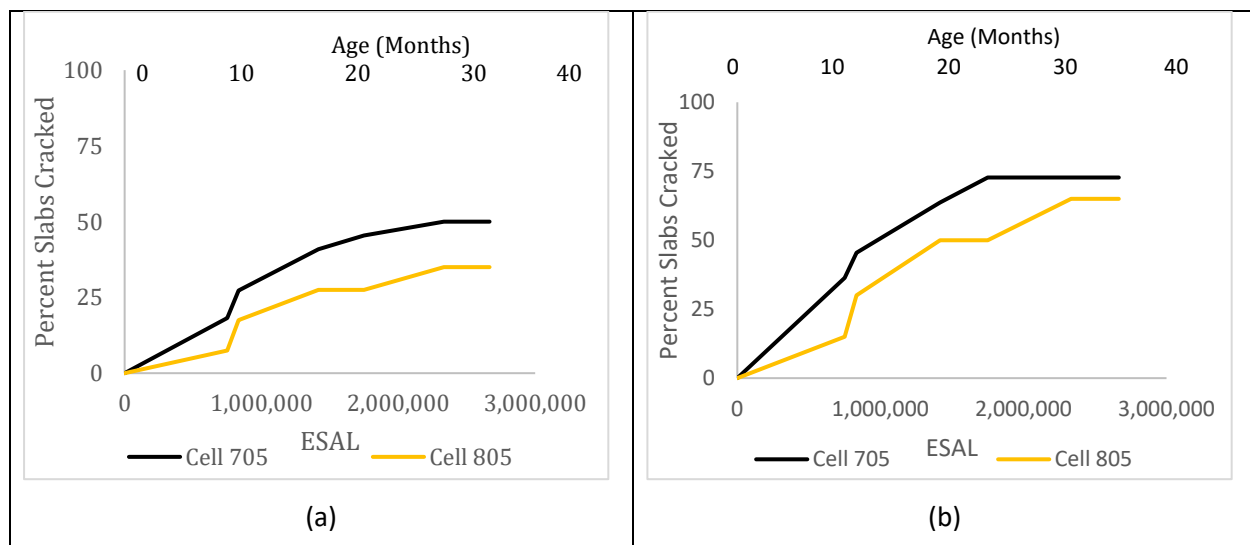
Figure 3-35. Percent slabs cracked vs ESAL for Cells 705 and 805 (a) Driving and Passing lane combined (b) Driving lane only.
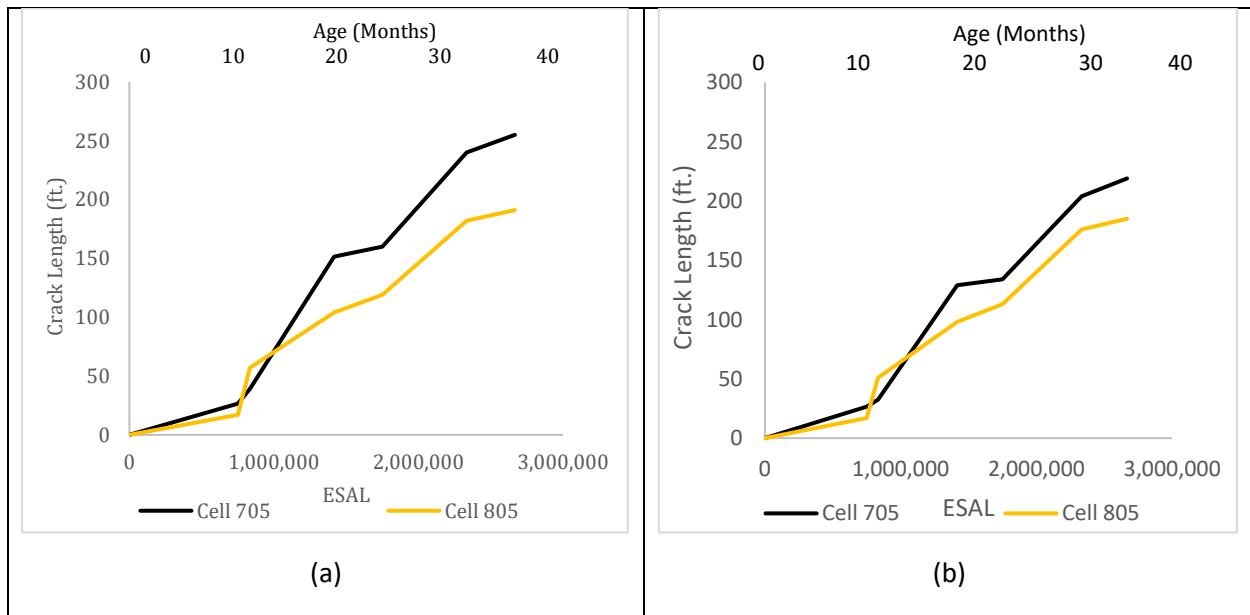
Figure 3-36. Crack Length vs ESAL for Cells 705 and 805 (a) Driving and Passing lane combined (b) Driving Lane only.
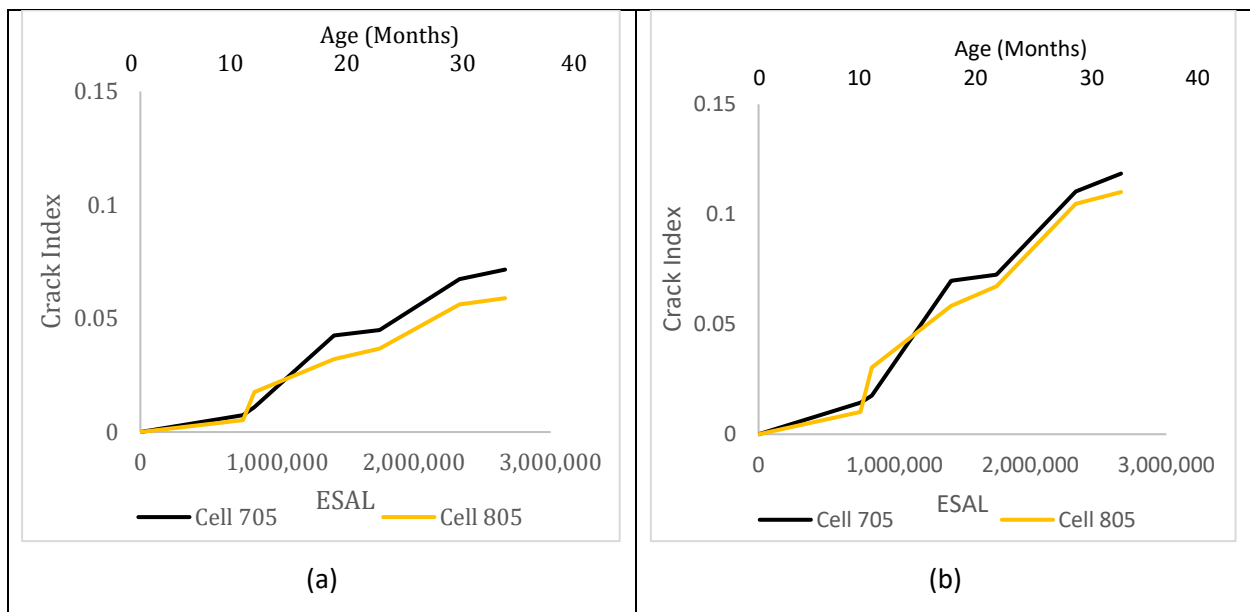
Figure 3-37. Crack Length vs ESAL for Cells 705 and 805 (a) Driving and Passing lane combined (b) Driving Lane only.

3.3 FATIGUE CRACKING PREDICTION EQUATIONS

As observed in the previous sections, Cells 506 through 806 did not experience enough fatigue cracks to derive any conclusions about the influence of fibers on the fatigue cracks. But this observation does not indicate that fibers do not contribute to the mitigation of fatigue cracks. Several previous studies indicated that synthetic structural fibers increase the slab capacity, post-crack flexural performance, which are the indicators of better fatigue resistance. Cells 139 and 239, which experienced significant cracks, have identical fiber dosage and type. Nevertheless, cracking data for Cell 239 was used to study the correlation between the fatigue crack parameters and ESALs for a four-inch-thick FRC pavement on a marginal gravel base. Separate sets of predictive equations were developed for (i) two lanes combined and (ii) only the driving lane. The predictive equations for percentage cracked slabs, crack length, and crack index are provided in Table 3-2. Figure 3-38 shows the comparison between the fatigue crack parameters calculated from the field data and the same predicted by the predictive equations. It may be stated that these equations are only applicable for the four-inch-thick FRC pavements with comparable base thickness, material type, and subgrade properties.

Table 3-2: Prediction Equations (2-7) for Fatigue Cracking in Cell 239 (4-inch thick FRC pavement)

Fatigue crack parameters	Predictive equations	Standard Error (S)	Traffic
Crack percentage (CP)	$CP = 0.0231303\ ESAL_{total}^{0.569941}$	2.24	
Total crack length (CL)	$CL = 0.030972\ ESAL_{total}^{0.734535}$	19.9	$ESAL_{total}$ = Total ESALs in driving and passing lanes
Crack index (CI)	$CI = 4.88826e\text{-}06\ ESAL_{total}^{0.734535}$	0.00314	
Crack percentage (CP)	$CP = 0.00211199\ ESAL_{DL}^{0.825229}$	4.94	
Total crack length (CL)	$CL = 0.00227361\ ESAL_{DL}^{0.957248}$	21.55	$ESAL_{DL}$ = ESALS only in the driving lane
Crack index (CI)	$CI = 7.17679e\text{-}07\ ESAL_{DL}^{0.957248}$	0.0068	
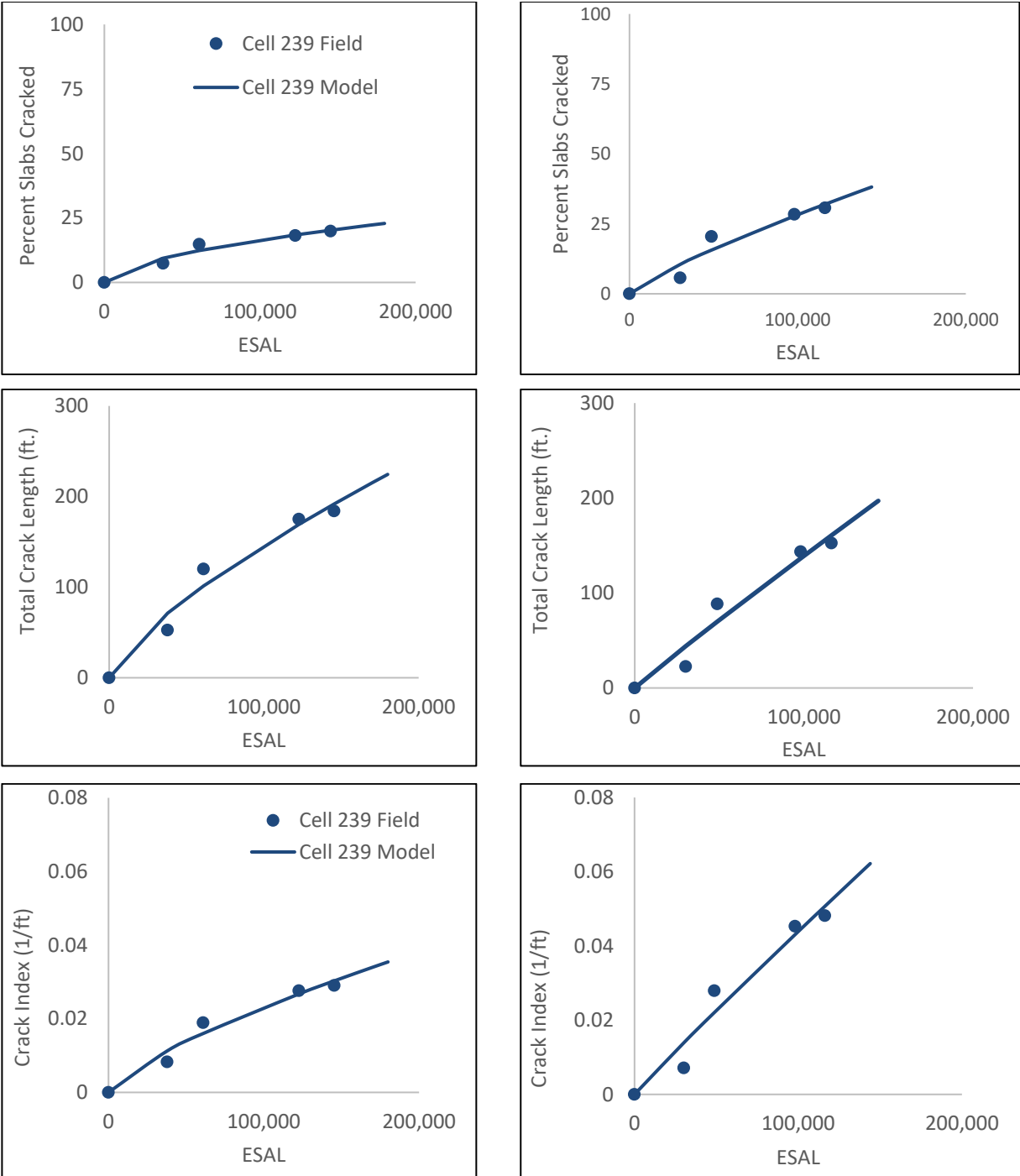
Figure 3-38. Correlation between the fatigue crack parameters and ESAL for Cell 239 (ultra-thin pavement). Plots on the left are for both lanes, and the right-side plots are for the only driving lane.

Unbonded concrete overlays Cells 705, and 805 have sufficient data for developing fatigue cracking prediction equations. Separate fatigue parameters prediction equations were developed for (i) both lanes combined and (ii) for the driving lane alone. Prediction equations are provided in Table 3-3. Figure 3-39 shows the comparison of the fatigue crack parameters calculated from the field data and the same predicted by the predictive equations. It may be stated that these equations are only applicable for the 5 inches thick FRC overlays that have field conditions comparable to Cells 705 and 805. The effect of the interlayer, base layer, and subgrade could not be included in this study because of the lack of data.

Table 3-3: Prediction Equations (8-13) for Fatigue cracking in 5 inches thick unbonded concrete overlays.

Fatigue crack parameters	Predictive equations	Standard Error (S)	Traffic
Crack percentage (CP)	$CP = ESAL_{total}{}^{.60}$ x (0.00238127 +3.5327e-05 x SA)	3.99	$ESAL_{total}$ = Total ESALs in driving and passing lanes SA = Slab area (ft^2)
Total crack length (CL)	$CL = ESAL_{total}{}^{.74}$ x (0.00209012 +1.36573e-05 x SA)	32.95	
Crack index (CI)	$CI = ESAL_{total}{}^{.74}$ x (3.01071e-07 +5.81385e-09 x SA)	0.011	
Crack percentage (CP)	$CP = ESAL_{DL}{}^{.60}$ x (0.00754828 +3.88817e-05 x SA)	6.8	$ESAL_{DL}$ = ESALs only in the driving lane
Total crack length (CL)	$CL = ESAL_{DL}{}^{.74}$ x (0.00287066 +8.41359e-06 x SA)	29.14	
Crack index (CI)	$CI = ESAL_{DL}{}^{.74}$ x (9.084e-07 + 9.03187e-09x SA)	0.02	
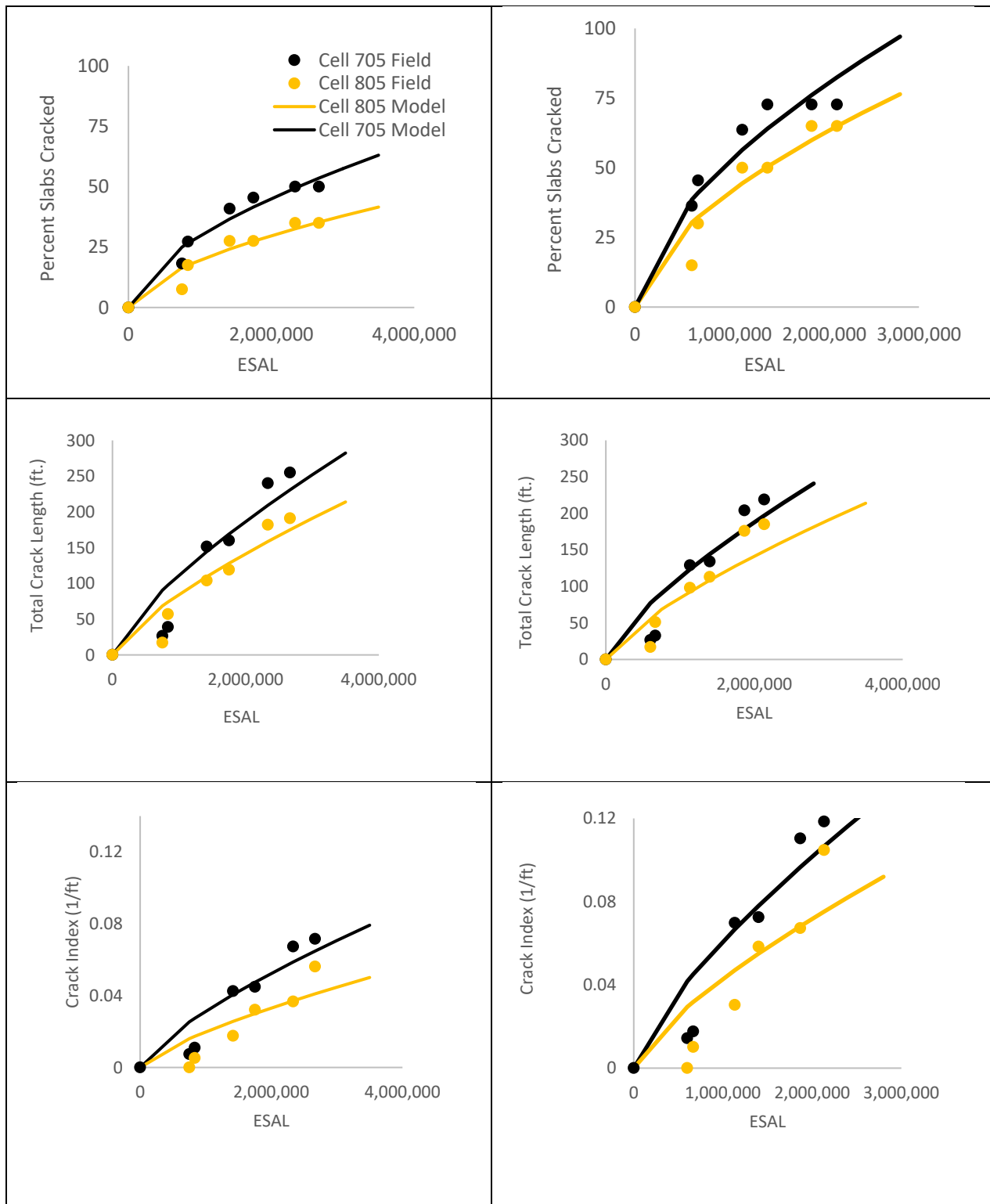
Figure 3-39. Correlation between the fatigue crack parameters and ESAL for 5 inches thick concrete overlays. Plots on the left are for both lanes, and the right-side plots are for the only driving lane.

51

3.4 FEM ANALYSIS TO DETERMINE THE INFLUENCE OF FIBERS ON FATIGUE LIFE

The objective of the construction of the Cells 506 through 806, with various fiber dosages, was to study the influence of the synthetic structural fibers in mitigating fatigue cracks, including keeping cracks tight. Owing to the stiff 11 inches thick base layer, these cells, however, did not experience significant numbers of cracks that could be used to quantify the influence of fibers on mitigating fatigue cracks. Because of this data limitation, a finite element analysis (using ANSYS™) was performed to understand the influence of the fibers on the stress ratio that dictates the development of the fatigue cracking.

Synthetic structural fibers are expected to maintain high joint load transfer efficiency (LTE) and joint stiffness over time, which may reduce the stress and stress-ratio (the ratio of stress in the slab and the modulus of rupture) in the slabs and increase the fatigue life. In order to quantify the increase in LTE because of fibers, the FWD data collected in this project (provided in Chapter 5 of this report) was revisited. It was found that the LTEs measured at the early age were comparable between the FRC and non-FRC cells, but the LTEs of the non-FRC cells dropped relatively faster with time than the FRC cells. For the FEM analysis, LTEs measured at three different ESAL levels (at 1, 1.75, and 1.83 million ESALs) were compared between the four cells, Cells 506 through 806, that have various fiber dosages (Figure 3-40). The above-mentioned three different ESALs were selected because of the availability of the FWD test data at those ESALs. The LTEs measured at 1, and 1.75 million ESALs gave somewhat good correlations between the LTEs and ESALs. The LTEs measured at 1.83 million ESAL did not yield a good correlation as the joints have supposedly deteriorated and fibers' effect had likely minimized. While a very accurate quantification of the LTE gain from a specific dosage of fiber is not possible from this study, looking at all the LTE data collected at different times, it is conservatively assumed that every 2 to 2.5 lbs. /cy fiber dosage (specific to the fibers used in this particular study) may be capable of increasing the LTE by 10% approximately. However, it is cautioned that this may vary with fiber types, pavement slab thickness, and concrete mixture type, etc.
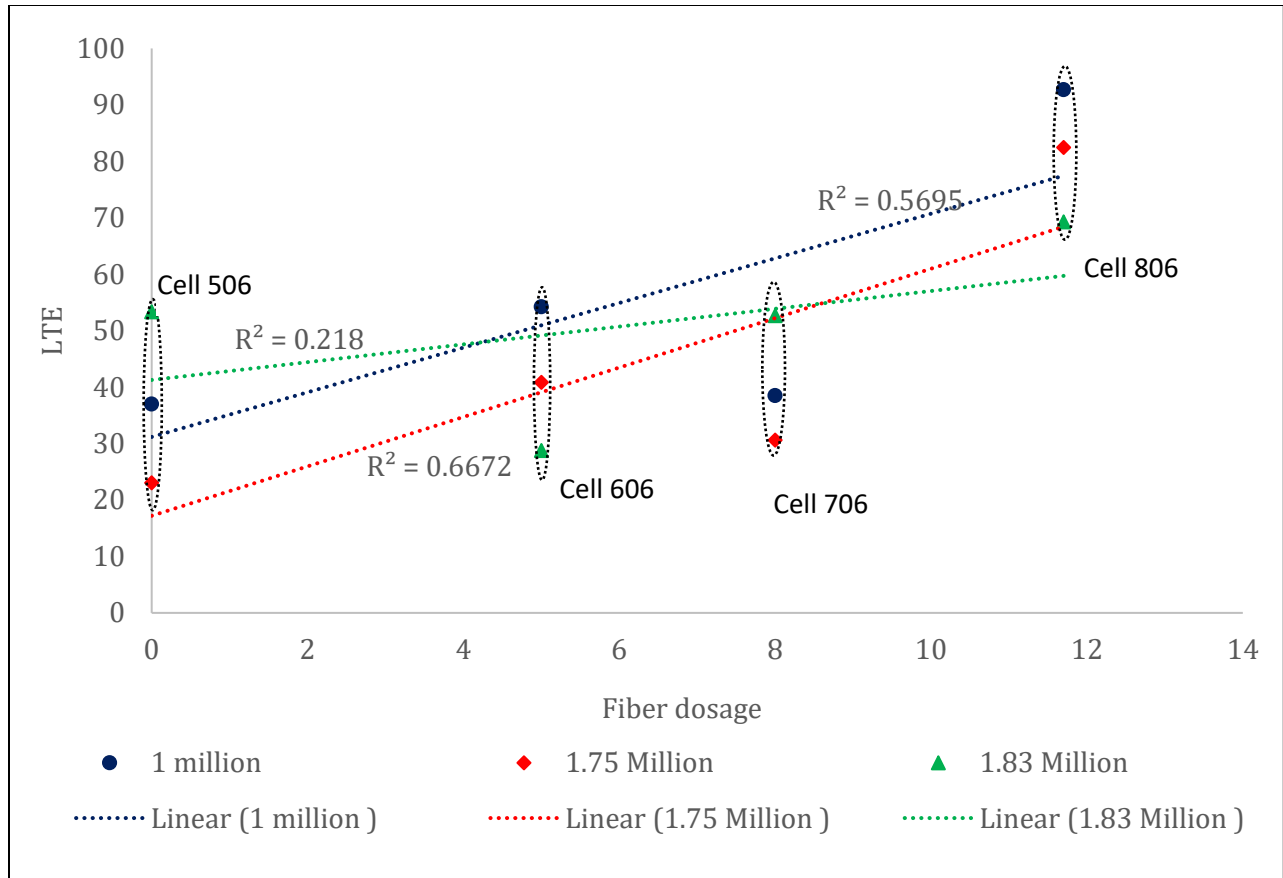
Figure 3-40: Influence of fiber dosage on the LTE.

Cells 506 through 806 were constructed with strain measuring sensors (static and dynamic). Those sensors were installed at the mid-slab, both near the top and bottom of the slab (0.5-inch inside the slab), which is not necessarily the most critical location for the fatigue crack initiation in ultra-thin and thin concrete pavements on the un-stabilized base layer. To determine stress and strain at the critical location of a slab, FEM models were developed for all four cells. Figure 3-41 shows a screenshot of the FEM model. Six concrete slabs were considered in the model. The dimensions of the slabs, other layers, and shoulder were the same as was in the field. Properties of concrete and other layers were also matched with the as-built conditions to the extent possible. The transverse and longitudinal joints were modeled using three-dimensional springs (Matrix 27 element), with spring constants representing the joint shear stiffness (function of LTE, modulus of subgrade condition, the radius of relative stiffness, etc.) and fiber tensile stiffness (resistance offered by fibers against crack width opening) at joints. The spring

constants for fibers were derived using the load versus crack width relationships determined in previous laboratory studies conducted at UMD by Barman and Hansen (2018) and Crick (2019).

Wheel load was applied on the outer wheel path near the transverse joint, as shown in Figure 3-41. The loading area and the stress were assumed to match with that of the MnROAD truck, which is used for applying load during dynamic strain measurements on both the LVR and mainline segments of MnROAD..
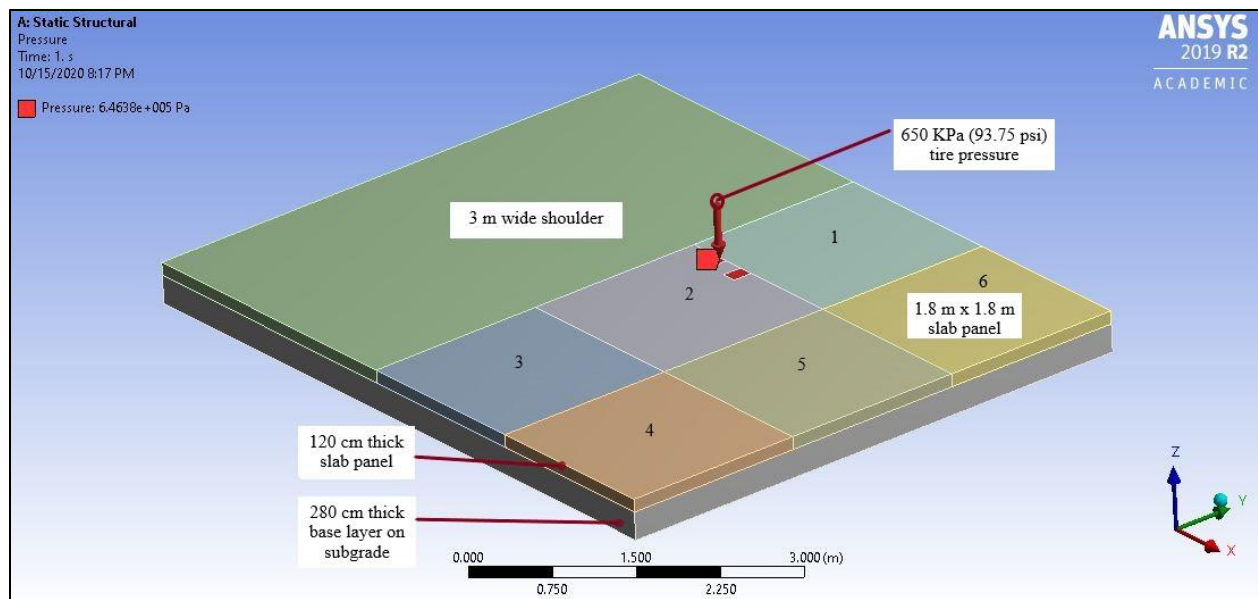
Figure 3-41: Screenshot of the FEM model.

In order to estimate the stress values from the strains measured by the strain sensors in the field, correlations were developed between the FEM computed strains and stresses (major principle) for each cell. As the concrete was considered as an elastic material, the obtained relationships were found linear as anticipated. Also, to determine the relationship between the field measured stress (computed from strains (reported in Chapter 5 of this report) and FEM computed stress values, they were compared for the mid-slab locations, where field strain data were available (sensor location). The conversion factors were then generated for each cell, which are 0.96, 0.80, 1.06, and 0.56 for the Cells 506, 606, 706, and 806, respectively. These conversion factors were used to convert the FEM calculated stresses to the corresponding field stresses.

Figure 3-42 shows the stress ratios computed at the critical locations for various LTEs for Cells 506 through 806. The reason for the lower stress ratios for the FRC cells compared to the plain concrete cell (Cell 506) are the (i) slightly higher modulus of rupture for the FRC cells and (ii) fiber stiffness, which acts against the crack width opening below the saw-cut joint. Figure 3-42 shows that the stress ratio is less in the FRC cells at a given LTE. It may be stated that the relationship between the stress ratio and the LTE presented in Figure 3-42 may change according to the field conditions; nevertheless, the analysis shows the potential to account for the fibers' contribution in calculating the design stress.
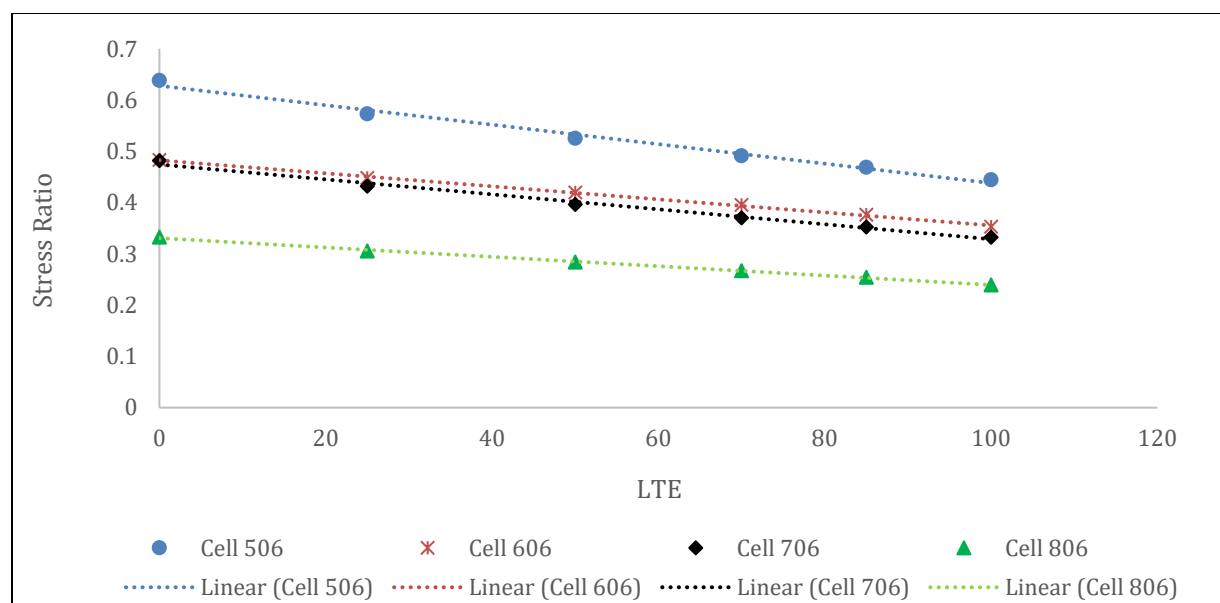
Figure 3-42: Stress ratio as a function of LTE for Cells 506 through 806.

The reduced stress ratio in the concrete slabs is likely to increase the fatigue life. Based on the limited literature survey conducted, it can be stated that there is no widely accepted fatigue model for ultra-thin and thin FRC pavements, where pavement is directly constructed on the un-stabilized base, and the fatigue crack propagation is considered to be affected by the fiber. Hence, the MEPDG fatigue model (ARA, 2004) provided below in Equation 14 was used to compute the fatigue lives for various stress ratios that depend on the concrete properties, crack width, and LTE (function of fiber dosages). Figure 3-43 shows the estimated fatigue lives for the four cells that were constructed with various fiber dosages. While an accurate quantification of fatigue life may not be possible with this limited analysis, Figure 3-43 shows that higher fatigue life can be achieved if the joints have higher LTE, which can be

obtained by using synthetic structural fibers. However, it shall be noted that the predicted fatigue life values presented in Figure 3-43 do not represent the real-world values, as LTE keeps changing with time and depends on many other variables. The other important fact is that Equation 14 is for plain concrete and does not depend on the post-crack properties of concrete. The FRCs' essential contribution is in their post-crack performance, so a more accurate prediction of the fatigue life of an FRC pavement or overlay should be determined using a fatigue model that accounts for the post-crack performance of concrete. Nevertheless, this analysis assures that if LTE can be increased by using fibers, so does the fatigue life.

$$\log\left(N_{i,j,k,l,m,n}\right) = C_1 \cdot \left(\frac{MR_i}{\sigma_{i,j,k,l,m,n}}\right)^{C_2} + 0.4371$$

where,

$$
\begin{array}{lll}
N_{i,j,k, \ldots} & = & \text{allowable number of load applications at condition } i, j, k, l, m, n \\
MR_i & = & \text{PCC modulus of rupture at age } i, \text{ psi} \\
\sigma_{i,j,k, \ldots} & = & \text{applied stress at condition } i, j, k, l, m, n \\
C_1 & = & \text{calibration constant} = 2.0 \\
C_2 & = & \text{calibration constant} = 1.22
\end{array}
$$

(14)
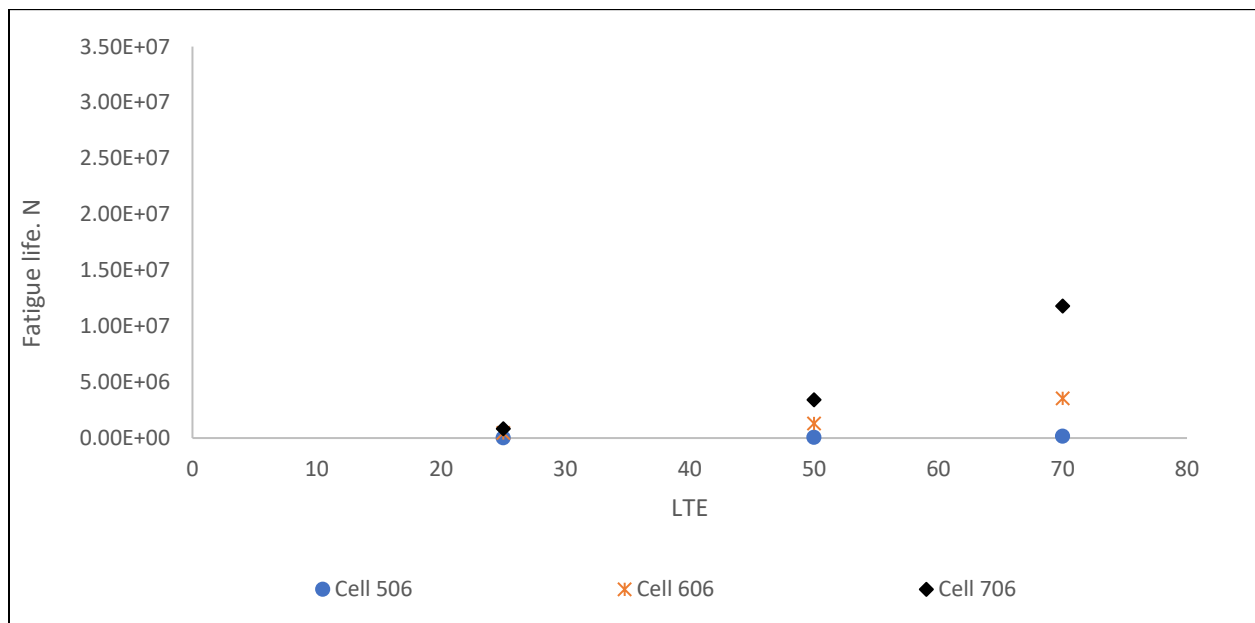
Figure 3-43. Demonstration of the benefit of fibers in Fatigue life (Cell 506- no fiber; Cell 606- 5lb/cy, Cell 706 – 8 lbs./cy fiber)

56

4 INFLUENCE OF FIBERS ON JOINT FAULTING AND IRI

The development of faulted joints can highly influence the ride quality of concrete pavement. As discussed in the previous section, faulting was measured at ten randomly selected transverse joints of every cell, and four readings were noted at every joint. The ride quality of MnROAD test cells was evaluated by determining the international roughness index. This chapter presents the transverse joint faulting and IRI results.

4.1 JOINT FAULTING DATA

4.1.1 Cells 139 and 239

Figure 4-1 shows the faulting measured at ten various transverse joints of Cells 139 and 239, marked as Joint 1 through 10. It shall be noted that the joint numbers in these plots for Cells 139 and 239 and for all other cells are just serial numbers of joints where faulting was measured, which are different from MnDOT's assigned numbers for each transverse joint.

As previously mentioned, a portion of Cell 139 in the inside lane had developed significant depression along the wheel path, so it may not be appropriate to compare the faulting results between Cells 139 and 239. Interestingly, faulting results for Cell 239 mainly showed negative values. Negative faulting is usually not typical (Selezneva et al., 2000), but since the magnitude of the faulting in Cell 239 is below -1 mm until the third year of service, it can be stated that there was not any notable faulting that developed at least at the joints where the faulting values were recorded. This shows that only three years of data (approximately 150,000 ESALs) is not enough to comment on the joint faulting trends of Cells 139 and 239. Additionally, it can be stated that the joint faulting was not the dominant distress for Cells 139 and 239; the fatigue cracking was the dominant distress by far, as discussed in the previous chapter.
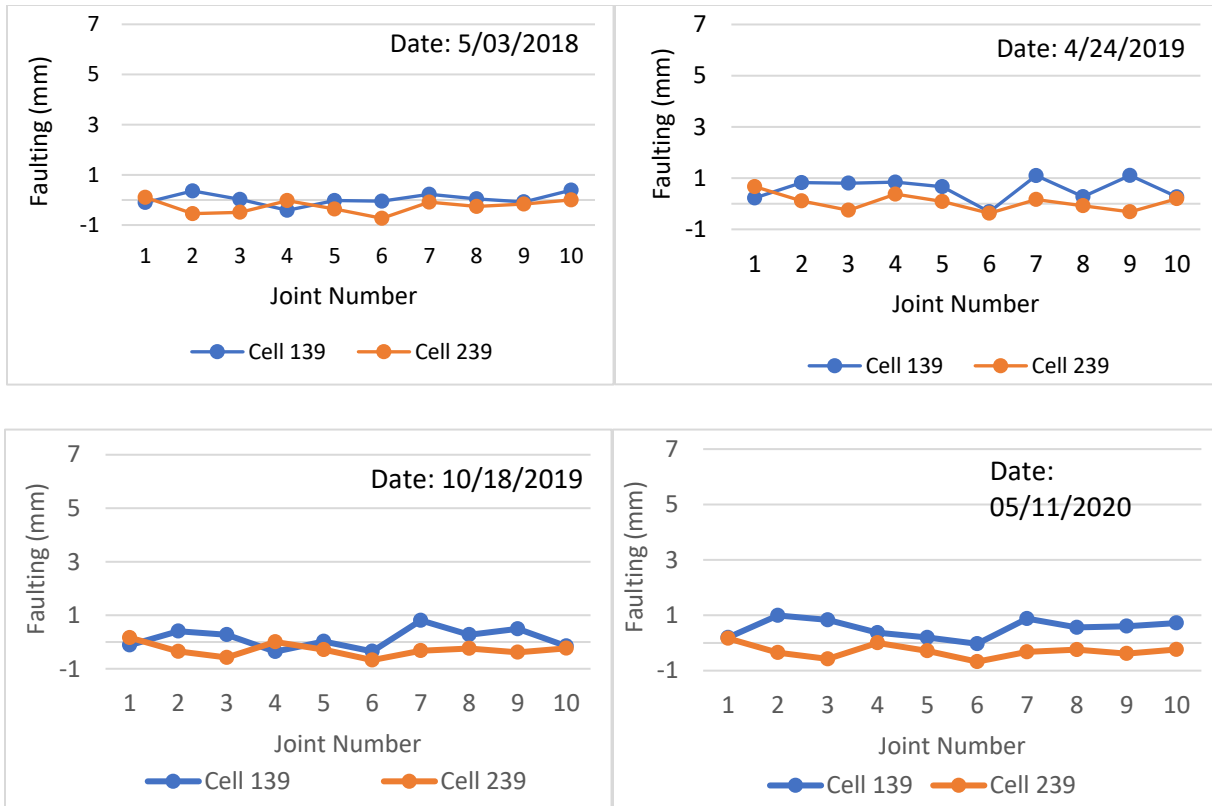
Figure 4-1. Faulting summary of Cells 139 and 239 at four different dates until May 11, 2020.

4.1.2 Cells 506 through 806

Figure 4-2 shows the faulting measured in Cells 506, 606, 706, and 806 until May 2020. Cell 506, which was constructed with plain concrete, experienced the highest faulting (up to 5 mm) among the four cells. Figure 4-3 shows a photograph of noticeable faulting in Cell 506 (note that there is a sunken corner crack in the leave slab, which exaggerated the faulting in the photo). Figure 4-4 shows the trend of average faulting versus fiber dosage. Cell 606, which was 6-inch thick (higher aggregate interlock) and constructed with a fiber dosage of 5 lbs/cy experienced approximately 82% less faulting than Cell 506 until May 2020. Cell 706, with a fiber dosage of 8 lbs./cy, also underwent less faulting than Cell 506. Cell 806, which had the highest fiber dosage at 11.7 lbs./cy, experienced significantly lower faulting compared to any other FRC cell.

58
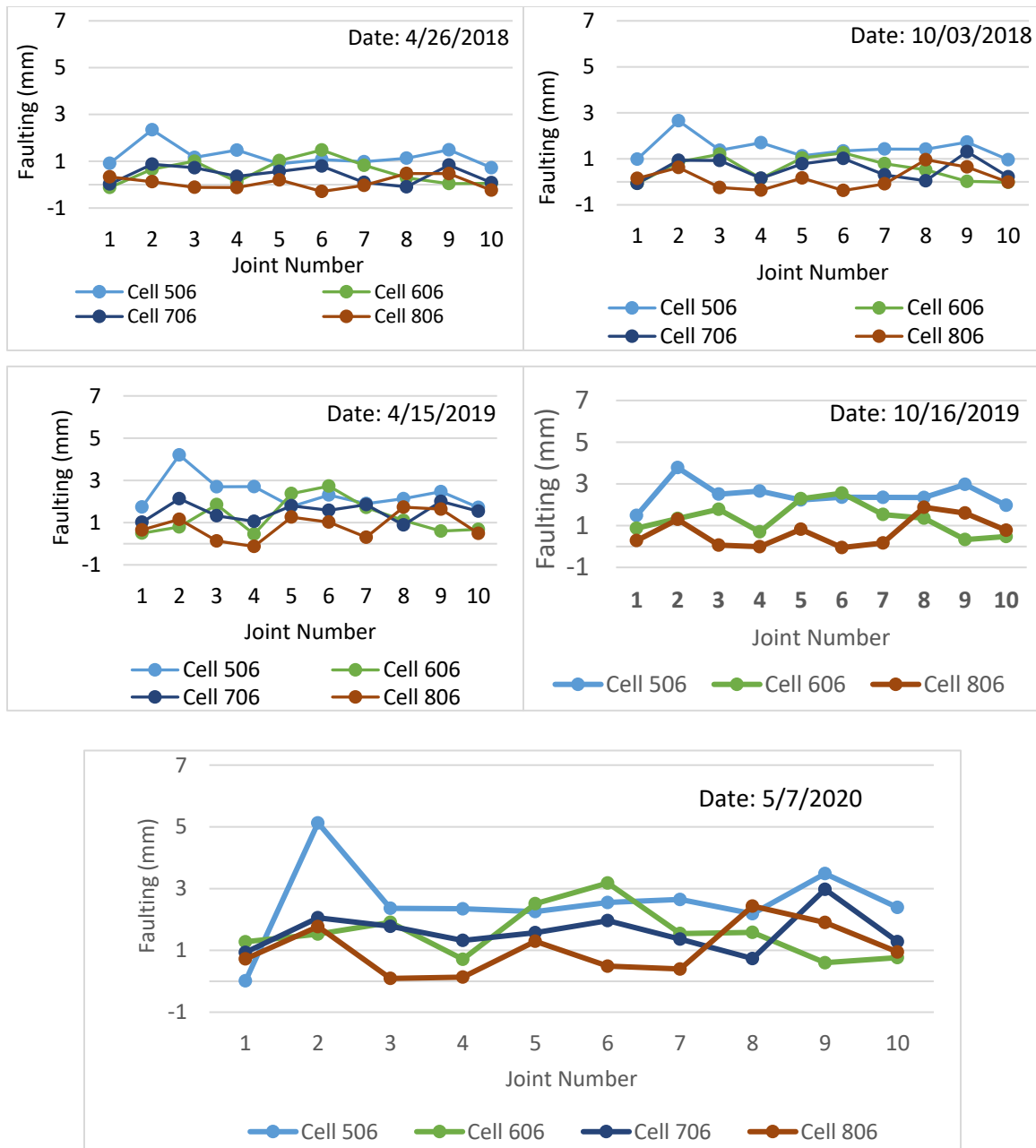
Figure 4-2. Faulting summary of Cells 506 through 806 until May 2020.

Figure 4-3. Photograph of faulting of Cell 506 (non-FRC). Note that faulting is exaggerated due to the broken corner in the slab on leave slab.
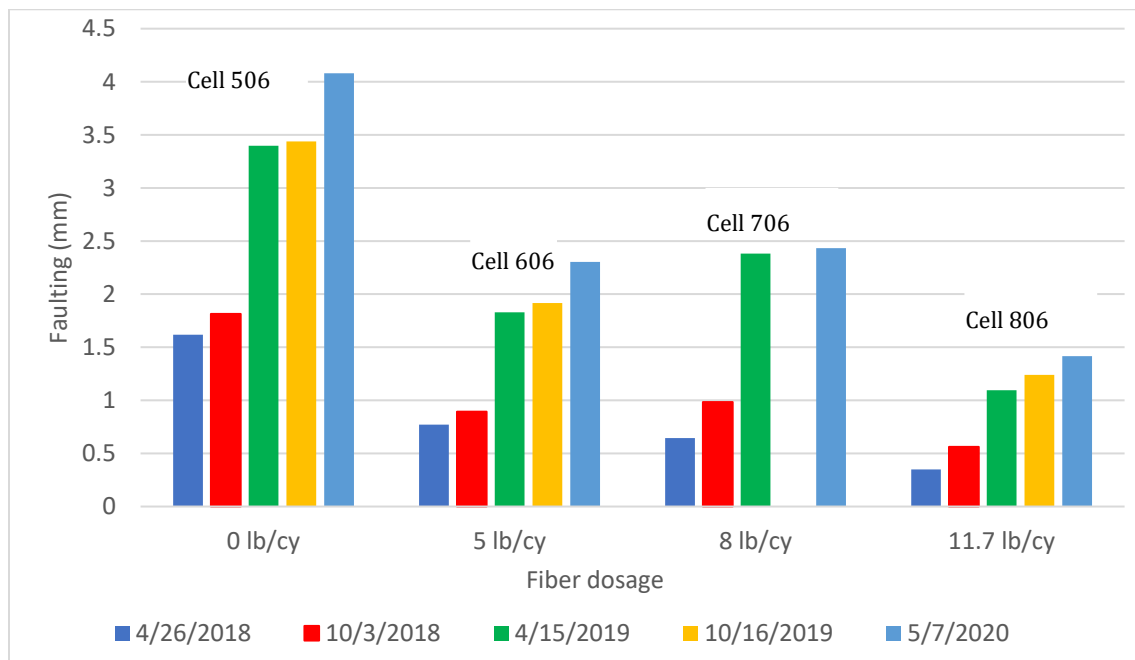
(a)
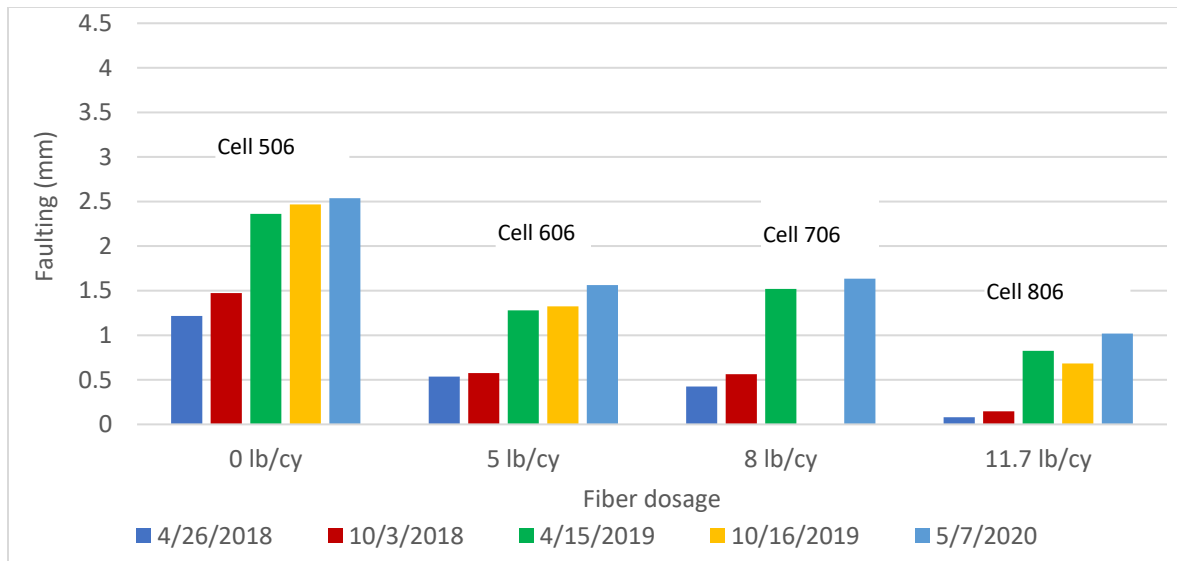
(b)

Figure 4-4. Faulting for Cells 506 through 806 with respect to fiber dosage (a) Only driving lane joints (b) average of the driving and passing lane joints.

Note: Faulting for each cell is the average of all the faulting readings taken in a cell.
Faulting data of Cell 706 for April 2019 was erroneous, so discarded.

4.1.3   Cells 705 and 805

Figure 4-5 shows the faulting for Cells 705 and 805 until May 2020. Both Cells 705 and 805 had shown mostly positive faulting. One noticeable observation was that the faulting at Joint numbers 2 and 4 of Cell 705 was higher in April 2019 (spring) than what was measured in October 2019. May 2020 data showed Joint 4 having more faulting than the previous year's measurement, but Joint number 2 surprisingly reported the exact faulting measurement as in October 2019. Even though the faulting values in these cells were around 1 to 2 mm, Cell 805 experienced a slightly higher amount of faulting. It may happen that the narrower and lighter slabs in Cell 805 compared to Cell 705 move relatively more under the wheel load.

It is interesting that faulting developed at all in these cells, given the presence of a fabric interlayer. It is likely permanent deformation in the fabric, along with differential curling up of the slabs that resulted in measured faulting. It will be interesting to see in the future if the faulting levels out as time progresses

61

due to the limited compression of the fabric. Some of the faulting might be caused by broken panels that shift and settle.
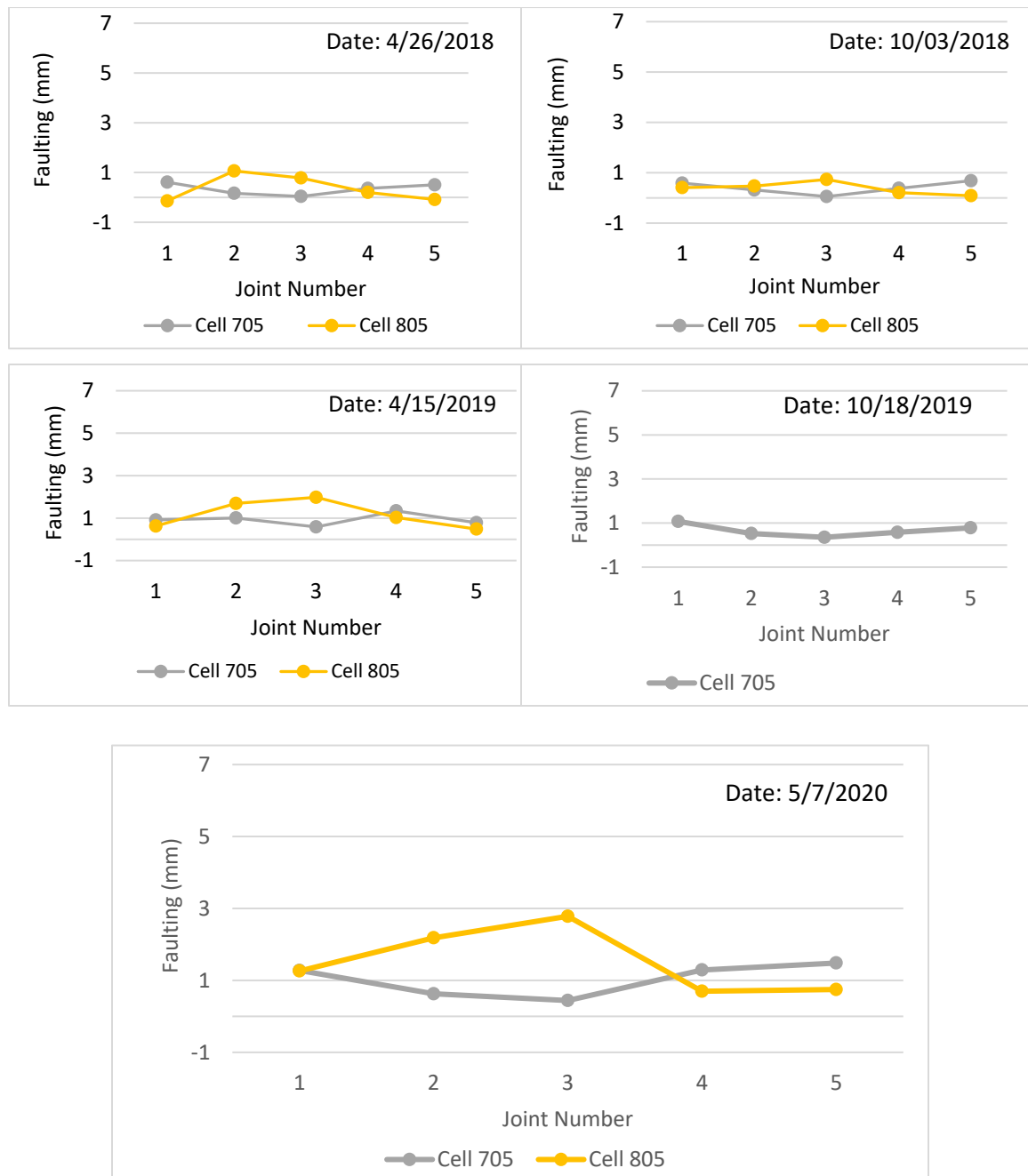
Figure 4-5. Faulting summary of Cells 705 and 805 until May 2020.

4.2   FAULTING PROGRESSION WITH AGE

Figure 4-6 shows the trend of faulting with respect to age for Cells 139 and 239. It is evident from the plot that faulting increased with age, and Cell 239 (4-inch thick) compared to Cell 139 (3-inch thick) experienced slightly less faulting. However, as the measured faulting for these two cells was around 1 mm (0.04 inch) until May 2019, this minor difference in the faulting magnitudes between the two cells shall not be underscored.

Figure 4-7 shows the faulting for the Cells 506 to 806 with respect to age, where fiber dosage varied between the cells. Faulting increased with the age as anticipated. The development of faulting decreased with the increase in fiber dosage. Cell 506, which did not have any fiber, experienced the largest magnitude of faulting among the four thin pavement cells; whereas, Cell 806, which had the maximum fiber dosage, experienced the lowest magnitude of faulting (3 times less than Cell 506).

Figure 4-8 shows that for thin unbonded concrete pavement overlays, faulting was slightly affected by slab size and increased with age. Cell 705 with larger slabs (driving lane 14 ft X 12 ft, passing lane 12 ft X 12 ft) experienced slightly less faulting as compared to Cell 805 with smaller slabs (driving lane 8 ft X 12 ft, passing lane 6 ft X 12 ft).
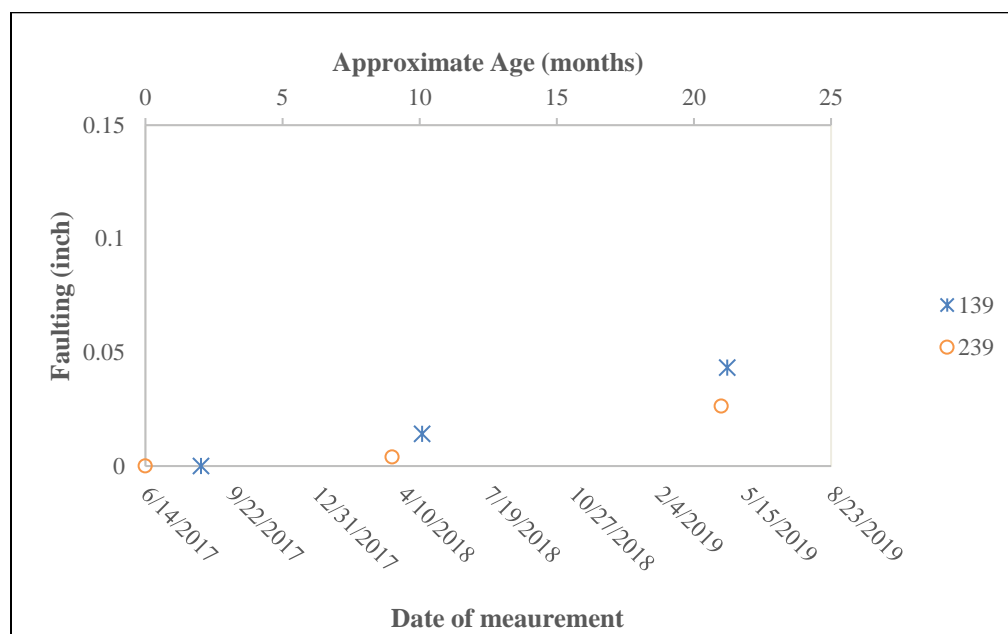
Figure 4-6. Faulting vs. Age for Cells 139 & 239.

63
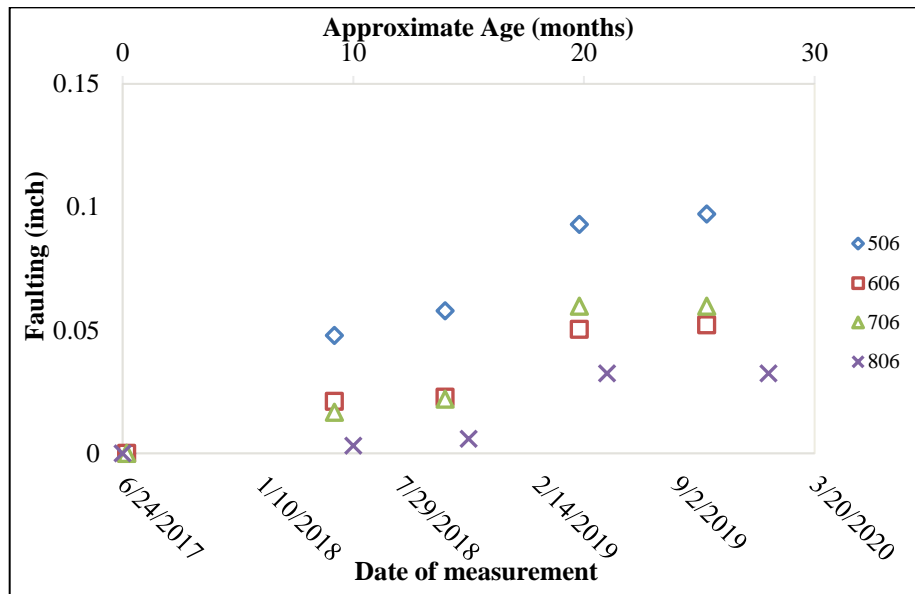
Figure 4-7: Faulting vs. Age for Cells 506,606,706 & 806.
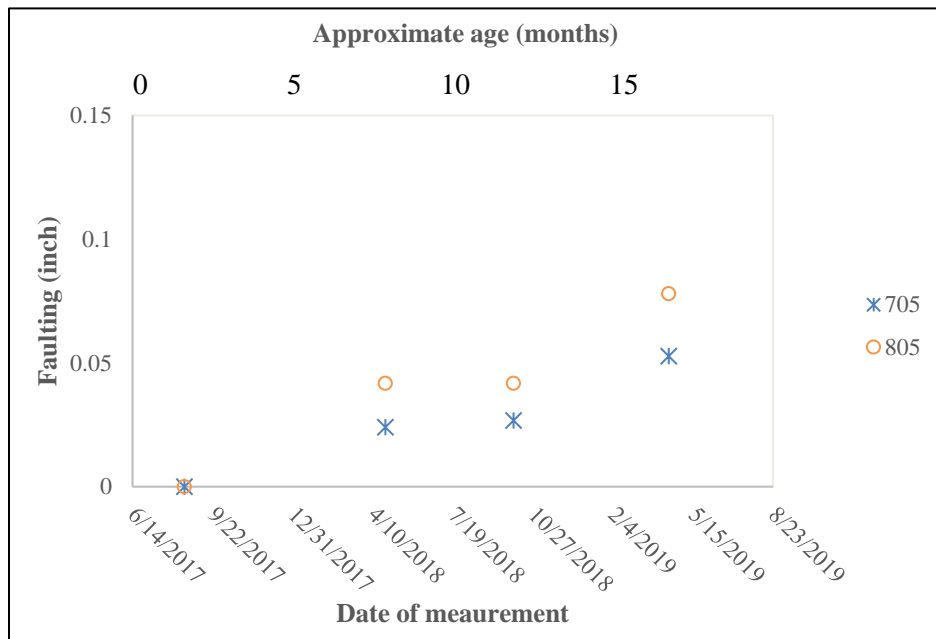
Figure 4-8: Faulting vs. Age for Cells 705 & 805.

4.3 FAULTING PROGRESSION WITH TRAFFIC (ESAL)

Figure 4-9 shows the measured faulting for Cells 139 and 239 with respect to ESAL. Note that the estimated ESAL for a given number of axle load repetitions is higher for the 3-inch thick cells than the 4-inch thick cell. When this slab thickness effect was considered in the ESAL calculation, it appeared that the difference in the faulting values between Cells 139 and 239 was insignificant. Figure 4-10 shows the variation of faulting for Cells 506 to 806; this figure also shows the significant contribution of fibers in Cell 806. The sudden increase of the faulting at 1.8 million ESALs (during Spring 2019) for all the thinner cells indicates a weakening of the joint conditions during the springtime when the underlying layers were relatively weak. There is no significant difference between the measured faulting values for Cells 606 and 706. This might be reasonable because even though Cell 706 (5-inch) is one inch thinner than Cell 606 (6-inch), it contains 3 lbs./cy more fibers than Cell 606; the residual strength of Cell 606 concrete is 124.16 psi compared to 156.4 psi for the Cell 706. Figure 4-11 compares the faulting values of all the ultra-thin and thin cells with respect to ESAL. This figure shows a higher rate of faulting accumulation with respect to the ESALs for the ultra-thin cells (Cells 139 and 239) compared to the thin cells (Cells 506 to 806). Figure 4-12 shows that the wider slabs in Cell 705 developed less faulting compared to the narrower-sized slabs in Cell 805, and the faulting propagation rates with respect to ESAL are similar for both cells.
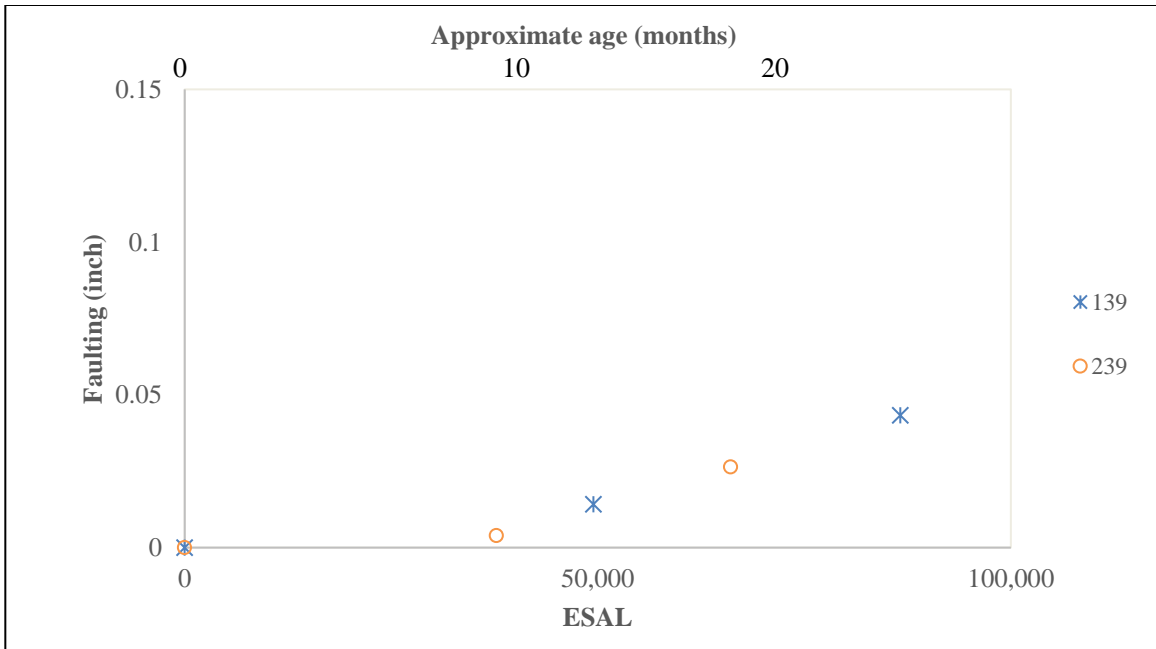
Figure 4-9: Faulting vs. ESALs for Cells 139 & 239.
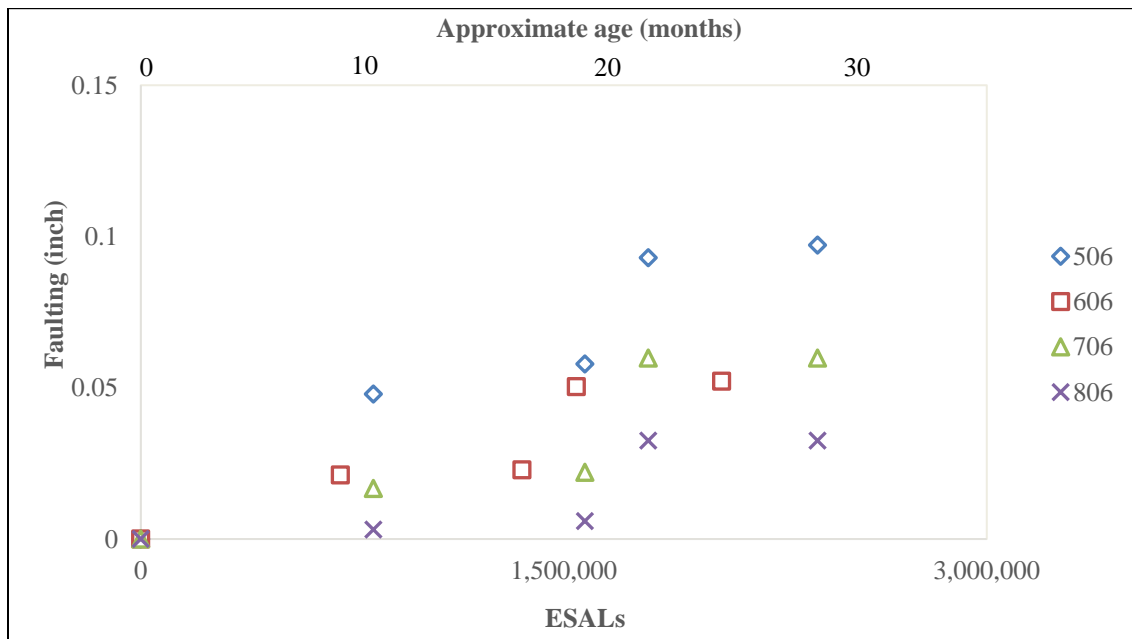
Figure 4-10: Faulting vs. ESALs for Cells 506,606,706 & 806.
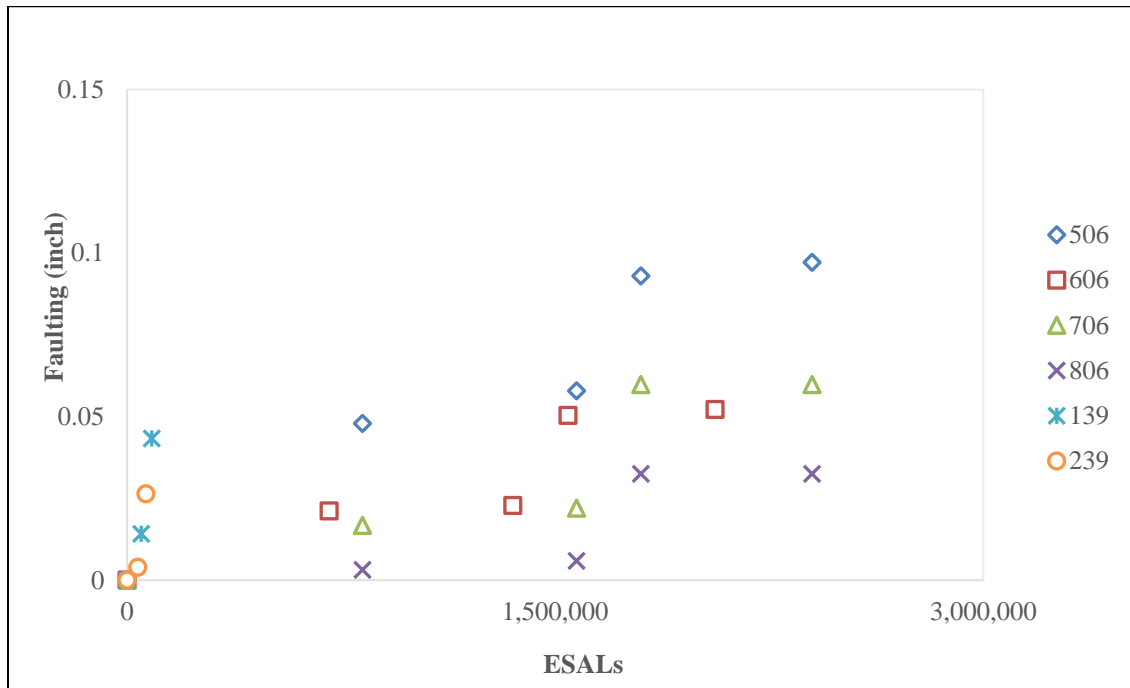
Figure 4-11: Comparison between low volume cells (139 and 239) and high-volume cells (506,606,706, and 806).
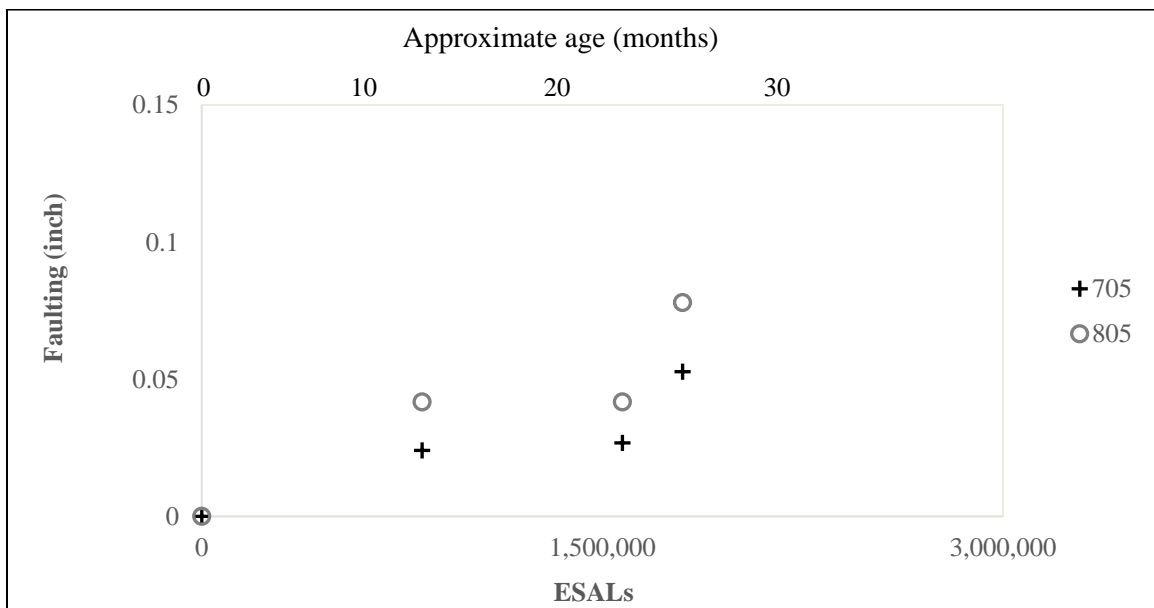
Figure 4-12: Faulting vs. ESALs for Cells 705 & 805.

4.4 FAULTING PREDICTION EQUATION

The data presented in the previous section verified that synthetic structural fibers could have a significant influence on transverse joint faulting. The mechanistic-empirical design of fiber-reinforced thin concrete pavements should thus account for structural fibers in faulting prediction. The faulting of a concrete pavement depends on many parameters. The National Cooperative Highway Research Program's (ARA, 2003) final report for transverse joint faulting summarized influential pavement variables considered in various faulting predicting models for conventional concrete pavements. It appears that ESAL, drainage coefficient, modulus of subgrade reaction, slab thickness, joint spacing, and shoulder types are some influential variables for faulting, with fiber properties now a logical addition to such parameters.

Based on the faulting measurements and pavement variables considered in this study, an effort was made to develop a faulting prediction equation for thin fiber-reinforced concrete pavements. Because of the lack of data, such equations were not developed for the ultra-thin pavement cells and unbonded overlays. A few trial equations were developed using various sets of pavement design variables, material properties, and then the best one was chosen based on the predictability. The final faulting prediction equation (Equation 15) is provided below. The influence of ESAL, slab thickness, fiber property (residual strength of concrete), and sub-layer properties were considered in the faulting prediction equation.

$$FAULT \ = \ ESAL^{0.54} * (A + B * h + C * RS + D * k_{comb}) \hspace{2cm} (15)$$

Where,

FAULT = Predicted faulting, inch.

ESAL = Equivalent number of 18-kip standard axles

h = Slab thickness, in.

R.S. = Residual strength of concrete, psi.

K_{comb} = Combined modulus of subgrade reaction, psi/in.

 A, B, C, and D are parametric constants; A= 0.000055, B= -0.0000033, C = -0.000000096, and D= -0.0000000107. The R^2 and SSE for this equation is 0.9117 and 0.0019 inch, respectively. Figure 4-13 (a) shows the comparison between the predicted and measured faulting values for thin pavement cells

(Cells 506 - 806). Figure 4-13 (b) shows the predictability of the proposed faulting prediction equation. The faulting prediction equation was validated with the final faulting data set, recorded in May 2020; this set of data was not used in the equation development. Figure 4-14 shows the validation result for the proposed faulting prediction equation.

(a)

(b)
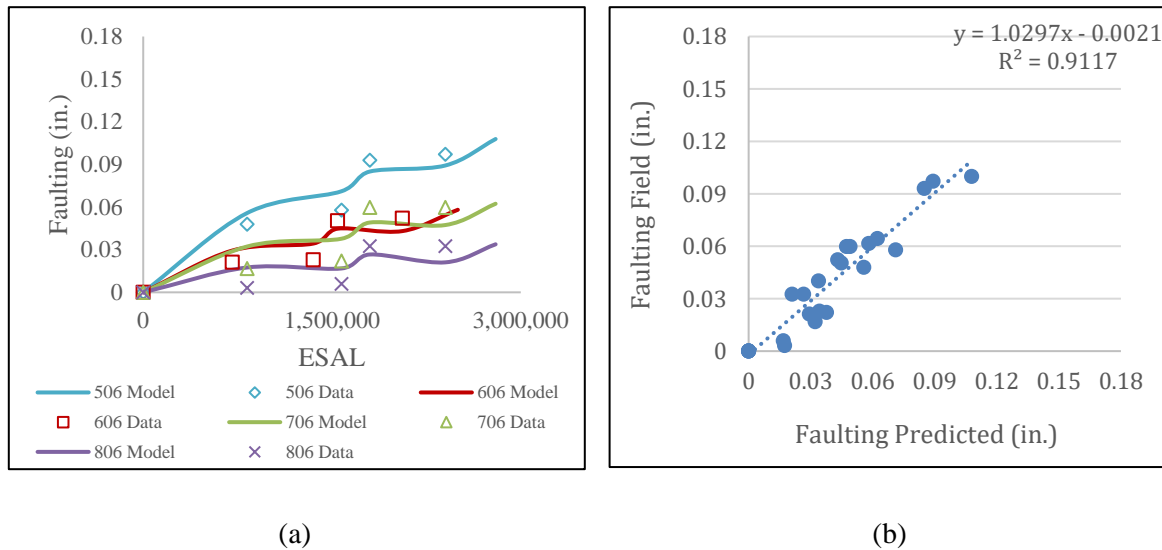
Figure 4-13: (a) Comparison of the measured faulting and predicted faulting, (b) Predictability of the proposed faulting prediction equation.
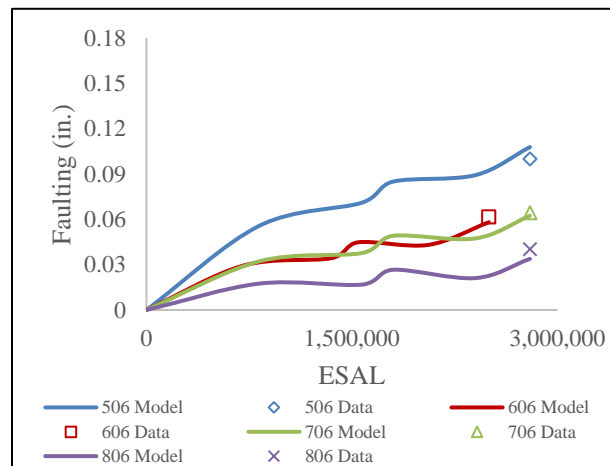
Figure 4-14: Validation of the proposed faulting prediction equation.

4.5   RIDE QUALITY - INTERNATIONAL ROUGHNESS INDEX

International roughness index data was collected on various cells to study the pavement surface ride quality and verify the fibers' influence on the same. Figure 4-15 shows the variation of IRI with respect to ESAL for the four thin pavement cells. Cell 506, having no fibers, showed higher IRI values consistently. Cell 606, 706, and 806, which have fibers, showed lower IRI values compared to Cell 506. In the year 2018, at 825,000 ESALs, the IRI value for Cell 506 was 180 inches/mile, which was already in the range of poor ride quality index (RQI) (Table 2-6). At the same time and same ESAL, Cell 806, having maximum fiber dosage, had an IRI value of 139 inches /mile, which is within the fair RQI rating. However, after 2.4 million ESALs, Cell 806 also reported a poor RQI rating (IRI>173 inches/mile). This suggests that thin concrete pavements with fiber reinforcement can keep the pavement roughness within an admittable range for up to the approximately 2 million ESALs, which is probably the anticipated design life for such thin pavements, then fibers' influence keeps decreasing. It may be noted that due to the short length of each test cell, higher initial IRI values are common at MnROAD; therefore one should look at the change in IRI relative to the initial IRI. Since these cells were exposed to much higher levels of traffic than would typically be placed on these thin designs, the rate of IRI development would likely be far less on typical projects in the network.
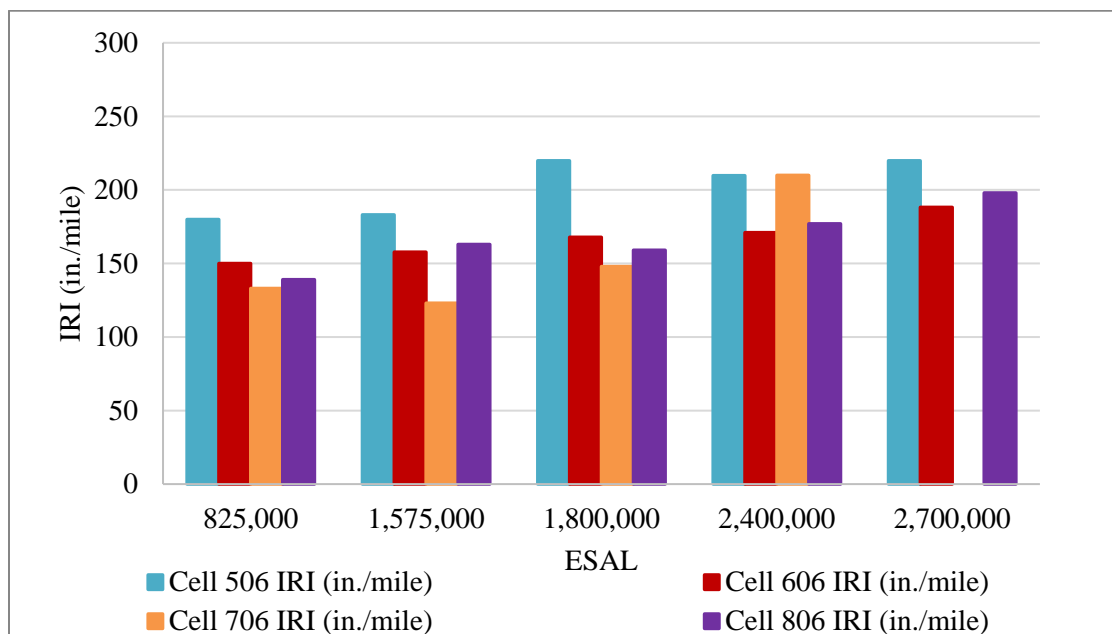
Figure 4-15: Variation of International Roughness Index (IRI) with respect to ESALs for Cells 506-806.

Figure 4-16 presents the IRI results of Cells 705 and 805. Recall that the percentage of cracked slabs for Cell 705 was 15% more than Cell 805 even though the crack index (length of cracks/ unit surface area) for both the cells were comparable. The IRI for both the cells was within the admittable range until approximately 2 million ESALs, with slightly less value for the Cell 805. At 2.4 million ESALs, both cells deteriorated, and the IRI significantly increased, more for the Cell 805 (narrower slabs).
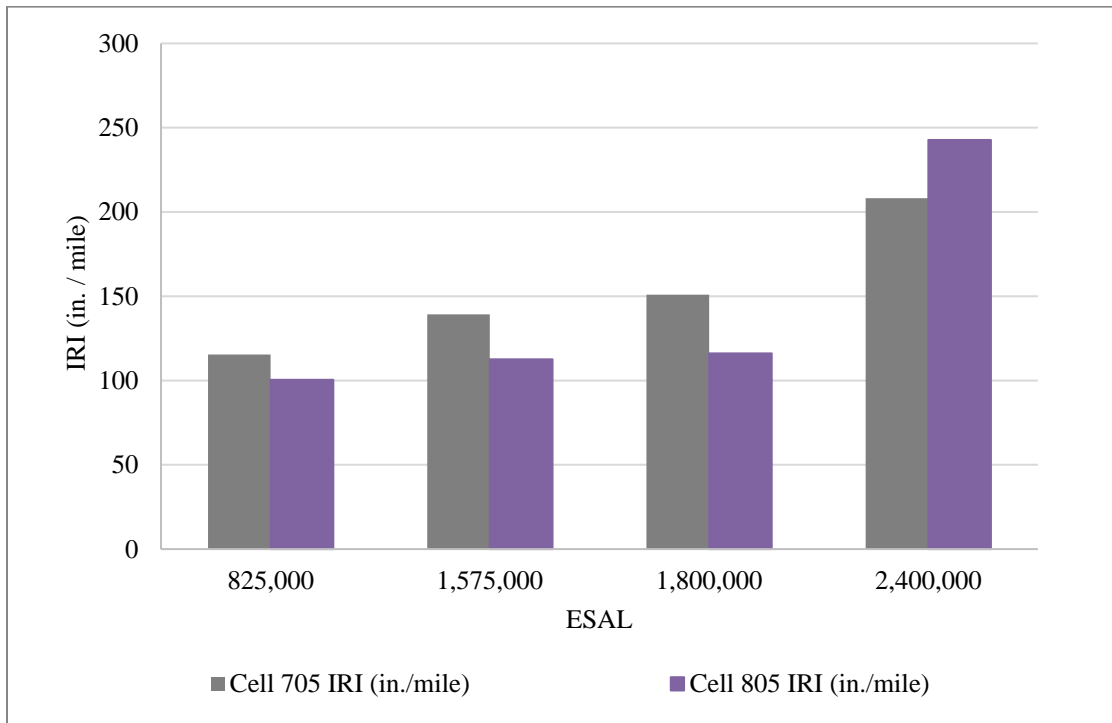
Figure 4-16: Variation of International Roughness Index (IRI) with respect to ESALs for Cells 705 and 805.

4.6   FAULTING VS IRI

This section compares faulting with the international roughness index. As the faulting was measured only at ten joints for each cell, a parameter named 'Faulting Index (FI)' was introduced to account for the faulting in all the joints and to compare with IRI. The units for the FI is inches/mile, the same as the IRI's unit. The faulting index is was determined using the following equation.

$$FI = \frac{Average\ faulting\ at\ a\ joint * Total\ no.\ of\ joints\ in\ the\ cell * 5280}{Total\ length\ of\ the\ Cell} \qquad (16)$$

Figure 4-17 shows the IRI and FI together for Cells 506 through 806, and Figure 4-18 shows the same for Cells 705 and 805. Both FI and IRI indicate the highest value for Cell 506 and lowest for Cell 806. Both the parameters increased with the ESAL, and a higher increase is observed after approximately 2 million ESALs. The differences in the faulting index values are, however, prominent between the cells. The FI values of Cell 606 (6 inches thick) and 706 (5 inches thick but contains 3 lbs/cy more fibers) are close to each other. Figure 4-18 shows that Cell 805 experienced higher FI than Cell 705 consistently, as was the faulting. Figure 4-19 indicates that the IRI ad correlates well with an R^2 = 0.67.
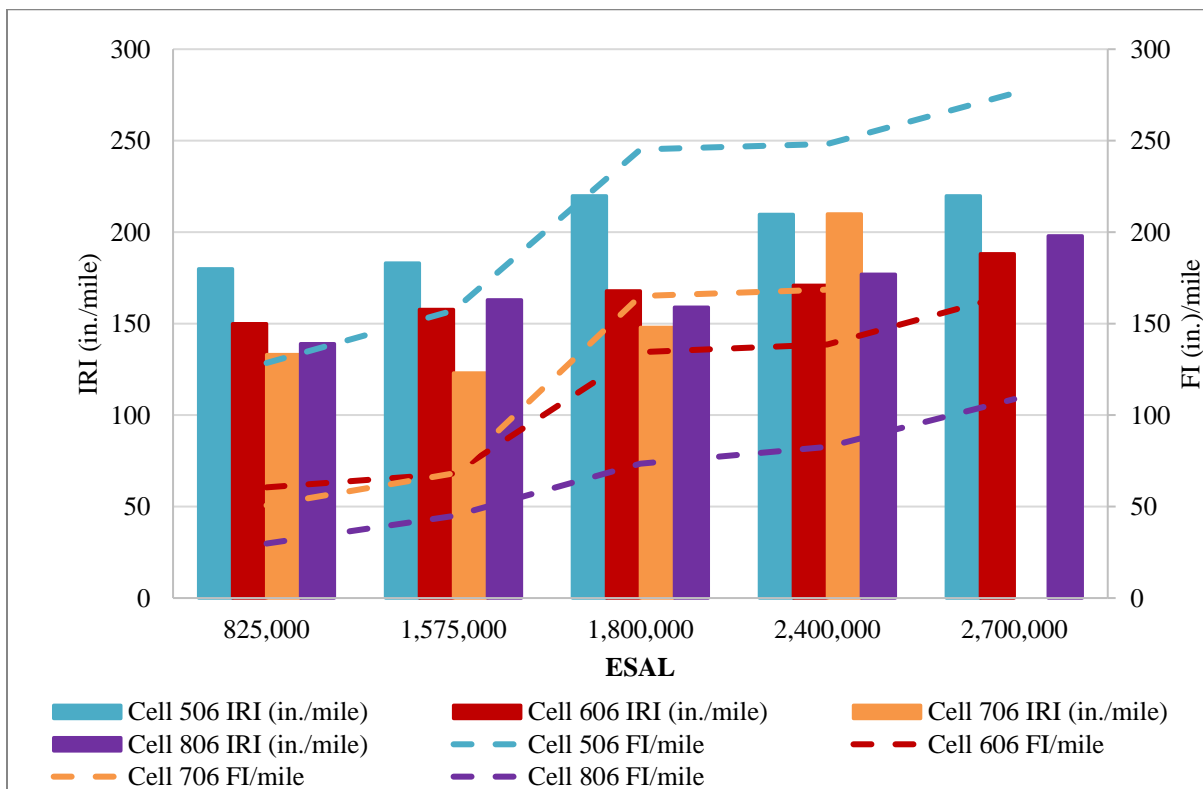
Figure 4-17: Variation of IRI and Faulting Index with respect to ESALs for Cells 506-806.
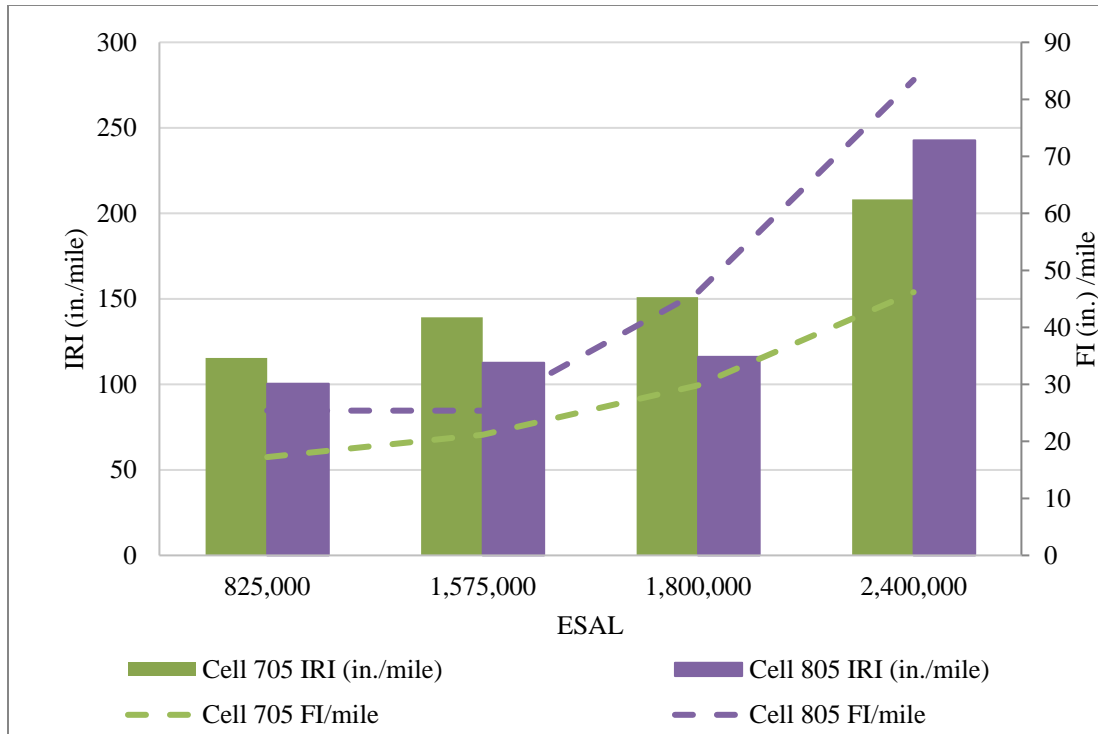
Figure 4-18: Variation of IRI and Faulting Index with respect to ESALs for Cells 705 and 805.
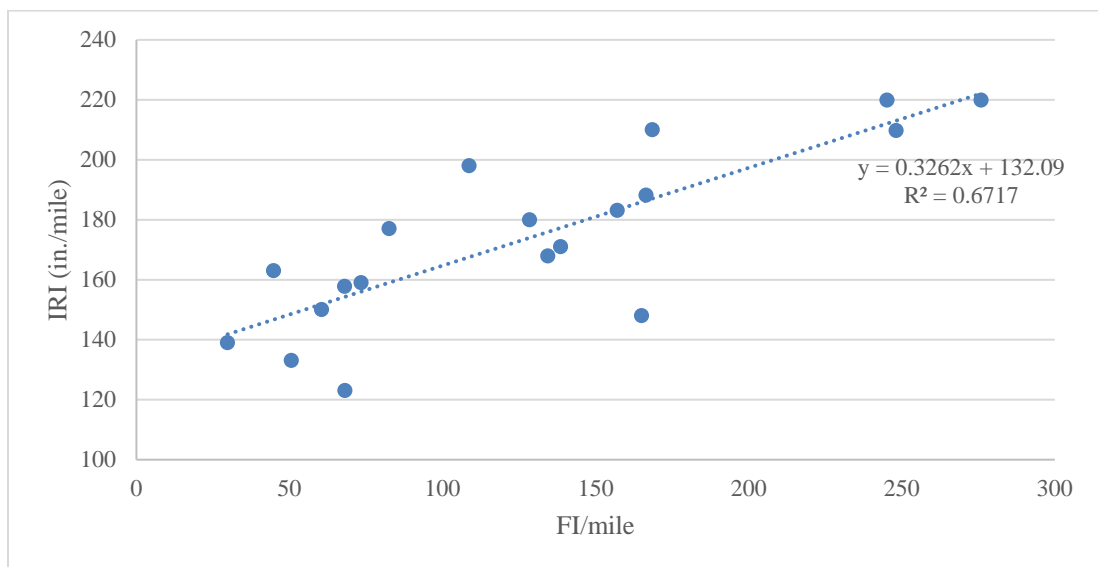
Figure 4-19: Correlation between IRI and faulting index.

5 INFLUENCE OF FIBERS ON STRUCTURAL RESPONSES

This chapter discusses the structural responses of the test cells, including the FWD test results and the results from different sensors installed in the pavement. The temperature and temperature-gradient, environmental strain, dynamic strain, transverse joint opening, etc., are discussed and compared between the cells. The joint performance with respect to the LTE, differential displacement, and loaded-side displacement are also discussed.

5.1 TEMPERATURE AND HUMIDITY

Ambient temperature and relative humidity data were collected at MnROAD using an external weather station. Figure 5-1 shows the variation of the ambient temperatures collected from mid-June 2017 to November 2020. As shown in this figure, January 29, 2019, was the coldest day with a temperature of -34.2°C, and December 31, 2017, was the second coldest day at MnROAD with -29.5°C temperature. On the other side, May 28, 2018, was the warmest day, with a temperature of 37°C. The variation of the relative humidity at the MnROAD Project site from 2017 summer to 2020 winter is provided in Figure 5-2.
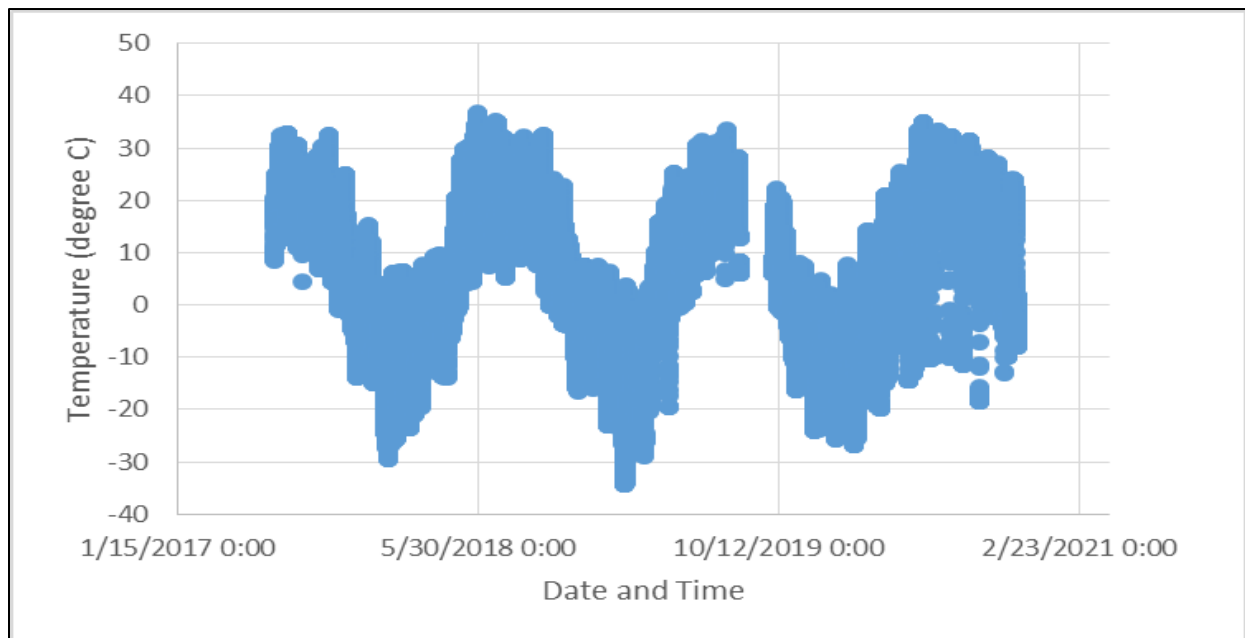
Figure 5-1. The ambient temperature at the MnROAD Project site.
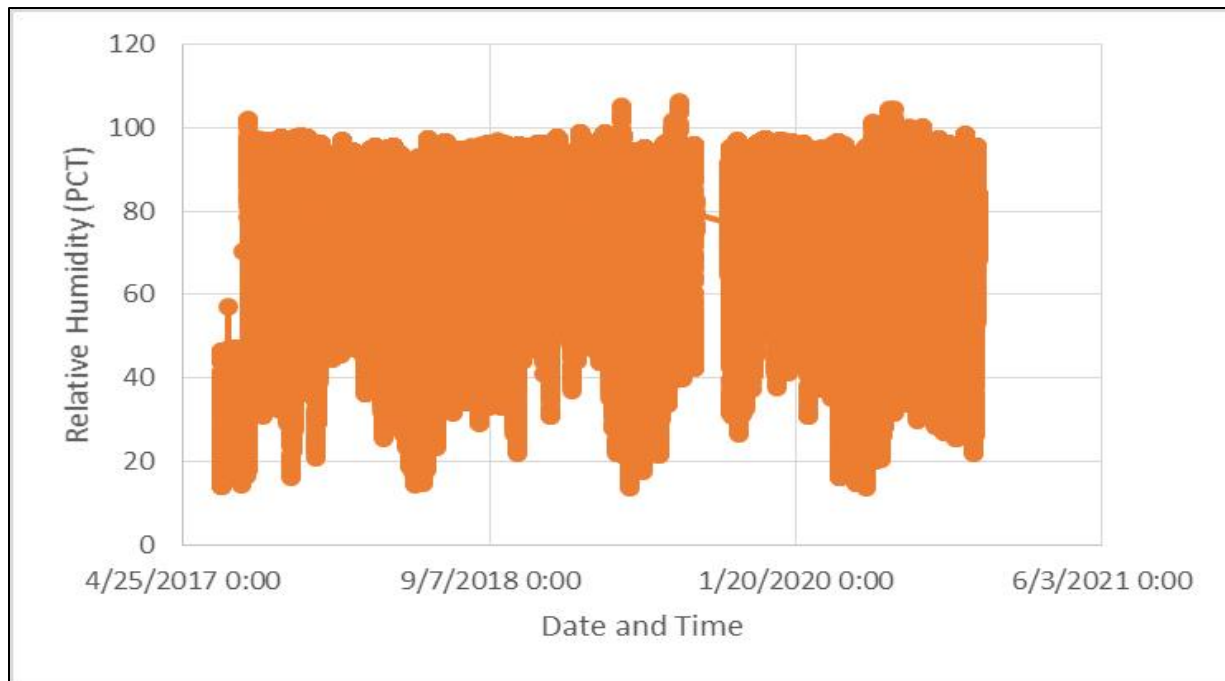
Figure 5-2. Relative humidity variation at the MnROAD Project site.

5.1.1 Pavement Temperature

The pavement slab temperature data for the cells equipped with thermocouples are shown in Figure 5-3 through Figure 5-9. These figures contain several plots, each with temperatures recorded at different depths of the slab. As expected, the general trends of the seasonal temperature variations are similar for all the cells and align well with the ambient temperature trend, shown in Figure 5-1. The maximum and minimum temperatures recorded for each cell and their respective dates of occurrence and times are summarized in Table 5-1. The dates of the coldest temperatures for all the cells were recorded on January 30, 2019, except for Cells 705 and 805, which recorded the coldest temperature on December 31, 2017. Cell 239 outer sensor and Cell 805 experienced their warmest day on May 28, 2018. Cell 139 experienced the warmest day on the date of its paving, i.e., July 17, 2017. The inner thermocouple tree of Cell 239 also experienced the warmest temperature on July 17, 2017, on its paving date. These observations indicate that Cells 139 and 239 were constructed on a relatively warmer day, and the recorded highest temperatures probably were influenced by the heat of hydration of the cement. Two thermocouple sensors of Cell 705 stopped working after October 2019. Although the sensor trees beneath the Cell 705 slab continued to work, they were outside the boundary of interest and hence not added in Figure 5-6.

75
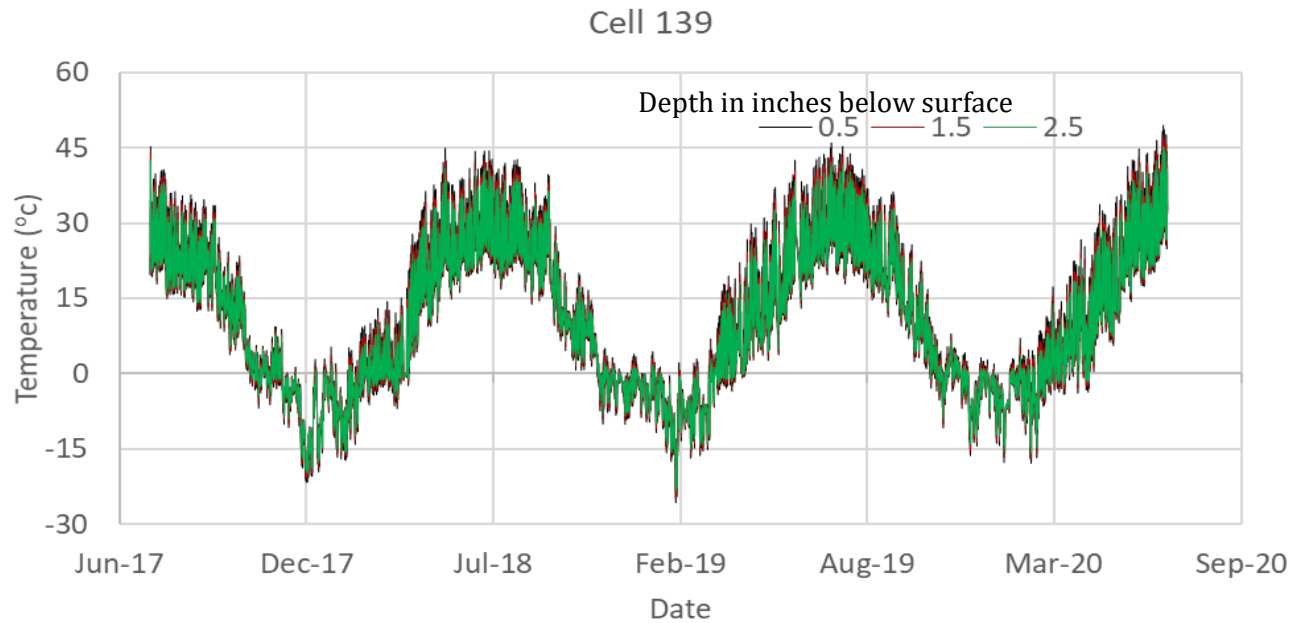
Figure 5-3. Temperature profile of Cell 139.
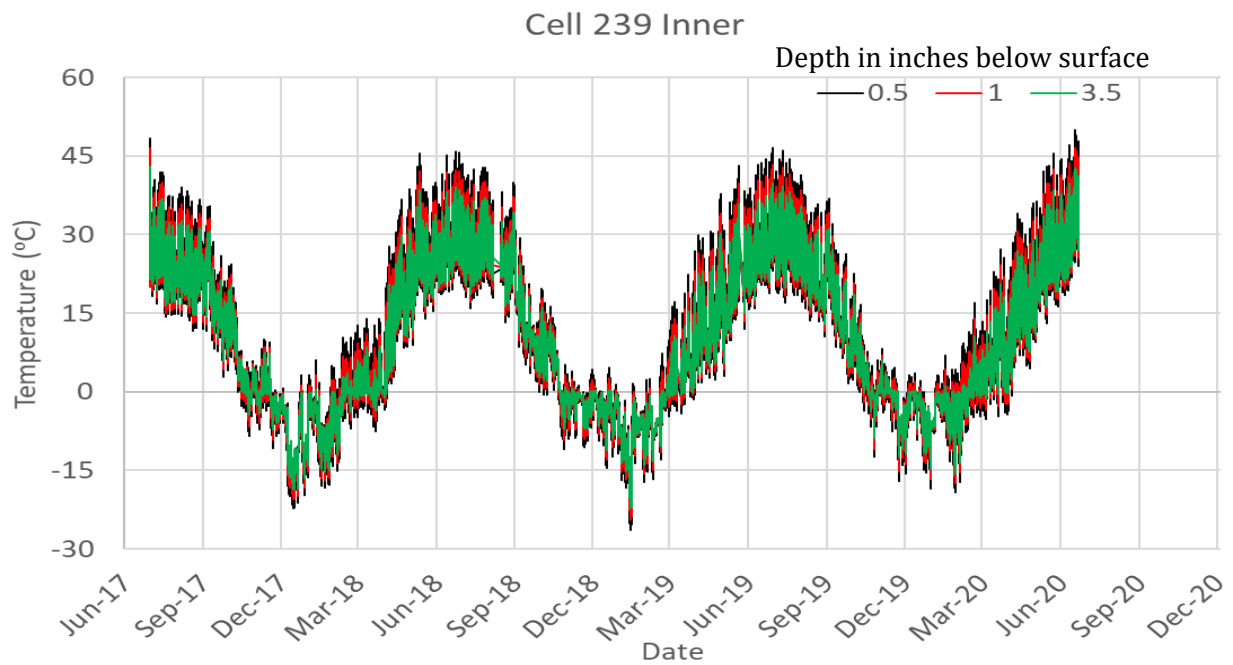
Figure 5-4. Temperature profile of Cell 239 inner lane.

76
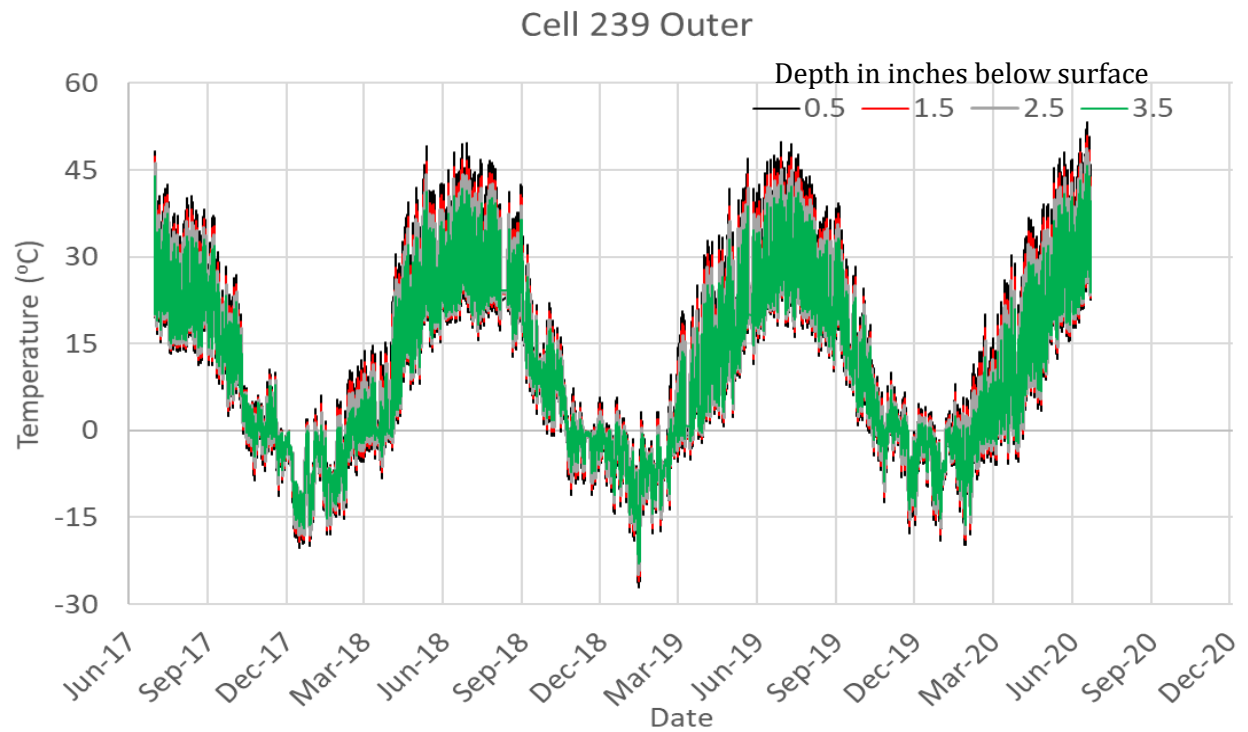
Figure 5-5. Temperature profile of Cell 239 outer lane.
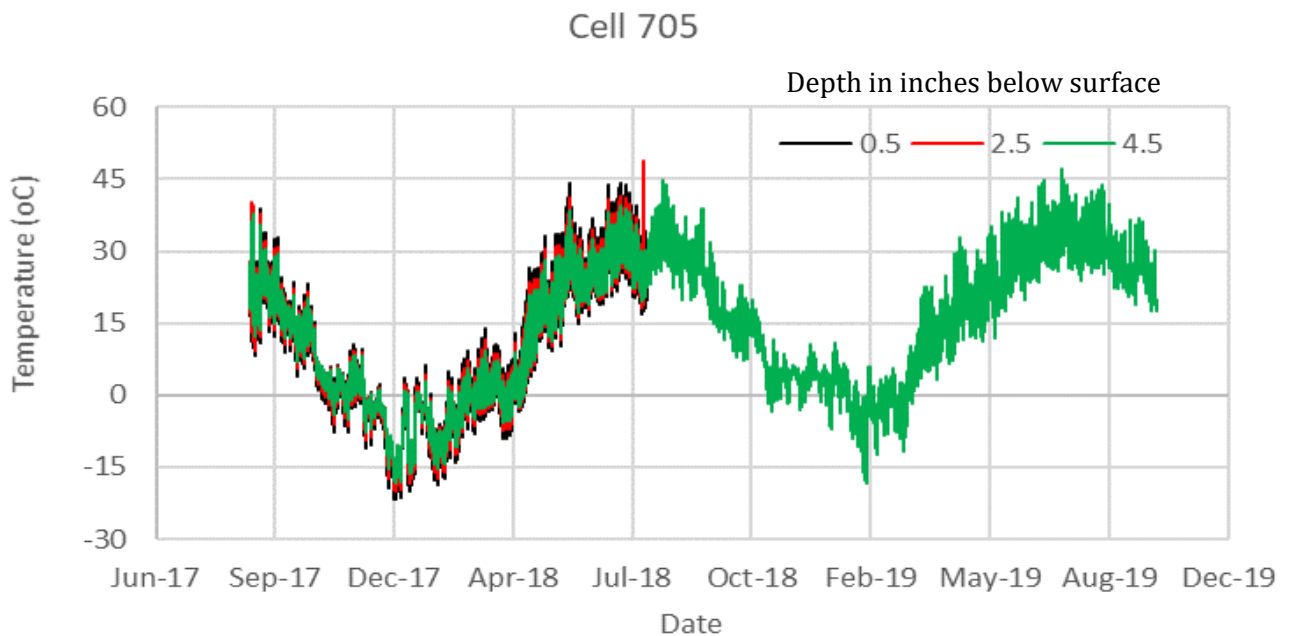
Figure 5-6. Temperature profile of Cell 705.

77
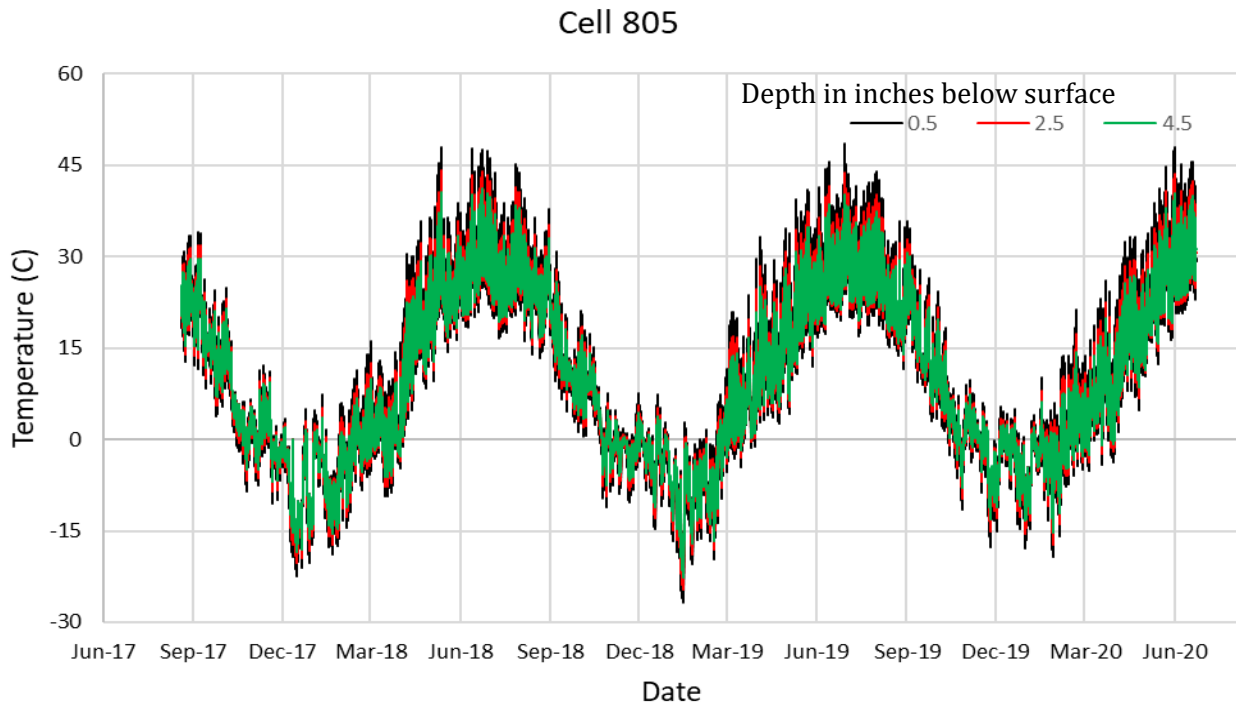
Figure 5-7. Temperature profile of Cell 805.
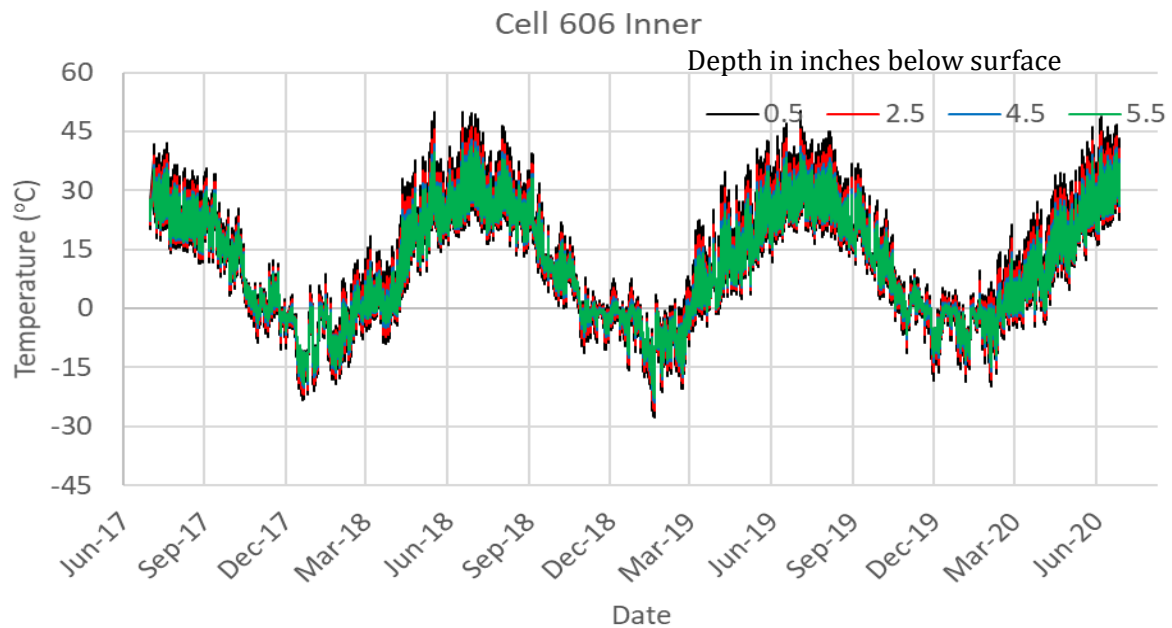
Figure 5-8. Temperature profile of Cell 606 inner lane.

78
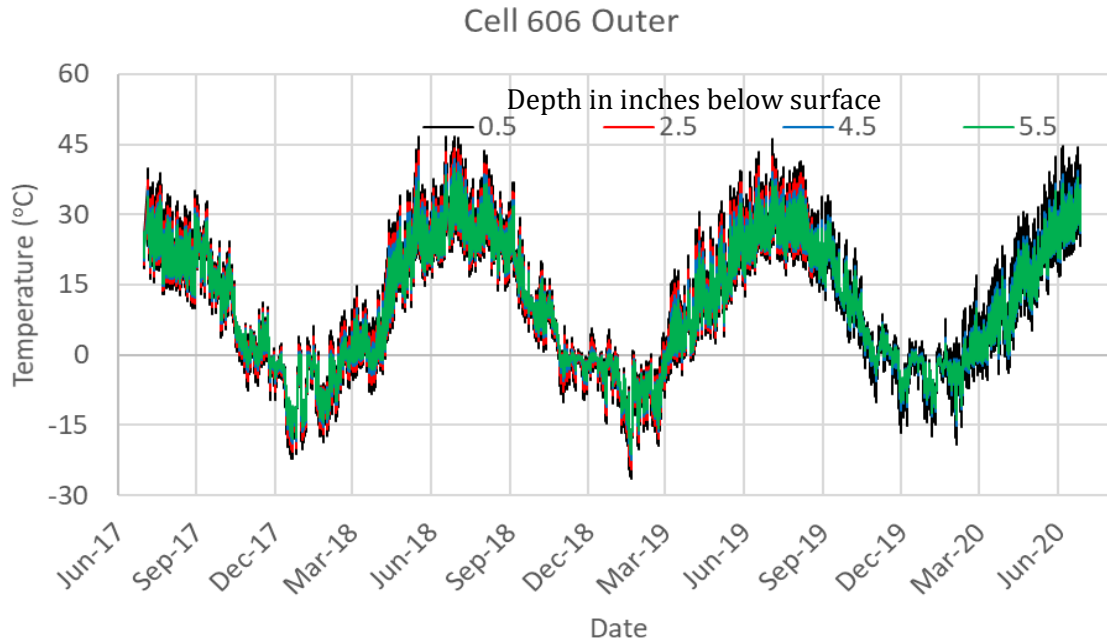
Figure 5-9. Temperature profile of Cell 606 outer lane.

Table 5-1. Cell extreme temperatures and respective dates and times.

Cell		Temperature °C	Date	Time
139	Max	49.51	7/4/2020	2:45 PM
	Min	-25.68	1/30/2019	7:45 AM
239	Max Outer	49.77	5/28/18	2:15 PM
	Min Outer	-27.21	1/30/19	7:30 AM
	Max Inner	48.33	7/17/17	2:45 PM
	Min Inner	-26.43	1/30/19	7:00 AM
705	Max	47.2	7/15/19	3:45 PM
	Min	-21.82	12/31/17	8:45 AM
805	Max	47.92	5/28/18	2:45 PM
	Min	-22.42	12/31/17	8:45 AM
606	Max Outer	46.71	7/9/2018	3:45 PM
	Min Outer	-26.41	1/31/2019	7:30 AM
	Max Inner	50.25	7/15/2019	3:15 PM
	Min Inner	-27.7	1/31/2019	7:30 AM

Note: Temperature readings collected at different depths of slabs are considered.

The relationship between the temperature and depth of the slab was studied to determine the nature of the temperature variation (either linear or non-linear). Figure 5-10 and Figure 5-11 show the temperature profiles of various cells during their coldest and warmest temperature events, respectively. Temperature profiles for various cells at an intermediate temperature, observed on April 24, 2019, are studied as well, as shown in Figure 5-12. The general nature of the temperature variation with respect to the depth of the slab was linear, except for Cell 239, which showed a slightly non-linear nature; the reason for a distinct trend of the temperature variation in Cell 239 is not known. One possible reason could be that the thermocouple attached to the tree at one-inch depth moved downwards because of the construction-related issue. The relatively lower thickness of the slabs in this study compared to the conventional concrete pavements may be the reason for the linear temperature gradients in all other cells. As the cells (except Cell 239) experienced linear temperature gradients, the analysis has been restricted to the linear temperature gradient only.

5.1.2 Linear Temperature Gradient (LTG)

The linear temperature gradient (LTG) is the ratio of the temperature difference between the top and bottom sensors and the vertical distance between them. A negative temperature gradient indicates that the pavement is colder at the top and warmer at the bottom, and a positive temperature gradient indicates the opposite scenario. At negative and positive temperature gradients, slabs experience upward and downward curling, respectively.

Table 5-2 shows the monthly maximum and minimum LTGs for Cells 139 and 239. Cell 139 had the highest positive LTG of 2.68°C/cm in December 2019. The highest negative LTG for cell 139 was -0.99 °C/cm in July 2019. The outer sensor tree of Cell 239 had the highest LTG of 1.79 °C/cm in June 2020 and the highest negative LTG of -2.53°C/cm in December 2019, while the inner sensor tree had the highest positive LTG of 1.81°C/cm in September 2019 and the lowest LTG of -2.49 °C/cm in December 2019.
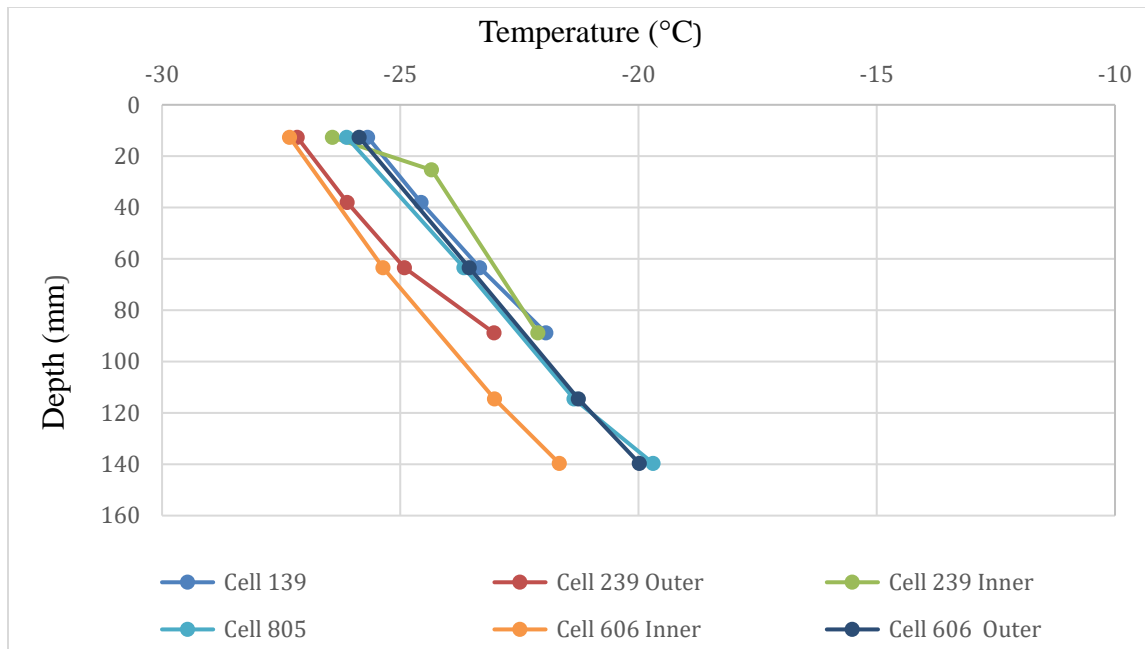
Figure 5-10. Temperature vs. slab depth on the coldest day, January 30, 2019, 7:45 AM.
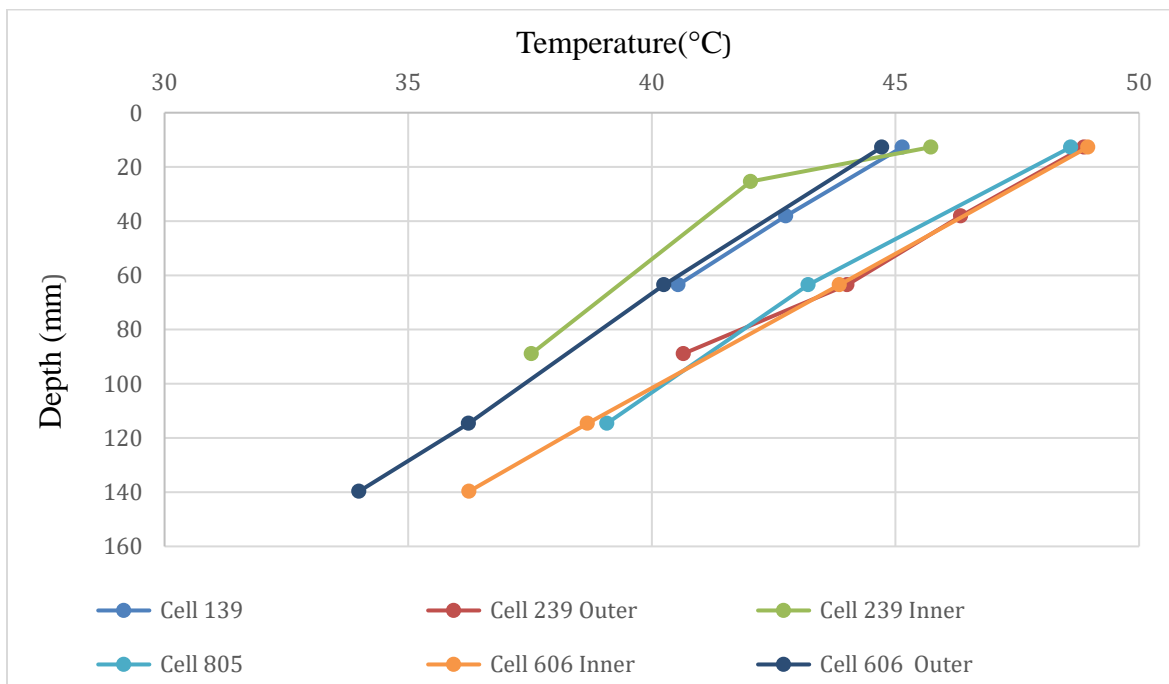
Figure 5-11. Temperature vs. slab depth on the warmest day, July 15, 2019, 2:30 PM.

81
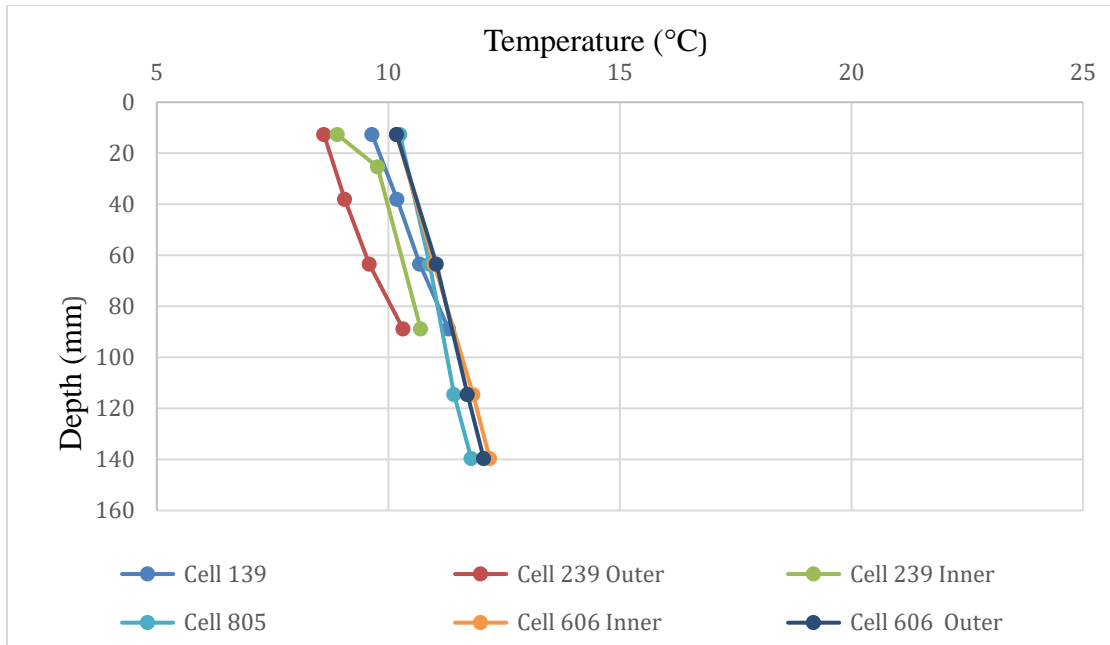
Figure 5-12. Temperature vs. slab depth at an intermediate temperature on April 24, 2019, 4:15 AM.

Cells 705 and 805 are thin unbonded fiber reinforced concrete overlays on concrete pavements. Table 5-3 shows the monthly maximum and minimum LTGs for both Cells 705 and 805. From the available data for Cell 705, the maximum positive LTG was found as 1.00 °C/cm, and the maximum negative was -0.74 °C/cm. Cell 805 had a maximum positive LTG of 1.11 °C/cm and a maximum negative LTG of -0.90 °C/cm. For Cell 705, the maximum positive LTGs occurred in July 2018, and for Cell 805, the same occurred in April and November 2019. The maximum negative LTG for Cell 705 occurred in September 2017, and for Cell 805, it occurred in September 2018 and November 2019. Overall, the maximum LTGs for Cell 805, which were constructed with 6 ft wide slabs, were slightly higher than Cell 705 that had 12 ft. wide slabs.

Table 5-2. Max. and Min. linear temperature gradient results for Cells 139 and 239.

	Temperature Gradient (°C/cm)					
	Cell 139 (3-inch)		Cell 239 (4-inch)			
	Inner		Outer		Inner	
Month	Negative	Positive	Negative	Positive	Negative	Positive
Jul-17	-0.65	0.81	-0.91	0.95	-0.59	1.07
Aug-17	-0.58	0.87	-0.68	1.25	-0.61	1.14
Sep-17	-0.52	0.79	-0.85	1.08	-0.49	0.98
Oct-17	-0.38	0.72	-0.45	0.94	-0.41	0.88
Nov-17	-0.49	0.60	-0.59	0.80	-0.51	0.75
Dec-17	-0.48	0.41	-0.58	0.40	-0.52	0.59
Jan-18	-0.51	0.68	-0.67	0.72	-0.47	0.82
Feb-18	-0.51	0.98	-0.64	1.06	-0.51	1.17
Mar-18	-0.43	1.04	-0.52	1.15	-0.47	1.29
Apr-18	-0.52	1.09	-0.66	1.61	-0.56	1.34
May-18	-0.62	1.09	-1.07	1.41	-0.53	1.35
Jun-18	-0.76	1.16	-0.63	1.56	-0.49	1.32
Jul-18	-0.92	1.19	-0.91	1.41	-0.63	1.10
Aug-18	-0.86	1.18	-0.91	1.54	-0.62	1.18
Sep-18	-0.95	1.19	-0.81	1.24	-0.50	0.89
Oct-18	-0.95	0.89	-0.54	0.90	-0.68	0.99
Nov-18	-0.81	0.95	-1.08	0.74	-0.91	0.67
Dec-18	-0.82	1.04	-0.57	0.63	-0.62	0.54
Jan-19	-0.61	0.92	-0.88	0.65	-0.62	0.47
Feb-19	-0.51	0.70	-0.71	0.84	-0.61	0.62
Mar-19	-0.44	1.04	-0.47	1.24	-0.45	1.12
Apr-19	-0.91	1.19	-0.71	1.45	-0.38	1.18
May-19	-0.62	1.16	-0.63	1.45	-0.57	1.16
Jun-19	-0.55	1.11	-0.83	2.22	-0.57	1.35
Jul-19	**-0.99**	1.12	-1.63	1.43	-1.15	1.15
Aug-19	-0.72	1.06	-1.06	1.41	-0.73	1.06
Sep-19	-0.51	0.76	-0.72	1.34	-0.65	**1.81**
Oct-19	-0.47	0.99	-1.22	1.55	-1.17	0.98
Nov-19	-0.74	0.61	-2.21	0.68	-1.05	0.75
Dec-19	-0.79	**2.68**	**-2.53**	1.12	**-2.49**	0.64
Jan-20	-0.44	0.43	-0.90	0.60	-0.56	0.46

Feb-20	-0.63	0.98	-0.81	1.13	-0.74	1.22
Mar-20	-0.44	1.12	-0.55	1.43	-0.62	1.35
Apr-20	-0.35	0.48	-0.55	1.48	-0.82	1.32
May-20	-0.46	1.26	-1.13	1.60	-0.59	1.51
Jun-20	-0.78	1.11	-1.24	**1.79**	-0.90	1.31

Table 5-3. Linear temperature gradient results for Cells 705 and 805.

Temperature Gradient (°C/cm)				
	Cell 705 (5-inch)		Cell 805 (5-inch)	
Month	Negative	Positive	Negative	Positive
Sep-17	**-0.74**	0.53	-0.39	0.57
Oct-17	-0.35	0.41	-0.38	0.57
Nov-17	-0.40	0.35	-0.41	0.48
Dec-17	-0.45	0.19	-0.47	0.30
Jan-18	-0.48	0.44	-0.50	0.56
Feb-18	-0.44	0.53	-0.46	0.66
Mar-18	-0.37	0.64	-0.43	0.83
Apr-18	-0.39	0.74	-0.43	1.01
May-18	-0.35	0.81	-0.48	1.04
Jun-18	-0.38	0.77	-0.25	-0.24
Jul-18	-0.62	**1.00**	-0.70	1.08
Aug-18			-0.67	1.05
Sep-18			**-0.90**	1.02
Oct-18			-0.82	0.64
Nov-18			-0.88	0.58
Dec-18			-0.88	0.61
Jan-19			-0.57	0.40
Feb-19			-0.53	0.80
Mar-19			-0.46	0.93
Apr-19			-0.76	**1.11**

Temperature Gradient (ºC/cm)				
	Cell 705 (5-inch)		Cell 805 (5-inch)	
Month	Negative	Positive	Negative	Positive
May-19			-0.45	1.10
Jun-19			-0.39	0.97
Jul-19			-0.60	0.98
Aug-19			-0.44	0.92
Sep-19			-0.35	0.87
Oct-19			-0.36	0.61
Nov-19			**-0.90**	**1.11**
Dec-19			-0.52	0.44
Jan-20			-0.49	0.40
Feb-20			-0.61	0.83
Mar-20			-0.32	0.89
Apr-20			-0.36	0.89
May-20			-0.45	0.86
Jun-20			-0.57	1.03
* Data collection for cell 805 started on September 5th 2017				

Out of the four Cells 506 through 806 in the mainline test track, only Cell 606 had thermocouples. Two sensor trees were included in this cell. The LTGs for both sensor trees are provided in Table 5-4. For the inner sensor tree, the maximum positive LTG was 2.77 ºC/cm, and the maximum negative TG was -4.16 ºC/cm. The outer sensor tree has maximum positive and negative LTGs of 1.59 ºC/cm and -1.56 ºC/cm, respectively. For outer and inner sensor trees, the positive maximum LTG occurred in September and November 2019, respectively, whereas the maximum negative LTGs for the outer and inner sensor trees occurred in December 2019 and November 2019, respectively.

Table 5-4. Linear temperature gradient results for Cell 606.

	Temperature Gradient (ºC/cm)			
	Cell 606 Inner (5-inch)		Cell 606 Outer (5-inch)	
Month	Negative	Positive	Negative	Positive
Jul-17	-0.38	0.74	-0.28	0.62
Aug-17	-0.50	0.74	-0.33	0.62
Sep-17	-0.37	0.64	-0.33	0.61
Oct-17	-0.34	0.55	-0.34	0.42
Nov-17	-0.43	0.52	-0.41	0.39
Dec-17	-0.47	0.33	-0.43	0.22
Jan-18	-0.49	0.61	-0.47	0.49
Feb-18	-0.47	0.72	-0.43	0.56
Mar-18	-0.47	0.91	-0.39	0.72
Apr-18	-0.47	1.06	-0.44	0.84
May-18	-0.53	1.12	-0.34	0.92
Jun-18	-0.40	1.04	-0.36	0.85
Jul-18	-0.40	0.99	-0.38	0.77
Aug-18	-0.35	0.93	-0.35	0.73
Sep-18	-0.48	0.71	-0.38	0.56
Oct-18	-0.39	0.68	-0.37	0.54
Nov-18	-0.47	0.55	-0.48	0.45
Dec-18	-0.43	0.54	-0.41	0.43
Jan-19	-0.56	0.56	-0.55	0.43
Feb-19	-0.47	0.61	-0.44	0.47
Mar-19	-0.46	0.98	-0.43	0.80
Apr-19	-0.33	1.17	-0.33	0.97
May-19	-0.45	1.17	-0.35	0.93
Jun-19	-0.41	1.04	-0.38	0.82
Jul-19	-0.64	1.03	-0.38	0.86
Aug-19	-0.45	0.99	-0.39	0.76

Temperature Gradient (°C/cm)				
	Cell 606 Inner (5-inch)		Cell 606 Outer (5-inch)	
Month	**Negative**	**Positive**	**Negative**	**Positive**
Sep-19	-0.56	1.25	-0.44	**1.59**
Oct-19	-0.80	0.68	-1.14	0.60
Nov-19	**-4.16**	**2.77**	-1.41	0.45
Dec-19	-1.40	0.51	**-1.56**	0.36
Jan-20	-0.49	0.38	-0.48	0.32
Feb-20	-0.58	0.94	-0.59	0.71
Mar-20	-0.35	0.95	-0.34	0.75
Apr-20	-0.36	0.96	-0.38	0.76
May-20	-0.45	0.92	-0.44	0.73
Jun-20	-0.54	0.90	-0.40	0.77
*Data collection started July 7th, 2017				

5.1.3 Frequency Distribution of Linear Temperature Gradients

In order to determine the common LTG ranges, the frequency distributions of the LTGs were plotted for each cell, as shown in Figure 5-13. The frequency distributions of Cells 139 and 239 did not show a significant difference. In Cell 239, the trends between the two sensor trees were similar, with the exception that the outer sensor tree had a higher number of frequencies for an LTG range of -0.5 to -0.25 °C/cm than the inner one. The Cell 239 inner sensor tree and Cell 139 provided very similar LTGs. The maximum frequency for Cell 139 and the inner tree in Cell 239 occurred in the LTG range of -0.15 to 0 °C/cm. The maximum frequency for the outer sensor tree in Cell 239 occurred in the range of -0.5 and -0.25 °C/cm. Cell 705 and 805 have similar trends, with the maximum for both cells occurring between -0.15 and 0 °C/cm. The trends of the LTGs measured at the inner and outer trees of Cell 606 were also the same, with the maximum frequency occurring between -0.15 and 0 °C/cm.
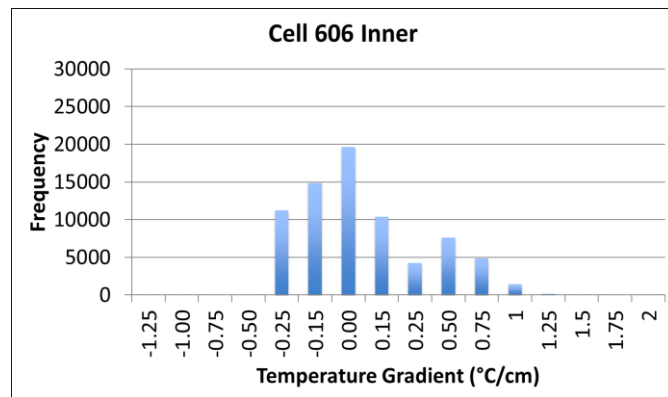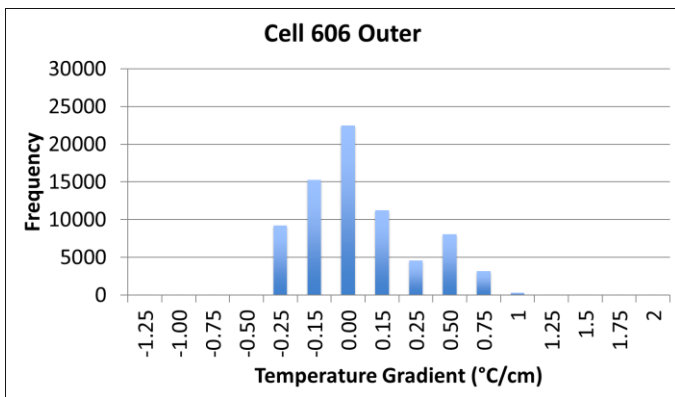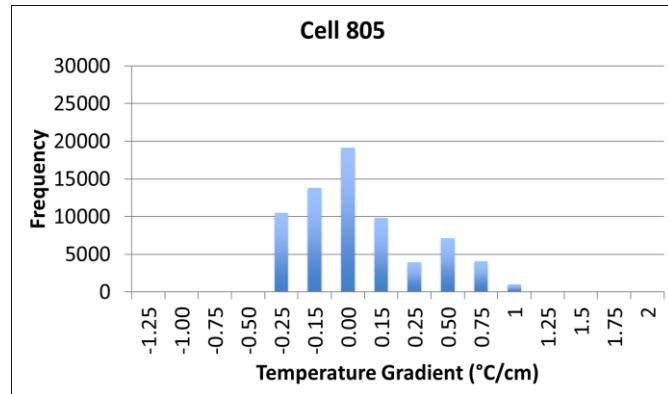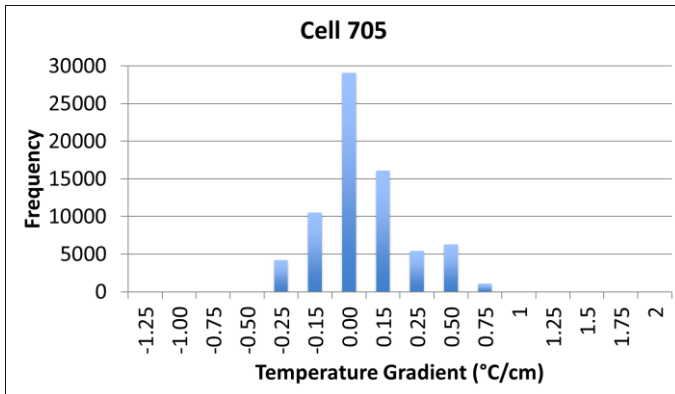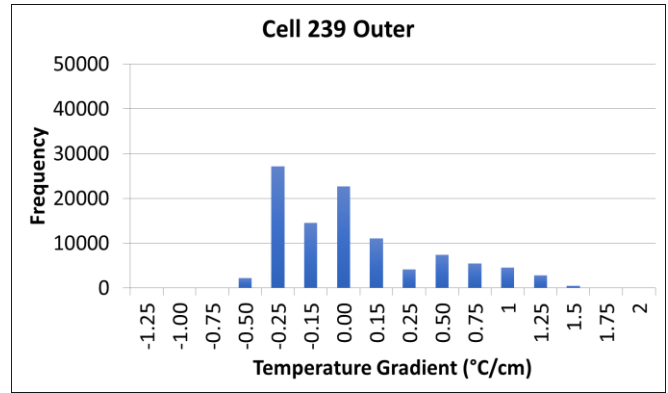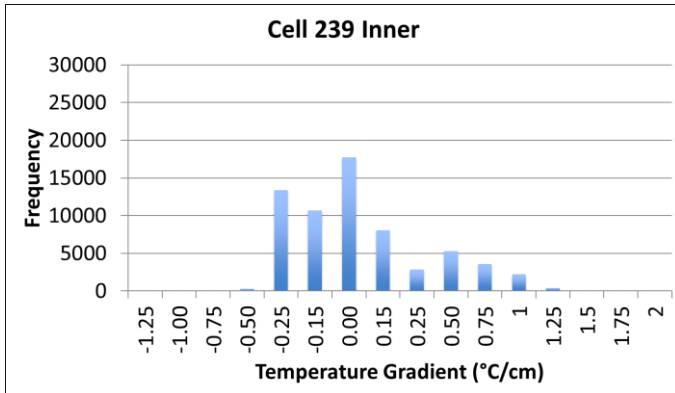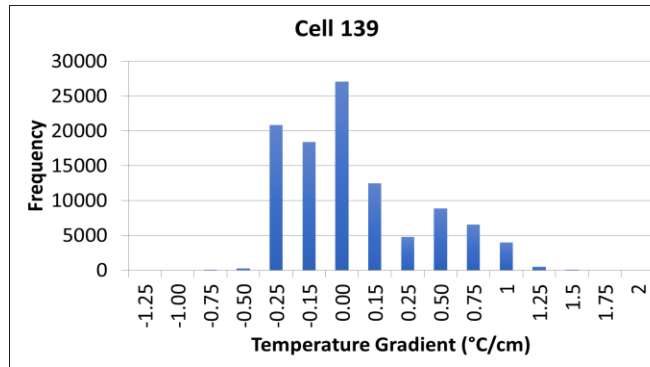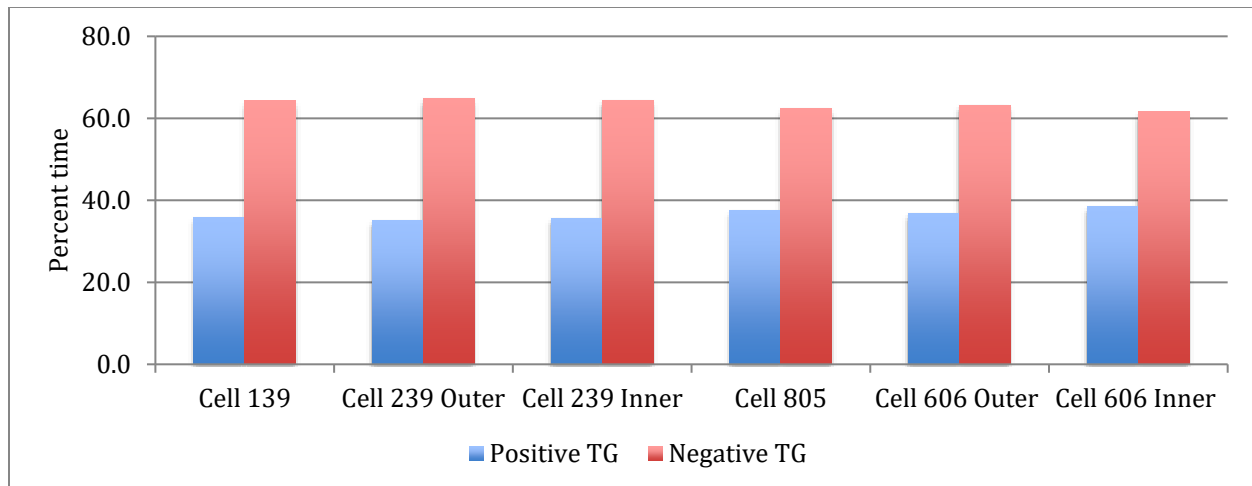
Figure 5-13. Frequency distributions of the linear temperature gradient for various cells.

88

Figure 5-14. Percent times of positive and negative LTGs.

Figure 5-14 shows the percent time that the LTG was positive and negative. Overall, the percent time that the LTG was positive or negative was consistent between the cells. It appeared that all the cells experienced negative temperature gradients for more than 60 percent time.

5.2   ENVIRONMENTAL STRAIN

MnDOT has an established procedure for converting the raw vibrating wire data into a meaningful strain. One of the essential steps in the vibrating wire data analysis procedure is to determine the initial strain value, which corresponds to the first reading when the concrete has hardened sufficiently to fully engage the sensor, and the temperature difference between the nearby top and bottom temperature sensors is approximately '0'. The initial strain value serves as the baseline value for subsequent readings. In order to determine the above-mentioned initial strain value, temperatures at the top and bottom of the slab and the raw frequency data are plotted together. An example of such plots is provided in Figure 5-15; these plots are related to one of the vibrating sensors of Cell 139 (Sensor 1, longitudinal direction). Using these plots, the time of the first 0-temperature gradient is determined after the raw frequency data started proper cycling; the corresponding strain at this time is considered as the initial strain value. In Figure 5-15, it can be seen that the initial strain value was achieved around 8:30 AM of July 18, 2017 (approximately 11 hours after the paving), when the temperature gradient was nearly 0.

89

The first reading when the concrete has hardened sufficiently to engage the sensor fully.
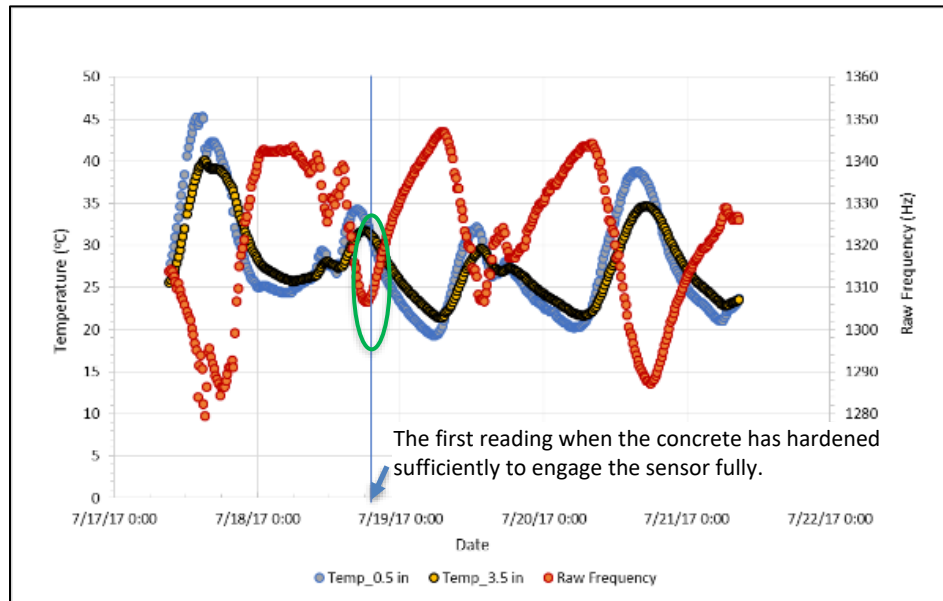
Figure 5-15. Temperature vs. raw frequency, Cell 139, Sensor 1.

5.2.1 Cells 139 and 239

In Cell 139, four vibrating wire sensors were installed, two in the longitudinal direction and two in transverse directions, all at the bottom of the slab, at a depth of 2.5 inches (a half-inch from the bottom of the concrete). Figure 5-16 shows the environmental strains measured by the four sensors; sensor data is available until July 2019. Three out of four sensors showed a similar trend, while the fourth sensor, which was in the transverse direction, showed a completely different and higher negative (tensile) strain compared to the other three. The less variation between the two sensors in the transverse direction and one longitudinal direction may be attributed to the small panel size and somewhat similar boundary conditions along three sides of each slab.

Nevertheless, all the sensors have provided negative strains, indicating that slabs were in a state of contraction. A close look at all these plots suggests that the negative strains in all the sensors sharply increased from July 18, 2017, until the mid of August 2017. Although the temperature declined during this period, the drying shrinkage could have played an influencing role. After that, the strains in all the

90

sensors followed the temperature variation, recording higher tensile strain during the winter, and lower tensile strain at warm temperatures.
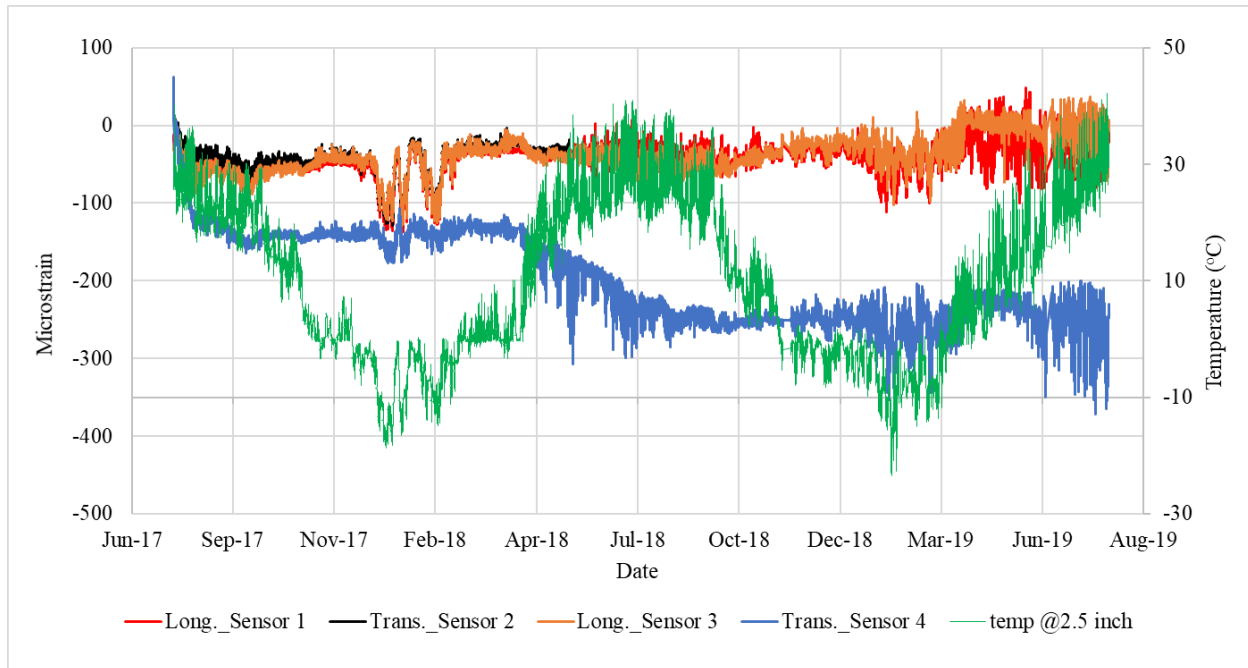
Figure 5-16. Environmental strains and slab temperature for Cell 139.

Figure 5-17 shows plots for the environmental strains and temperature at the 3.5-inch depth of the slab for Cell 239. Like Cell 139, vibrating wire sensors were installed only at the bottom of the slab because of the thickness limitation. As can be seen in Figure 5-17, the strains varied with the seasonal temperature and also experienced a sharp increase in negative strain until the mid of August 2017. The strain measured during the winter was relatively high, in general. Sensor 7, which was placed along the longitudinal direction shown a higher amount of strains than the other three sensors in the cell. The overall trend of the strains measured in Cell 239 was like what was observed in Sensor 4 of Cell 139, indicating an increase in the strain values with the age of the pavement. Compared to the sensors in the transverse directions, the sensors in the longitudinal direction experienced greater strains. The difference in magnitude of the environmental strains in both Cells 139 and 239 was not large.

91
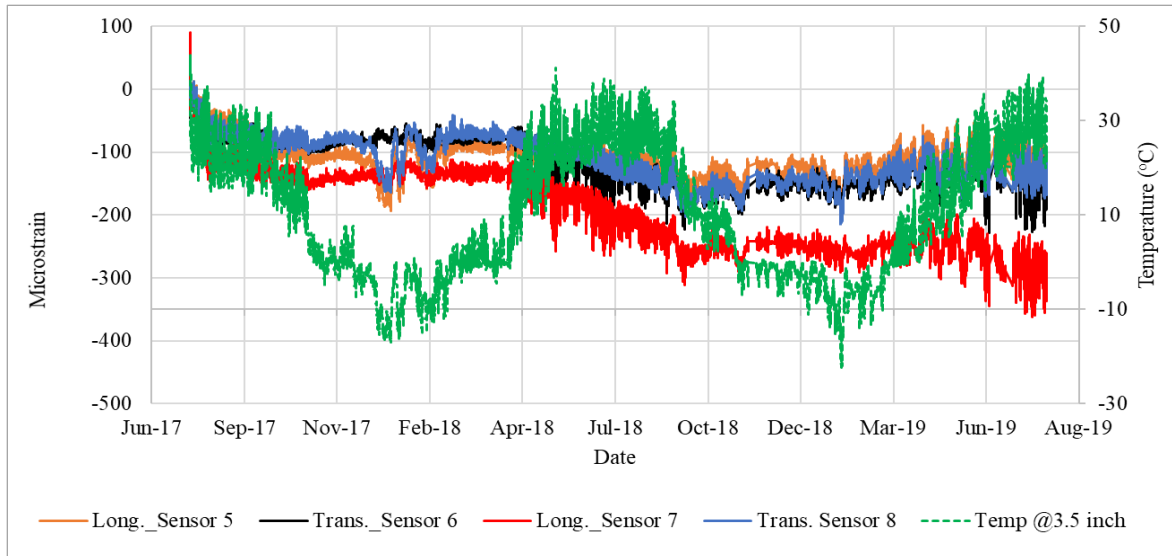
Figure 5-17. Environmental strains and slab temperature for Cell 239.

5.2.2 Cells 705 and 805

In Cell 705, eight vibrating wire sensors were installed in two slabs, four in each slab. In each slab, sensors were installed in the longitudinal and transverse directions. The longitudinal sensors were located at the center of the slab, and the transverse sensors were adjacent to the transverse joints. Two sensors were installed at each location, one at the top and the other at the bottom of the slab, one-half-inch inside the concrete. Figure 5-18 and Figure 5-19 show the strains measured in the first slab and second slab, respectively. Like the other two cells discussed above, the sensors in this cell also showed a correlation with the seasonal temperature. In the first slab, it appeared that the sensors placed at the top of the slabs experienced more strains irrespective of their location, with all the sensors recording higher negative strain values in the cold temperatures. Two sensors (6 and 7) in the second slab recorded higher tensile strain compared to all the other six sensors in this cell. Sensor 6, which was placed at the bottom of the slab along the longitudinal direction, recorded high tensile strain from an early age, whereas Sensor 7 picked up the high strain since summer 2018. The strain measured in these two sensors ranged from 350 to 450 microstrain from September 2018 until August 2019.

Like Cell 705, a total of eight vibrating wire sensors were installed in Cell 805. All the sensors were installed at the center of the slabs, both near the top and bottom of the slab, half-inch inside the

concrete. This report included the results of three sensors installed in the first slab. The results of the three sensors in Cell 805, as can be seen in Figure 5-20, also showed a great correlation with the seasonal temperature variation. Sensor 1, which was placed in the transverse direction, recorded the highest strain, around 300 to 375 micro-strain during the winter (including the strain due to the shrinkage during the initial period).
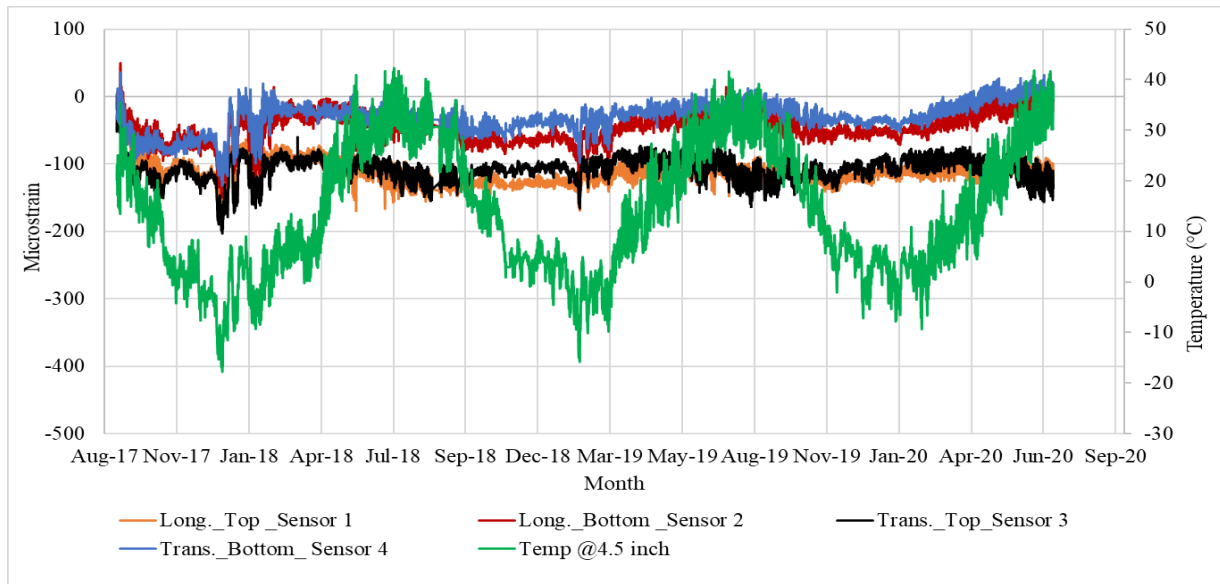
Figure 5-18. Environmental strains and slab temperature for Cell 705, first slab.
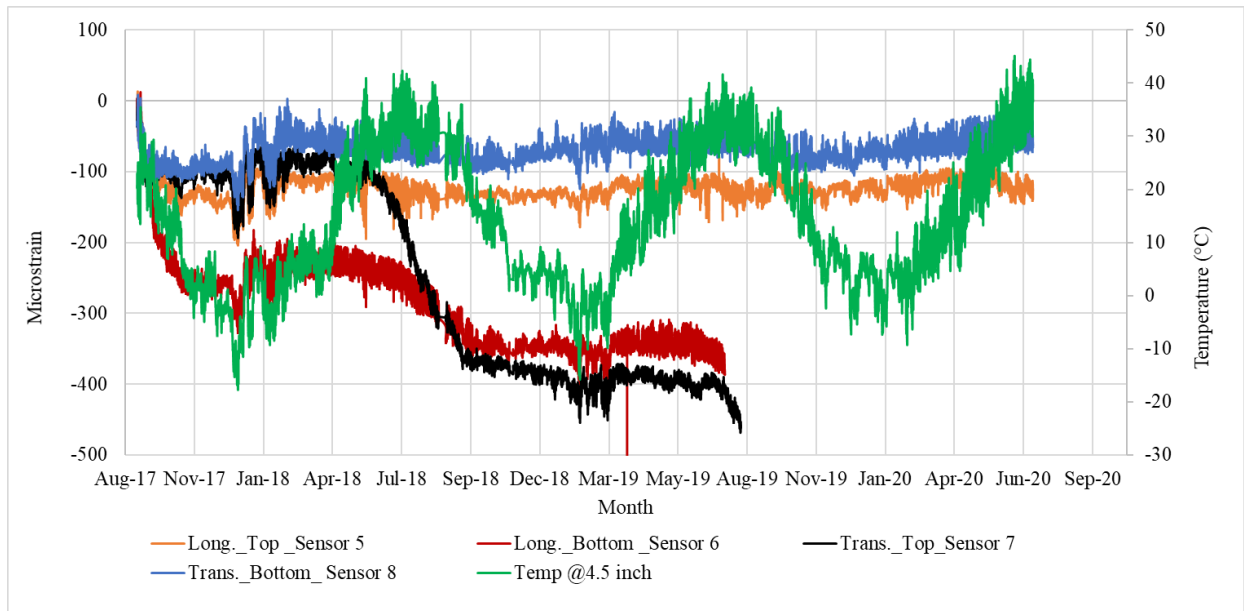
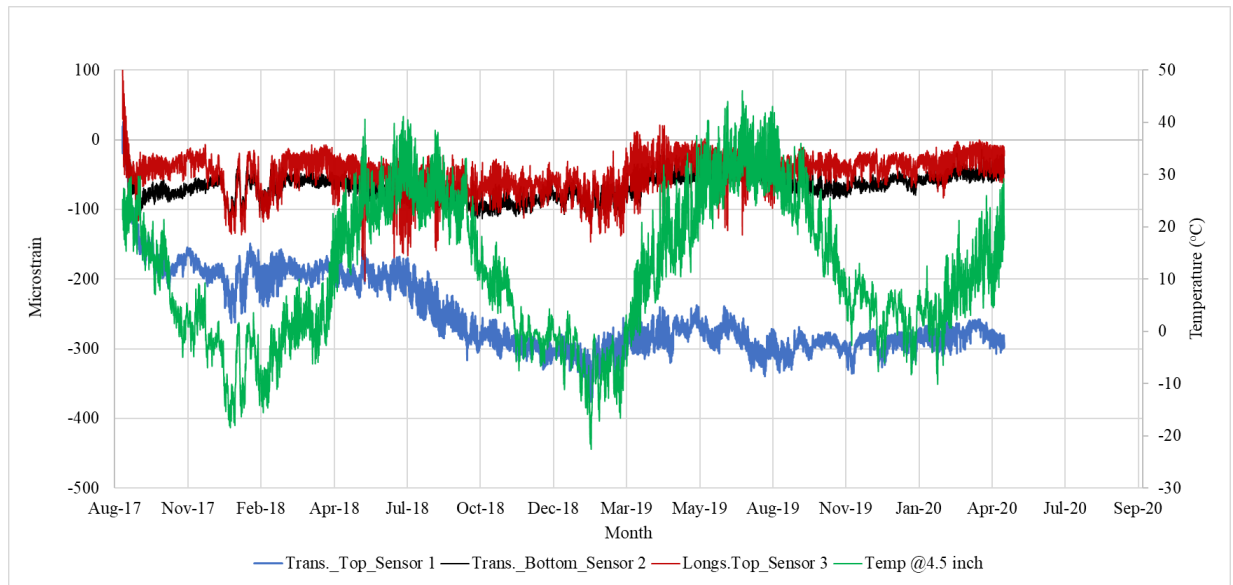**Figure 5-19. Environmental strains and slab temperature for Cell 705, second slab.**
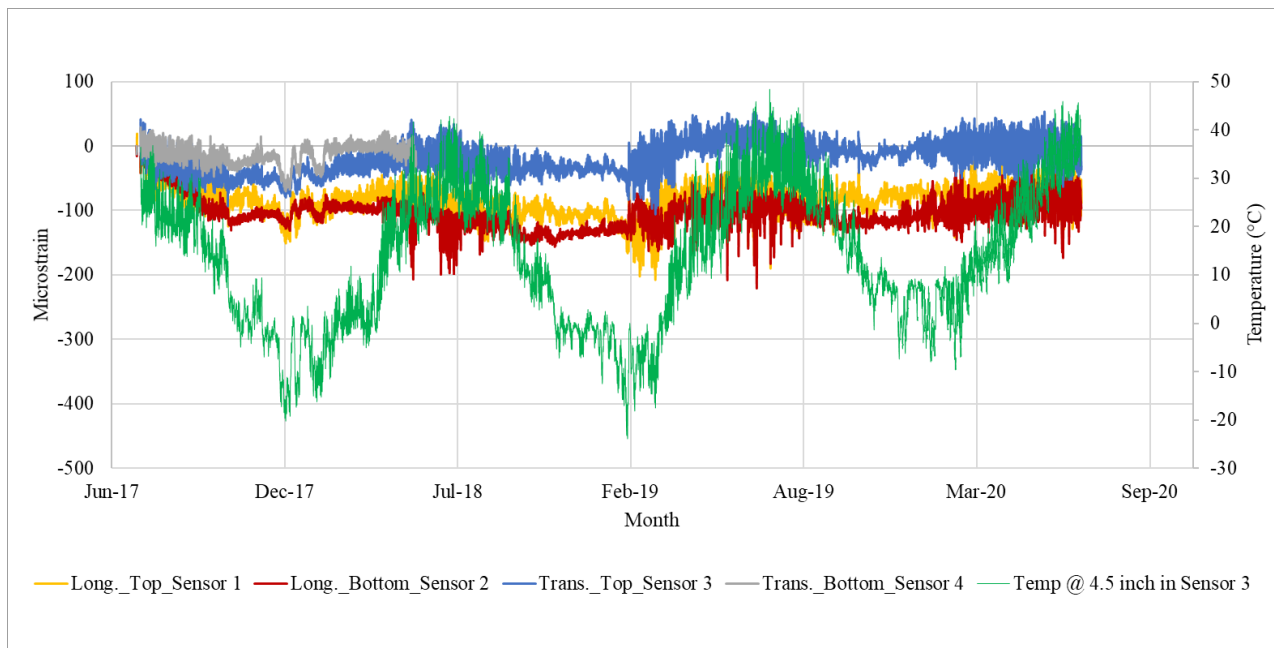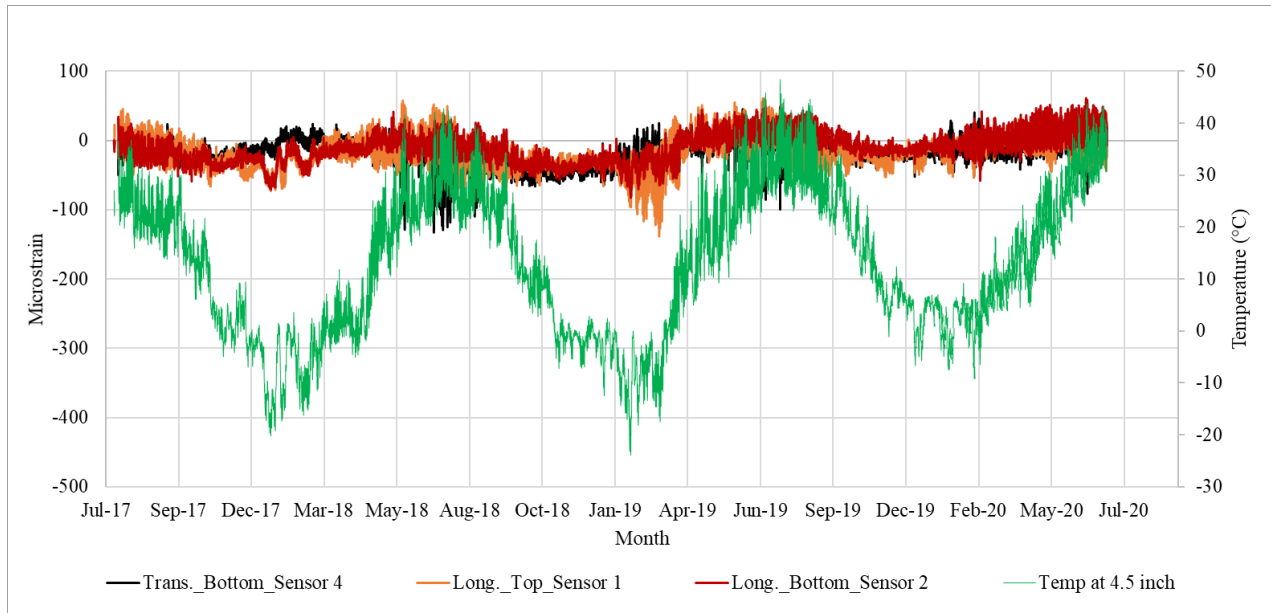

Figure 5-20. Environmental strains and slab temperature for Cell 805, first slab.

5.2.3 Cells 506 through 806

As previously mentioned, the vibrating wire and temperature data for the initial period are used to zero out the subsequent strain values. For Cells 506-806, some vibrating wire data for the first couple of weeks were not available. The vibration wire and temperature data for other cells were thereby studied, and their trends were used to populate the initial strain values for these cells. Figure 5-21 through Figure 5-24 show the environmental strains calculated for these cells. Each of these cells has four sensors, two in the transverse direction in one slab and the other two in the longitudinal direction in another slab. The strains measured in all these cells are relatively low compared to the other four cells discussed above. The strain values have shown a correlation with the slab temperature, and values were high during the winter months as anticipated.
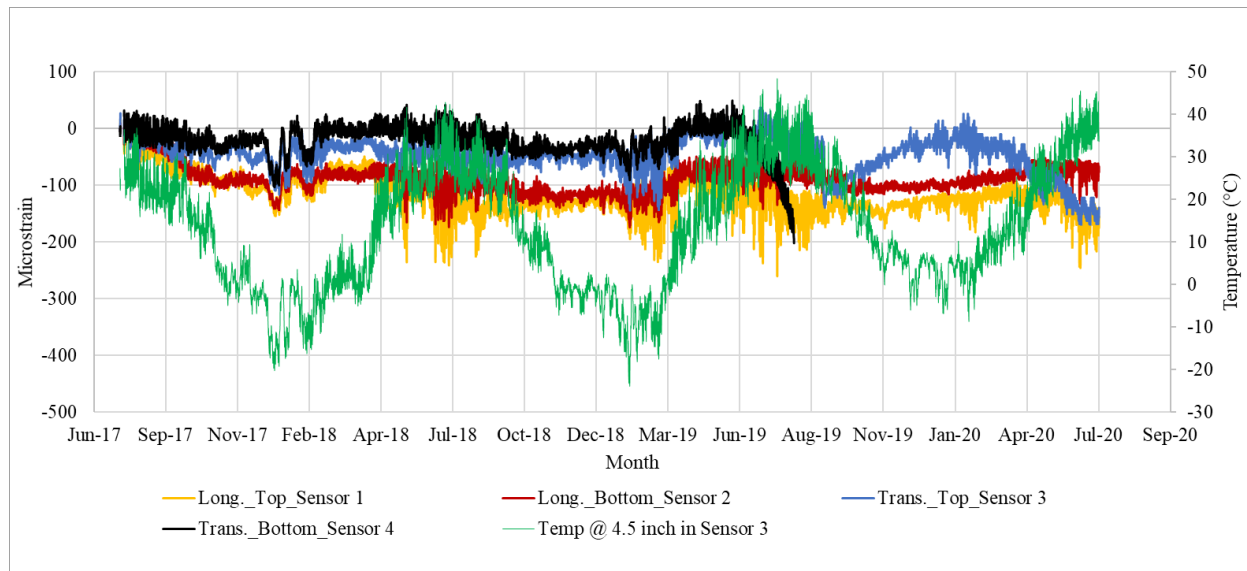

Figure 5-21. Environmental strains and slab temperature for Cell 506.

Figure 5-22. Environmental strains and slab temperature for Cell 606.
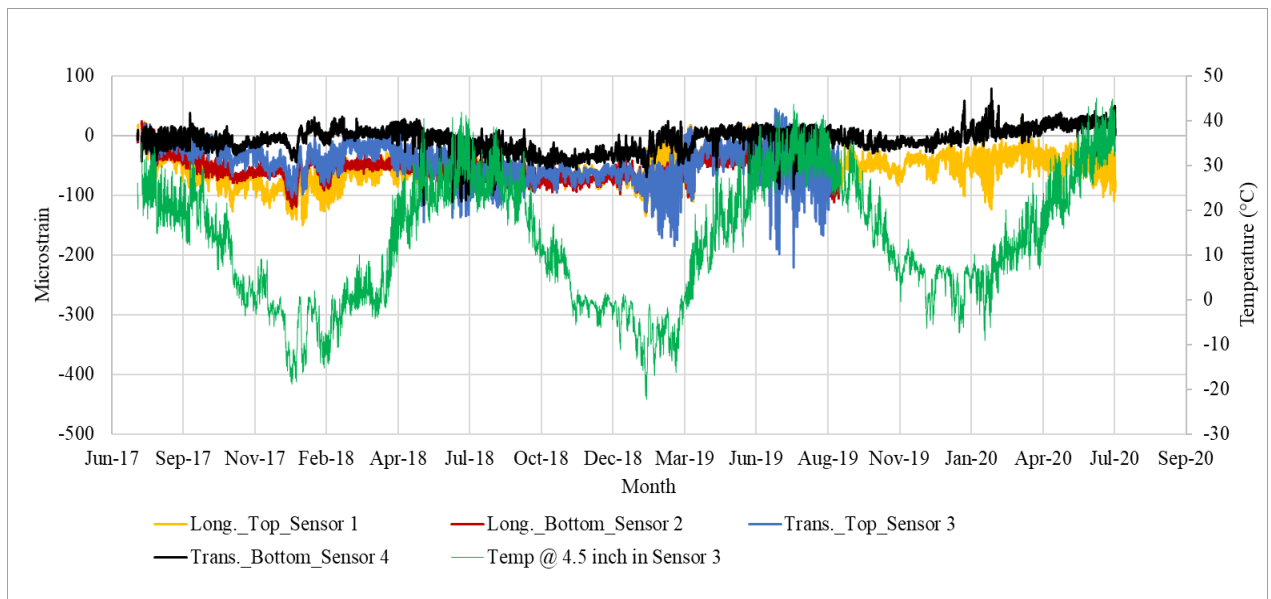
Figure 5-23. Environmental strains and slab temperature for Cell 706.

96

Figure 5-24. Environmental strains and slab temperature for Cell 806.

In summary, it can be stated that the strains recorded by almost all of the sensors were influenced by the seasonal temperature; strains were high during the winter and low in summer. Some sensors also have shown increasing strains with the age of the pavement, probably because of the fatiguing of the slabs and damage accumulation in the overall structure. Strains in ultra-thin (3-and 4-inch thick) concrete pavements were relatively higher than the thin concrete pavements (Cells 506-806). This may be because of more curling and warping effect. The difference in the strains between the sensors placed either in the transverse or longitudinal directions and the top and bottom of the slabs could not be clearly established from the data analyzed. A distinct influence of the fibers on measured environmental strain has not been observed from the data and the analysis presented in this report.

5.2.4 **Effect of Environmental Strain on Slab Curvature**

Environmental strain directly affects the slab curvature. As fibers at the transverse and longitudinal joints connect the slabs, they may influence the slab curvature. The difference in the strain values at the top and bottom of the slabs were used to calculate slab curvature using the following equation (Asbahan and Vandenbossche, 2011):

$$\rho = -\frac{\varepsilon_t - \varepsilon_b}{D(1 + \varepsilon_t + \varepsilon_b)} \qquad (17)$$

Where,

ρ = slab curvature (positive values indicate upward curvature) in units 1/ft.

ε_t = strain measured by the top sensor of the slab at the time of interest.

ε_b = strain measured by the bottom sensor of the slab at the time of interest.

D = Distance between the top and bottom of the slab where strain is calculated in m.

Environmental strains measured in the test cells were analyzed to quantify slab curvatures for the various cells constructed in this study and to investigate the effects of fibers on environmental strain-induced slab curvatures. Figure 5-25 to Figure 5-28 shows slab curvature plots for Cells 506-806.
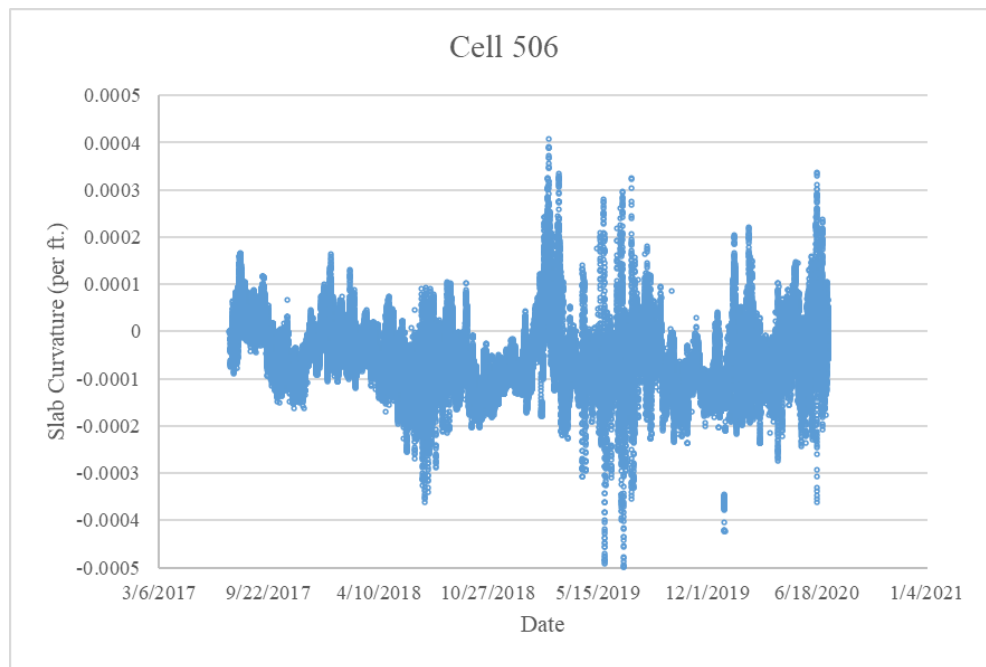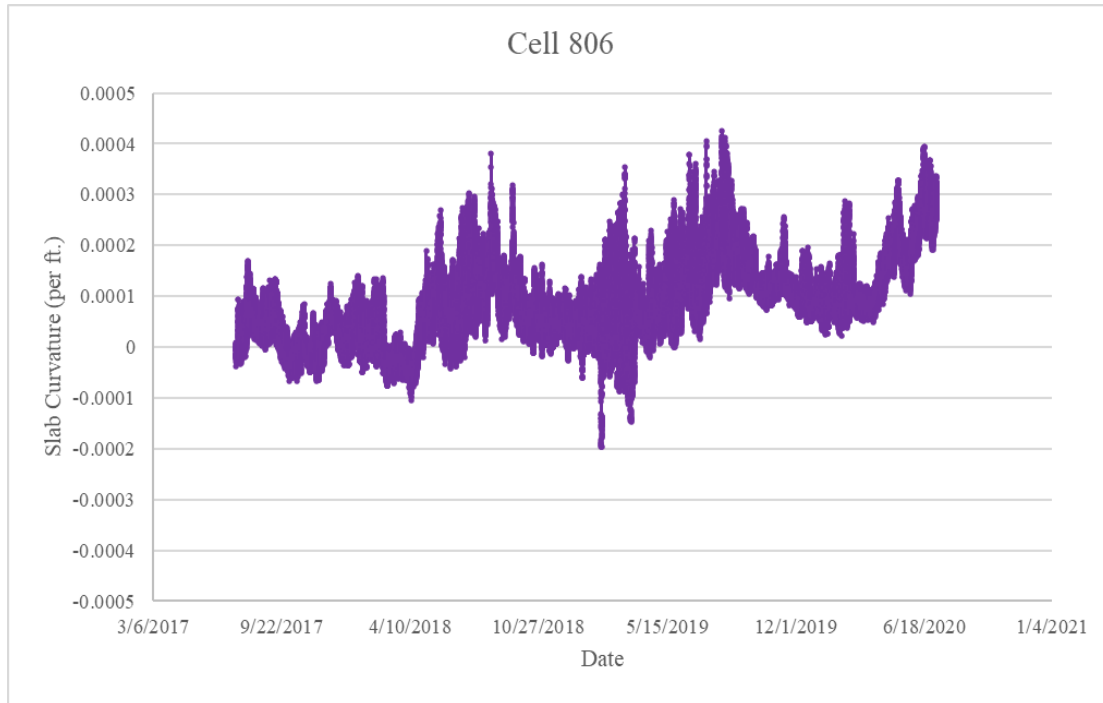

Figure 5-25: Seasonal Variation of Slab Curvature for Cell 506.
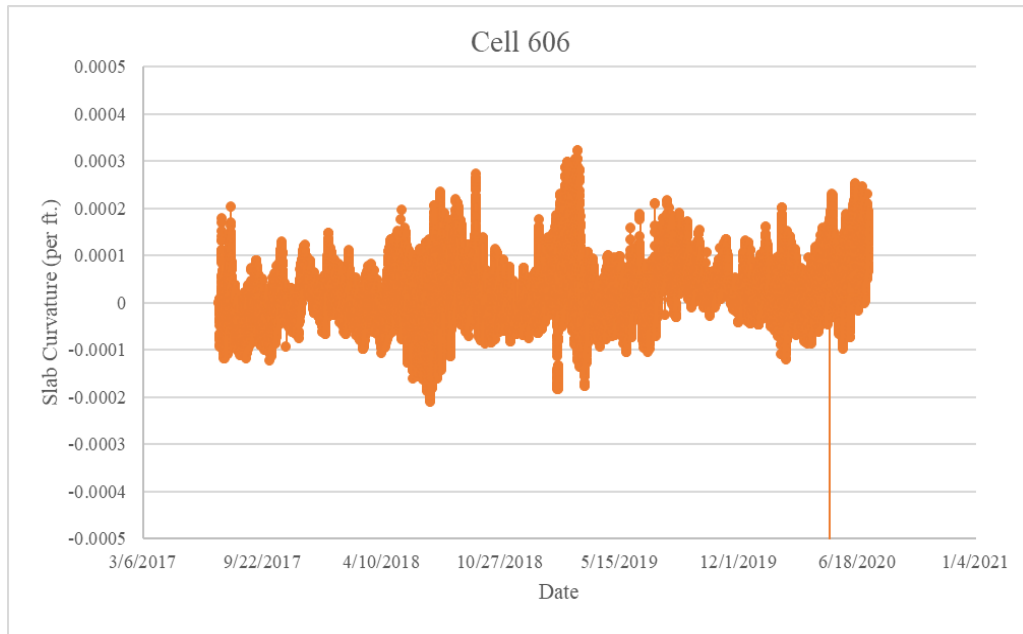
Figure 5-26: Seasonal Variation of Slab Curvature for Cell 606.
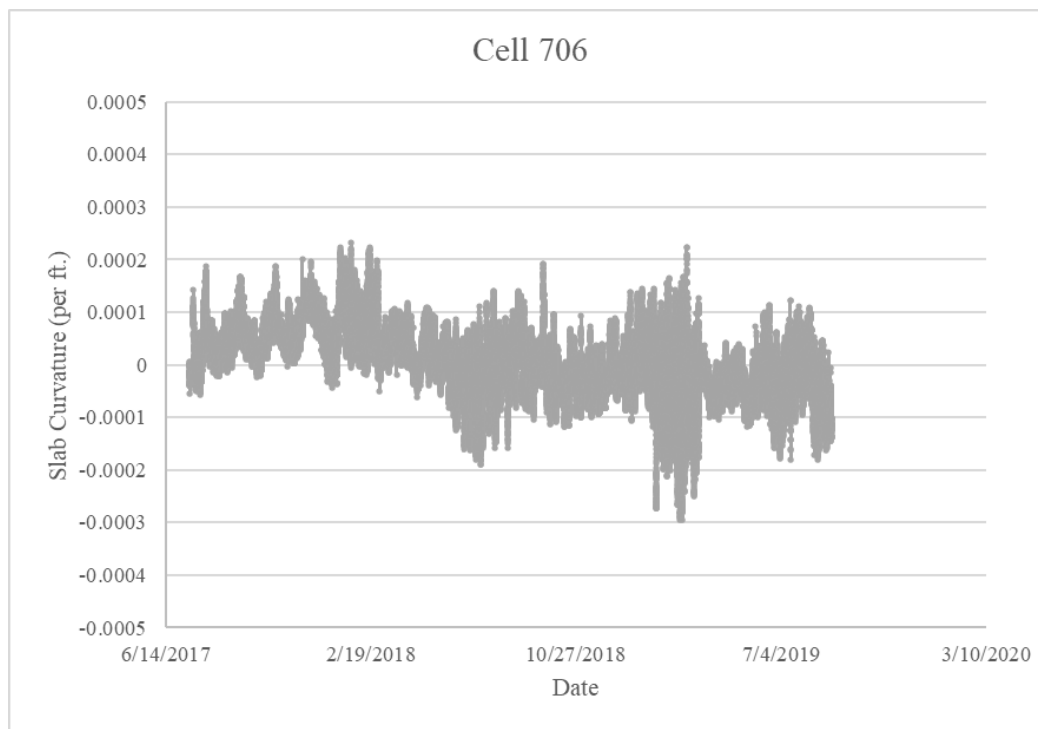
Figure 5-27: Seasonal Variation of Slab Curvature for Cell 706.

99

Figure 5-28: Seasonal Variation of Slab Curvature for Cell 806.

Among all the cells, Cell 506 recorded a maximum positive (upward) slab curvature of 0.00041/ft during the winter of late 2018 or early 2019 and a maximum negative (downward) slab curvature of -0.0005/ft during the summer of 2019. The observation makes sense because cold winter nights are supposed to create greater upward slab curvature, and warm summer days will result in downward slab curvature.

Cell 606 recorded a maximum positive (upward) slab curvature of 0.00032/ft during the winter of late 2018 or early 2019 and a maximum negative (downward) slab curvature of -0.00022/ft during the summer of 2018. Cell 706 recorded maximum positive curvature of 0.00023/ft during the winter of late 2017 and early 2018 and a maximum negative curvature of -0.0003/ft during the summer of 2019. Cell 806 observed the maximum positive and negative slab curvature of 0.00043/ft.in late 2019 and -0.0002/ft during the spring of 2019.

Comparing Cells 506-806 slab curvature plots, it may be noted that as the fiber dosage increases from Cell 506 (no fiber) to Cell 806 (11.7 lbs. /cy), the daily variation of upward and downward curvatures of slab decreases in general, which might reduce the initiation of fatigue cracks. For this study, the effects of built-in curl and moisture gradient were not considered on slab curvature. As a result, any firm conclusion may not be drawn, but it is identified that the structural fibers used in this study might have

affected the rate of change of slab curvature with daily and seasonal temperature variation, which eventually can affect fatigue cracking.
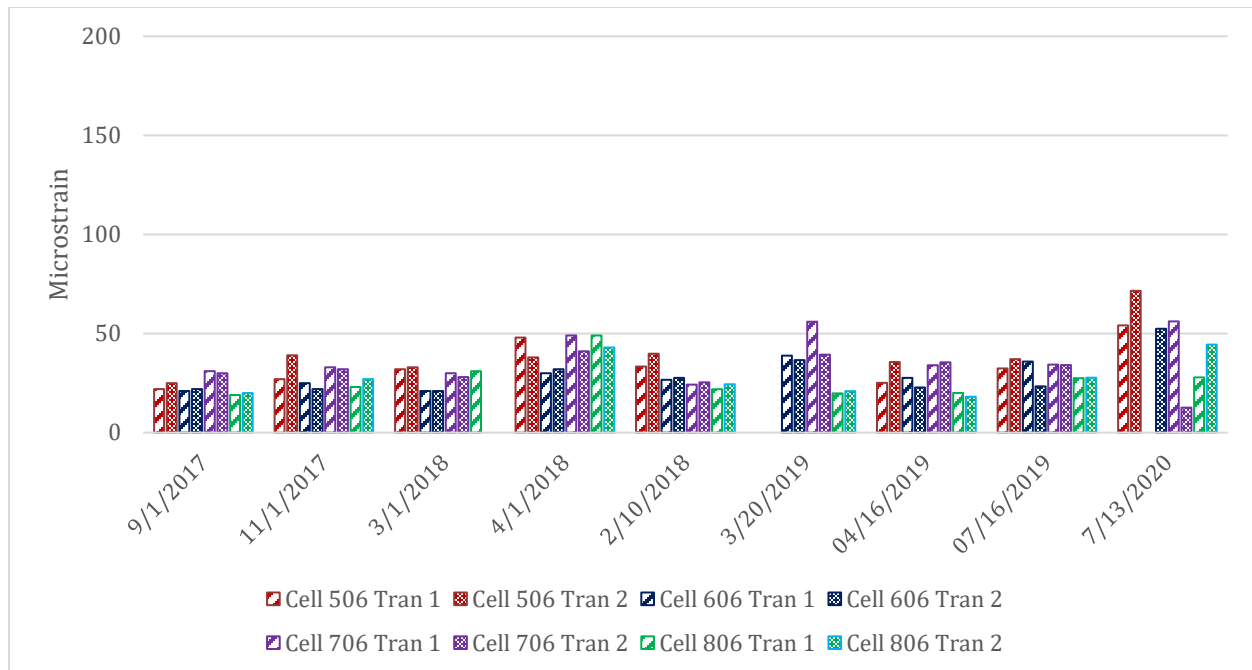
5.3 DYNAMIC STRAIN

Figure 5-29 shows the dynamic strains recorded by the sensors in longitudinal and transverse directions for Cells 139 and 239. Some strain values are missing at multiple dates because of the malfunction of some sensors; also, no data were collected for these two cells in 2020. Overall, the magnitude of the strains in Cell 139 was higher than that was recorded in Cell 239. One sensor in Cell 139, placed in the longitudinal direction, showed that the magnitude of the strain increased with time. Other sensors did not show any trend.
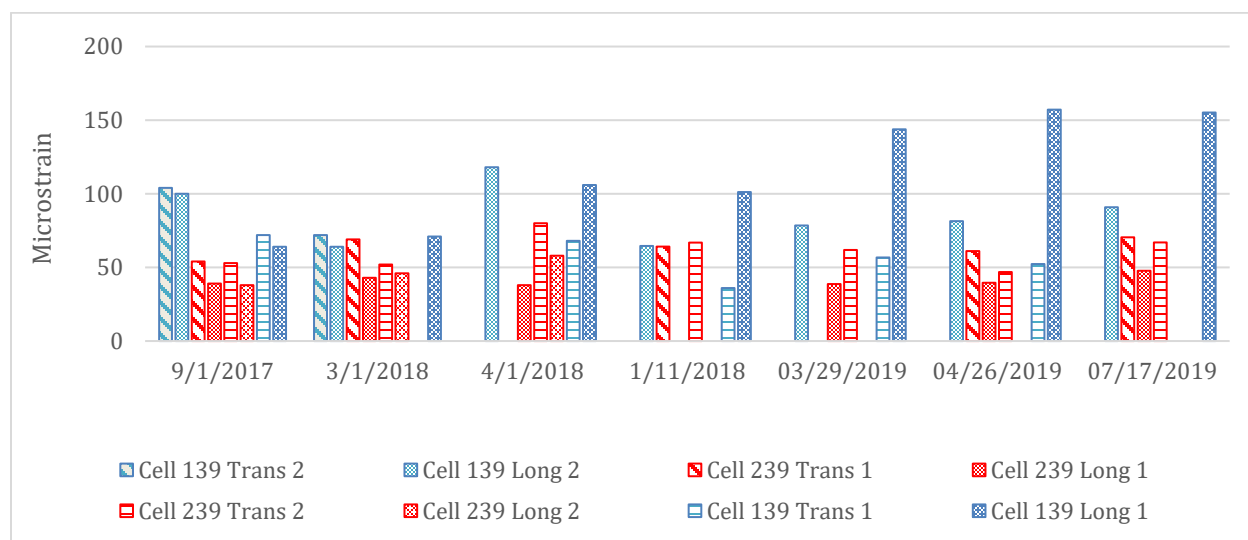
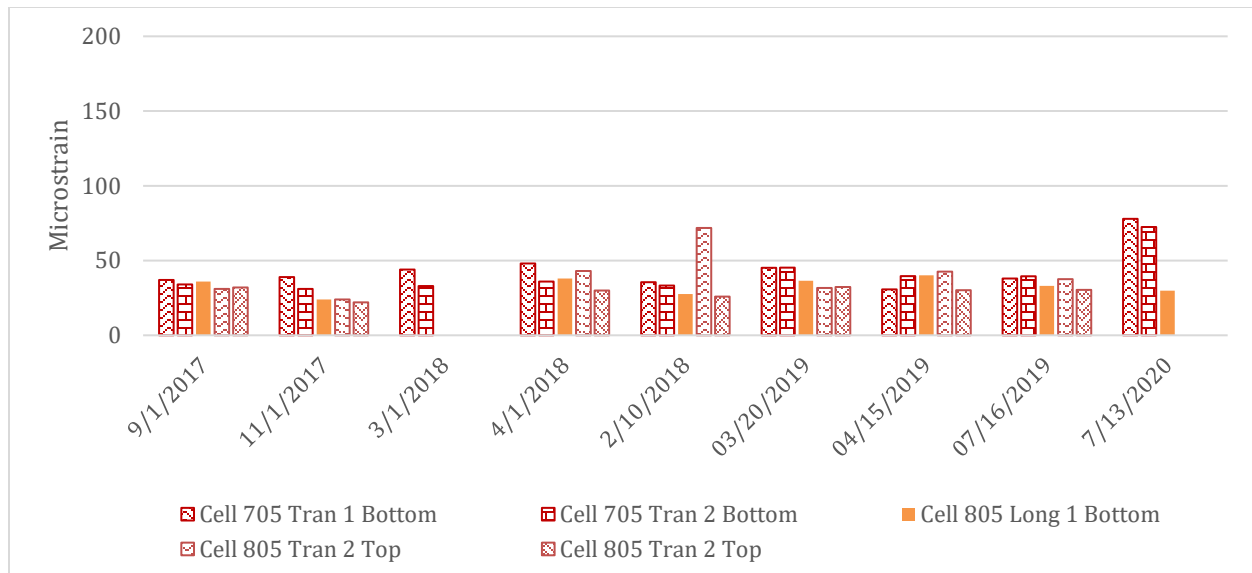**Figure 5-29. Dynamic strains recorded in Cells 139 and 239.**

Cells 506, 606, 706, and 806 are the cells that compare the performance for different dosages of fibers. Dynamic sensors in these cells were laid in the transverse direction only. The magnitudes of the dynamic strains in these cells are comparable. As noted previously, strains measurement were conducted with the load from the MnROAD truck, not from the live traffic. Data collected in 2020, presented in Figure 5-30, shows that Cell 506 (no fiber) recorded a slightly higher strain value compared to other cells.

Figure 5-30. Dynamic strains recorded in Cells 506 through 806.

Figure 5-31 shows the comparison of dynamic strains between Cells 705 and 805. Compared to Cells 139 and 239, Cells 705 and 805 experienced far lower strains. The strain measured in 2020 was almost double the previous reading. The strains recorded in the Cell 705 and 805 did not show a significant difference, with slightly higher strain recorded for Cell 705 for some dates. Overall, the highest dynamic strains were measured in Cell 139, which is the thinnest among all the test cells.

Figure 5-31. Dynamic strains recorded in Cells 705 and 805.

5.4 JOINT MOVEMENT

Figure 5-32 shows a plot of relative joint opening recorded by a joint opening sensor in Cell 506. The first joint opening reading was used to zero the subsequent joint opening readings. In this figure, there are two jumps in joint movement data, one in August of 2017 and the other one around October 2017. The first jump in Figure 5-33 is assumed to be related to the joint deployment. When the joints deploy, the sensor readings are supposed to show a jump. Some sensors didn't record any jump. The reason for this is either the deployment occurred before collecting the initial reading, the jump was not recognizable because of a minimal crack width change, or the joint did not deploy at all. The second jump is related to the reinstallation of the sensor.

Most of the joint opening sensors had to be re-installed after their first installation; protection for the sensor was applied during the re-installation time. For the sensors that were reinstalled, data were adjusted to neutralize the re-installation-related jump (Figure 5-33). For the sensor data presented in Figure 5-33, it can also be seen that some erroneous data was recorded for some duration between September 2018 through January 2019. Figure 5-34 provides an example of joint movement readings collected by Sensor 3 of Cell 706; in this case, the joint in question probably did deploy before the

collection of the first reading. This plot provides a good example of a relative joint opening with respect to the first reading. The joint opening was maximum during the winter months, after which the joint opening reduced with the temperature increment. Some sensor readings were discarded because of erroneous data, where the crack opening readings fluctuated significantly.
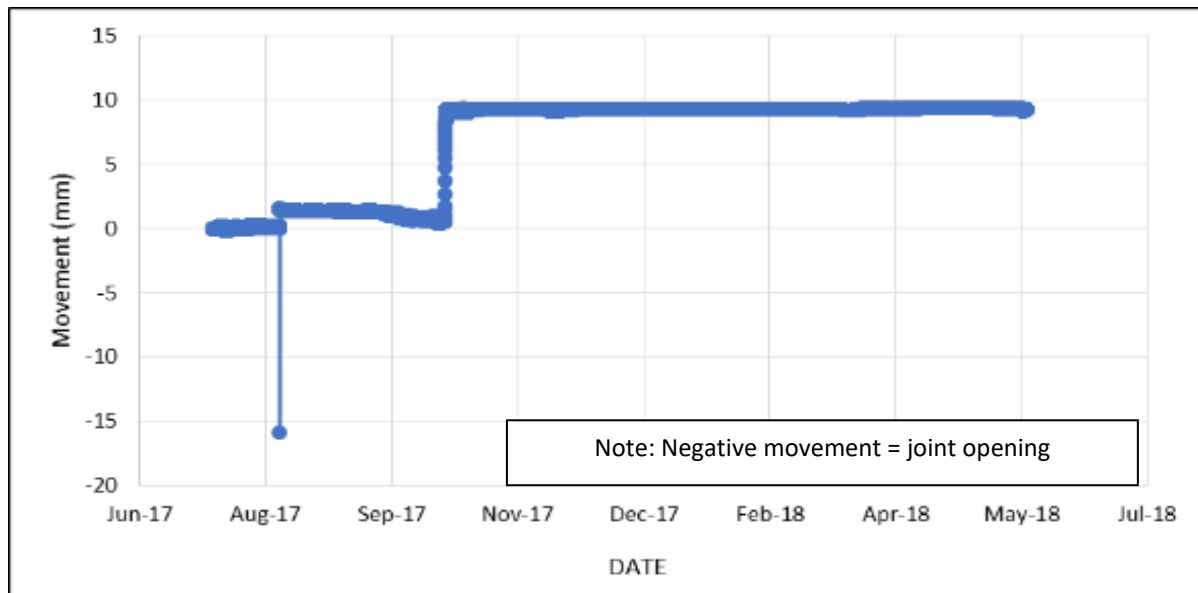

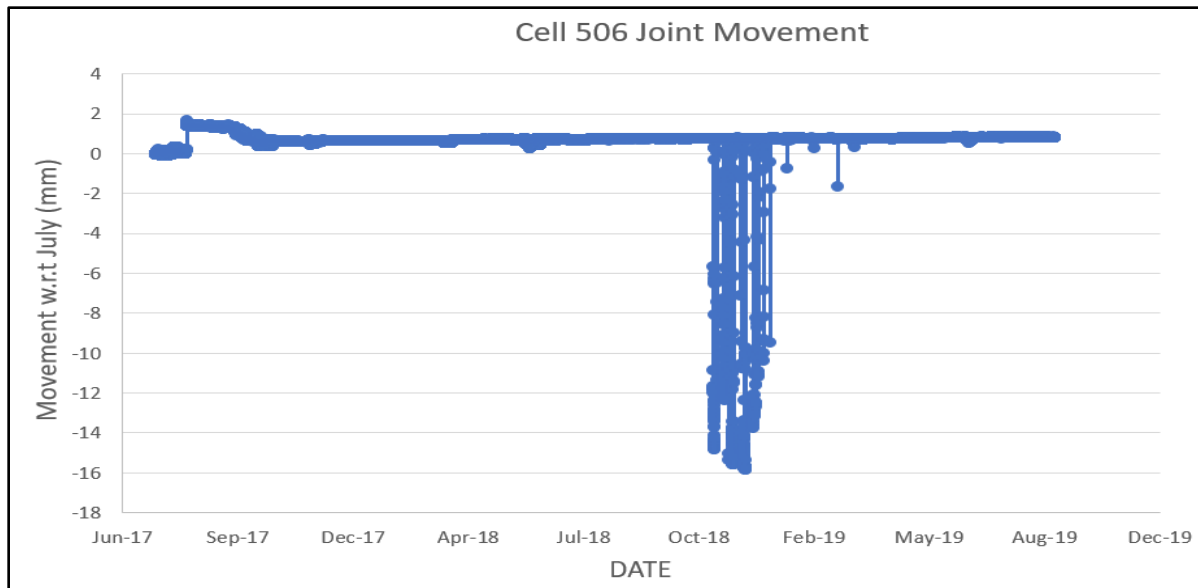**Figure 5-32. Joint movement recorded by Sensor 1 of Cell 506, before adjustment for re-installation was made.**

Figure 5-33. Joint movement recorded by Sensor 1 of Cell 506, after adjustment for re-installation was made.
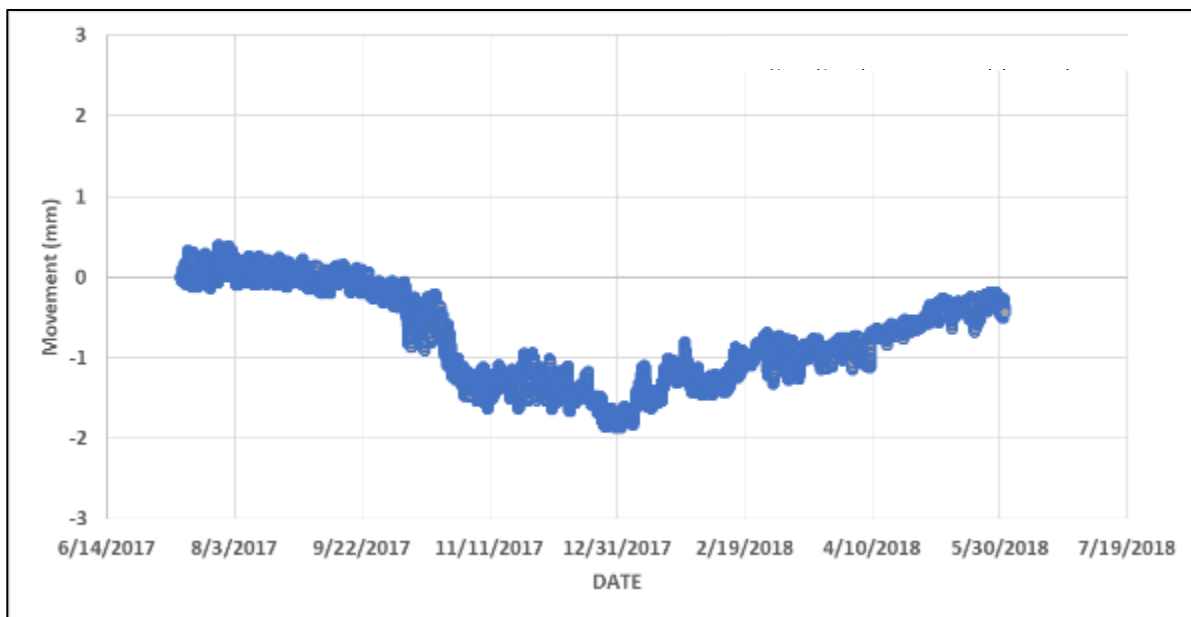
(Note- diff. scale in the y-axis).

Figure 5-34. Movement recorded by Sensor 3 of Cell 706; no adjustment was required.

(Note diff. scale in y-axis).

Because of the considerable variations in the data quality in some sensors, compelling trends could not be achieved for all the cells, but the results of many sensors are reasonable. In order to investigate the seasonal variation of joint opening, the monthly average relative joint opening was calculated for each cell and plotted in Figure 5-35 through Figure 5-42. The averages for Cells 705 and 805 were zeroed with respect to September 2017, and all the other cells were zeroed with regard to July 2017. Cells 705 and 805 were zeroed using the later month because they were constructed later than the other cells. In Cell 139, two sensors did not show a significant variation in the joint opening, but Sensor 1 showed that the joint opening increased during the winter months compared to the first reading taken in July 2017. Based on the data, the joints of the Cell 239 (at least where the sensors were installed) remained relatively dormant for most of the year, with slight expansion recorded by Sensor 3 in the winter months.
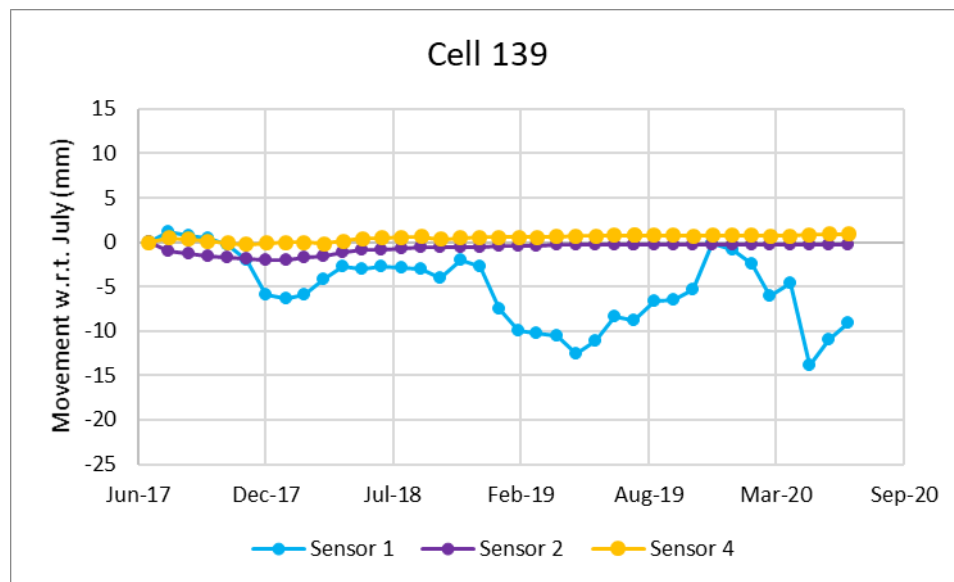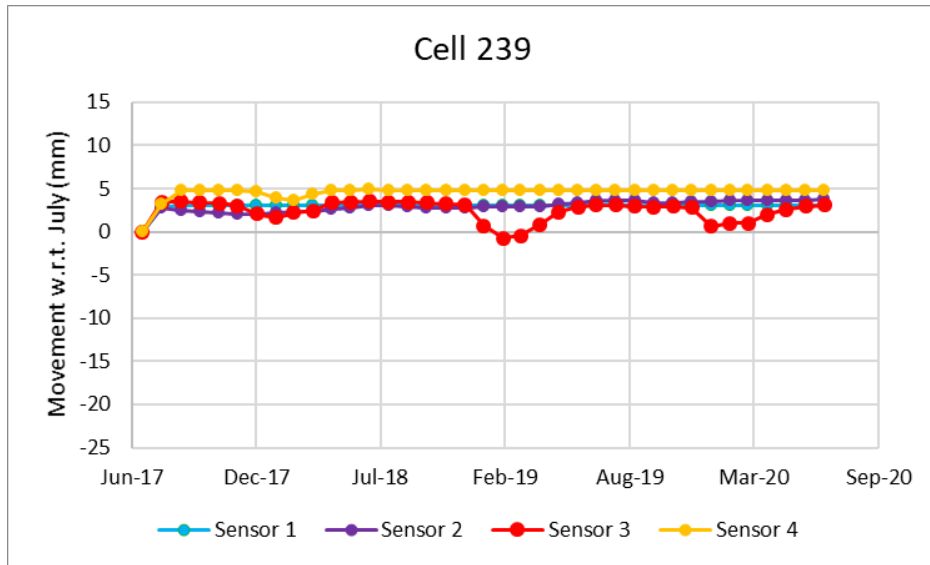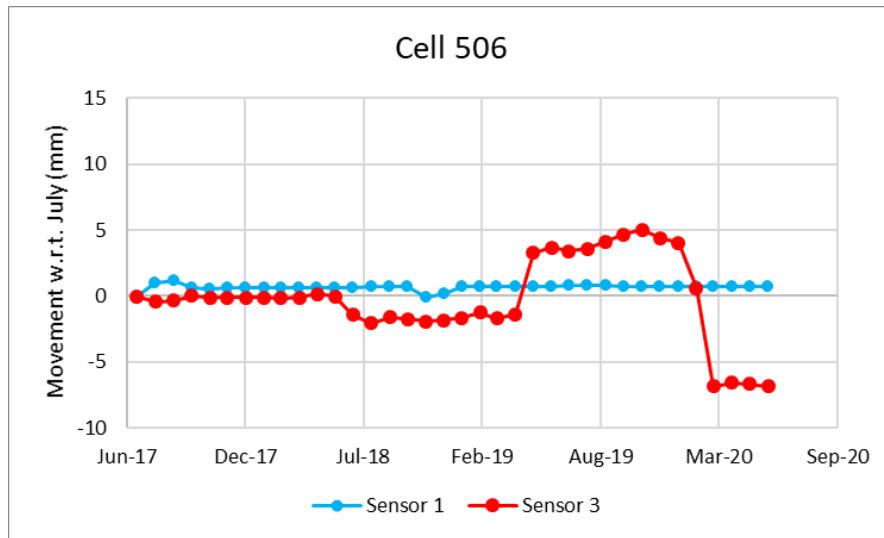

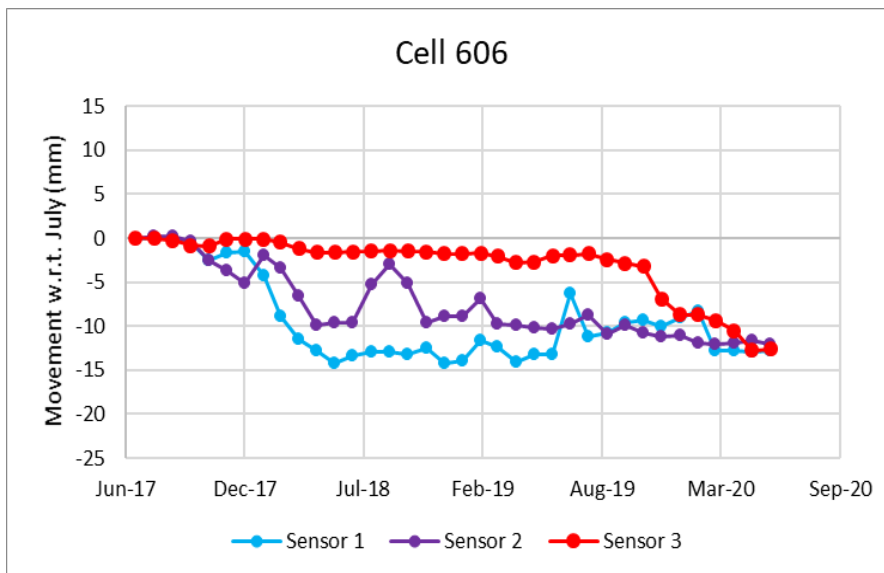Figure 5-35. Monthly average relative joint movement for Cell 139.

Figure 5-36. Monthly average relative joint movement for Cell 239.

Cell 506 does not contain fibers, and it was anticipated that larger joint openings would be observed in this cell compared to its counterparts (Cells 606 to 806). One sensor in this cell remained dormant throughout the three service years. Two sensors in this cell indicate that the joints did not close in summer once they opened in the first winter. The other sensor of Cell 606 shows joint opening in the fall of 2019. Joints of Cells 706 and 806 showed movement after the 2019-2020 winter.

Figure 5-37. Monthly average relative joint movement for Cell 506.

Figure 5-38. Monthly average relative joint movement for Cell 606.
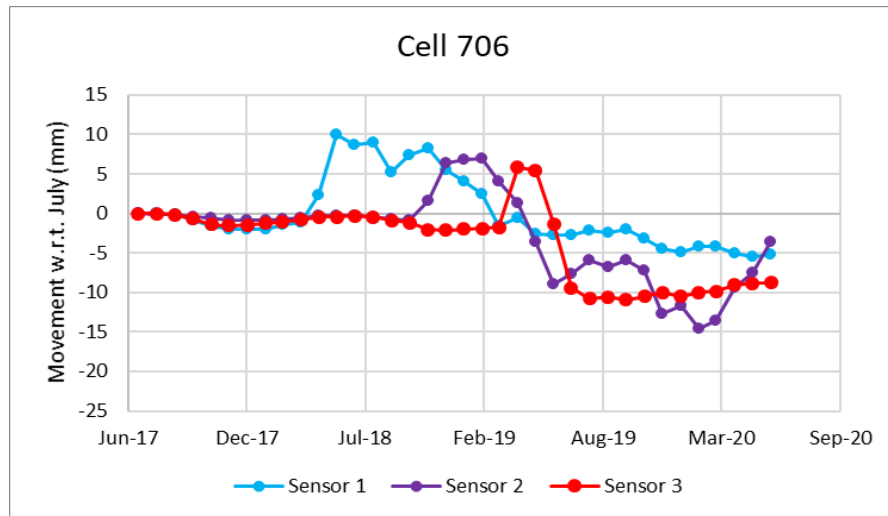
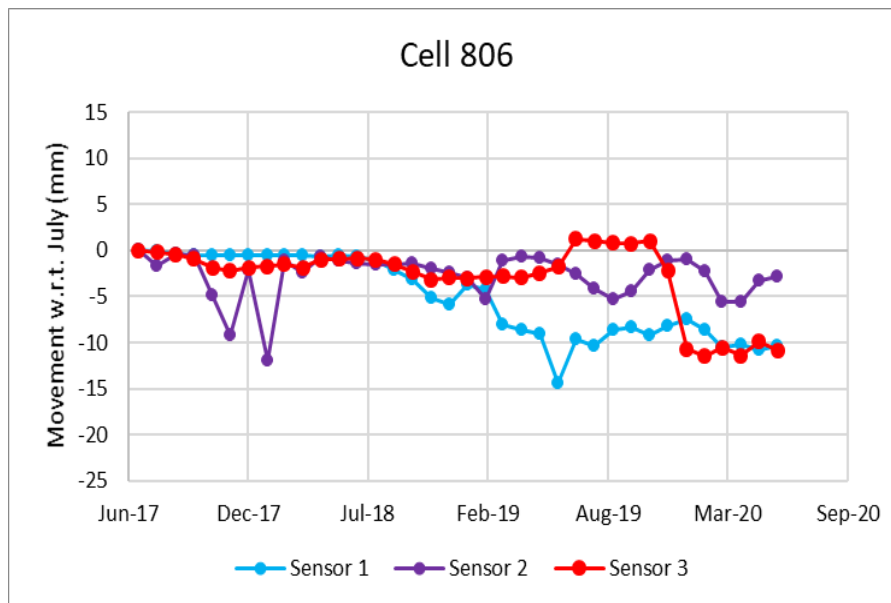**Figure 5-39. Monthly average relative joint movement for Cell 706.**

Figure 5-40. Monthly average relative joint movement for Cell 806.

Cells 705 and 805 had experienced the largest joint opening movement among all the eight cells, and a difference in the joint movements between these two cells is not apparent. While a few sensors installed in these two cells remained dormant, others showed significant movements and did not show a

meaningful correlation with seasonal temperature change. The cells are unbonded concrete overlays and have unwoven geotextile at the interface (less friction), which might have influenced the slab movements. It may happen that some slabs were being migrated with the traffic load and distressed that influenced the joint movement.
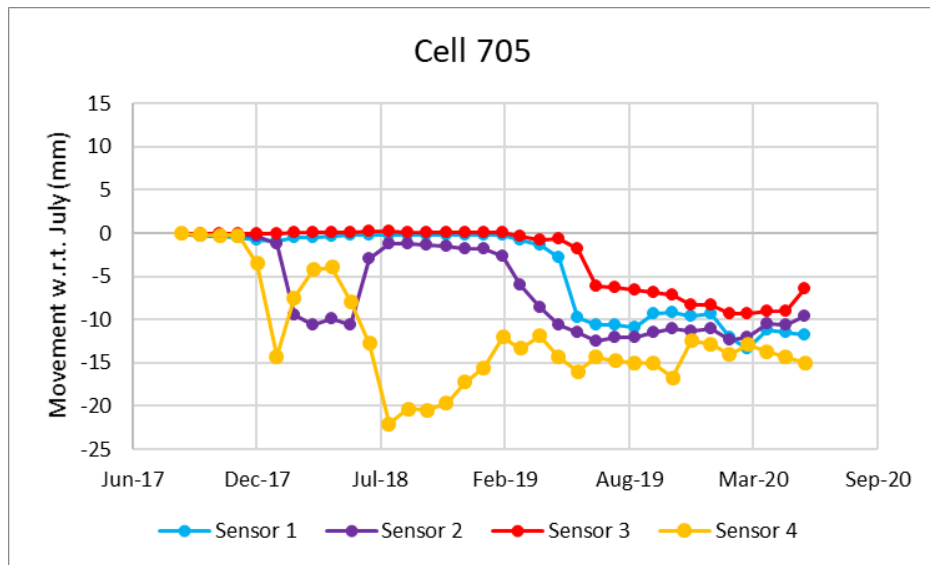

Figure 5-41. Monthly average relative joint movement for Cell 705.
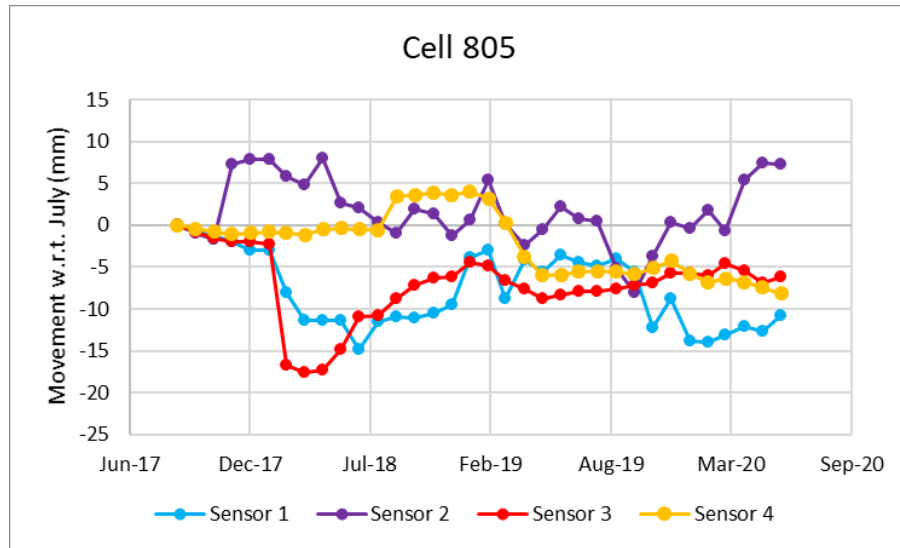
Figure 5-42. Monthly average relative joint movement for Cell 805.

5.5 JOINT PERFORMANCE

5.5.1 Load Transfer Efficiency (LTE)

Figure 5-43 through Figure 5-54 show the LTE computed for various test dates for all the test cells. The LTE data of the Cells 139 and 239 were comparable when the first test was conducted on September 6, 2017, and it ranged between 85 and 94%. The LTE of these two cells then continued to decrease with age. The outside lane of both the cells, where traffic load is not applied, showed consistently higher LTE values than the inside lane, even though Cell 139 experienced some LTE drops with age. In 2020, the Cell 139 inner lane showed higher LTE when it was expected to be less than the previous years. Slab ID 23 showed the maximum LTE, which is understandable because this slab was replaced by September 2018, and since then, it has been performing better when compared to the other slabs of Cell 139, which were not replaced. Although, slab IDs 7, 15, and 40 were not replaced. Hence their increase in LTE is not understood.
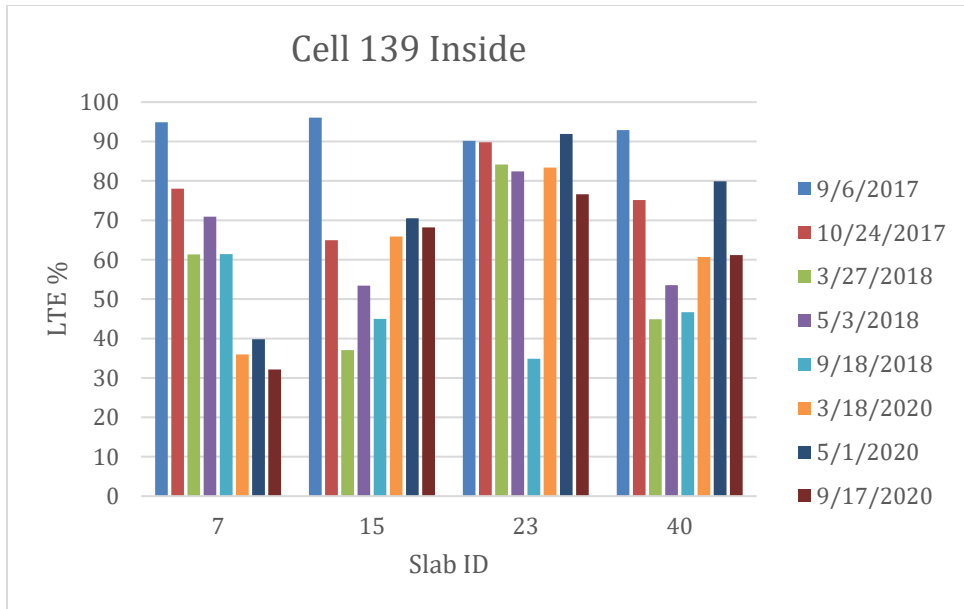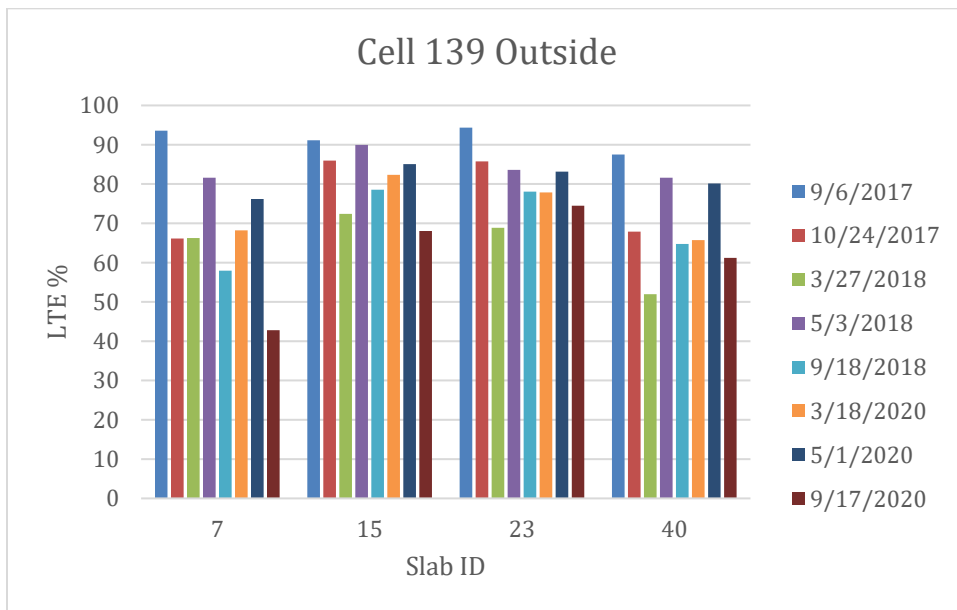
111

Figure 5-43. LTE of Cell 139 inside lane.

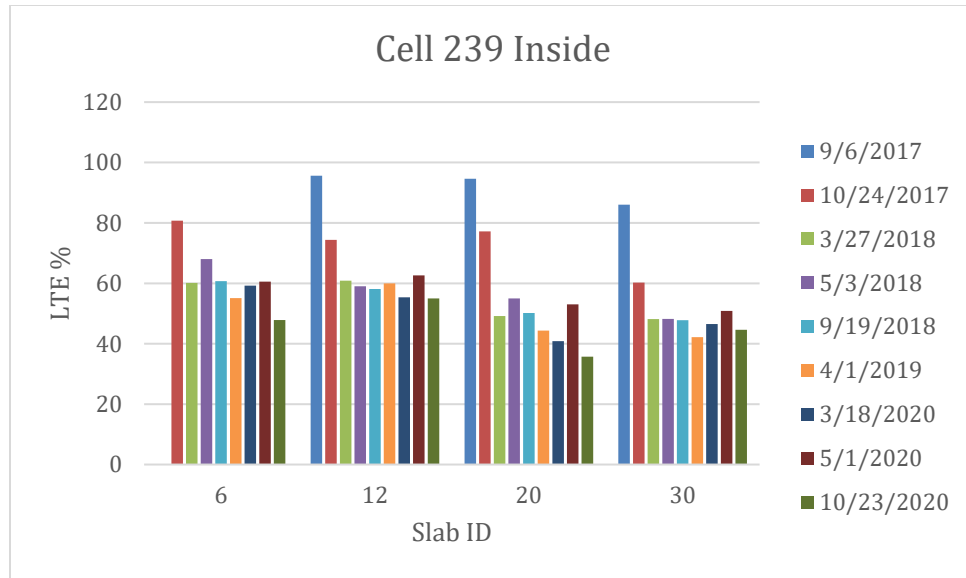**Figure 5-44. LTE of Cell 139 outside lane.**

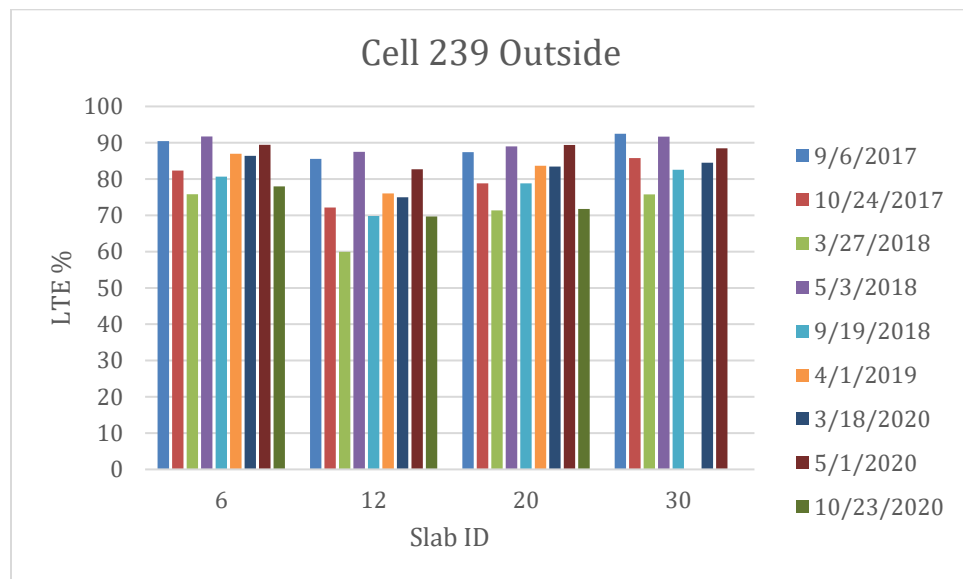**Figure 5-45. LTE of Cell 239 inside lane.**

Figure 5-46. LTE of Cell 239 outside lane.

The LTE results of Cells 506 through 806 clearly reveal the contribution of structural fibers in maintaining higher LTE values for a longer time. For Cell 506, even though the FWD test conducted on the driving

lane in September 2017 showed a range of LTEs between 75 and 85%, the LTE afterward significantly decreased overall. Surprisingly, the FWD tests conducted during April 2019, shown relatively higher LTE at all the three joints considered.

The LTE results of Cell 606, which is 6-inch thick, were at or above 90% when measured in September 2017, except for one joint in the passing lane, which always did show a low LTE (around 25 to 50%). The LTE for this cell had dropped significantly over time. The FWD tests conducted on Cell 606 over the third year of service showed a gradual decrease in LTE for all the joints, which was expected. The LTE in the passing lane has also dropped significantly.
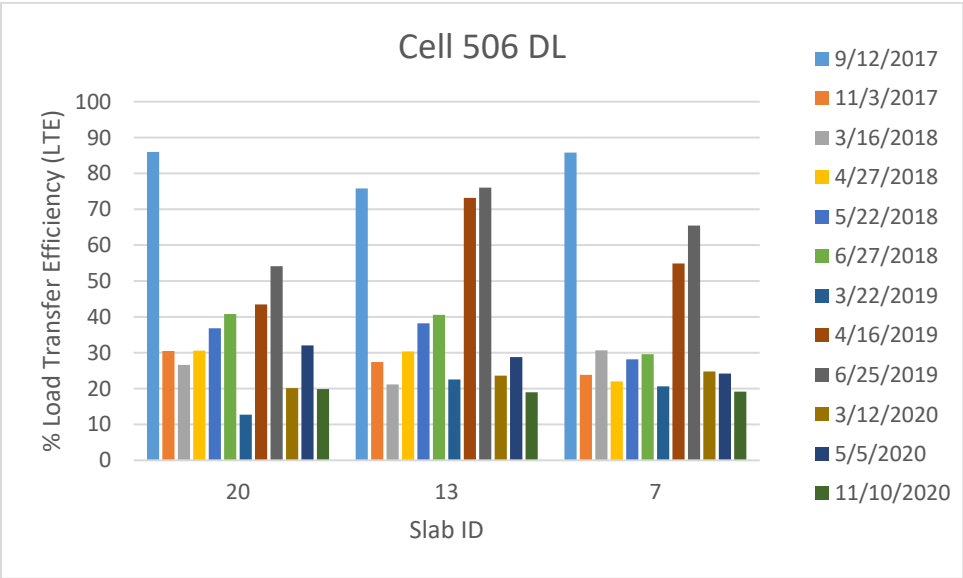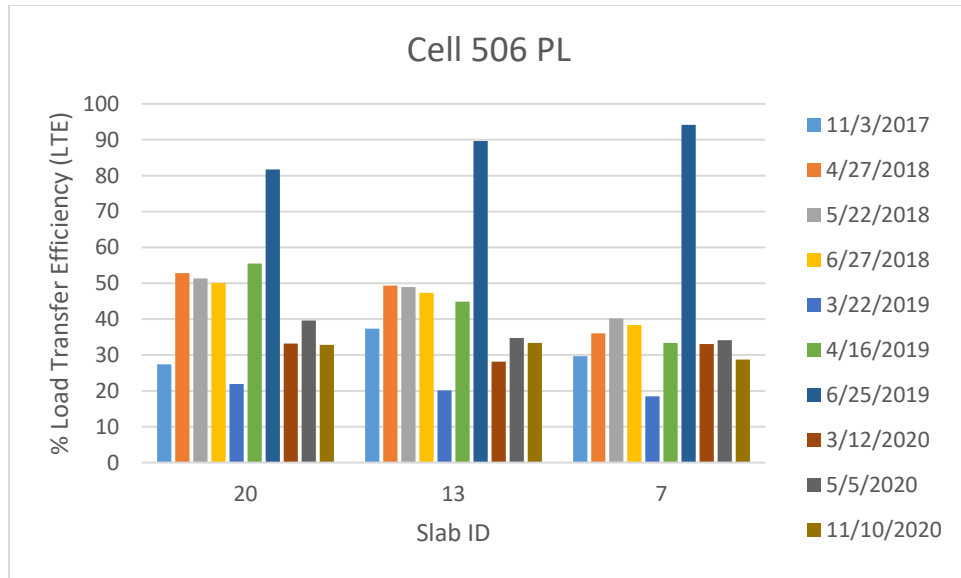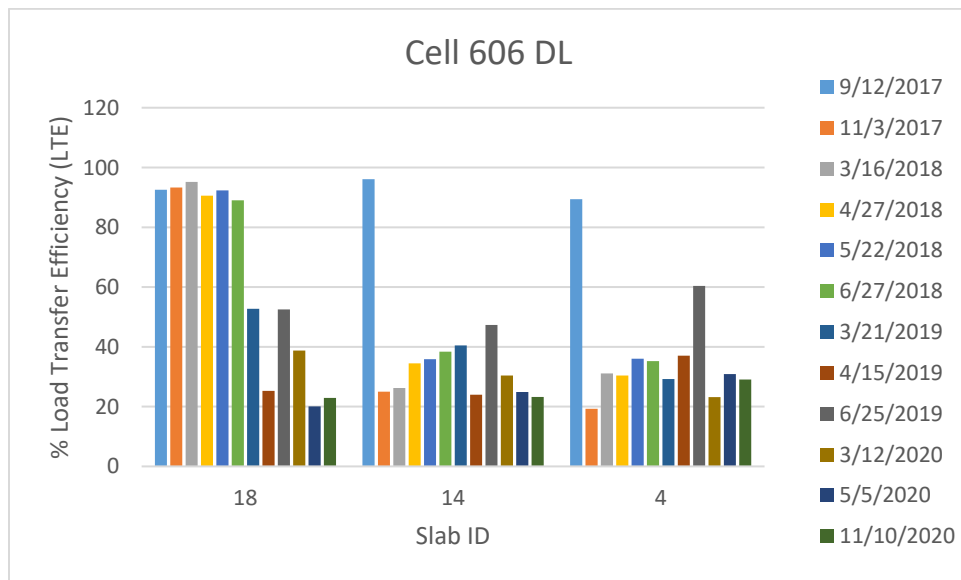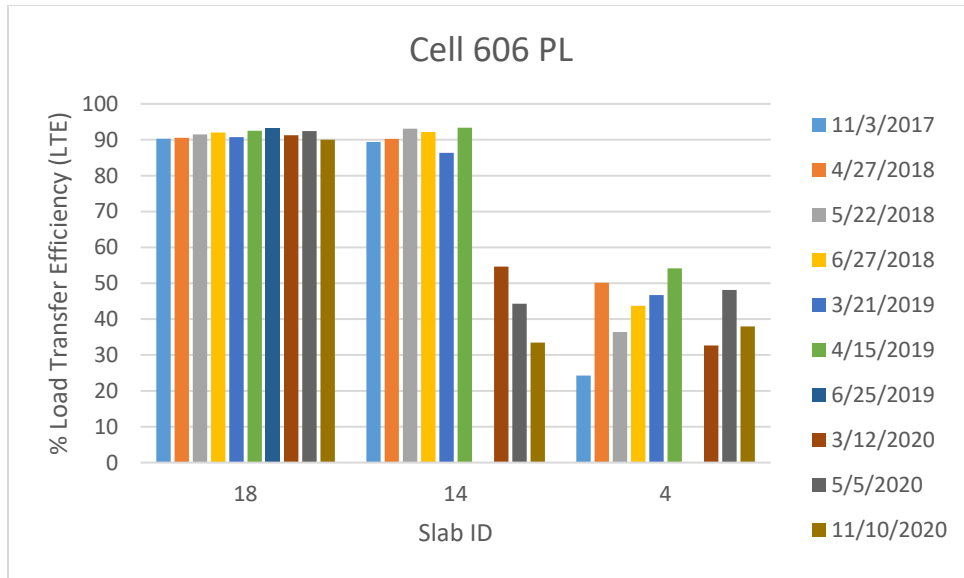

Figure 5-47. LTE of Cell 506 driving lane.

Figure 5-48. LTE of Cell 506 passing lane.

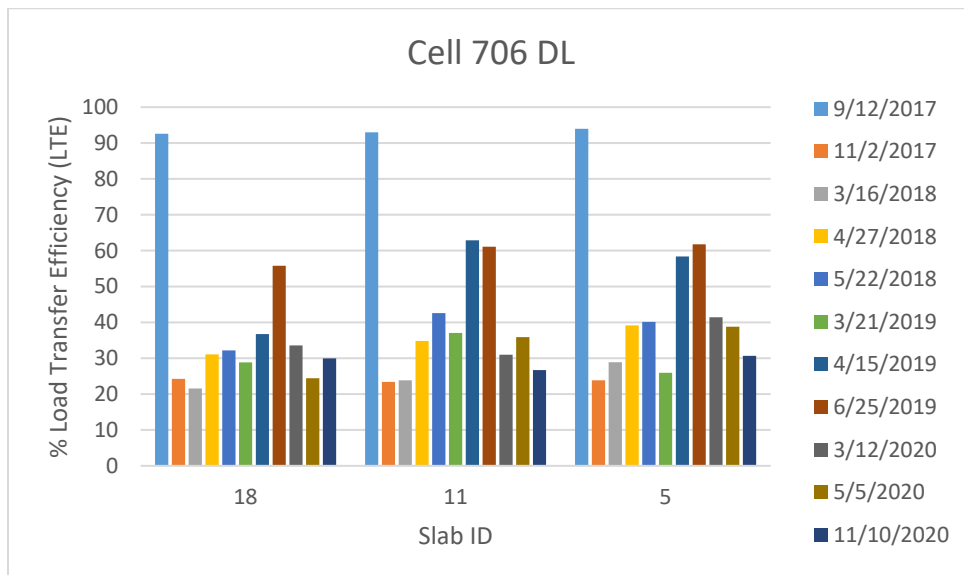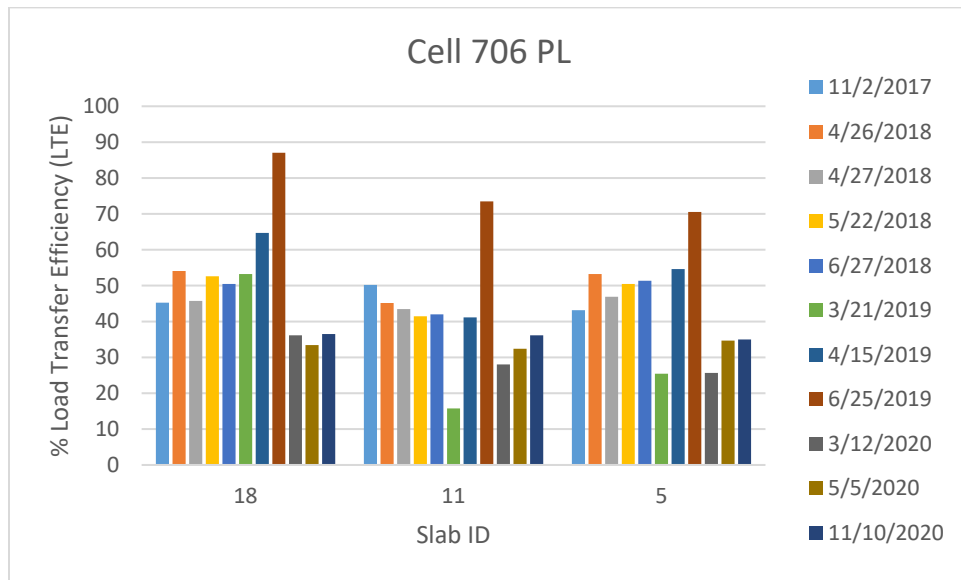**Figure 5-49. LTE of Cell 606 driving lane.**

115

Figure 5-50. LTE of Cell 606 passing lane.

The LTE of Cell 706, which is 5-inch thick and contains 8 lbs./cy fibers, was initially high at three joints (at the driving lane) out of a total of six joints measured. However, when measured at later dates, these joints exhibited 40 to 56% LTE.

Figure 5-51. LTE of Cell 706 driving lane.

Figure 5-52. LTE of Cell 706 passing lane.

Cell 806, which is 5-inch thick and contains 11.7 lbs./cy of fibers, consistently exhibited the highest LTE among all the cells until 2019. Notably, all the joints were able to maintain a very good LTE between 88 to 94% throughout the first two years of service life. The higher LTE of this cell helped in keeping the faulting to the lowest among all the eight cells. Third-year data for Cell 806 showed that for the driving lane, the LTE decreased overall to an average of 30%. However, the passing lane LTE showed an average value of 90%, which was significantly higher when compared to all the other cells. The dramatic decrease in the LTE values for the Cell 806 driving lane indicates that the contribution of fibers and/ or aggregate interlock has significantly reduced after approximately 2.5 million ESALs.

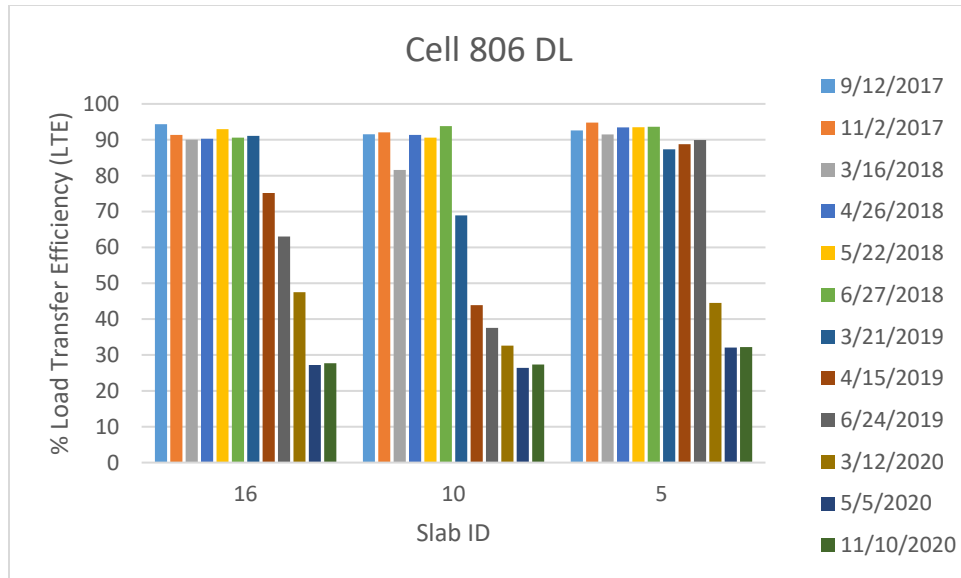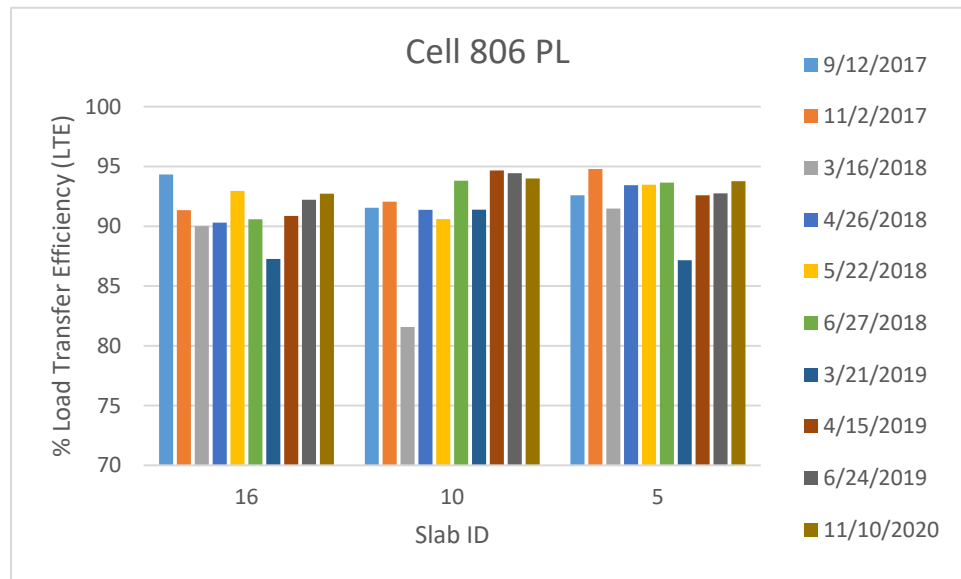**Figure 5-53. LTE of Cell 806 driving lane.**

Figure 5-54. LTE of Cell 806 passing lane.

The wide joint opening of Cells 705 and 805 appeared to have influenced the LTE significantly. Contrary to the low faulting results, these two cells exhibited surprisingly very low LTE, at least in the joints considered in FWD testing. Based on the joint opening sensor data, some of the cracks were wider than

10 mm. The LTE of concrete pavement at such a wide joint opening is usually very low. The FWD test conducted during April and June 2019, however, shown some increase in the LTE in the driving lane of these two cells. The exact reason for this increase is not known; however, upon investigating the joint movement data, it was found that some joint movement sensors detected joint contraction during Spring 2019. It might happen that the thawed water in the spring swollen slabs leading to joint contraction. The co-author of this report, Mr. Tom Burnham, mentioned observing such joint contraction during spring at much lower temperatures than the recommended FWD testing cut-off limit of 75°F in the summer. The LTE for these cells again dramatically decreased in 2020.
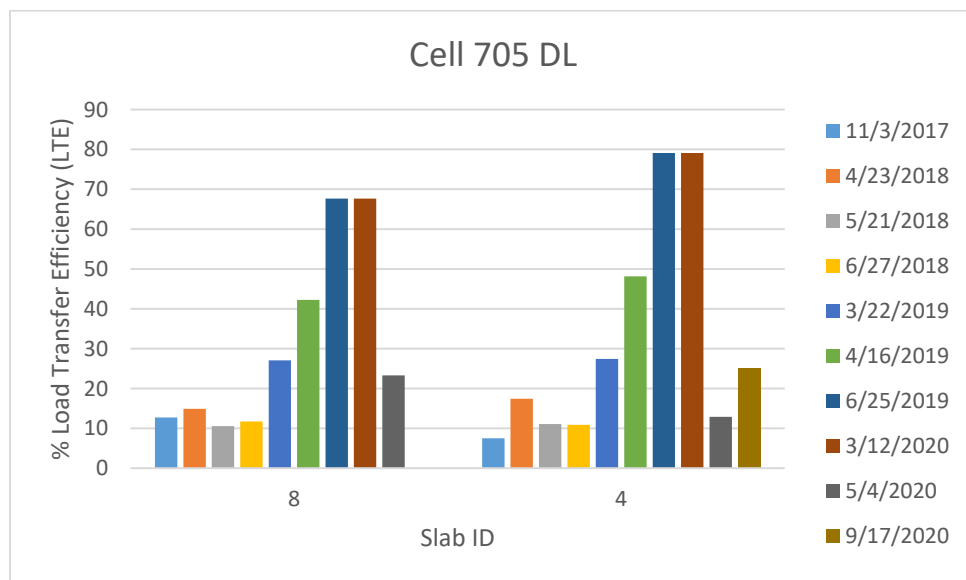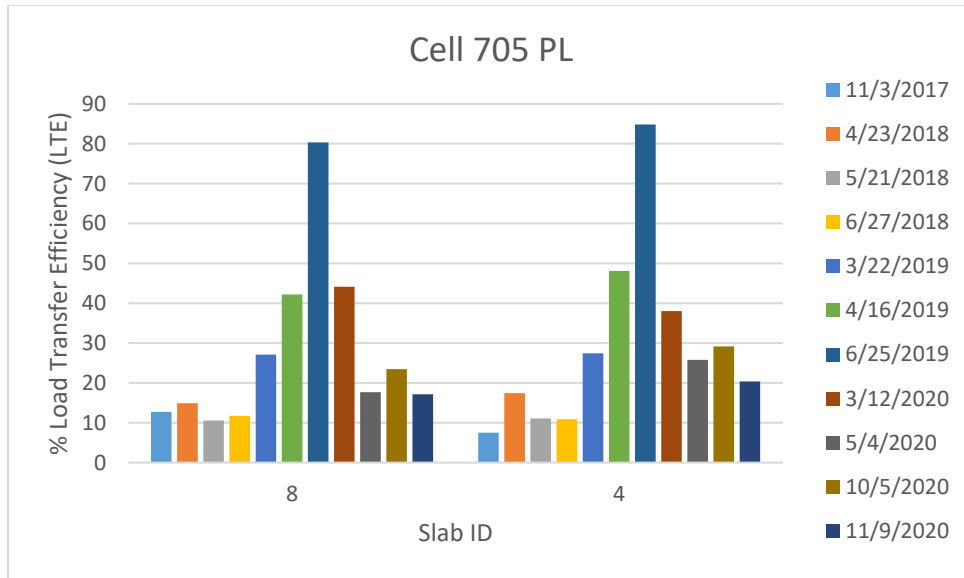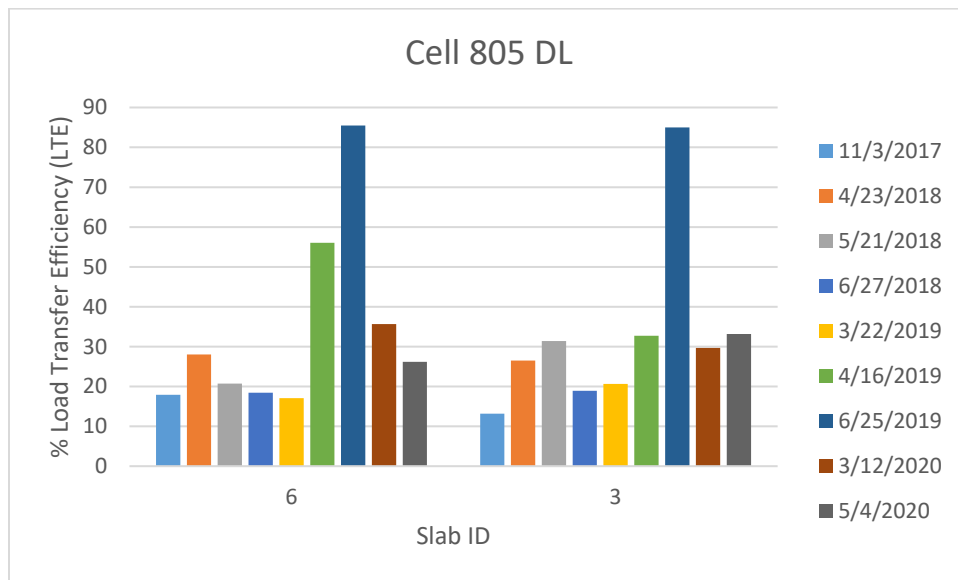

Figure 5-55. LTE of Cell 705 driving lane.

Figure 5-56. LTE of Cell 705 passing lane.

Figure 5-57. LTE of Cell 805 driving lane.

120
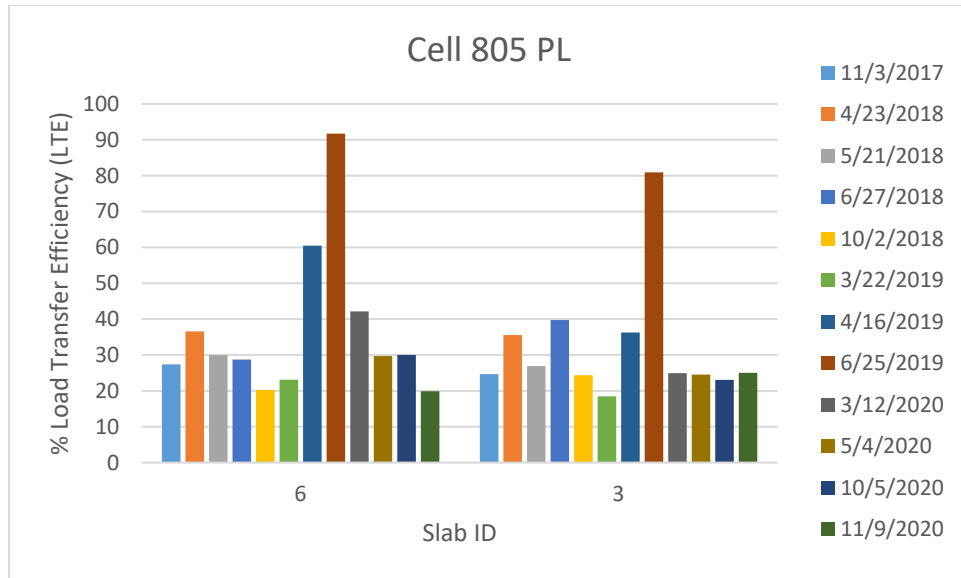
Figure 5-58. LTE of Cell 805 passing lane.

5.5.2 Differential Displacement

Figure 5-59 through Figure 5-70 show the plots for differential displacements for all the cells. The general trend of the differential displacement is similar to the trends observed for the LTE. The differential displacements for both Cells 139 and 239 continuously increased with the traffic load. The FWD test result for Joint 23 of cell 139 resulted in a very high value of differential displacement; also, the 2020 data shows excessive differential displacement in most of the joints of Cell 139. For Cell 239, as anticipated, the driving lane showed higher differential displacement compared to the passing lane and overall significantly lower than Cell 139.

Figure 5-59. Differential displacement of Cell 139 inside line.

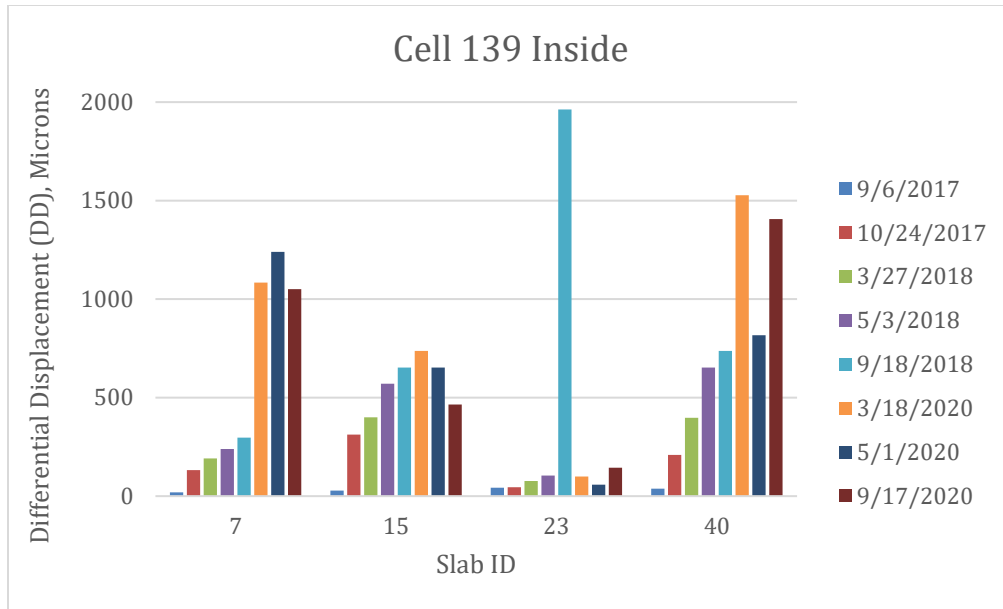**Figure 5-60. Differential displacement of Cell 139 outside line.**
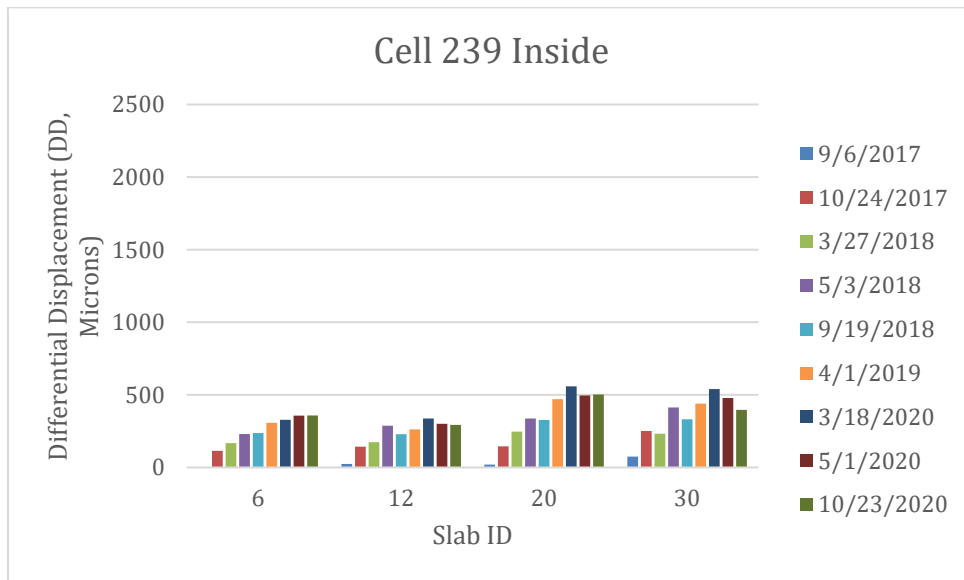
Figure 5-61. Differential displacement of Cell 239 inside line.
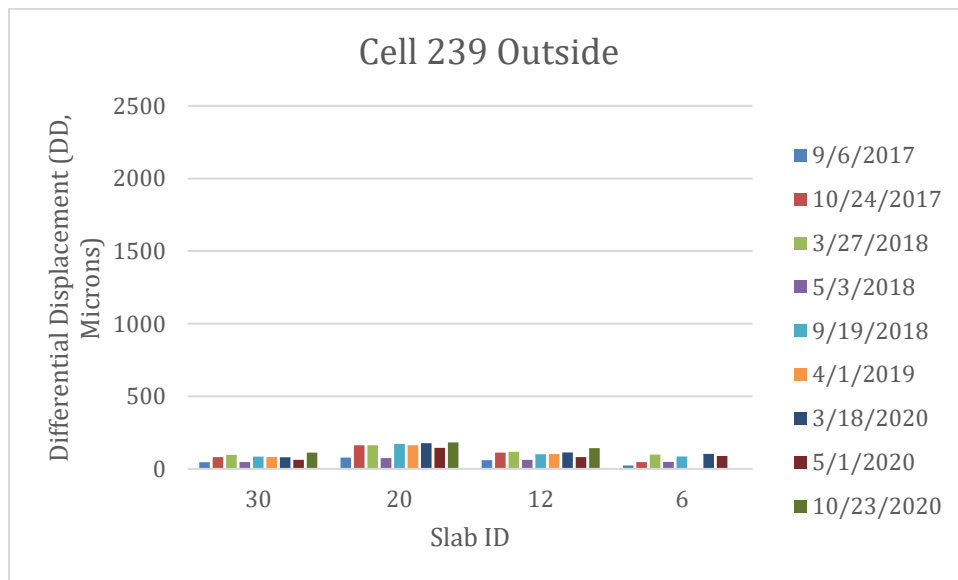
Figure 5-62. Differential displacement of Cell 239 outside line.

123

The contribution of fibers in joint performance can also be seen in the differential displacement plots for Cell 506 through 806. The driving lanes of Cells 506, 606, and 706 exhibited higher differential displacements than Cell 806. Cell 506 showed higher differential deflection initially, but then decreased with traffic and then again increased in 2020. The Cell 806 driving lane had negligible differential deflection compared to other cells until spring of 2020, when it started increasing with the traffic (matches with the LTE observations).

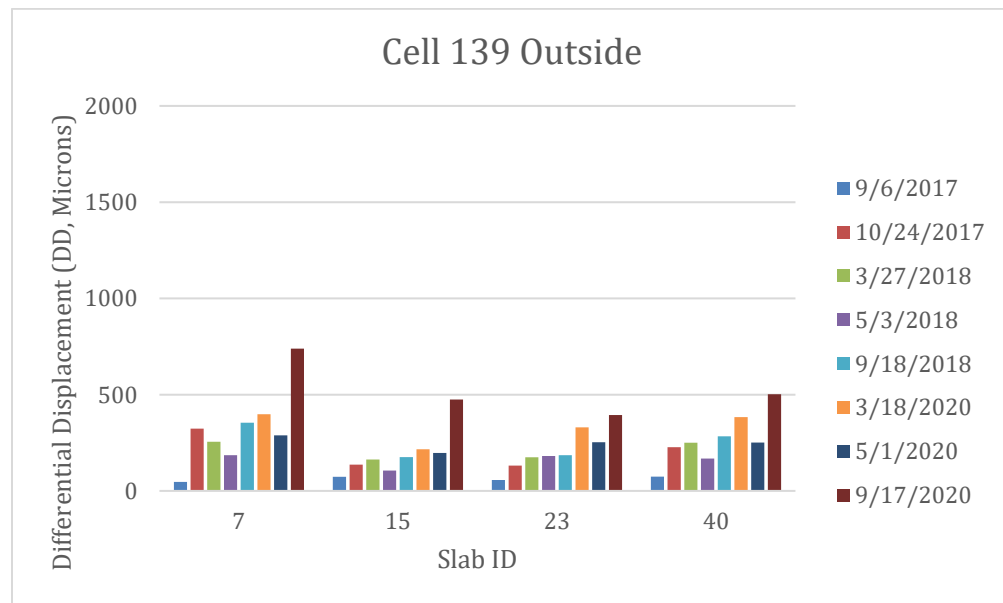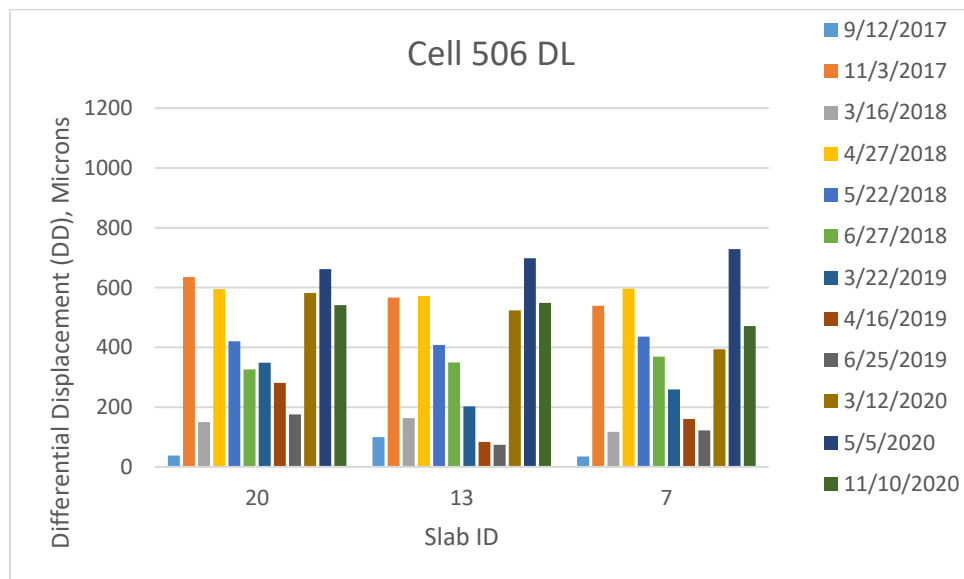**Figure 5-63. Differential displacement of Cell 506 driving lane.**
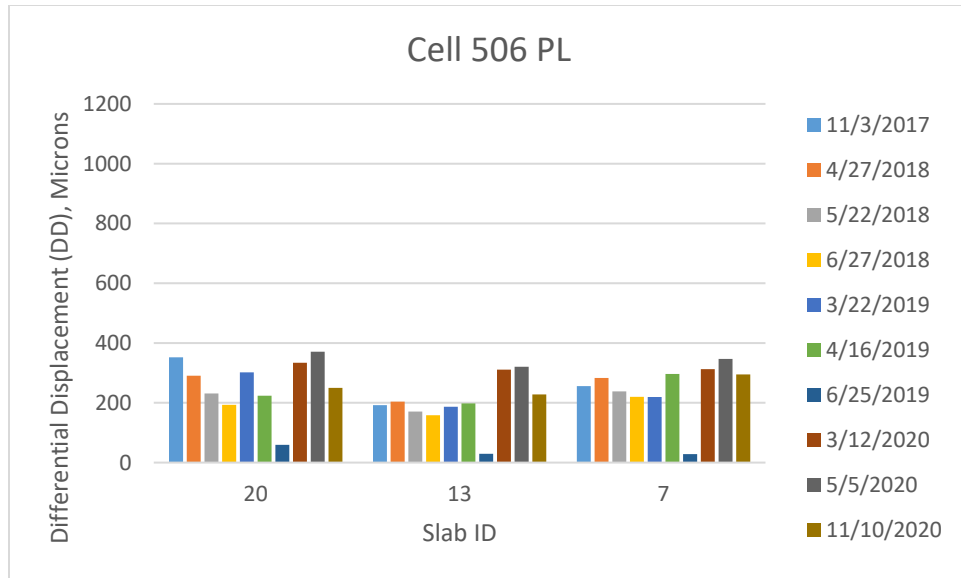
Figure 5-64. Differential displacement of Cell 506 passing lane.
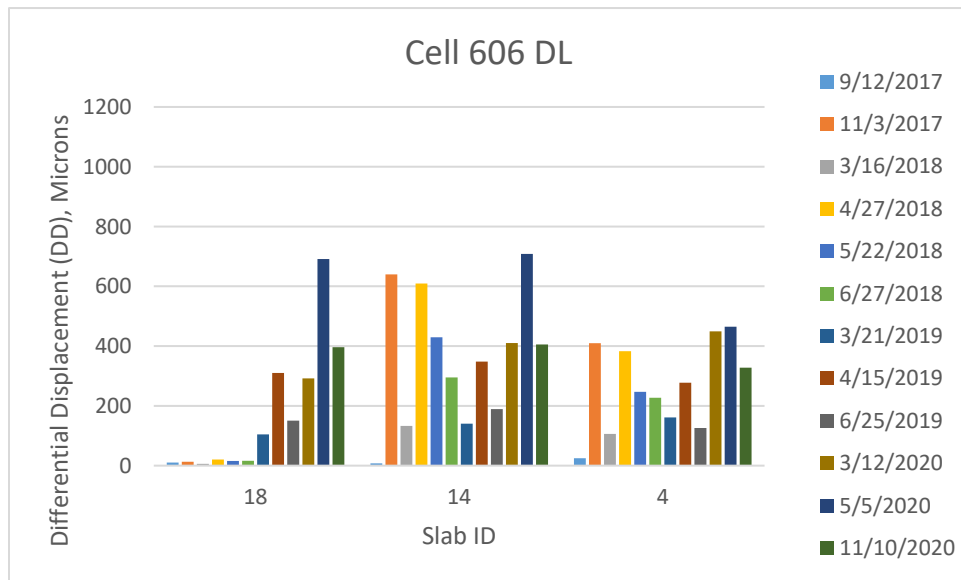
Figure 5-65. Differential displacement of Cell 606 driving lane.
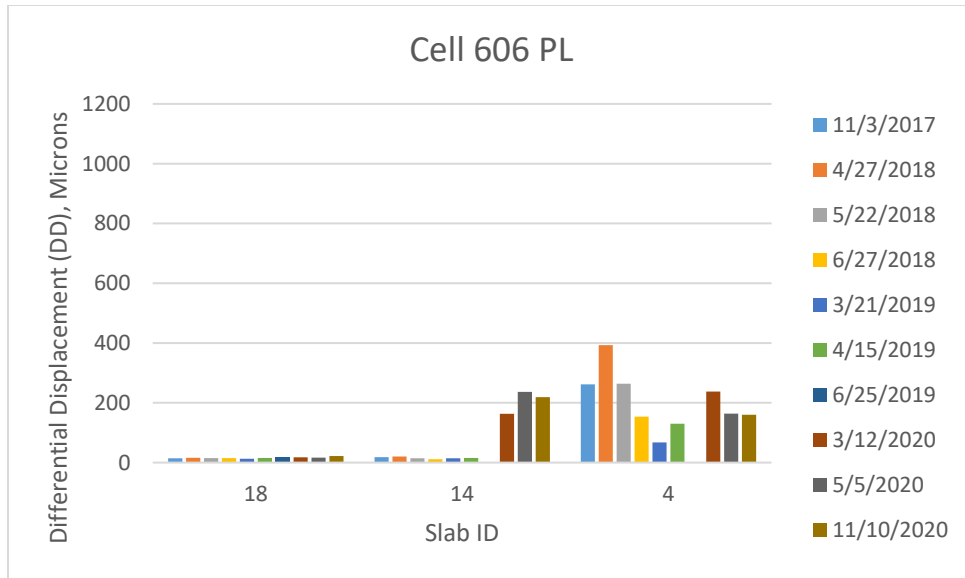
Figure 5-66. Differential displacement of Cell 606 passing lane.

Figure 5-67. Differential displacement of Cell 706 driving lane.

126

Figure 5-68. Differential displacement of Cell 706 passing lane.
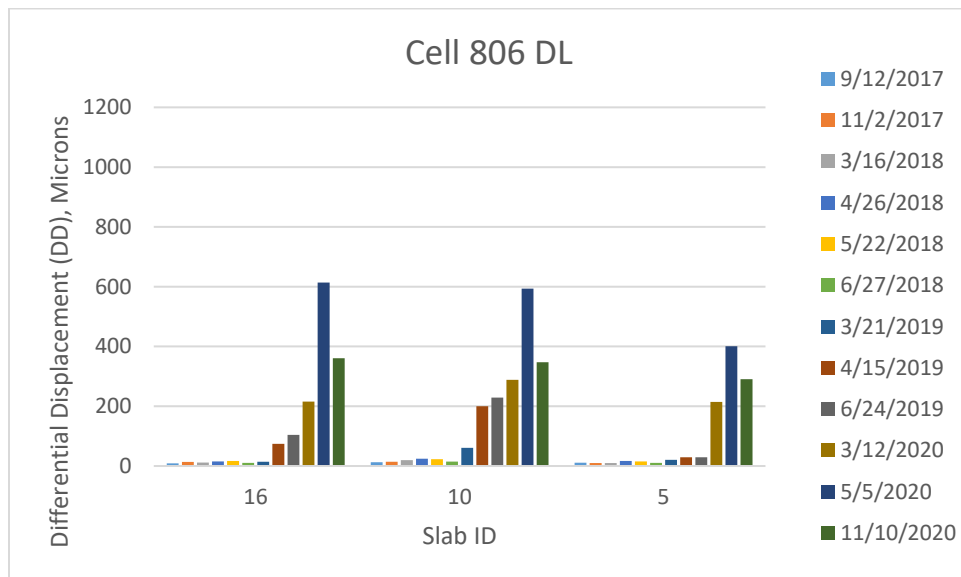
Figure 5-69. Differential displacement of Cell 806 driving lane.
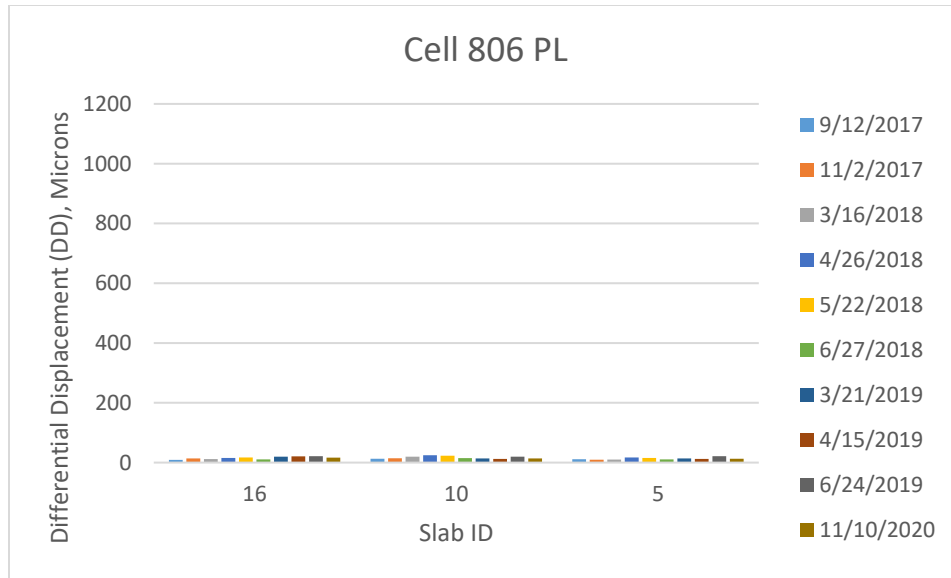
Figure 5-70. Differential displacement of Cell 806 driving lane.

Cells 705 and 805 both have experienced high differential displacements at the transverse joints; the differential displacements of Cell 705 (~1000 micron) was almost twice of Cell 805 (~460 microns). Even though the differential displacements were relatively high, the fabric interlayer provided in these cells probably limited the faulting. The other notable observation is that the differential displacement for Cell 705 decreased with traffic. This is surprising, but it may be possible if the joint support condition weakened and both the slabs experience higher overall displacement. The development of the cracks could have played a role as well. The driving lane of Cell 805 showed a steady increase in the differential displacement, while the passing lane showed somewhat similar values over the years.

Figure 5-71. Differential displacement of Cell 705 driving lane.

Figure 5-72. Differential displacement of Cell 705 passing lane.

Note: the y-axis is different than Cells 139 and 239
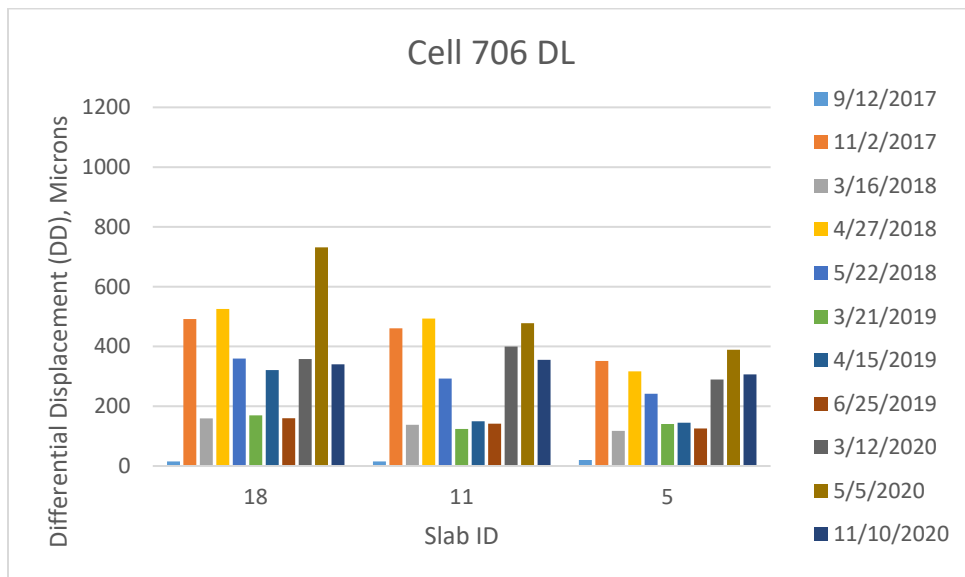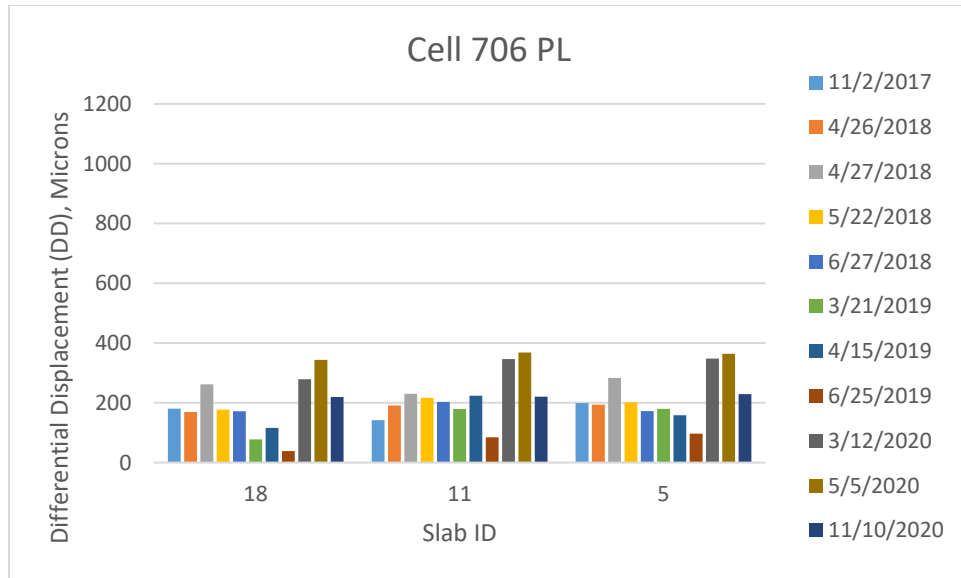
129
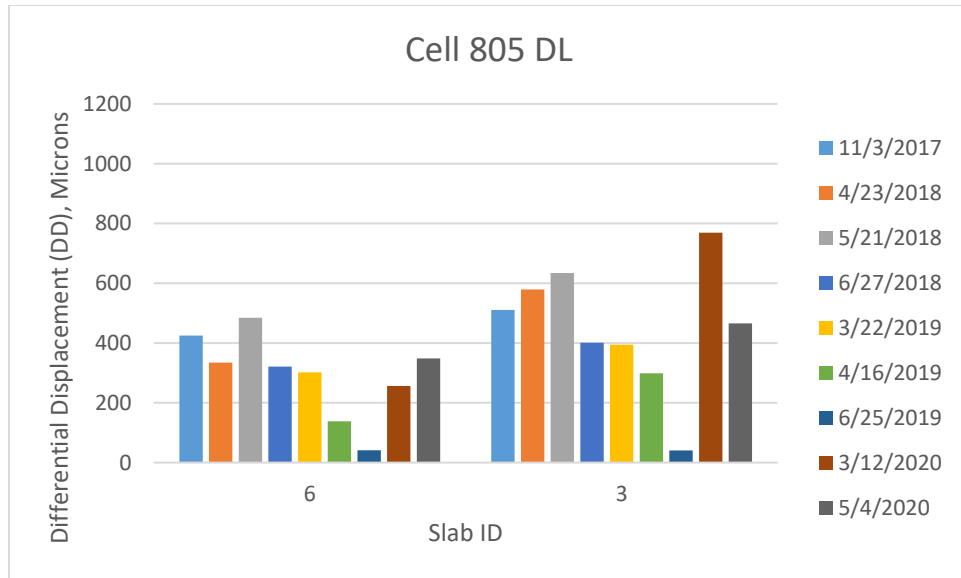
Figure 5-73. Differential displacement of Cell 805 driving lane.

Figure 5-74. Differential displacement of Cell 805 passing lane.

5.5.3 Loaded-side Displacement

Figure 5-75 through Figure 5-86 shows loaded-side displacement, which is a good indicator of joint performance. Even though the LTEs and differential displacements for Cells 139 and 239 were somewhat comparable, Cell 139 had significantly higher loaded-side displacement. This clearly indicates that cell 139 had poorer joint stiffness or weaker support compared to Cell 239.

Figure 5-75. Loaded-side displacement of Cell 139 inside lane.
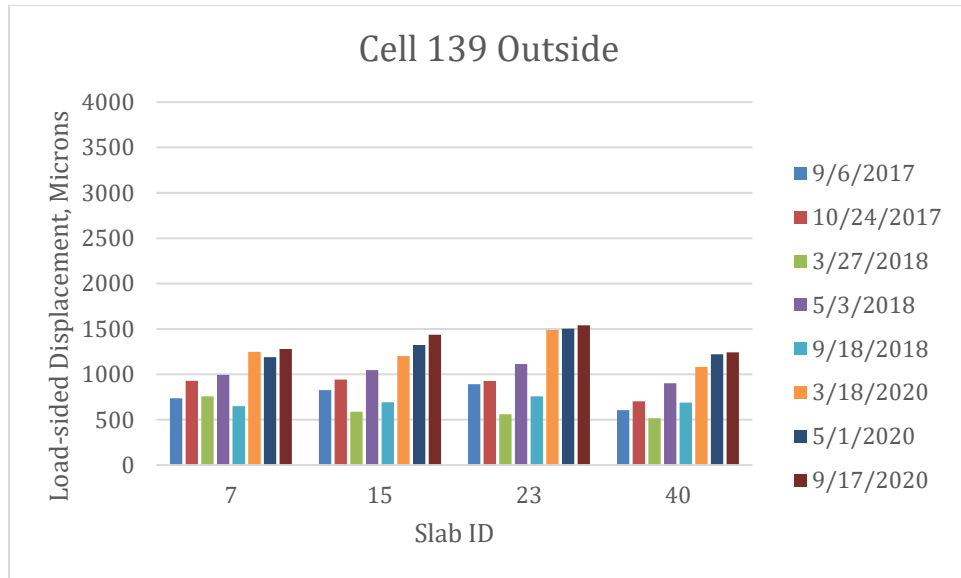
Figure 5-76. Loaded-side displacement of Cell 139 outside lane.
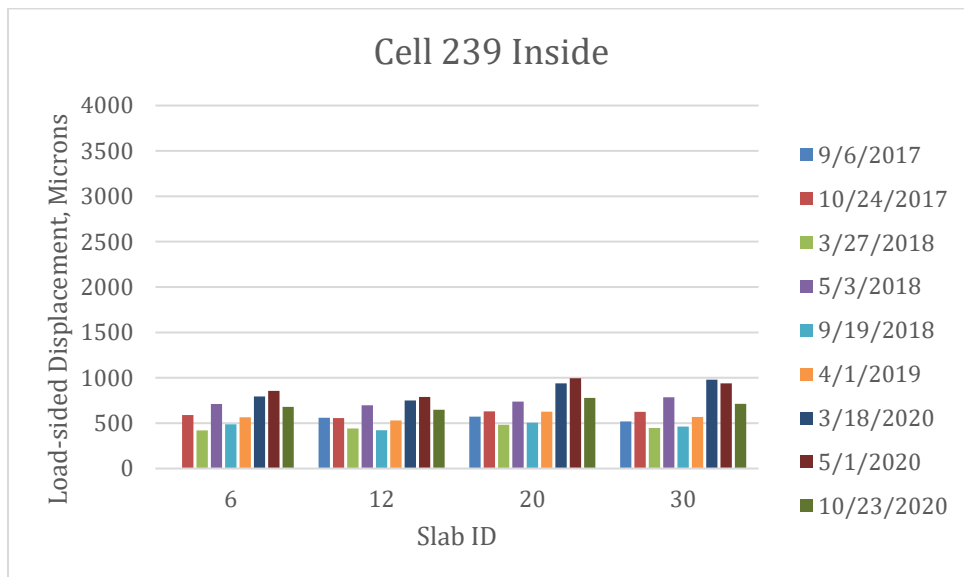
Figure 5-77. Loaded-side displacement of Cell 239 inside lane.
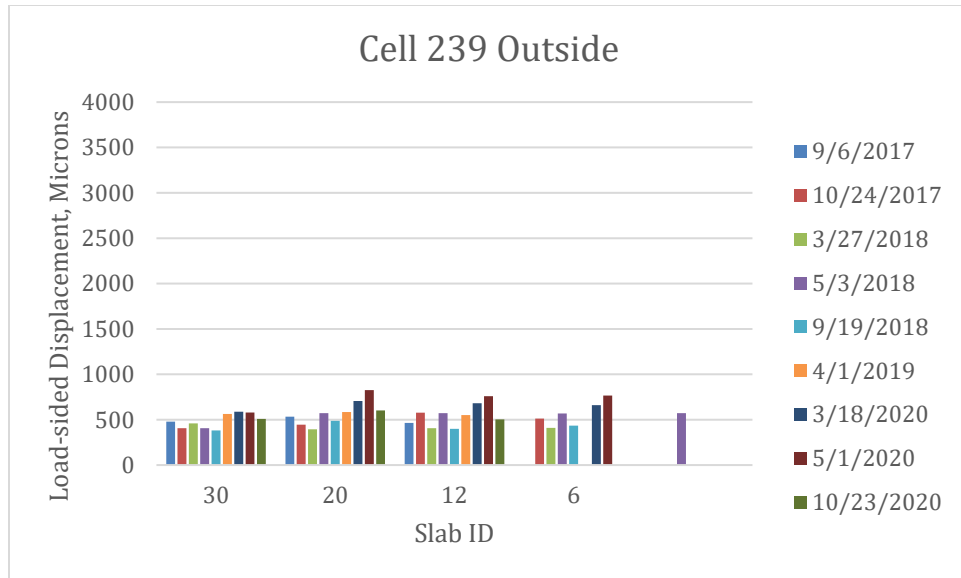
Figure 5-78. Loaded-side displacement of Cell 239 outside lane.

The loaded-side displacement of Cells 506 through 806 also showed that the 806 performed better than the other three cells initially until approximately 2.5 million ESALs. The 2020 readings (beyond 2.5 million ESALs) indicate that all four cells have similar loaded-side displacement, with Cell 506 (no fiber) slightly higher than the other three. Overall, it can be stated that the influence of fibers has diminished after 2.5 million ESALs. Cell 705 compared to Cell 805 had experienced higher and as much as twice the loaded-side displacements initially. But then the 2020 readings indicate that Cell 805 has higher loaded-side displacement.

Figure 5-79. Loaded-side displacement of Cell 506 driving lane.
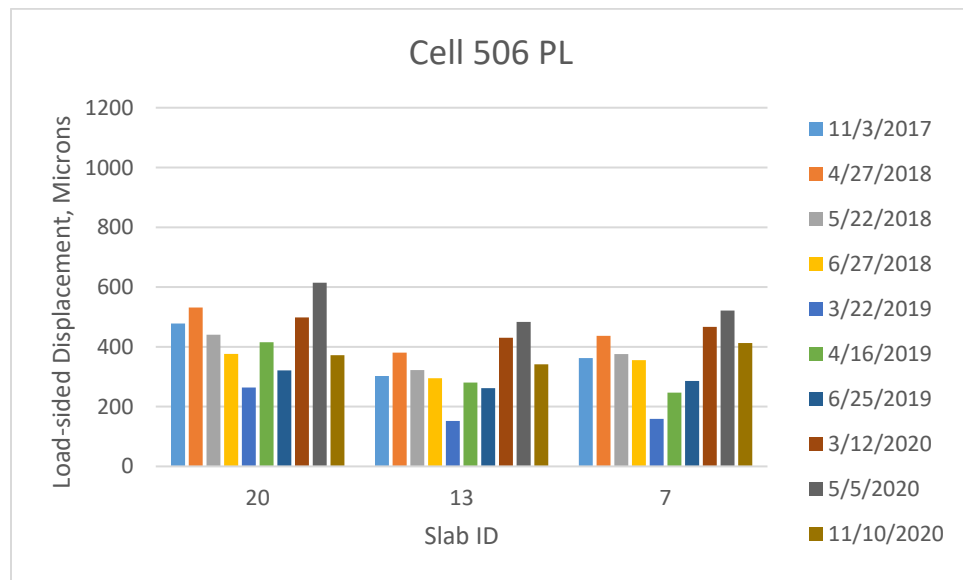
Figure 5-80. Loaded-side displacement of Cell 506 passing lane.
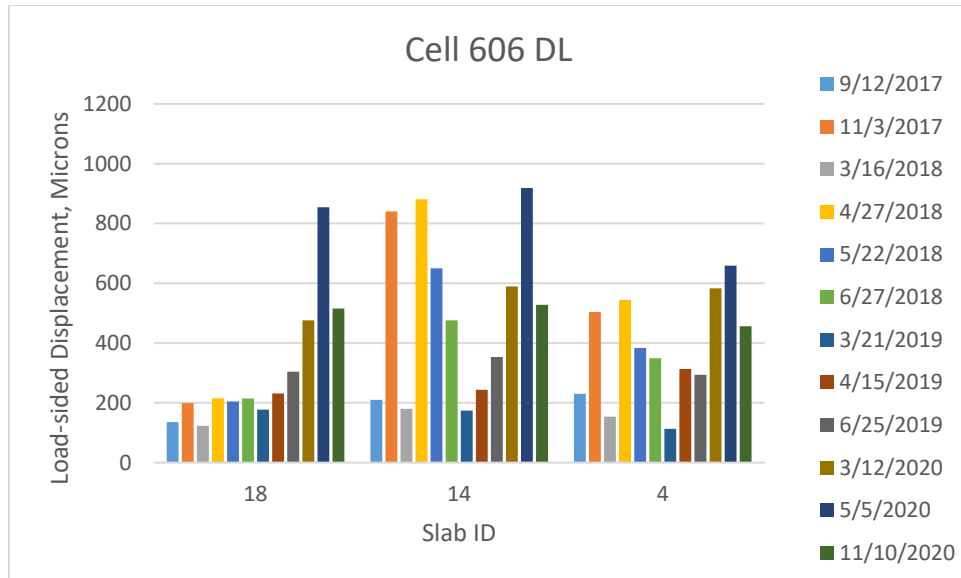
Figure 5-81. Loaded-side displacement of Cell 566 driving lane.
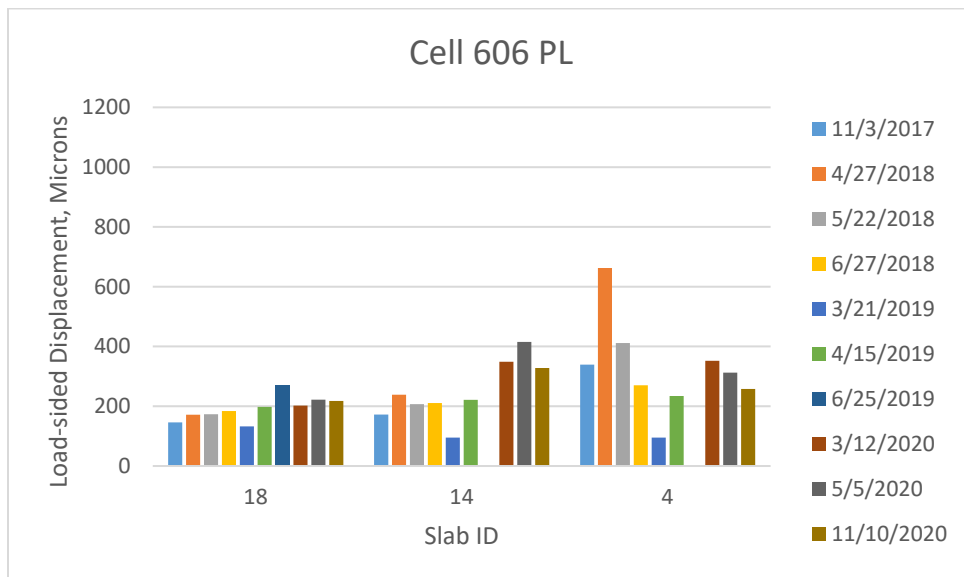
Figure 5-82. Loaded-side displacement of Cell 606 passing lane.
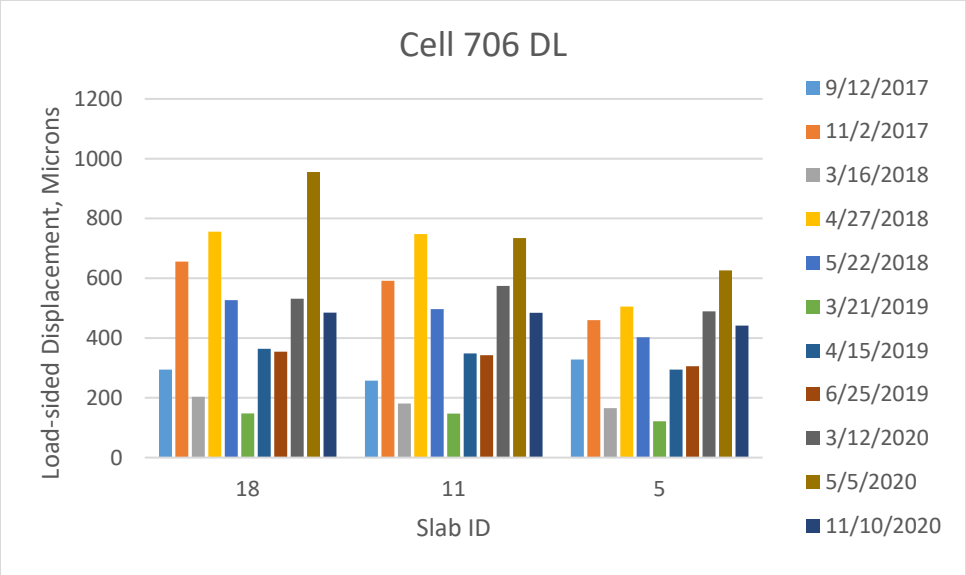
Figure 5-83. Loaded-side displacement of Cell 706 driving lane.
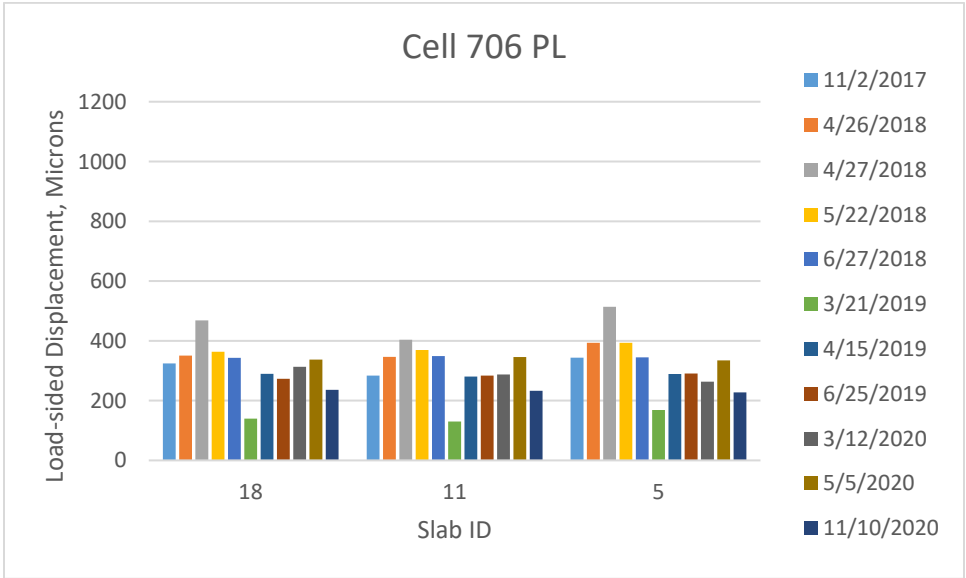
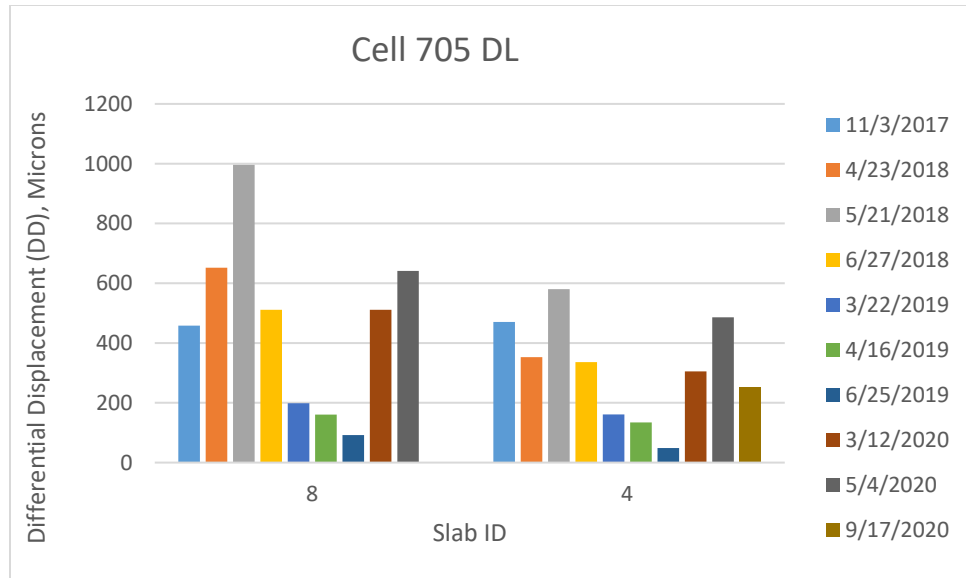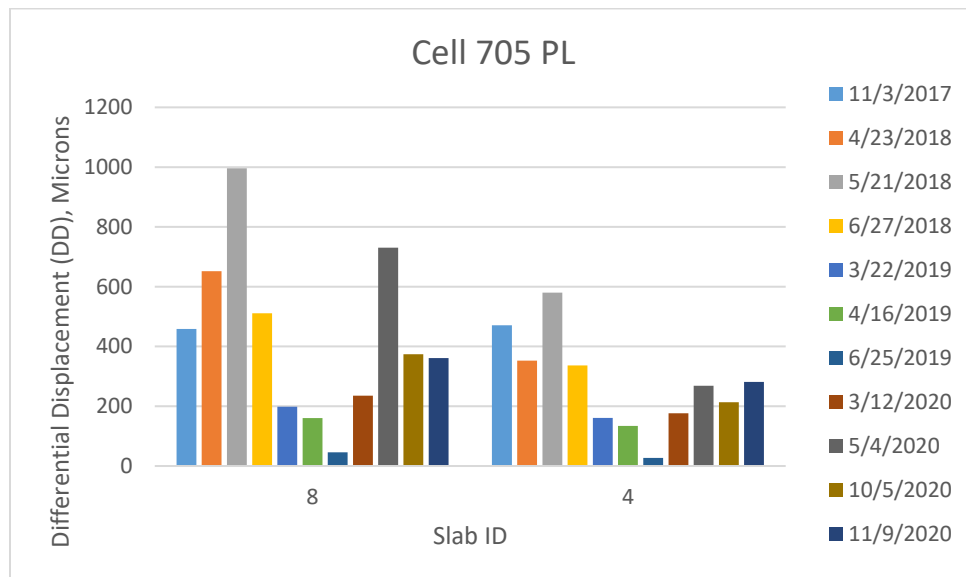**Figure 5-84. Loaded-side displacement of Cell 706 passing lane.**
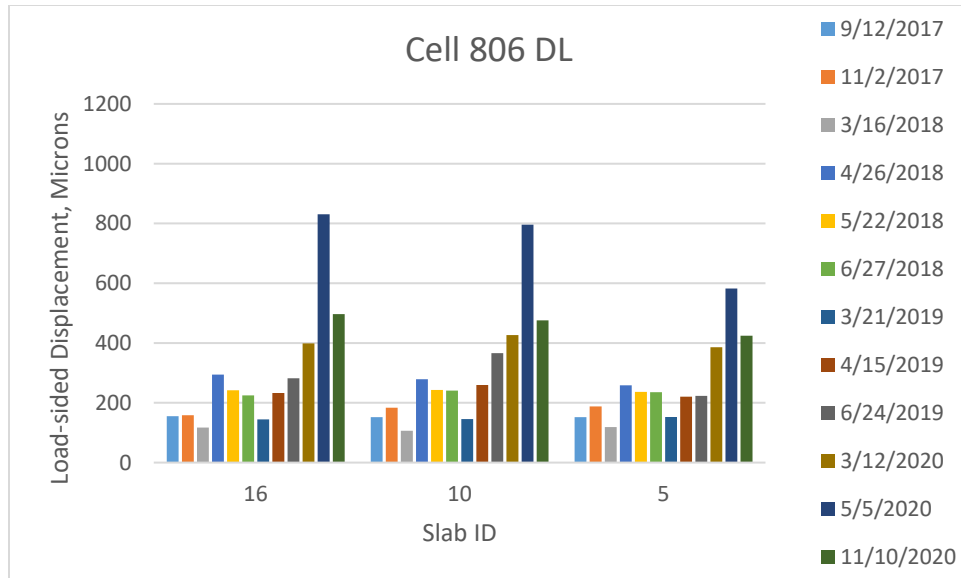
Figure 5-85. Loaded-side displacement of Cell 806 driving lane.
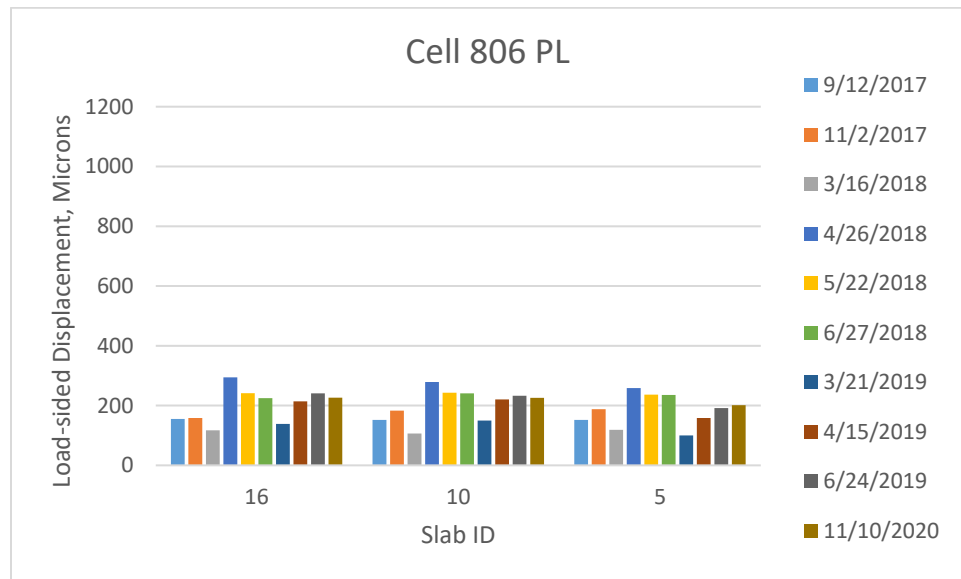
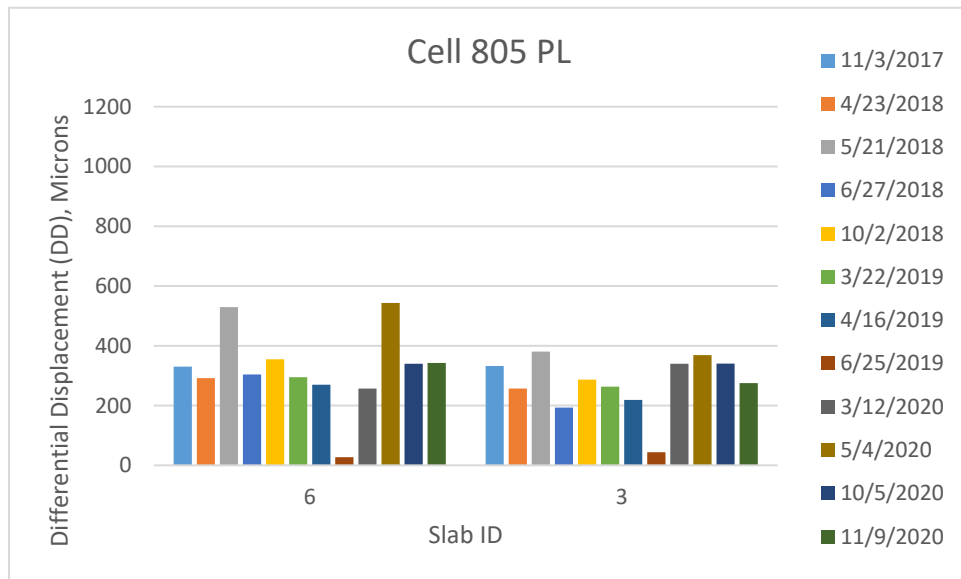**Figure 5-86. Loaded-side displacement of Cell 506 passing lane.**
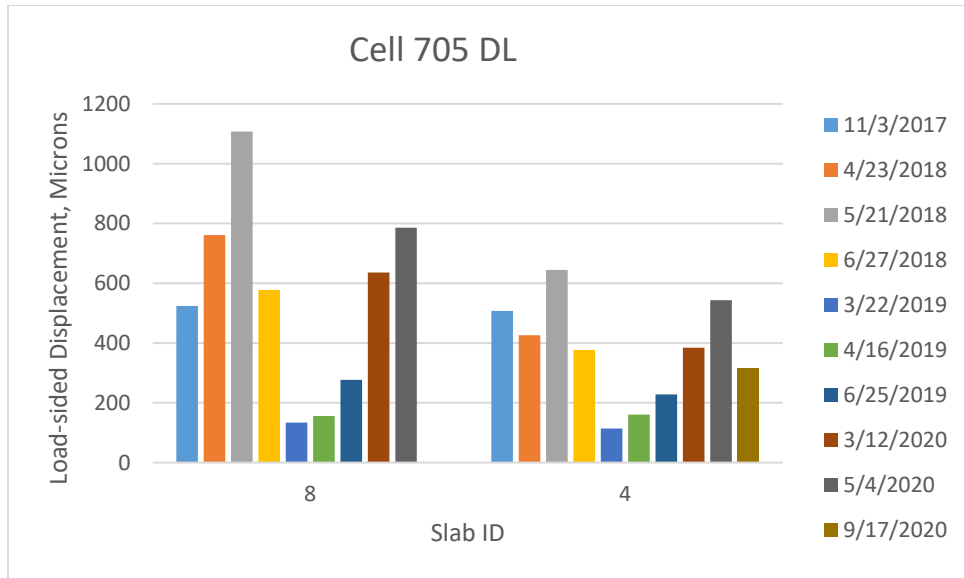
Figure 5-87. Loaded-side displacement of Cell 705 driving lane.

Note: the y-axis is different than Cells 139 and 239

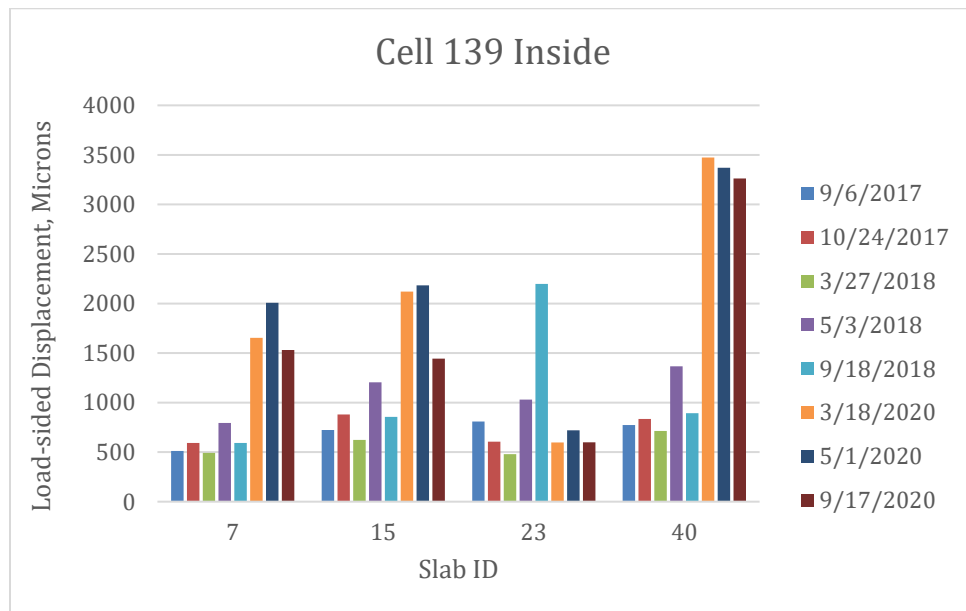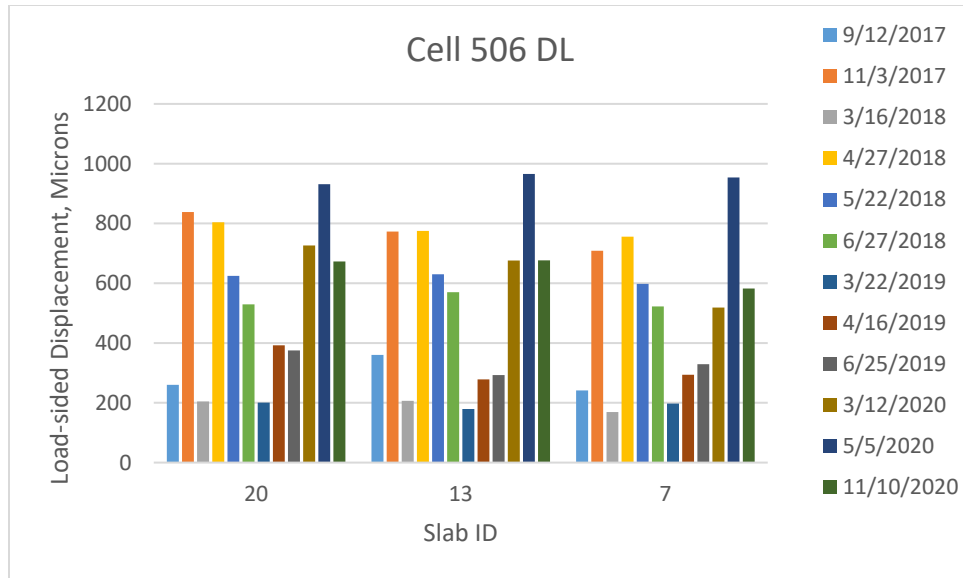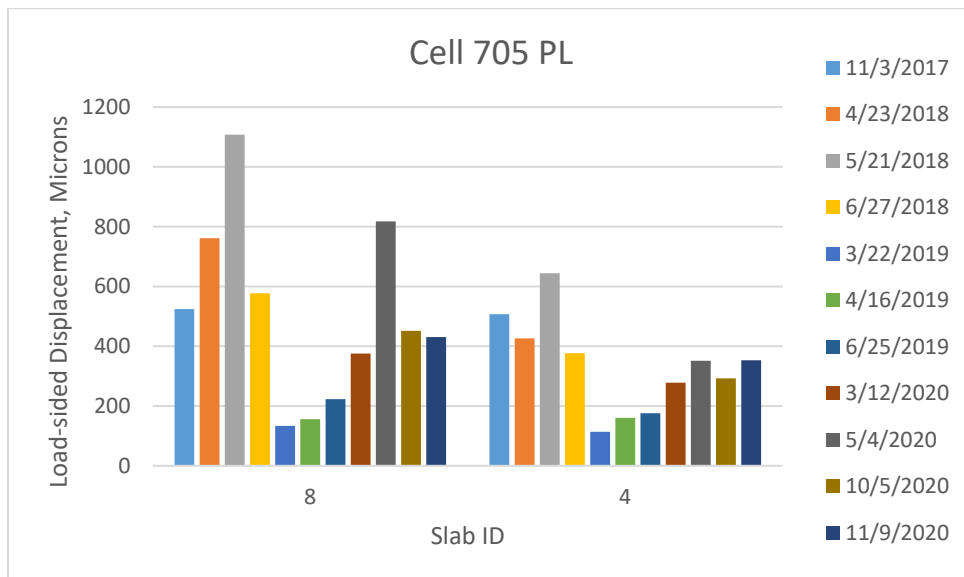**Figure 5-88. Loaded-side displacement of Cell 705 passing lane.**
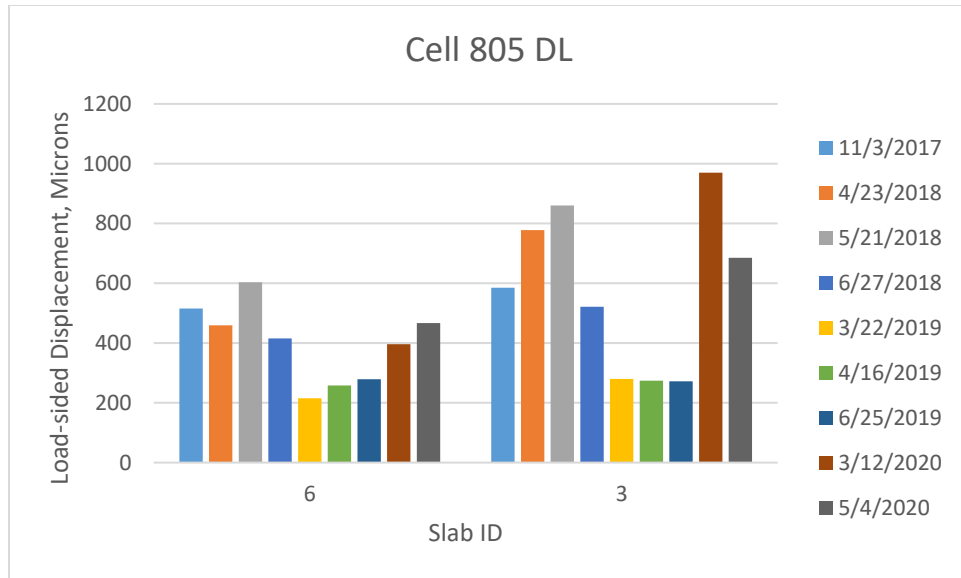
Figure 5-89. Loaded-side displacement of Cell 805 driving lane.
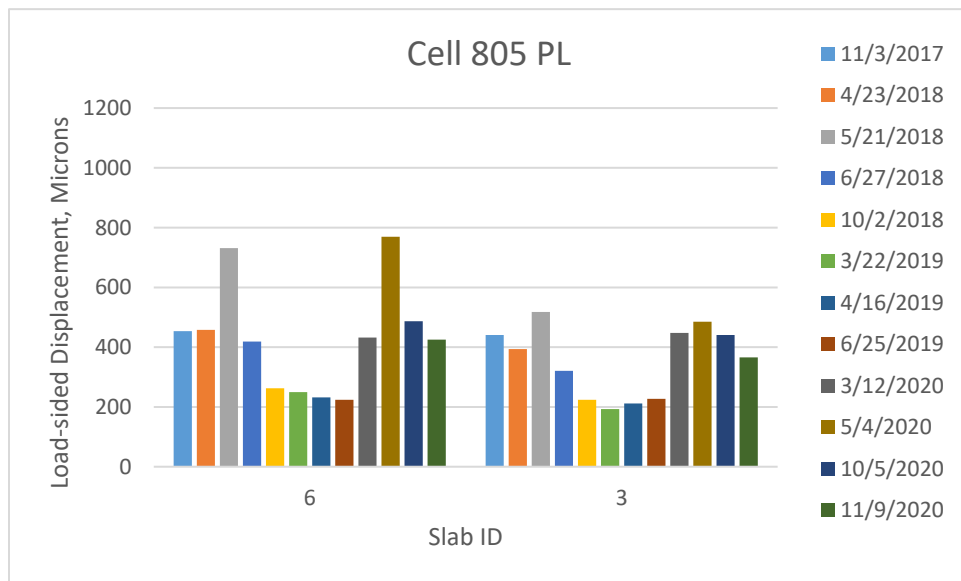
Figure 5-90. Loaded-side displacement of Cell 805 passing lane.

5.5.4 Void Analysis

Crovetti and Darter (1985) proposed a method to investigate the presence of voids underneath concrete pavement slabs using FWD test results. As shown in Figure 5-91, FWD-measured corner deflections are plotted against the applied loads in this procedure. In such a plot, if the intercept of a deflection line (at zero load) is two mils or below, then it is assumed that the chance of void presence is low. A similar concept was adopted in the current study to identify the presence of voids under the slabs and to understand the influence of the fiber if any. One exception in the current study was the use of slab deflections along the wheel path at the transverse joint instead of corner deflections. Also, it may be noted that the deflection data collected at the leave slab with the load on the leave slab was used for the void detection analysis because of the probability of more voids present under the leave slabs. Figure 5-92 (a) and (b) compare the deflection vs. FWD applied load at one slab in Cell 506 (plain concrete cell) and Cell 806 (the highest fiber dosage). Deflections were measured at different seasons for both the cells. While it appears that the deflection intercept determined for the spring-thaw times were relatively higher than the other seasons for both the cells, Cell 506 had higher values than Cell 806. Figure 5-93 summarizes the deflection intercept for all the ultra-thin and thin pavement cells for various slab and test dates. Cells 705 and 805 were not considered for this analysis as they were overlays and had geofabric layer underneath the slabs.
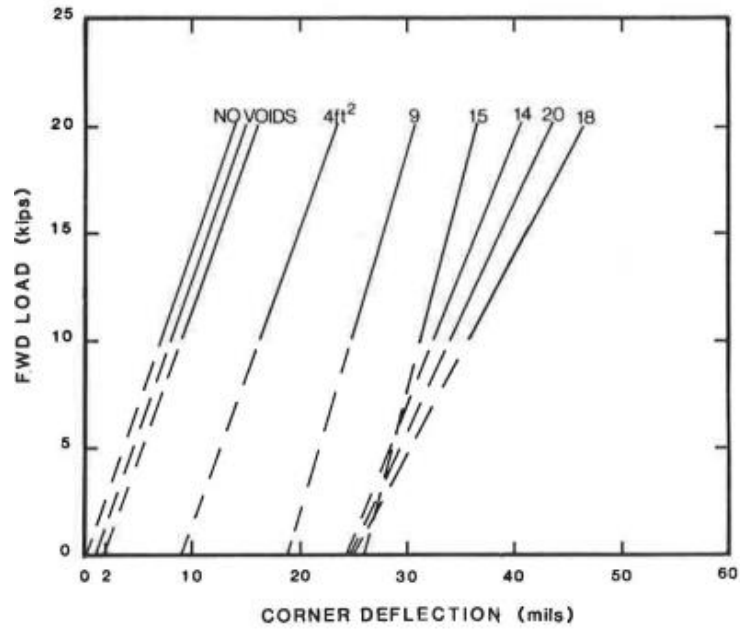
Figure 5-91: Use of FWD test data conducted at different load level to identify possible presence of voids (Crovetti and Darter, 1985)
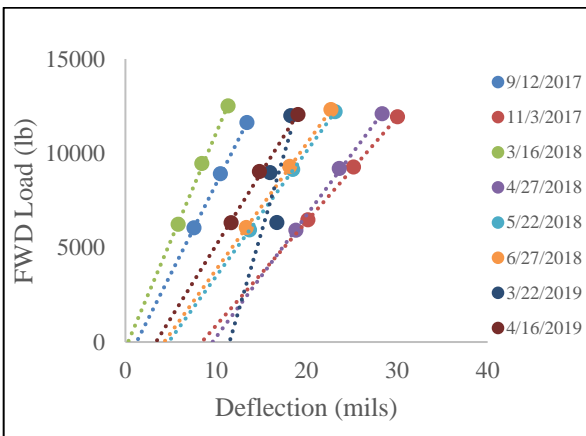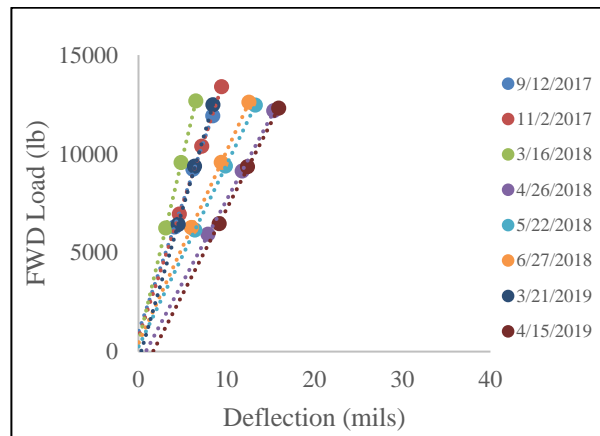
(a)   (b)

Figure 5-92: Deflection vs FWD load for (a) Cell 506 (b) Cell 806
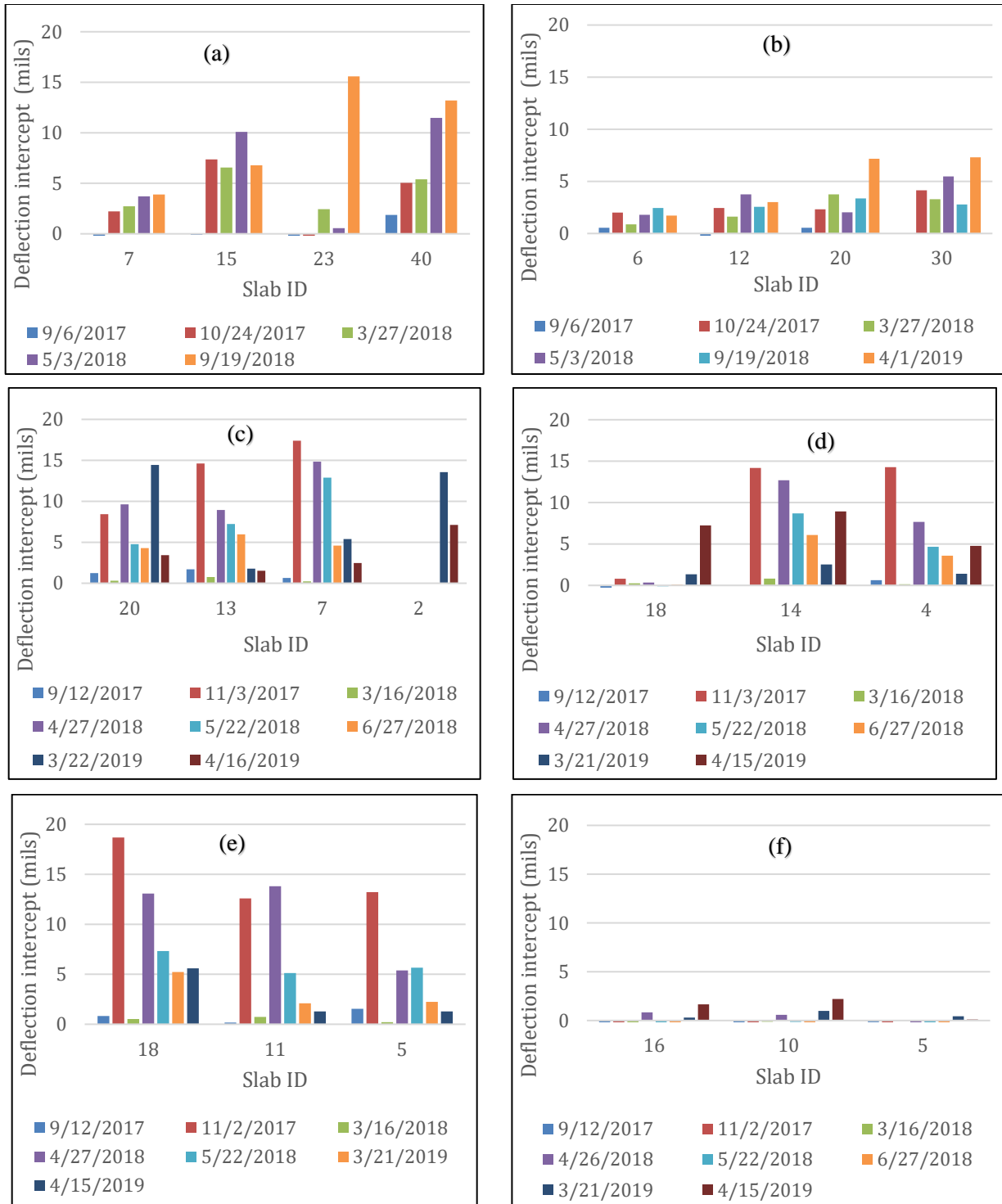
Figure 5-93: Deflection values under variable FWD load stresses for NRRA test Cells (a) 139 (b) 239 (c) 506 (d) 606 (e) 706 and (f) 806.

142

The deflection intercept values calculated for different seasons for all the cells were used to determine a factor, referred to as 'void index (VI),' to quantify the influence of fibers on the void accumulation underneath the slab, especially at the wheel path-transverse joint intersection. This void index depends on the amount of FWD detected voids present under slabs, with 5 being the best condition with no voids and 0 being the worst condition with excessive voids underneath the slab. Table 5-5 presents the proposed scale of VI for different ranges of deflection-intercepts. This scale was used to determine the VI for all the cells at different seasons using their respective deflection intercept, as presented in Table 7. It appears that Cell 139 shows a good trend with VI, decreasing from 3 to 1 in one year; Cell 239 had better VI values than Cell 139, and it did not decrease much with age. The comparison of VI values between Cell 806 and other cells indicates that the higher fibers in Cell 806 were able to significantly protect this cell from void (FWD detected) formation underneath the slab. The results for the Cells 506, 606, and 706 indicate that these cells seem to have significant FWD detected voids underneath their slabs, and the recent declines in LTE and increases in the faulting agree with this finding.

Table 5-5: Scale of the proposed void index.

VI	Voids possibility	Deflection
5	Nil	<2 mils
4	Very less	2-4 mils
3	Less	4-8 mils
2	Moderate	8-12 mils
1	Severe	12-16 mils
0	Very Severe	<16 mils

Table 5-6: Void index values for different cells at different seasons

Cell	Void Index (VI) values				
	Fall 2017	Spring 2018	Summer 2018	Fall 2018	Spring 2019
139	3	2	-	1	-
239	4	3	-	3	3
506	0	0	0	-	0
606	1	1	1	-	1
706	0	0	-	-	0
806	5	5	5	-	4

5.5.5 LTE vs. Pavement Temperature

The load transfer behavior of fiber reinforced concrete is dictated by the aggregate interlock and dowel action of the fibers. Both parameters are influenced by crack width variation, which is a function of the temperature and the relative humidity of the slabs to a certain extent. In the summertime, when the temperature remains high, the crack width closes, and the LTE increases. The exact opposite occurs in winter, but the frozen base and subbase then play a supporting role in transferring the wheel loads. During the spring-thaw season, the joint width remains wide, in which case the weak support conditions of the granular base can result in low LTE.

Figure 5-94 to Figure 5-96 shows that the LTE for almost all the cells increases when the pavement surface temperature increases. Figure 5-94 shows that Cell 139 and 239 have almost similar characteristics when it comes to variation of LTE with pavement surface temperature. Cell 705 and 805, as shown in Figure 5-95, had the least reported LTE of all the eight cells, but they did not vary much with the temperature. It was observed that the variation of LTE with temperature was more sensitive in 705 compared to 805 (narrower slabs).

However, the most interesting observation is the influence of fibers on the LTE vs. temperature relationship. Figure 5-96 shows Cell 806 experienced the least change in LTE with respect to temperature, indicating the contribution of fibers toward increasing load transfer through dowel action in the wider cracks at low temperatures. The fibers are also likely serving to increase the aggregate interlock by keeping the joint widths tight. LTE variation was more pronounced for Cell 506 (plain concrete). The slope of the LTE vs. temperature line for Cell 706 is also sharp, which indicates the greater influence of the temperature. The exact reason for Cell 706's low joint performance is not known; however, the data indicate that the joints considered for the FWD test probably experienced damages because of the higher load side displacement, differential displacement, and presence of voids underneath at a very early age. Note that even though the design RSR for this cell was 30%, the beam samples prepared at the field only resulted in 23% RSR, close to Cell 606's RSR.
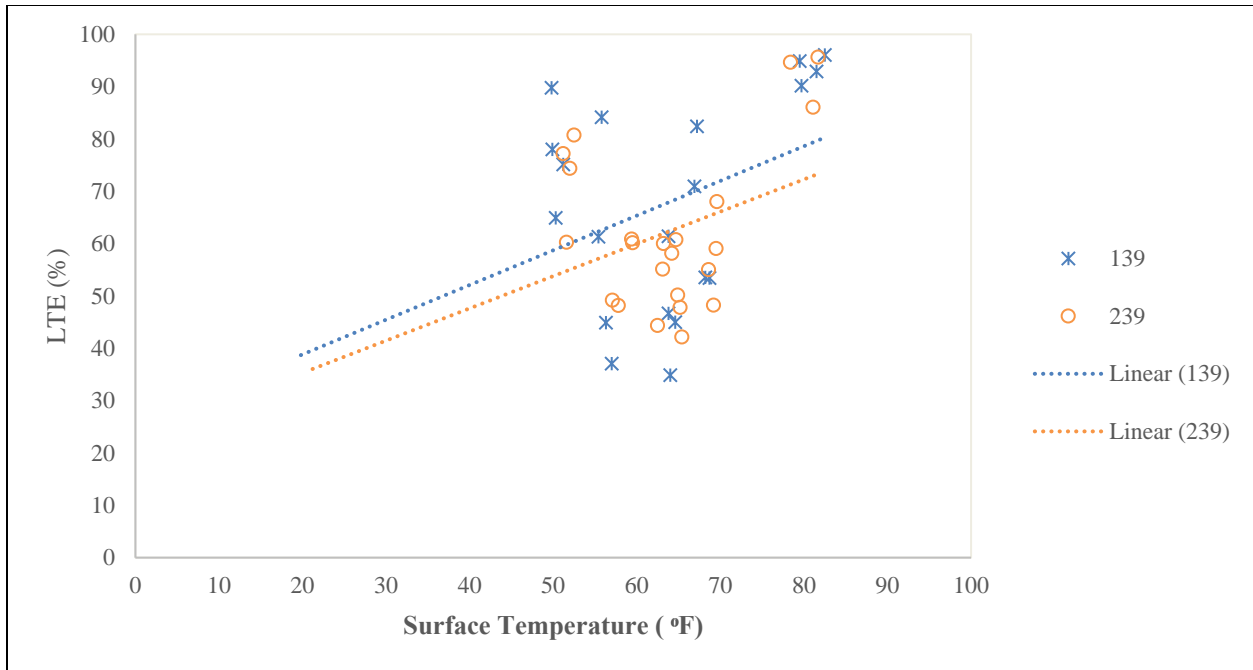
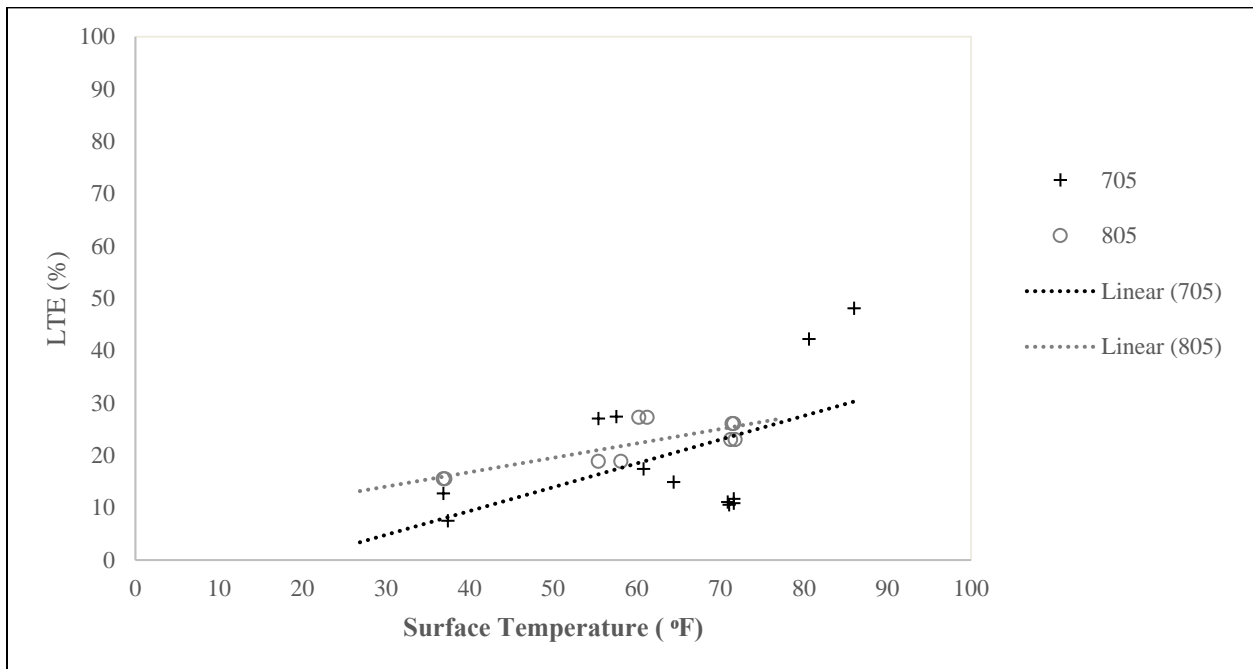**Figure 5-94: LTE vs. Pavement surface temperature for Cells 139 and 239.**

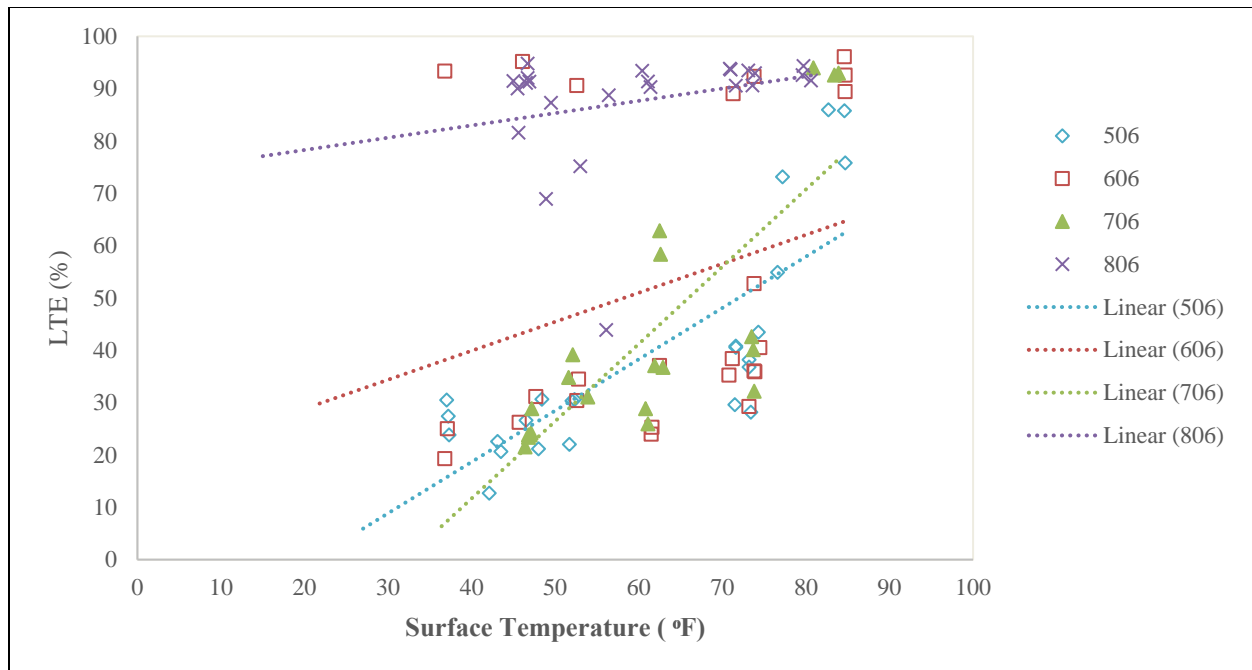**Figure 5-95: LTE vs. Pavement surface temperature for Cells 705 and 805.**

Figure 5-96: LTE vs. Pavement surface temperature for Cells 506, 606, 706 and 806.

6 CONCLUSIONS AND RECOMMENDATIONS

Fiber-reinforced concrete overlays and pavements have been constructed in the United States and many other countries for many decades. However, a comparison between the performances of fiber reinforced concrete pavements or overlays and their plain concrete counterparts was not available because of the lack of companion sections. The National Road Research Alliance funded and MnDOT constructed 2017 FRC test cells to provide an excellent opportunity to achieve such a comparison and quantify the contribution of synthetic structural fibers in mitigating cracks, faulting, and other distresses. This report discussed the objectives and methodology of the research conducted, including the construction of the MnROAD test cells, instrumentation, traffic load application, and data collection and analysis procedures. The distresses observed, such as fatigue cracking, faulting, and the joint performance measured in each cell were discussed and compared to conclude the influence of the synthetic structural fibers on them. The following major conclusions can be drawn from this study.

Fatigue Cracking

- In Cell 139, 75% of slabs cracked after approximately ~80,000 ESALs. Given the 3-inch thickness of the slabs, and the fact that fibers contribute most after cracking has occurred, it can be stated that the overall pavement structure in this test cell was too weak for this particular type of fiber and dosage (@8lb/cy fiber, 30% RSR) to significantly benefit performance. At the same time, however, the fibers in this cell clearly contributed to extending pavement life by the fact that although permanent deflections were extremely high, the individual pieces of shattered concrete remained interconnected via the fibers for a short time.
- Cell 239 (4-inch thick) has performed much better than Cell 139. It appears that one-inch thicker FRC concrete may, in this case, result in double the service life compared to 3" thick Cell 139. The primary distress for Cell 239 was longitudinal cracking along the wheel path. This observation concludes that such thin FRC pavement structures do not fail by the typical mid-slab transverse fatigue cracks, unlike thicker (> 6 inches) conventional concrete pavements.
- Cells 506 through 806 performed better than all other cells with respect to fatigue cracking, with only a few cracks forming in three slabs of Cell 506 (no fiber). As these cells have not experienced enough cracks yet, it is hard to quantify the contribution of fibers in mitigating fatigue cracking. These cells have successfully carried 3.5 million ESALs until December 2020. This observation indicates that the

critical distress for the small panel thin concrete pavements on the relatively stiff base layer may not be the fatigue cracking but other distress like faulting.

- Cell 506 experienced spalling along transverse joints in many locations, but the primary cause was the presence of hardened saw-cut residue stuck within the saw-cuts of joints.

- Regarding the thin FRC overlays (Cells 705 and 805), it was seen that Cell 805 with narrower slabs resulted in less percentage of cracked slabs (35%) than Cell 705 (50%) after three years of interstate traffic and climate. While Cell 705 experienced more longitudinal cracks, Cell 805, developed more transverse cracks. It seems the combination of virtually no layer bonding with the fabric interlayer and higher slab curvature for thin overlays can create more longitudinal cracks in wider panels. The number of transverse and corner cracks in Cell 705 and 805 were comparable.

- This study has proposed a parameter known as 'crack index,' which considers the crack length over the unit pavement surface area. Even though Cell 705 showed 15% more cracked slabs than Cell 805, their crack indexes were comparable throughout their service lives.

- Compared to the thin FRC pavement cells placed on a gravel base, the thin unbonded FRC overlays experienced significantly higher fatigue cracks (Cells 705 and 805 vs. Cells 606 through 806). One theory for this behavior might be the ability for large thin slabs to freely curl up due to the lack of bonding between the old concrete and fabric interlayer.

- The cells in the mainline (Cells 705, 805, 506-806) had approximately 3.5 million ESALs on them by the end of 2020, well beyond the typical traffic load for low-volume road designs. So many distresses that occurred in 2020 may not form if such designs were placed in more typical settings.

- Although data were limited, preliminary fatigue cracking predictive equations were developed for Cell 239. Correlation with field distress data was reasonable.

Joint Faulting and International Roughness Index

- Cells 139 and 239 have developed low levels of joint faulting (1 to 2 mm) to this point in time.

- The contribution of the fibers toward impacting faulting results was clearly evident when examining Cells 506 to 806. Cell 506, which was constructed with plain concrete, experienced considerably higher faulting than the three FRC Cells (606, 706, and 806). Compared to these three cells, the magnitude of the faulting in Cell 506 was more than double after three years of interstate traffic. The faulting increment rate with respect to ESAL was also higher for Cell 506 than the other cells. Note that it was not until the highest dosage of the fibers used in these cells that the development of

148

faulting was noticeably slowed, and even in that case, faulting continues to increase with traffic loadings.

- Cells 705 and 805 (overlay with nonwoven geotextile) experienced lower faulting than the concrete pavement cells (Cells 506 -806). Permanent compression of the geofabric interlayer likely contributes toward much of the measured faulting, while its resilience should limit the maximum amount of faulting that can develop long term.

- This study used faulting results to compute a 'faulting index' that accounts for every joint over a mile of the pavement. This index and IRI results indicated that even though the Cells 506-806 have not failed in fatigue cracking, their ride quality decreased considerably at around 3 million ESALs, with a poor ride quality rating (IRI below 173 inches/mile).

- The IRI result for Cell 506 indicates that the ride quality for this cell was poor even when the first measurement was performed at 825,000 ESALs. At the same ESALs, all other thin FRC n pavement cells had IRI values lower than 173 inches/mile.

- The IRI results for Cells 705 and 805 shows that they developed lower IRI values and stayed around the admittable range until 2.4 million ESALs, when IRI suddenly increased with the development of more severe distresses.

Structural Response

- The joint performance behavior evaluated by the falling weight deflectometer (FWD) revealed that synthetic structural fibers could positively influence the load transfer efficiency (LTE) or other joint performance parameters for thin concrete pavements, depending on the fiber type and dosage.

- Between the four thin pavement cells (506 through 806) in which the fiber dosage was varied, the LTE of Cell 806 (the highest fiber dosage, 11.7 lb/cy) was significantly greater than the Cell 506 (no fiber). The contribution of the fibers in enhancing joint performance results of two other cells (606 and 706) was less or not significant in terms of both magnitude and rate of decline over time. In fact it was not until the highest dosage of the fibers used in these cells that the rate of decrease in LTE was noticeably affected.

- Fibers helped in reducing vertical joint displacement (e.g., Cell 506 vs Cell 806) until about 2.5 million ESALs. The LTE of all cells decreased significantly after 2.5 million ESALs.

- Although the LTEs in Cells 705 and 805 were always lower than other FRC cells, these cells did not develop significant faulting. It was difficult to quantify a difference in the performance of Cells 705 and 805 in terms of the contribution of synthetic structure fibers.

- The temperature gradients in all these thin cells were found to be linear to a great extent. As much as 60% of the time, slabs experienced a negative temperature gradient.

- The environmental strains that were measured in the FRC cells showed that they possess a good relationship with the temperature, but no verifiable correlations with the fiber types, dosages, and slab sizes monitored in this study.

- The measured dynamic strains were higher in general during the springtime when the base and subgrade support were weak. Dynamic strains in the ultra-thin cells (Cells 139 and 239) were higher than the other FRC cells.

- Joint opening sensor data provided mixed results. Some cells showed greater joint openings than the other cells, irrespective of the fiber dosages and cell designs.

Lastly, it should be cautioned that the results from this experiment represent the behavior of three dosages of one synthetic fiber. It should not be construed that the results represent the behavior of other types and dosages of synthetic structural fibers or concrete mixtures, for that matter.

6.1   RECOMMENDATIOns

The research conducted in this study was limited with respect to the pavement design variables and materials. Only one fiber type was used, and the concrete mixtures were similar between the cells, except for minor changes due to the changes in the fiber dosages. The recommendations listed below are quite preliminary and shall be further verified with future studies.

1) Construction of 3-inch thick ultra-thin pavements on a marginal base layer may not be a good design, as it may fail before the anticipated design life irrespective of fibers' inclusion or not. Placement of a 3" thick FRC pavement on a stiffer stabilized base may lead to different results and thus might be considered in future experiments. As mentioned early, however, this design may require the full flexural strength to develop in the slabs before heavier loads could be placed on it, which might limit its practical applications.

2) Thin (5 to 6 inches) pavements with smaller panels placed on relatively strong base layers seem to be a safe design with respect to the fatigue cracking for lower volume roads (~ 2 million design

ESALs). Fibers have been shown in this study to reduce the magnitude of joint faulting and keep the riding quality reasonable l through the design period, but similar designs without fibers may not offer the same. Also, since it took the highest dosage of the fibers to affect the development of faulting, it is recommended that a cost-benefit analysis be done in the future to see whether the additional cost of such high dosages of fibers can be justified.

3) The thin unbonded FRC overlays in this study revealed that wider paneled designs might develop higher levels of cracking, faulting, and IRI than narrow-paneled ones. However, other factors like ease of repair of the cracked slabs for the wide vs narrow-paneled overlays, cost of the saw cuts, etc., should be considered for making the decision on the width of the panel. It appears that smaller panels develop cracking at a slower pace, which may be an advantage to delay the repair work. But whether it is easy to repair more numbers of narrower panels than a smaller number of wider panels is a different question and should be considered.

4) This study has provided quantifiable evidence that synthetic structural fibers can positively influence joint performance, transverse joint faulting, IRI, etc. Therefore, it will be prudent to take the initiative to incorporate the performance benefits of the structural fibers into the mechanistic-empirical design procedure, which in their current form frequently accounts for fibers by artificially increasing the flexural strength of the concrete.

REFERENCES

1. ARA, Inc., ERES Division. Guide for Mechanistic-Empirical Design of New and Rehabilitated Pavement Structure: Appendix JJ Transverse Joint Faulting Model. National Cooperative Highway Research Program, Transportation Research Board, National Research Council, August 2003.

2. Asbahan, R. E., & Vandenbossche, J. M. (2011). Effects of temperature and moisture gradients on slab deformation for jointed plain concrete pavements. *Journal of Transportation Engineering, 137(8),* 563-570.

3. Barman, M., (2014). Joint Performance Characterization of Bonded Whitetopping Overlays. Ph. D Dissertation, Pittsburgh: University of Pittsburgh.Advisor: Vandenbossche, J.

4. Barman, M., & Hansen, B. (2018). Comparison of Performances of Structural Fibers and Development of a Specification for Using Them in Thin Concrete Overlays.

5. Burnham and Tewfik (2007). Development of a Computer Program for Selecting Peak Dynamic Sensor Responses from Pavement Testing. Minnesota Department of Transportation. St. Paul, MN.

6. Burnham, T., & Izevbekhai, B. (2012). Performance of thin jointed concrete pavements subjected to accelerated traffic loading at the MnROAD facility. *Advances in Pavement Design through Full-Scale Accelerated Pavement Testing*, 289-297.

7. Crick, C. (2020). Crack Creep and Joint Performance Behavior of Fiber Reinforced Concrete.

8. Crovetti, J. A., & Darter, M. I. (1985). *Void detection for jointed concrete pavements* (No. 1041).

9. Federal Highway Administration—Office of Research, Development, and Technology: Infrastructure R&D (2017), *The Long-Term Pavement Performance Program,* FHWA-HRT-15-049, Federal Highway Administration, Washington D.C.

10. Janisch, D. (2015). An overview of Mn/DOT's pavement condition rating procedures and indices. *Minnesota Department of Transportation, Saint Paul, MN*.

11. Khazanovich, L., & Yu, H. T. (2001). Modeling of jointed plain concrete pavement fatigue cracking in Pavespec 3.0. *Transportation research record*, *1778*(1), 33-42.

12. Khazanovich, L., Darter, M. I., & Yu, H. T. (2004). Mechanistic-empirical model to predict transverse joint faulting. *Transportation Research Record*, *1896*(1), 34-45.

13. MnDOT (2018). Report on 2017 MnROAD Construction Activities, Report Number: MN/RC 2018-16, Minnesota Department of Transportation, St. Paul, Minnesota.

14. NEW, ON. (2004). Guide for Mechanistic-Empirical Design. *Washington DC*.

15. Selezneva, O., Jiang, J., & Tayabji, S. D. (2000). Preliminary evaluation and analysis of LTPP faulting data-final report (No. FHWA-RD-00-076,).

16. Stone, J. (1991). *THE GEORGIA DIGITAL FAULTMETER. DESIGN, OPERATION AND MAINTENANCE MANUAL. IMPLEMENTATION PACKAGE* (No. FHWA-GA-91-SP9010).

17. Tsai, Y. J. (2016). *Enhancing GDOT's Jointed Plain Concrete Pavement (JPCP) Rehabilitation Program Using Emerging 3D Sensing Technology and Historical Concrete Condition Survey Data* (No. FHWA-GA-17-1319). Georgia. Department of Transportation. Office of Performance-Based Management & Research.

18. Tsai, Y. J., & Wu, Y. C. (2019). *Developing a Comprehensive Pavement Condition Evaluation System for Rigid Pavements in Georgia* (No. FHWA-GA-19-1502). Georgia. Dept. of Transportation.

APPENDIX

Table A-1. ASTM C1609 test results

Specimen ID	MOR (psi)	Residual Strength Ratio (%)	Residual Strength (psi)
Cell 506-7day #1	465	-	-
Cell 506-7day #2		-	-
Cell 506-28day #1	650	-	-
Cell 606-7day #1	465	26.4	122.7
Cell 606-7day #2			
Cell 606-28day #1	635	19.4	124.1
Cell 606-28day #2			
Cell 706-7day #1	480	29.3	140.6
Cell 706-7day #2			
Cell 706-28day #1	675	23	156.4
Cell 706-28day #2			
Cell 806-7day #1	525	45.2	237.3
Cell 806-7day #2			
Cell 806-28day #1	680	37.4	254.3
Cell 806-28day #2			
Cell 139/239-28day #1	610	30.4	185.4
Cell 139/239-28day #2			
Cell 139/239-28day #3			
Cell 705/805-28day #1	542	21.5	116.5
Cell 705/805-28day #2			
Cell 705/805-28day #3			
Cell 705/805-28day #4			

Table A-2. Properties of Concrete used in the NRRA cells

Fresh Concrete Properties								
Cell No.	139	239	705	805	506	606	706	806
Box Test	1,1,1,1	1,1,1,1	2,1,1,2	2,1,1,2	2,2,1,2	2,1,2,2	1,2,2,2	2,1,1,2
SAM No.	0.27	0.3	0.33	0.3	0.3	0.3	0.23	0.31
ASTM C231, Fresh air (%)	8.1	8.0	6.0	7.5	5.4	7.7	7.2	6.6
Hardened Concrete Properties								
Cell No.	139	239	705	805	506	606	706	806
Compressive strength, psi	1,910 (3 days)		2,990 (3 days)		2,740	2,360	2,690	2,510
	2,630 (7 days)		3,720 (7 days)		3,360	3,020	3,050	3,170
	3,800 (28 days)		- (28 days)		4,520	4,050	4,140	4,120
Surface resistivity 28 days, KW-cm	21.3		-		24.3	22.2	23.4	24.4
Air Content, %	8.3		-		5.8	8.5	6.3	6.5
Spacing factor, in.	0.0015		-		0.002	0.002	0.002	0.002
Specific surface, in2/in3	1,485		-		1,600	1,540	1,990	1,630
Dynamic Modulus of elasticity, 28 days	-		-		6.22×10^6 psi	5.21×10^6 psi	5.56×10^6 psi	4.97×10^6 psi
Poisson's Ratio	-		-		0.20	0.20	0.18	0.21
Static Modulus of Elasticity, 28 days	-		-		5.4×10^6 psi	4.3×10^6 psi	4.72×10^6 psi	4.61×10^6 psi

MnDOT Instrumentation plan
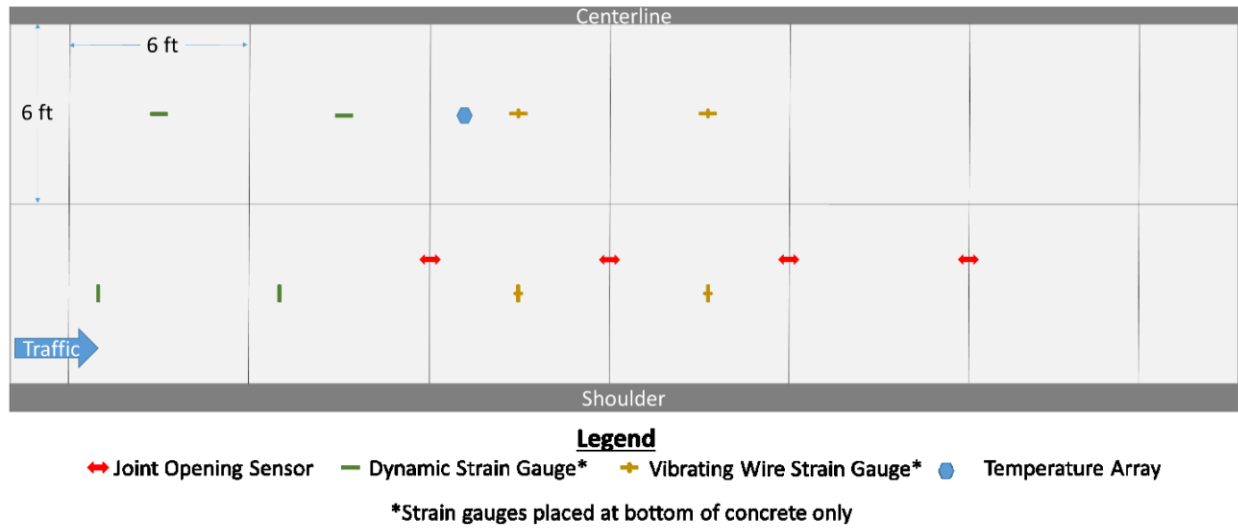
Figure A- 1. Sensor plan for Cell 139, inner lane (MnDOT, 2018).

Figure A- 2. Sensor plan for Cell 239, inner lane (MnDOT, 2018).

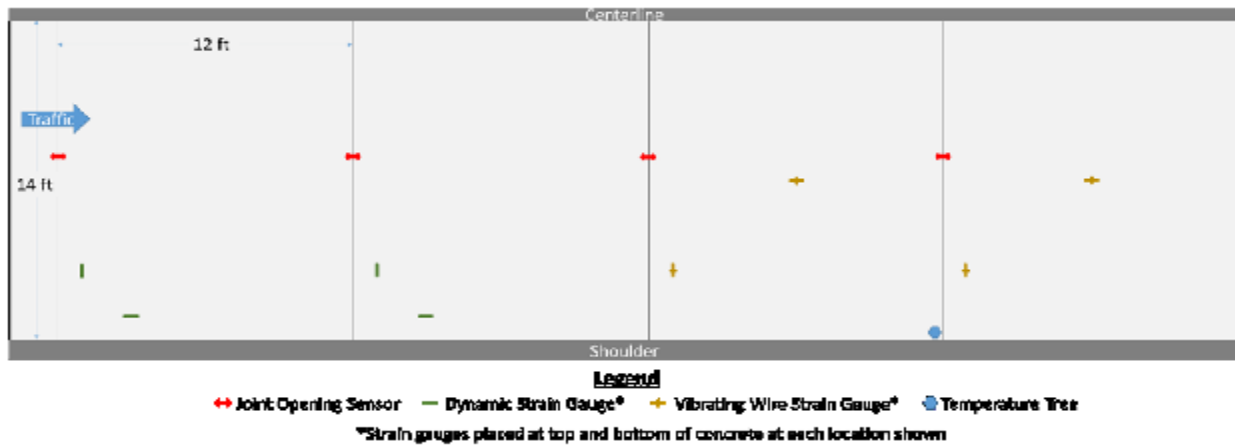*Note: Temperature trees are installed in the outer lane.*

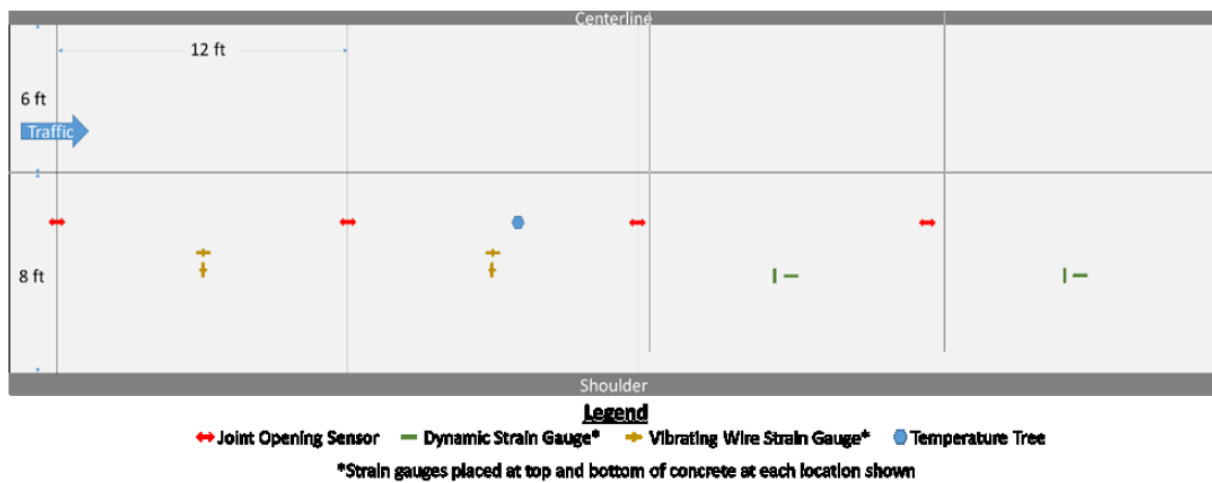Figure A- 3. Sensor plan for Cell 705, driving lane (MnDOT, 2018).

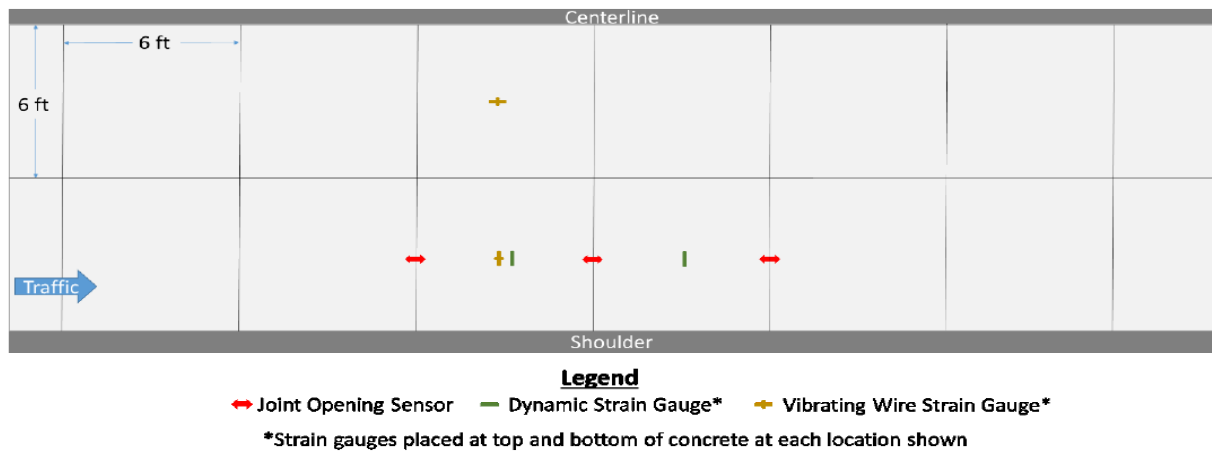Figure A- 4. Sensor plan for Cell 805, driving lane (MnDOT, 2018)

Figure A- 5. Sensor plan for Cell 506, driving lane (MnDOT, 2018).
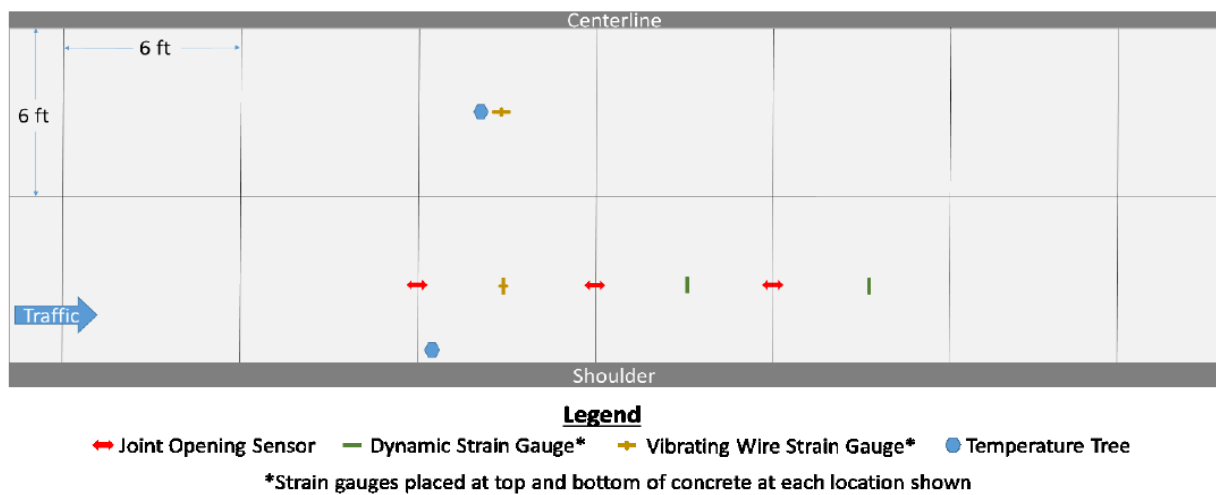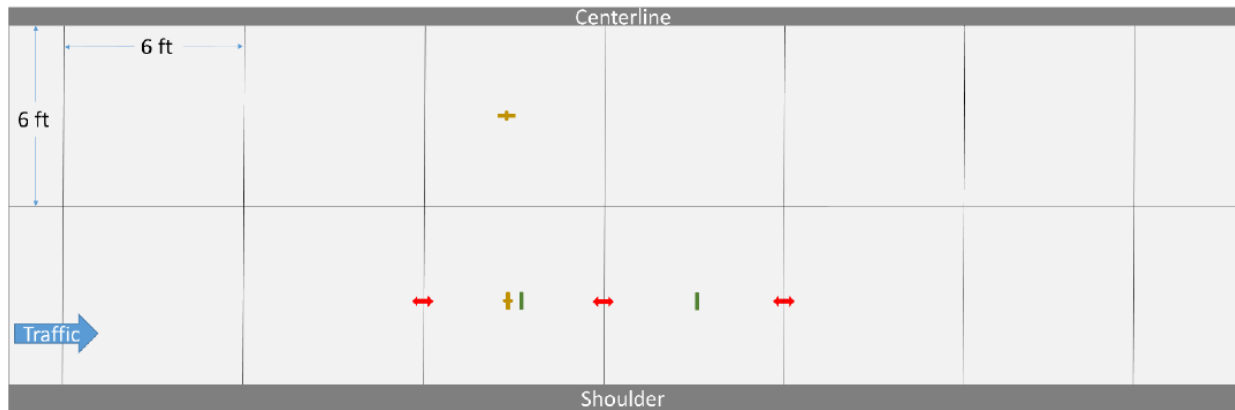

Figure A- 6. Sensor plan for Cell 606, driving lane.

Figure A- 7. Sensor plan for Cell 706, driving lane.
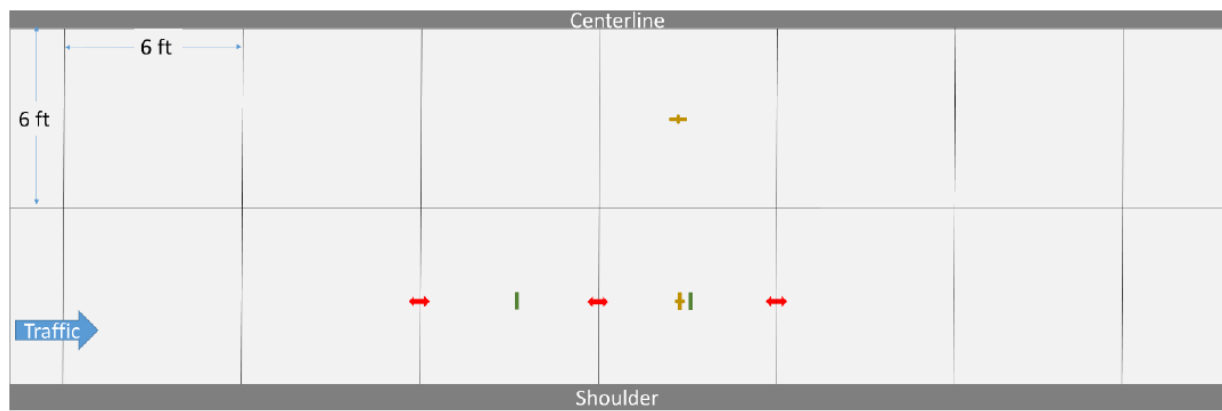
Figure A- 8. Sensor plan for Cell 806, driving lane.
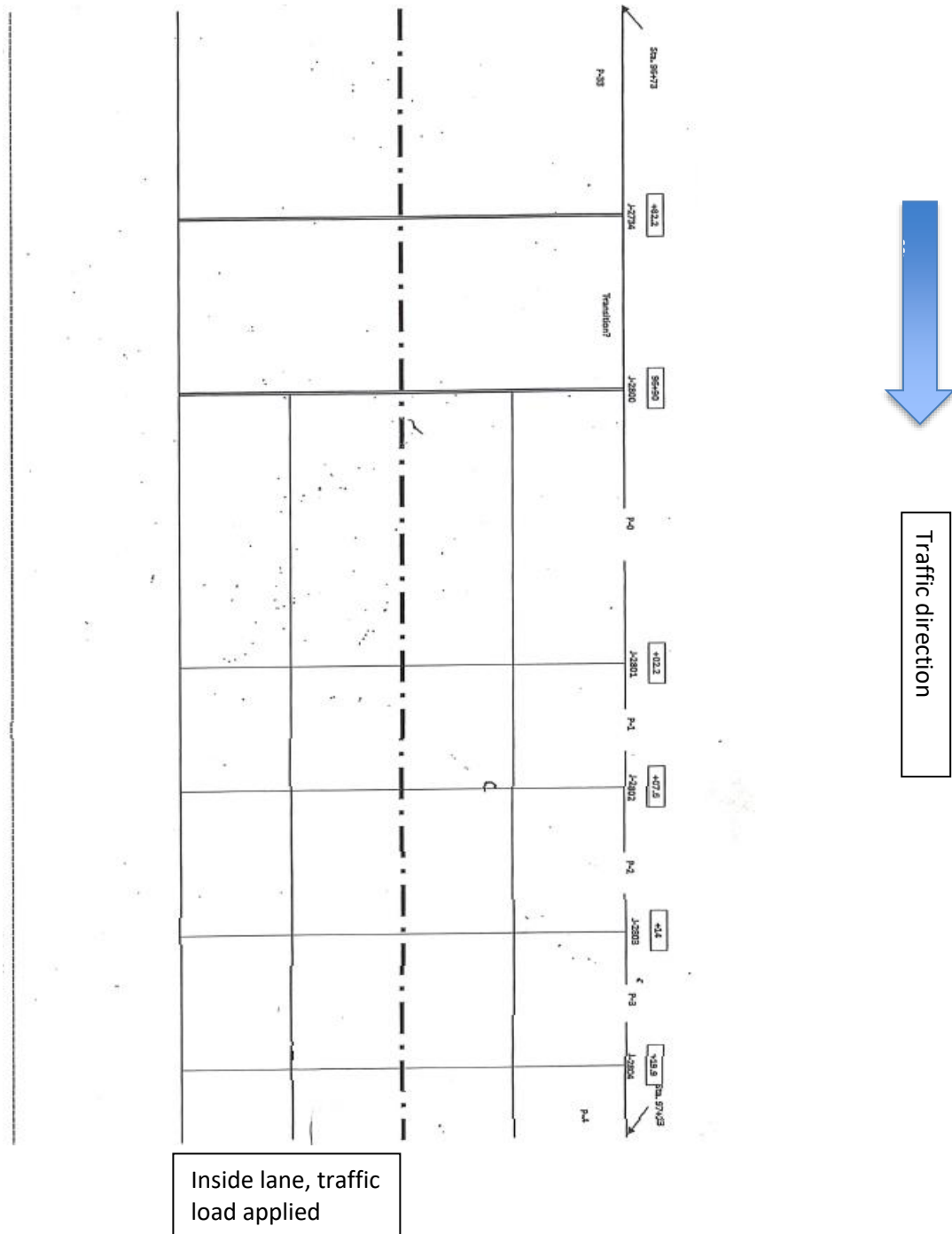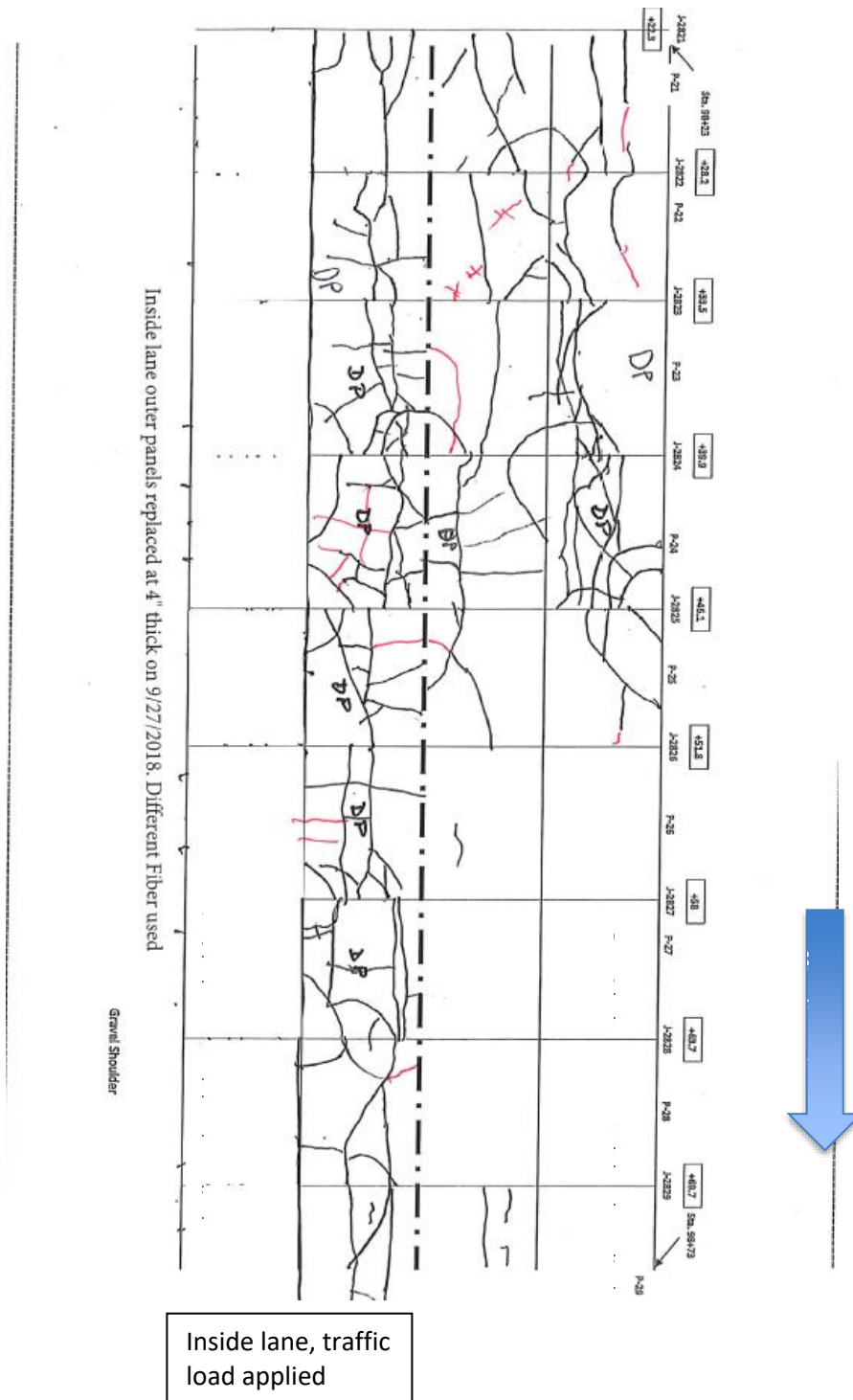
Figure A- 9: Distress map for Cell 139
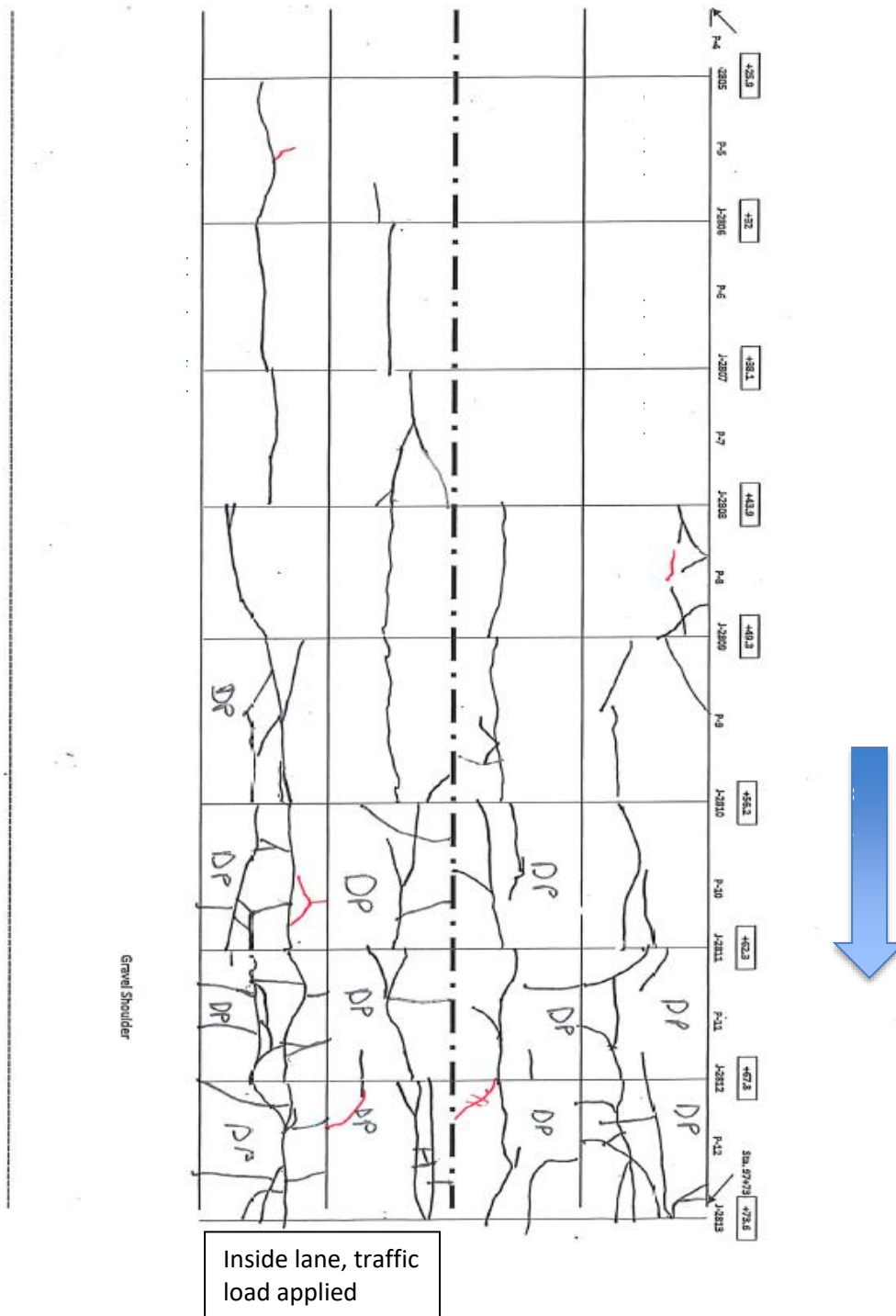
Cracks until March 2020; cracks colored red were documented on March 24, 2020.
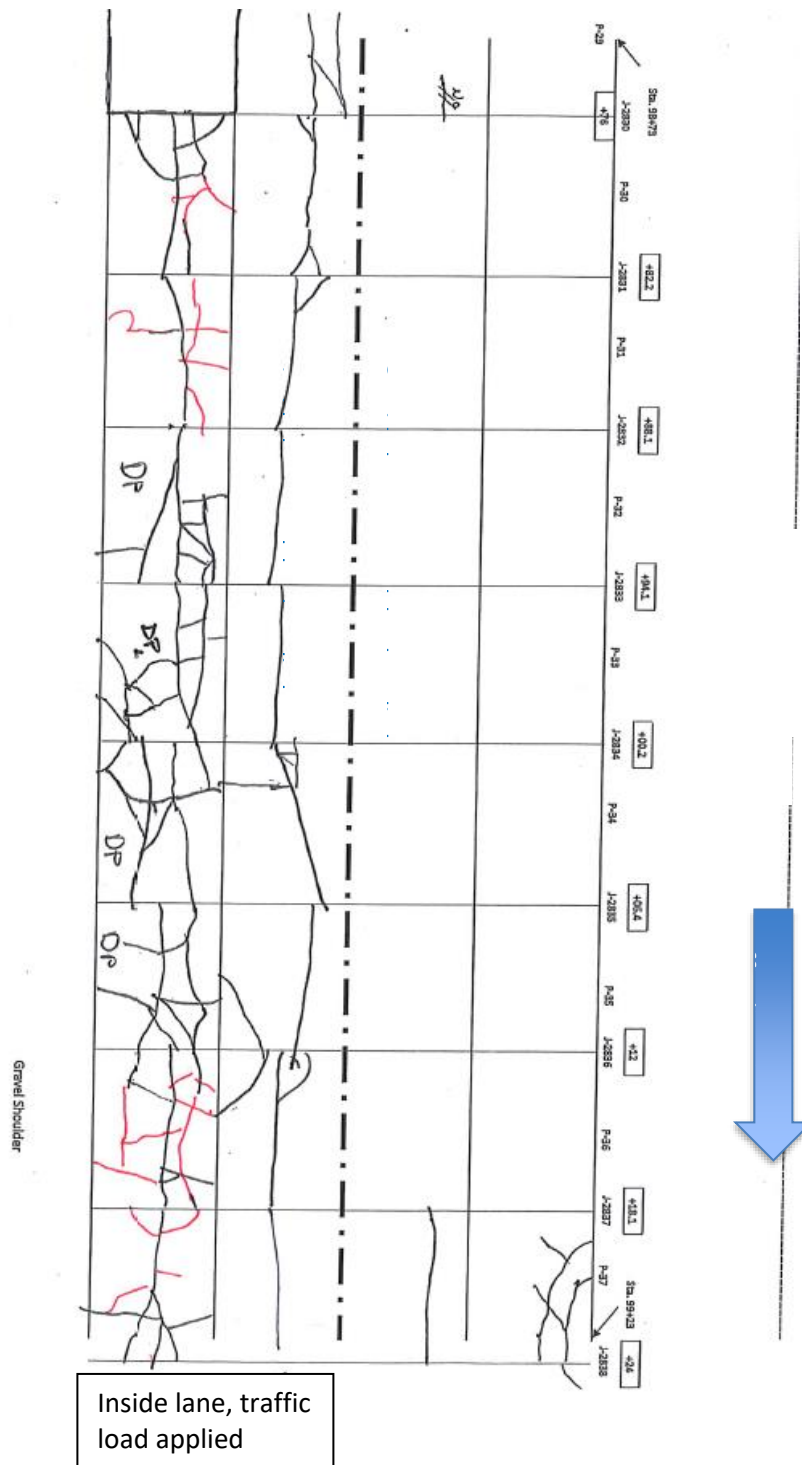
Figure A- 10: Distress map for Cell 139 contd.
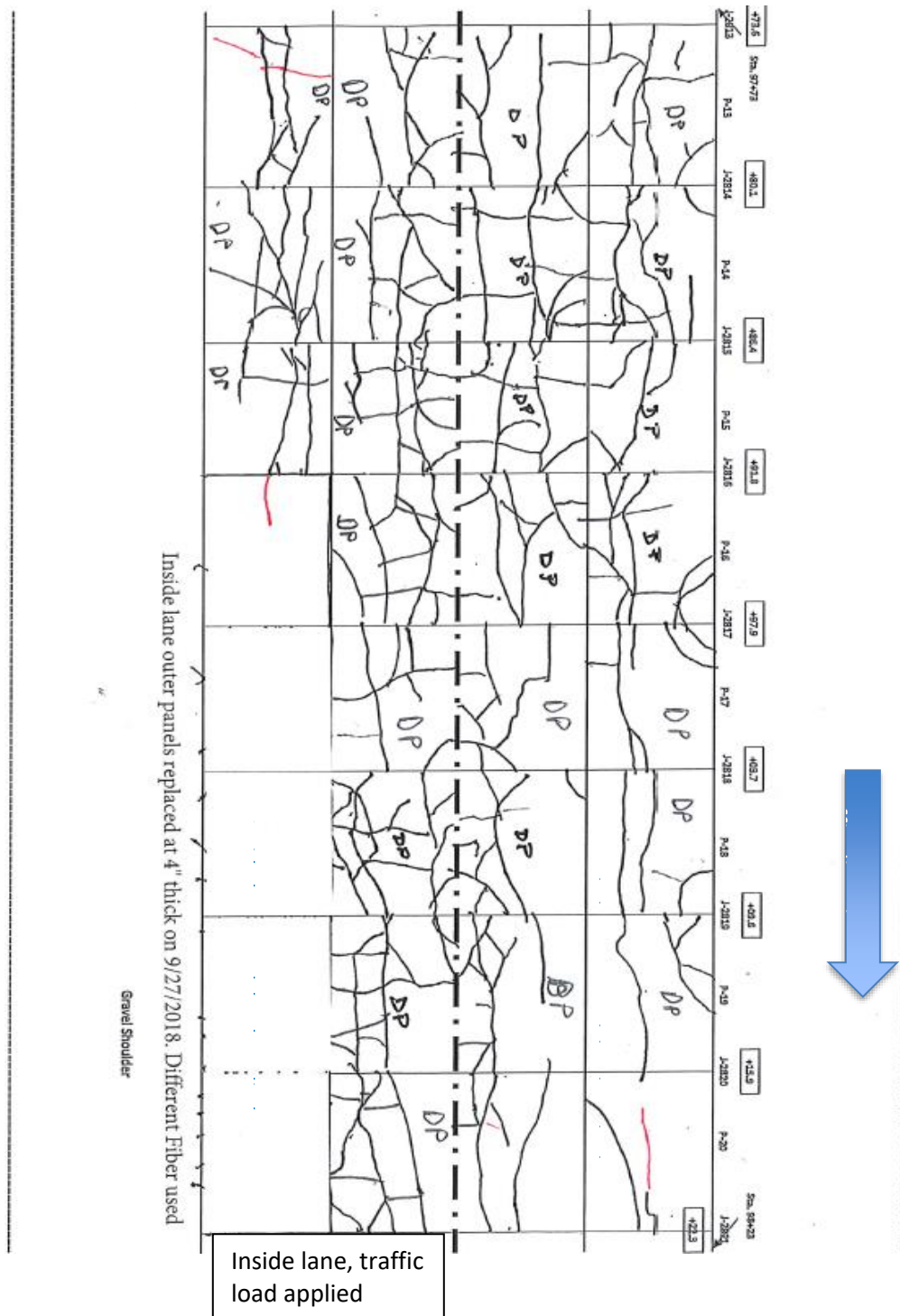
Cracks until March 2020; cracks colored red were documented on March 24, 2020.

Figure A- 11: Distress map for Cell 139 contd.

Cracks until March 2020; cracks colored red were documented on March 24, 2020.
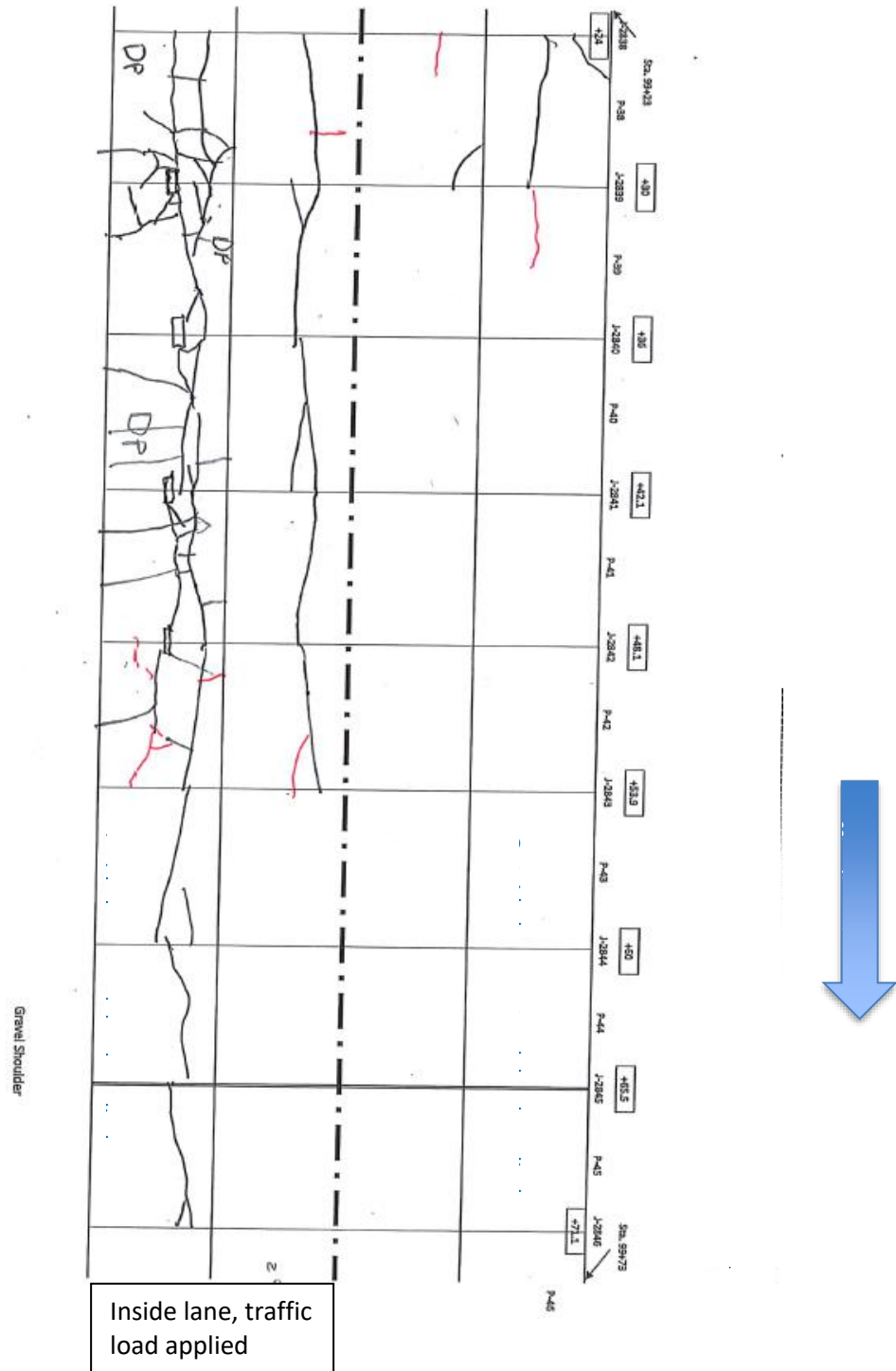
Figure A- 12: Distress map for Cell 139 contd.

Cracks until March 2020; cracks colored red was documented on March 24, 2020.

Figure A- 13: Distress map for Cell 139 contd.

Cracks until March 2020; cracks colored red was documented on March 24, 2020.

Figure A- 14: Distress map for Cell 139.